Characterization of a c-Fos reporter system for in vivo imaging in the mouse auditory cortex

Dissertation

Zur Erlangung des Grades

Doktor der Naturwissenschaften

Am Fachbereich Biologie

Der Johannes Gutenberg-Universität Mainz

Sarah Muller

geb. am 09.08.1989 in Neuchâtel (NE, Schweiz)

Mainz, 2023

Dekan: Prof. Dr. Eckhard Thines

1. Berichterstatter: Prof. Dr. Simon Rumpel

2. Berichterstatter: Prof. Dr. Carsten Duch

Tag der mündlichen Prüfung: 12.09.2023

Acknowledgments

All experimental work and analyses included in this thesis was performed by Sarah Muller[1], with the exception of:

The cloning and viral production, which were executed by Eike Kienle[1] and Dominik Aschauer[1], under the supervision of Simon Rumpel[1].

The primary derived cortical cell culture experiment, which was performed by Jonas Schroer[2], under the supervision of Anne Sinning[2]. These findings were included in order to better characterize the mouse model I used for my experiments, and therefore interpret the measurements in vivo. I would like to thank you both for the very nice collaboration.

The development of the in vivo pipeline to image chronically the same neuronal populations, localised by their nuclei, which was developed by Dominik Aschauer[1].

The development of the image pre-processing pipeline for c-Fos signal in chapters 4-7, which was accomplished by David Lüdke[3], and the development of the image processing pipeline for c-Fos and calcium signals in chapters 4-7, which was done by Bastian Eppler[3] and Dominik Aschauer[1], both under the supervision of Matthias Kaschube[3] and Simon Rumpel[1].

The analyses of the calcium signal in chapters 6 and 7, which was performed by Johannes Seiler[1]. This collaboration was a tremendous help and joy. Thank you also for the relentless enthusiasm and the rich conversation to try and understand the results of the thesis.

I would like to thank also my colleagues Giuseppe Cazzetta[1] and Takahiro Noda[1] for their endless support throughout my whole PhD. This project would not have been possible without you.

I would like to thank my supervisor, Simon Rumpel[1], whose continuous help for every aspect of my PhD project allowed me to learn a lot and grow as a scientist.

Thanks also to Carsten Duch and Thomas Mittmann for the nice supervision during my PhD, in their quality as members of the thesis advisory committee.

And finally, a big thanks to my family and my husband Alexandre who never stopped believe in me, and support me in any way possible.

Affiliations

1. Arbeitsgruppe Prof. Simon Rumpel, Institut für Physiologie, Universitätsmedizin, Johannes Gutenberg-Universität, Mainz

2. Arbeitsgruppe Prof. Heiko Luhmann, Institut für Physiologie, Universitätsmedizin, Johannes Gutenberg-Universität, Mainz

3. Research Group of Matthias Kaschube, Frankfurt Institute for Advanced Studies, Johann Wolfgang Goethe-Universität, Frankfurt am Main

Abstract

Introduction and objective: c-Fos is an immediate early gene: first genes expressed upon depolarisation. It is coding for a transcription factor controlling the expression of late genes, involved in many cellular processes like apoptosis, proliferation and differentiation. Since the eighties, it is a very popular tool to tag and manipulate active neurons in the brains. It has recently been linked to memory, as cells expressing the gene during fear conditioning, reactivated a few days later can elicit freezing in mice. However, the gene is unspecific to neurons and neuronal activity. Moreover, the causal link between this IEG and neuronal activity or memory remains unclear. Therefore, we wanted to investigate how tight is the correlation of c-Fos levels and neuronal activity.

Method: To study the correlation between c-Fos expression and neuronal activity, we created a mouse model expressing a c-Fos reporter (tet-off system derived from TetTag mice: c-Fos-tTA + TRE-BFP) and the widely used calcium indicator GCaMP6m. To track the same cells over weeks, we used a nuclear marker, the fusion protein H2B-mCherry. DNA coding for the three markers were packaged into adeno-associated viral particles (AAV2/8) and injected in the auditory cortex of adult black six mice (C57BL/6J). GCaMP6m and H2B-mCherry were expressed specifically in neurons, thanks to the human synapsin promoter (hSyn). We chronically observed the same cells expressing the three markers through a cranial window, under a two-photon microscope, for up to three weeks, under basal conditioning, during sound presentation and during fear conditioning.

Results: The model is not capturing the subtle dynamics of activity-induced c-Fos, because of unspecific triggering of gene expression (stress, inflammation and exposure to novel environment). In addition, the slow synthesis time due to two layers of TetTag system and slow decaying time of BFP result in a poor temporal resolution of c-Fos reporter. However, when classifying cells as c-Fos positive and negative, we could observe a systematic difference in neuronal activity. c-Fos positive cells are responsive to a broader range of sounds and present a higher rate of replay events in their spontaneous activity, once more suggesting a role of the IEG in memory.

Conclusion: Rather than reflecting purely neuronal activity, c-Fos in sensory cortices may play a role in population coding to generalise stimuli and to create memory. Hence, the IEG is probably not suited to tag active neurons, but seems adequate to label engrams.

Table of Contents

Abbreviations

ACx: auditory cortex

A1/A2/AAF: primary/secondary/anterior auditory field

(r)AAV(2/8): (recombinant) adeno-associated virus (genome from serotype 2, capsid from serotype 8)

BFP: blue fluorescent protein

C57BL/6JRj: C57 black 6 mouse inbred strain (originate from Jackson laboratory, bred in Janvier laboratory)

CCD camera: charge couple device-based camera

c-Fos: cellular Finkel-Biskis-jinkins Osteogenic Sarcoma

CS: conditioning sound

ctl gr.: control group

DIV: day in vitro

DM: dorsomedial field or dichroic mirror

Dox: doxycycline

ΔF/F0: change in fluorescence-resting fluorescence ratio

FC gr.: fear-conditioned group

FOV: field of view

GCaMP(6m): green fluorescent protein, calmodulin, M13 peptide=myosine light-chain kinase peptide sequence 13 (version 6 medium)

GECI: genetically encoded calcium indicator

H2B: histone 2B

hSyn: human synapsin promoter

IEGs: immediate early genes

L2/3: cortical layer 2 and 3

mCherry: monomeric red fluorescent protein from mFruits family

MGV: mean grey value

NND: nearest neighbour distance

NNSI: normalised soma signal intensity

OFV: objective function value

PFA: paraformaldehyde

ROI: region of interest

SEM: standard error of the mean

SSN: soma Signal-to-Noise ratio

Tet-off: tetracycline-inducing expression off

TetTag: tetracycline inducible transgenic mice to tag c-Fos expressing cells

TRE: tetracycline-responsive element

t-serie: time-serie

tTA: tetracycline-controlled transactivator protein

TTX: Tetrodotoxin

Chapter 1. Introduction

1.1 C57BL6J mouse model for auditory research

Since the antiquity in ancient Greece, animals serve as model to understand and study human anatomy and physiology. Milestones in neurosciences were discovered using animal models. Here are some notable examples: brain is the seat of intelligence (6th century BC, Alcmaeon of Croton on dogs) (Ericsson, Crim, & Franklin, 2013), electricity is present in the nerves (18th century, by Luigi Galvani on frogs) (Piccolino, 1997), neurons are the functional units for the nervous system (19th century, by Ramon y Cajal and Wilhelm von Waldeyer-Hartz, on chicks) (Waldeyer, 1891), neurons are connected via synapses (1894, Charles Sherrington on frogs) (Sherrington, 1906), neurons use neurotransmitters to communicate (1921,Otto Loewi on frogs) (Loewi, 1921), the brains hemispheres are functionally specialized (1960s, Roger W. Sperry on cats),(Sperry, 1961) … specific cell ensembles in the hippocampus are able to store memory (2012, Liu et. Al on mice) (X. Liu et al., 2012).

Rodents fulfil several quality required for animal models: small size, short generation times, and capacity to be easily reared in the laboratory. Furthermore, as social mammals, they share a lot of similarity with the genome, anatomy, physiology and behaviour of humans. About 99% of mouse genes have orthologs in human genome (Bowl & Dawson, 2014). During the 20th century, rats were heavily used as a model for neuroscience, alongside with dogs, cats, rabbits and monkeys. The size of these animals was suited for the electrophysiology and brain lesions, the two main methods to investigate brain function at that time. It is with the development of inbreed techniques, in 1909, allowing minimal changes in genetic background (Ericsson et al., 2013; Ohlemiller, Jones, & Johnson, 2016), as well as the creation of transgenic animals from 1976 (Gordon, Scangos, Plotkin, Barbosa, & Ruddle, 1980; Jaenisch, 1976), allowing genetic engineering, that mice became the most popular animal model in all fields of research. In addition, the development of optical non-invasive techniques to measure neuronal activity in vivo (e.g. calcium imaging (Grienberger & Konnerth, 2012)), as well as genetic tools to manipulate neuronal activity (e.g. Optogenetic, (Aravanis et al., 2007)) in mice and rats made of rodents favourite models for neuroscientists (Ericsson et al., 2013; Keifer & Summers, 2016; White, 2016).

Regardless of the difference of hearing range of mice and human (3-100 kHz and 20 Hz-16 kHz, respectively) (Kanold, Nelken, & Polley, 2014), the inner ear (mammals cochlea composed with the receptor organ for hearing, organ of Corti) (Castro & Monteiro, 2022; L. Wang et al., 2020) and brain of mice work in a very similar way as in humans, with a high overlap of genes and proteins critical for hearing and balance function (Ohlemiller et al., 2016). Jackson laboratories originally bred C57BL/6J mice in 1948, and since then the strain is widely used in research, including the auditory neurophysiology (Bowen, Winkowski, & Kanold, 2020; Kendall & Schacht, 2014). Despite the known early hearing loss of the strain (Henry & Chloe, 1980; Johnson, Erway, Cook, Willott, & Zheng, 1997; Jones et al., 2006), and because presbycusis in the strain appears only from 3-6 months of age (Bowl & Dawson, 2014), young C57BL/6J mice are a reference in the auditory field. The main argument to choose the strain is the common genetic background with most of the transgenic mice available, and therefore the broad range of experimental design and manipulations possible, including in the central nervous system. In the auditory physiological research field, C57BL/6J mice have been used in studies involving two-photon calcium imaging (Bandyopadhyay, Shamma, & Kanold, 2010; Bathellier, Ushakova, & Rumpel, 2012; Honma et al., 2013; J. B. Issa et al., 2014), voltage sensitive imaging (Sawatari et al., 2011; Takahashi et al., 2006), anatomical studies (Barkat, Polley, & Hensch, 2011; Hackett, Barkat, O'Brien, Hensch, & Polley, 2011; Hofstetter & Ehret, 1992; Oviedo, Bureau, Svoboda, & Zador, 2010), genetic manipulation (Barkat et al., 2011; Rotschafer & Razak, 2013) and behavioural analyses (Tsukano, Hishida, & Shibuki, 2011; Tsukano et al., 2015).

Unlike hippocampus and prefrontal cortex, stimuli to evoke neuronal activity in the primary sensory cortices are rather simple. Visual, auditory, olfactory, gustatory and somatosensory stimuli have several features though and multisensory responses should be kept in mind when interpreting neuronal activity in the respective brain regions. Nevertheless, the features of sounds for instance, can easily be reduced to a unique frequency (pure tone) and amplitude. The interpretation of pure tone evoked-activity is more conservative compared to activity driven by complex sounds, as suggested by the organisation of the auditory cortex depicted by tonotopic maps (Kanold et al., 2014; Tsukano et al., 2015). For this reason, the auditory cortex offers a unique way to limit the complexity of experimental designs and analysis of neuronal activity.

For this project, we used C57BL/6J mice to monitor neuronal activity in the auditory cortex during sound presentation and silent period.

1.2 Evoked and spontaneous activity in the auditory cortex

Inspired by Galvani's work on muscles and nerves during the 18th century, Richard Caton demonstrated for the first time during the 43rd meeting of the British Medical Association in Edinburgh, in 1875, that electricity is also present in the brain (on a rabbit and a monkey). This marked the beginning of measure of activity in the brain, and the development of electrophysiology and electroencephalography (Brazier, 1984). A few years before this meeting, Fritsch and Hitzing developed a method to electrically stimulate the brain (Fritsch & Hitzig, 1870) and could associate several part of the dogs brain to motricity and perception of senses. Following this trend, in 1875 David Ferrier was the first scientist to associate the auditory cortex to auditory perception by electrical stimulation in monkeys (Heffner, 1987). In 1898, Vladimir Efrimovich Larionov was the first to measure an increase in activity in the auditory cortex of dogs after presenting three different tone forks, today described as sound-evoked activity (Brazier, 1984).

Because the history of brain activity recording is tightly linked to brain stimulation, evoked activity was considered until the end of 20th century as the relevant information, and spontaneous activity as noise (Afrashteh et al., 2021). However, since the beginning of brain activity recording, scientists witnessed the constant activity of the brain, even in a resting state and in sensory cortices when no stimulation was presented. Only recently though, the importance of spontaneous activity to fully explain neuronal activity was acknowledged (Arieli, Sterkin, Grinvald, & Aertsen, 1996).

During the 20th century, most of the measures of brain activity in animals were performed under anesthesia, because of the invasive techniques, like electrophysiology, requiring craniotomies. But growing evidences show that activity in sensory cortices is different in anesthetised and awake animals (Filipchuk, Schwenkgrub, Destexhe, & Bathellier, 2022; Omer, Fekete, Ulchin, Hildesheim, & Grinvald, 2019; Sellers, Bennett, Hutt, Williams, & Fröhlich, 2015). In studies observing neuronal activity in visual and auditory cortices under anesthesia, spontaneous activity was observed to display similar patterns as those recorded from the stimuli-evoked activity, linking memory consolidation during sleep to replay events (Hoffman et al., 2007; Ji & Wilson, 2007; Sakata & Harris, 2009; Xu, Jiang, Poo, & Dan, 2012). But,

spontaneous activity recorded brain-wide in awake state displays complexity that cannot be attributed to replay events solely, but was suggested to be driven by behaviour in general, such as movements, wakefulness and motivation (Allen et al., 2019; Gründemann et al., 2019; Stringer et al., 2019).

Activity observed in sensory cortices can originate from the bottom-up sensory inputs (evoked activity), other sensory modalities, a phenomenon called multisensory processes (Bizley & Dai, 2020), and from top-down inputs, involving complex behaviours engaged in reward, task engagement and social context (Caras et al., 2022). Evidences for direct connections between the auditory cortex and the visual cortex (Campi, Bales, Grunewald, & Krubitzer, 2010), or somatosensory cortex (Smiley et al., 2008) provide a clear explanation for multisensory processes. In the auditory cortex, spontaneous activity in awake mice was linked to replay events, as well as multisensory processes, motor activity and complex behaviour described above (Bizley & Dai, 2020; Caras et al., 2022; Farley & Noreña, 2013; Kuchibhotla & Bathellier, 2018; Luczak, Barthó, & Harris, 2009; Sakata & Harris, 2009).

Here, we recorded chronically both evoked and spontaneous activity in the auditory cortex of awake mice, in order to include all activity observed in this brain region, and avoid considering spontaneous activity as noise, but rather as a necessary part for auditory information processing.

1.3 Representational drift

The functional unit of the brain, neuron, in contrast to all other cell types in mammals, can survive during the entire life of the organism and beyond (Magrassi, Leto, & Rossi, 2013). The structural stability of the brain, the intuitive notion that a sensory stimulation is perceived similarly from day to day, and the limitations of tools to measure neuronal activity at a single time point, shaped the idea that a stable ensemble of cells encodes a specific stimulation in the brain. This idea is also the foundation of the hypothesis about learning and memory formation. Plasticity, like changes observed in connections and neuronal activity, would be due to learning processes, when stable structures would represent the engraved memory (Driscoll, Duncker, & Harvey, 2022; Masset, Qin, & Zavatone-Veth, 2022; Rule, O'Leary, & Harvey, 2019). During the past 20 years, development of electrophysiology and optical imaging techniques allowing chronical measure of neuronal activity at a single neuron resolution, enabled several groups to witness shift in activity in neuronal populations observed over time and in response to

the same stimulations. This is true in several brain regions ranging from sensory cortices, motor cortex to hippocampus (Clopath, Bonhoeffer, Hübener, & Rose, 2017; Driscoll et al., 2022; Masset et al., 2022; Rule et al., 2019).

In our lab we recently observed a similar drift in the auditory cortex (Chambers, Aschauer, Eppler, Kaschube, & Rumpel, 2022). For this PhD project, we hypothesised that the function of neurons is modulated by gene expression, based on the central dogma of molecular biology (DNA makes RNA, and RNA makes protein, (Crick F. H., 1958)). To test the hypothesis, we used a similar design as our colleagues and further investigate the dynamics of sound-evoked activity at a gene expression level.

1.4 Tools to measure neuronal activity in the brain

To understand how the central nervous system is working, there has been historically two strategies: manipulation or measure of brain activity. Pierre Flourens pioneered experiments in neuroscience, developing the localised brain lesions in the beginning of 19th century, as well as the use of anesthesia for the procedures on animals (Pearce, 2009). As mentioned above, Fritsch and Hitzig developed electrical brain activation in 1870 (Fritsch & Hitzig, 1870). Only a few years after, the first brain activity recording was performed by Richard Caton, in 1875 (Brazier, 1984). Thus, manipulation in the brains preceded measure of the activity. Today, new methods to manipulate brain activity have proven very useful in the quest of unravelling the function of the brain (transcranial magnetic stimulation (TMS), optogenetic, designer receptor exclusively activated by designer drugs (DREADD)). However, in this section, I will only focus on the methods to measure neuronal activity, as in the course of my PhD project I used several of the latter.

When the brain is more active in a specific region, many local changes can be observed and used as a proxy to measure activity. Here is a list of a few methods widely used in research:

1. Microelectrode arrays (MEAs): measure of changes in membrane potential during depolarisation of a neuron. Alessandro Volta invented in 1799 the electrical battery, consisting in two electrodes (Sethi, 2016). As mentioned before, the first recording ever made in the brain was performed by Richard Caton and demonstrated in 1875. The first implantable electrode to record chronically neuronal activity in the brain was introduced in 1958 by Felix

Strumwasser (Strumwasser, 1958), and the first silicon-based multi electrode, a technique still widely used today, was produced by Wise et al. in 1970 (Wise, Angell, & Starr, 1970).

2. Electroencephalography (EEG): same measure as MEAs, but from the skull and not directly in the brain. The first published photograph of an electrical brain activity recording was in 1913 by Vladimir Vladimirovich Pravdich-Neminsky, from an anesthetised dog (Brazier, 1984). The first modern EEG recording, non-invasive, from the scalp, was performed by Hans Berger on a human subject, in 1929 (Berger, 1929).
3. Functional magnetic resonance imaging (fMRI): measure of changes in oxygen level in the blood, due to the increase metabolism of active neurons. Shortly after the discovery of the presence of electric currents in the brain, Charles Roy and Charles Sherrington discovered the link between the brain function and the blood circulation, in 1890 (C. S. Roy & Sherrington, 1890). In 1936, Linus Pauling and Charles Coryell discovered the different magnetic properties of oxygenated and non-oxygenated hemoglobin (Pauling & Coryell, 1936). Finally, in 1990, Seigi Ogawa exploited those discoveries to develop the blood-oxygen-level-dependent imaging technique (BOLD), used by fMRI (Ogawa, Lee, Nayak, & Glynn, 1990).
4. Optical imaging of intrinsic signals: similar measure as fMRI, based on hemodynamics. However, the recording is executed by a CCD camera, and the principle is based on the difference in light absorption properties of the oxygenated and deoxygenated hemoglobin (see 1.4.1).
5. Calcium imaging: measure of increase in calcium levels in neuron depolarised, following the opening of ligand- and voltage-gated calcium channels (see 1.4.2).
6. Measure of immediate early genes (IEGs) level: after depolarisation of a neuron, calcium dependent cascades of protein phosphorylation lead to the activation of cAMP response element binding protein (CREB), a transcription factor. CREB controls the expression of the IEGs; the first genes to be expressed after depolarisation (see 1.4.3).

Measuring the changes in membrane potential (MEAs, EEG), the decrease in oxygen level in the blood (fMRI, intrinsic imaging), the increase in calcium concentration (Calcium imaging) and the increase in immediate early genes expression (IEGs) is only a selection of observable readouts for brain activity. Indeed, the metabolic changes in

the brain can also be measured with the uptake of glucose by active cells (fluorodeoxyglucose in positron emission tomography, known as PET scanning) (Berti, Mosconi, & Pupi, 2014). Genetically encoded indicators to measure pH changes during neurotransmitter release in synaptic vesicles (pH sensors), and binding of neurotransmitters on post-synaptic receptors (neurotransmitter sensors) (Day-Cooney, Dalangin, Zhong, & Mao, 2022; Lin & Schnitzer, 2016; Papaioannou & Medini, 2022; Roth & Ding, 2020; H. Wang, Jing, & Li, 2018; W. Wang, Kim, & Ting, 2019) can as well be used for the same purpose. To be noted, a promising method to measure changes in membrane potential in a cell-type specific manner, with genetically encoded voltage indicators (GEVIs) is evolving greatly since the first GEVI developed in 1997 (Siegel & Isacoff, 1997).

The advantages of this plethora of methods is the variety of application possible, and the cross-validation of principles or observations in the central nervous system. What is very delicate though is to compare the results from the different techniques. One should keep in mind when comparing results from different group of research, the following sources of discrepancies:

- Measure vs manipulation (e.g. calcium imaging vs optogenetic)
- Invasive vs non-invasive measure (e.g. electrode vs EEG)
- Direct vs indirect measure (electrophysiology vs calcium imaging)
- In vitro vs in vivo experiment (e.g. cell culture vs model organism)
- Awake vs anesthetised animal
- Fixed vs freely moving animals (freely moving measurements possible with miniscopes (for review see (Stamatakis et al., 2021))
- Acute vs chronic measure (e.g. calcium dyes vs genetically encoded indicators)
- Cell-type specific vs whole tissue recording (only genetically encoded probes can allow cell-type specificity)
- Time resolution (e.g. nanoseconds with electrophysiology to hours with IEGs)
- Space resolution (molecule, cell, region, hemisphere, whole brain)
- Inter- and intra-species differences (mouse vs human, sex differences or differences in individual animals)
- Cortical layers differences (e.g. in sensory cortices, L2/3 neurons receive input from thalamus and L4 and project only in the cortex, whereas L5 neurons receive inputs from thalamus, L2/3, L4 and interneurons from layer 5, and project in the cortex and subcortical areas (Adesnik & Naka, 2018))
- Regional difference (e.g. Auditory cortex vs hippocampus)

1.4.1 Optical imaging of intrinsic signals

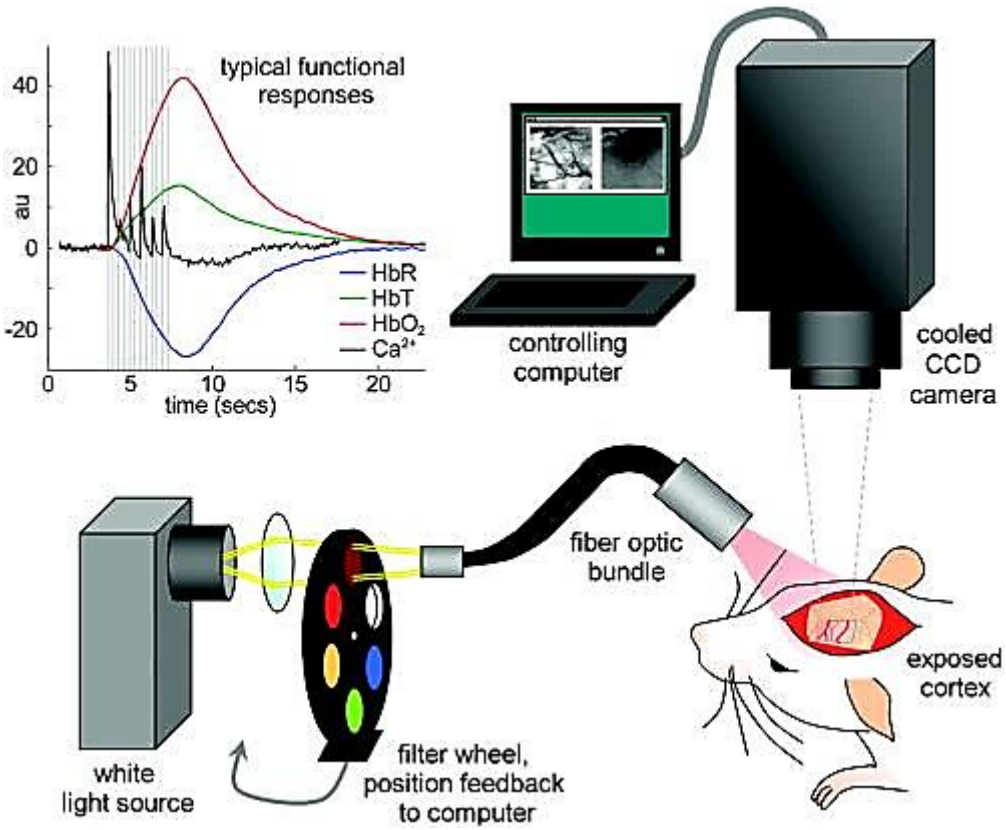

Figure 1. Typical setup for optical imaging of intrinsic signals.

(Hillman, 2007)

Illumination of the exposed cortex with specific wavelength allow to capture with a CCD camera changes in hemodynamic, like increase in deoxyhemoglobin and blood volume in active brain regions. The correlation between blood and the nervous system is called neurovascular coupling (Prakash et al., 2009; Soloukey et al., 2023). HbR=reduced hemoglobin, HbT=total hemoglobin

Optical imaging of intrinsic signals was developed in 1986, by Grinvald and colleagues (Grinvald, Lieke, Frostig, Gilbert, & Wiesel, 1986). The group measured activity in the barrel cortex of rats and cats when stimulating whiskers, with a photodetector array and a voltage sensitive dye. They could detect a difference in reflected light when the area was active or not, distinguishable from the light reflected by the dye. Since the development of the method, several sources were hypothesized to explain the changes observed in the reflection of light, when the brain is exposed to 500-700nm wavelengths (1. and 2.) or near-infrared lights (3.), 700-800nm: 1. Changes in oxygen saturation level of the hemoglobin. Indeed, oxyhemoglobin and deoxyhemoglobin do not only have different magnetic properties, but they also absorb different wavelength

of the light (Mansouri & Kashou, 2012; Prakash et al., 2009). 2. Changes in blood volume in active brain area, changing optical access to the area due to the difference in density. 3. Light-scattering changes due to ion/water movement, changes in extracellular spaces, in capillary diameter, and neurotransmitter release (Frostig, Lieke, Ts'o, & Grinvald, 1990; G. H. Kim, Kosterin, Obaid, & Salzberg, 2007; Salzberg, Obaid, & Gainer, 1985; Sato, Nariai, Momose-Sato, & Kamino, 2016).

Intrinsic imaging was successfully applied in visual and somatosensory cortices of several animal models from the beginning of the method (Kanold et al., 2014). For the auditory cortex, it was only from the development of tone sequences protocol in the beginning of the 21st century that the quality of the signal matched the one from the other sensory cortices (Nelken et al., 2004). One reason for the poor signal measured with the method in the auditory cortex was the deep anesthesia of the animal models, inhibiting the activity of the brain area (Kanold et al., 2014).

Advantages of the method are the large-scale mapping in a relatively short time, as well as the possibility to apply the method on lightly anesthetised animals, preventing the need for habituation of the animal model to the setup. However, hemodynamic is an indirect measure of neuronal activity and is very slow (Papaioannou & Medini, 2022). Plus, due to small amplitude changes of hemodynamic responses, imaging can only detect signal through thinned or removed skull, although recent efforts were made to allow intrinsic signal imaging through an intact skull (Nsiangani et al., 2022). Furthermore, intrinsic imaging has a limited resolution, not detecting very selective tuning cells isolated and with a poor response amplitude. Another limitation is also the layer specificity not measurable (Kanold et al., 2014; Sato et al., 2016). Also, even if the technology has been used during surgery on humans, to localise the foci of epileptic patients or brain tumours (Sato et al., 2016), the technology can't be used to measure neuronal activity in healthy humans.

For this project, we used the method to estimate the localisation of the auditory cortex during sound presentation, in order to validate the position of the cranial window implanted on mice. In addition, we could target the primary auditory field (A1), the anterior auditory field (AAF), the dorsomedial field (DM) and the secondary auditory field (A2) for the subsequent recording of neuronal activity (Tsukano et al., 2015).

1.4.2 Calcium imaging: CCaMP6

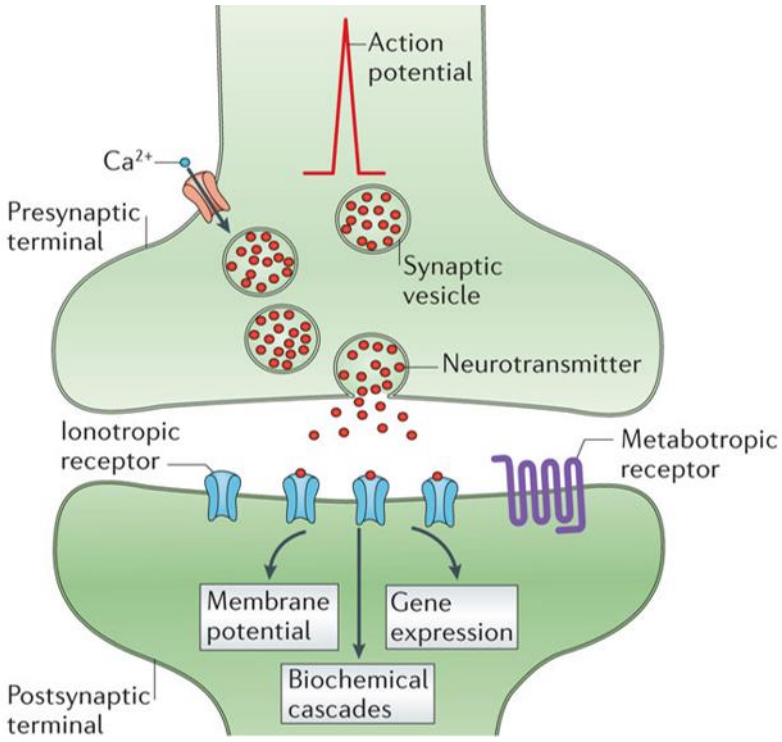

Figure 2. Neuronal activity-dependent calcium influx in chemical synapses.

(Pereda, 2014)

Upon suprathreshold action potential in a neuron, the membrane depolarises, voltage-gated calcium channels open in the presynaptic neuron terminal, calcium influx causes vesicles to release neurotransmitters. Transmitters bind to receptors on the post-synaptic neuron, opening or closing ligand-gated post-synaptic ions channels. Post-synaptic currents cause excitation or inhibition of the neuron, repeating the same steps in the postsynaptic neuron, in case of excitation above a threshold to create an action potential (W. Wang et al., 2019).

This oversimplified explanation of the coupling between neuronal depolarisation and calcium release, arise from an accumulation of knowledge from the 19th century. In light of this connection, calcium is nowadays used to report indirectly neuronal activity in a method called calcium imaging.

The history of calcium imaging brings together several research topics: the role of calcium in physiology, the fluorescence microscopy and the introduction of exogenous

genes into eukaryotic cells (Pérez Koldenkova & Nagai, 2013; Robbins, Christensen, Kaminski, & Zlatic, 2021).

Sydney Ringer first demonstrated the role of calcium in the physiology of cells in 1883, with an experiment on the contraction of frog hearts when exposed to different solutions containing calcium (Ringer, 1883). After a set of experiments on the giant axon of squids, Alan Hodgkin and Andrew Huxley explained the mechanism of action potential via change in membrane potential due to sodium and potassium currents (Hodgkin & Huxley, 1952). The next 15 years, several scientists could link the action potential to the increase of intracellular calcium concentration, in crustacean muscle fibres during contraction (Fatt & Ginsborg, 1958; Fatt & Katz, 1953), in barnacle muscle fibres (Hagiwara & Takahashi, 1967) and in cardiac Purkinje fibres from calf (Reuter, 1967). In the nervous system, Bernard Katz and Ricardo Miledi discovered the role of calcium in release of neurotransmitters in 1967, performing experiment in the axo-axonic giant synapse in the stellate ganglion of a squid (Katz & Miledi, 1967). From this moment, it became clear that calcium plays a crucial role in the function of neurons to communicate and transmit information. The precise mechanism linking calcium to action potential was studied thanks to two main inventions (Dolphin, 2018); the patch clamp technique, allowing to measure micro currents from single channels in cell membranes (Fenwick, Marty, & Neher, 1982; Sakmann & Neher, 1984), and calcium channel blockers (K. S. Lee & Tsien, 1983). With those tools, the different ligand-gated and voltage-gated calcium channels involved in muscle cells and neurons were one by one discovered (Fox, Nowyckyt, & Tsient, 1987; Nowycky, Fox, & Tsien, 1985; M. E. Williams et al., 1992).

The history of fluorescence microscopy began a few years before Ringer's discovery of the role of calcium in physiology. Indeed, the prism didn't only gave rise to the theory of colour by Isaac Newton in the beginning of 18th century (Newton, 1704), it also allowed George Stokes to make the observation in 1852 that the light emitted by fluorescent objects (quinine and fluorite crystal) has always a longer wavelength than the light used to excite it (Stokes, 1852). Autofluorescence always intrigued humanity, with the first written observation dating back to the 17th century, on minerals and plants (Valeur & Berberan-Santos, 2011). In the same century, the first microscopes were developed by Antonie van Leeuwenhoek to observe microscopic structures on animals, plants and micro-organisms (Lane, 2015). The technology to observe

fluorescence microscopic structures appeared only in 1911, with the first fluorescence microscope built in Germany by Oskar Heimstädt (Heimstädt, 1911). At that time, those microscopes were used exclusively to observe autofluorescence. Following this invention, fluorescence microscopy evolved to allow imaging in living cells and animals, with a better resolution, a higher depth and less photodamages (see 1.6). The idea that proteins and molecules can be attached to fluorescent proteins to be observed emerged from the experiment by Osamu Shimomura, when he and his colleagues isolated the green fluorescent protein (GFP) and the bioluminescent calcium sensitive protein aequorin, from the jellyfish Aequorea Victoria (Shimomura, Johnson, & Saiga, 1962).

This is where the two first fields of research merge. Calcium indicators are molecules that respond to the binding of calcium ions by fluorescence properties. The first calcium indicator used to visualise and quantify intracellular calcium was the aequorin discovered in 1962 (Blinks, 1990; Moisescu, Ashley, & Campbell, 1975). More specific calcium indicators, like the dye fura-2, were developed about 20 years later by Tsien and colleagues, and those indicators are still used nowadays for calcium imaging (Tsien, 1980). The next generation of calcium indicators is less invasive, enables cell-type specificity, and avoids high background fluorescence previously observed, because they do not stain the extracellular structures (Broussard, Liang, & Tian, 2014). Those are the genetically encoded indicators (GECIs). The first GECIs developed were fluorescence resonance energy transfer (FRET)-based (Heim & Tsien, 1996; Miyawaki et al., 1997; Romoser, Hinkle, & Persechini, 1997). The advantage of the latter is the signal is independent of the sensor expression level. Therefore, they are still used today and being developed for in vivo imaging (Day-Cooney et al., 2022). Nevertheless, the most widely used GECIs to date are the single fluorescent protein-based GCaMP family (Baird, Zacharias, & Tsien, 1999; Nakai, Ohkura, & Imoto, 2001), because of their higher response amplitude (Day-Cooney et al., 2022). GCaMPs consist of an enhanced GFP (EGFP), attached to the calcium binding protein calmodulin and the calmodulin peptide binding M13. When calcium binds to calmodulin, M13 interacts with the calmodulin and the EGFP changes its conformation, increasing the emitted fluorescence (Grienberger & Konnerth, 2012). Several updates of the original GCaMP indicator allowed imaging in vivo with a better temporal resolution, making of the GCaMP6 family (T. W. Chen et al., 2013) the most widely used calcium sensors. Two more generations have since been developed (Dana et al.,

2019; Y. Zhang et al., 2021), but despite the larger dynamic range and higher fluorescence, GCaMP6f provides the best temporal resolution to date (Day-Cooney et al., 2022).

One revolution attached to genetic engineering, including genetically encoded indicators, is the discovery of the ability of DNA to transform cells, and development of methods to transfer DNA from one organism to another (see 1.5).

The first calcium imaging in the nervous system, using a two-photon microscope (see 1.6) and the calcium indicator calcium-green-1, was performed on hippocampal slices of rats in 1995, to observe calcium dynamics in dendritic spines (Yuste & Denk, 1995). Two years later, Winfried Denk and colleagues performed the first calcium imaging in vivo in somatosensory cortex of rats, also in order to observe dendritic spines (Svoboda, Denk, Kleinfeld, & Tank, 1997). In mice, the in vivo calcium imaging came a few years later, to measure neuron activity in the olfactory bulb first (Wachowiak & Cohen, 2001), and later in other primary sensory cortices, like the auditory cortex (Bandyopadhyay et al., 2010; Rothschild, Nelken, & Mizrahi, 2010).

Advantages of calcium imaging include spatial resolution reaching subcellular levels and imaging of simultaneously thousands of cells in different brain regions (Broussard et al., 2014; T. W. Chen et al., 2013; Dana et al., 2019; M. Inoue, 2021). Contrary to recordings with electrodes, calcium imaging with GECIs can be cell type specific, and is less invasive (Broussard et al., 2014; T. W. Chen et al., 2013; M. Inoue, 2021; Miyawaki et al., 1997; Nakai et al., 2001; Pérez Koldenkova & Nagai, 2013; Roth & Ding, 2020). Unlike chemical calcium sensors, the signal is localised in the cells and not present in intercellular space (Broussard et al., 2014). Additionally, activity can be recorded chronically in the same cells for up to months, and to measure activity in awake mice, known to be very different from activity under anesthesia (Broussard et al., 2014; T. W. Chen et al., 2013; Dana et al., 2019; Day-Cooney et al., 2022; M. Inoue, 2021; Pérez Koldenkova & Nagai, 2013; Robbins et al., 2021; Roth & Ding, 2020; Russell, 2010). Lastly, development of miniscopes allows calcium imaging to be performed in freely behaving mice, and development of multicolour enables simultaneous recording of activity in different cell types or different cellular compartments (Day-Cooney et al., 2022; M. Inoue, 2021; Pérez Koldenkova & Nagai, 2013; Redolfi et al., 2021; Robbins et al., 2021; Roth & Ding, 2020). Limitations of calcium imaging are poor temporal resolution compared to electrophysiology, and

indirect measure of neuronal activity (Day-Cooney et al., 2022; Huang et al., 2021; Roth & Ding, 2020; Y. Zhang et al., 2021). Even though the brain can stay intact, the skull needs to be removed or thinned in order to image the indicator at a cellular resolution (Papaioannou & Medini, 2022; Redolfi et al., 2021; Roth & Ding, 2020). Additionally, indicators expressed in the brain can induce abnormal cortical activities, especially if expressed in transgenic mice, through the brain development, before adulthood (Papaioannou & Medini, 2022; Redolfi et al., 2021; Singh, Lujan, & Renden, 2018; Steinmetz et al., 2017). Lastly, an important factor contributing to the perturbation of neuronal physiology is the binding of calcium to the indicators, preventing the cell to use the cation for its natural and numerous functions (Grienberger & Konnerth, 2012; C. R. Lee, Najafizadeh, & Margolis, 2020). To be mentioned, due to the cytotoxicity of the indicators and the necessity of craniotomy to observe the neuronal populations, the technology is not used on humans.

Here, we used the calcium indicator GCaMP6m, for longitudinal recording of neuronal activity in the pyramidal cells in the auditory cortex of adult mice.

1.4.3 Immediate early genes (IEGs): c-Fos

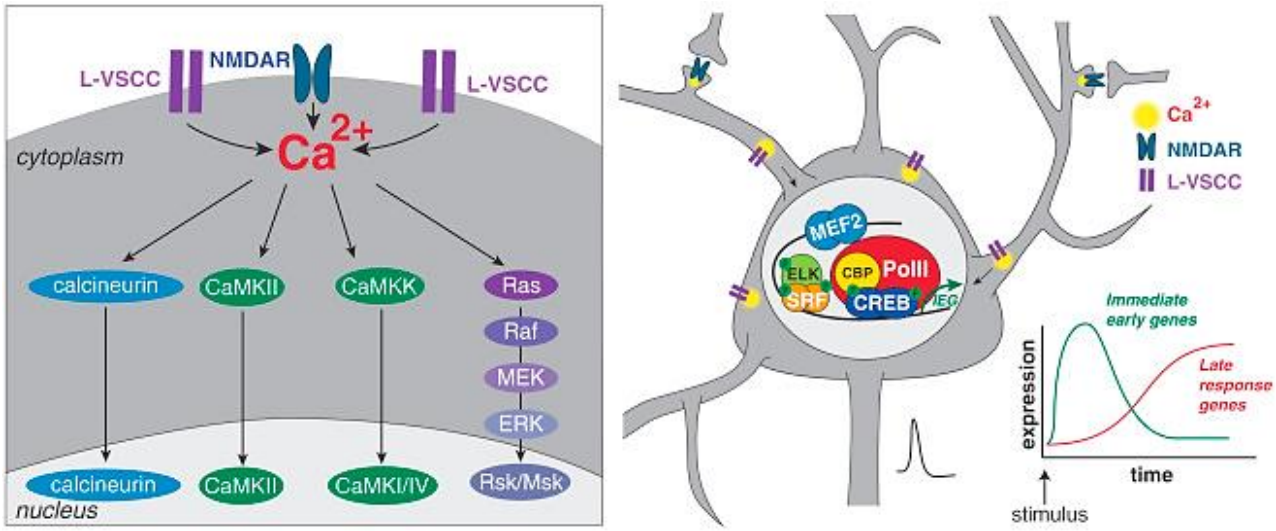

Figure 3. Neuronal activity-dependent transcription.

(Yap & Greenberg, 2018)

Extracellular signals like neurotransmitters, growth and survival factors, cytokines or hormones, can interact with receptors and channels on the membrane of neurons and other cell types. The later can bind to receptors or enter the cells through channels, triggering a calcium-dependent signalling cascade, like Ras-MAPK pathway, calcium/calmodulin-dependent protein kinases, and calcineurin-dependent signalling in neurons. These pathways activate, via phosphorylation, transcription factors like CREB, SRF/ELK and MEF2, inducing expression of the immediate early genes (IEGs) like Erg-1, c-Jun, c-Fos, Arc and Homer. Immediate early genes can be direct effectors, involved in receptor modulation, vesicle storage, or synaptic trafficking (arc and homer 1a). They can also code for inducible transcription factors, regulating the expression of downstream late-response genes (LRGs) involved in neuronal physiology (erg-1, c-jun, c-fos) (Kawashima et al., 2014; Okuno, 2011; Sommerlandt, Brockmann, Rössler, & Spaethe, 2019; Yap & Greenberg, 2018). L-VSCC = L-type voltage-sensitive calcium channels. NMDAR = N-methyl-D-aspartate receptor/glutamate receptor. POLII = RNA-polymerase 2.

The discovery of immediate early genes dates back from the eighties, when Roger Watson and Barklie Clements identified genes rapidly expressed in herpes simplex viruses infected hamster host cell line (Watson & Clements, 1980). This process happens without de novo protein synthesis and therefore necessitate pre-existing transcription factors (Okuno, 2011). From work on differentiation and proliferation, various stimuli like growth factor, hormones, or cytokines, were observed to trigger rapid gene expression in fibroblasts and other cell lines (Almendral et al., 1988; Greenberg & Ziff, 1984; Kelly, Cochran, Stiles, & Leder, 1983; Kruijer, Cooper, Hunter, & Verma, 1984; Lau & Nathans, 1985). This rapid increase in gene expression was

later also found in neurons, in response to drug-induced or in stimuli-induced activity (Dragunow, Yamada, Bilkey, & Lawlor, 1992; Herdegen, Leah, Manisali, Bravo, & Zimmermann, 1991; Morgan, Cohen, Hempstead, & Curran, 1987; Saffen et al., 1988; Worley et al., 1991). Immediate early genes are ever since widely used to tag and manipulate active neurons.

The most popular immediate early genes used as neuronal activity markers are c-Fos, egr-1 and Arc (Clayton, 2000; Gallo, Katche, Morici, Medina, & Weisstaub, 2018; Kawashima, Okuno, & Bito, 2014; Minatohara, Akiyoshi, & Okuno, 2016). In neurons, early growth response gene (erg-1), also known as zif268, has been linked to long-term potentiation (LTP), long-term memory and fear memory (Bozon, Davis, & Laroche, 2003; Maddox, Monsey, & Schafe, 2011; J. M. Williams et al., 2000). The genes targeted by this transcription factor are involved in vesicular transport and neurotransmitter release (Duclot & Kabbaj, 2015; Koldamova et al., 2014). Egr-1 also control the expression of Arc (Gallo et al., 2018). In the brain, the activity-regulated cytoskeletal (Arc) protein, also known as Arg3.1, is a synaptic protein interacting with the brain derived neurotrophic factor (BDNF), and involved in glutamatergic, dopaminergic and serotonin signalling (Chowdhury et al., 2006; Granado et al., 2008; Karabeg et al., 2013; Leal, Comprido, & Duarte, 2014; Managò et al., 2016; Mastwal, Cao, & Wang, 2016; Panja & Bramham, 2014; Pastuzyn et al., 2018). Arc also participates to the generation and maintenance of synapses (Gallo et al., 2018; Korb & Finkbeiner, 2011; Minatohara et al., 2016).

c-Fos (cellular Finkel-Biskis-jinkins Osteogenic Sarcoma) was the first immediate early gene whose expression was shown to be activity-dependent; highly expressed in rat hippocampus and pyriform cortex after drug-induced seizures (Morgan et al., 1987). The history of c-Fos begins in the field of virology and oncology, when Tom Curran and Natalie Teich isolated Fos from the serum of rats bearing tumours, induced by Finkel-Biskis-Jinkins Murine Osteogenic Sarcoma virus (FBJ-MSV). v-Fos was identified as an oncogene, responsible for the development of the tumours (Curran & Teich, 1982). The cloning of the homologous DNA sequence from mouse (BALB/c liver DNA) and human, was performed in 1983 by Tom Curran and colleagues (Curran, MacConnell, van Straaten, & Verma, 1983), and is the basis of the c-Fos promoters-based tools used to date. After the observation of c-Fos activity-dependent expression in 1987, several neuroscientists used and still use immunostaining to stain c-Fos protein and in

situ hybridization to stain c-Fos mRNA, in the brain of rats or mice after stimulation, to identify active cells (Clayton, 2000; Kawashima et al., 2014; Terstege & Epp, 2022; Yap & Greenberg, 2018). One popular method to measure Arc and c-Fos expression over time, at two time points, was the compartment analysis of temporal activity by fluorescence in-situ hybridization (catFISH) (Guzowski, McNaughton, Barnes, & Worley, 1999). Nevertheless, catFISH is restricted in time, since mRNA is rapidly degraded. In the 21st century, the popularity of c-Fos as a neuronal activity marker further increased thanks to the development of genetic tools to tag and manipulate neurons expressing c-Fos, shown to be directly involved in fear memory. Those tools include the FosGFP transgenic mouse, to measure c-Fos in vivo and chronically, not as restricted as catFISH (Barth, Gerkin, & Dean, 2004), the TetTag mouse to measure c-Fos expression in controlled time windows (L. G. Reijmers, Perkins, Matsuo, & Mayford, 2007) and TetTag in combination with adeno-associated viruses (AAVs), to manipulate the activity of cells expressing c-Fos. TetTag can either be combined to optogenetic, with AAVs packaging gene for light-gated cation channel, like channelrhodopsin-2 (X. Liu et al., 2012), or chemogenetic, with AAVs containing gene for designer receptors exclusively activated by designer drugs (DREADDs) (Garner et al., 2012). Xu Liu in Susumu Tonegawa's lab, as well as Aleena Garner in Mark Mayford's lab, could link c-Fos expression to fear memory formation. Indeed, when reactivating cells expressing c-Fos during fear conditioning, the groups observed increased freezing, suggesting the TetTag mice could remember the fearful event. These experiments are the foundation of the theory of engrams, the subset of cells hold responsible for memory formation and storage (Josselyn & Tonegawa, 2020).

Despite a tremendous literature on c-Fos expression in the brain, and especially in the hippocampus, the functions of the genes targeted by c-Fos that could enable to understand the role of c-Fos in the central nervous system remain unclear (Gallo et al., 2018; Leslie & Nedivi, 2011; Minatohara et al., 2016; Yap & Greenberg, 2018). What we do know though is that Fos protein dimerizes with members of the Jun family to form the activator protein complex (AP-1), a transcription factor. Several members of Fos family and Jun family can bind together to form different AP-1 dimers (Sheng & Greenberg, 1990). Based on genome-wide assessments studies in mice and rats cortical cells, AP-1 family has about 10^4 binding sites and control expression of 300-500 late-response genes (Benito & Barco, 2015; T. K. Kim et al., 2010; Malik et al., 2014). The targeted genes are cell-type specific (Hrvatin et al., 2018; Hu et al., 2017;

Lacar et al., 2016; Spiegel et al., 2014), and AP-1 complex appears to bind to distal enhancer elements rather than promoters (Heinz et al., 2013; Vierbuchen et al., 2017). To be noted, it has recently been suggested that enhancers confer cell-type specificity in place of promoters (Heintzman et al., 2009; Long, Prescott, & Wysocka, 2016). The extreme complexity of gene ensembles targeted by c-Fos may need new methods and further investigation in order to understand how the different parts collaborate and aim to a precise function in specific cell types and regions of the brain, during a specific task.

Advantages of the activity-based tools include the fact that they allow an insight in the gene expression level of neuronal activity. Additionally, they grant a good spatial resolution, with the possibility to image a whole mouse brain at a cellular resolution (Barbarosa & Silva, 2018; Q. He, Wang, & Hu, 2019; L. Reijmers & Mayford, 2009; Terstege & Epp, 2022). IEGs promoters can drive the expression of an unlimited range of proteins, resulting in a high number of tools to tag and manipulate activated cells (Kawashima et al., 2014; L. Reijmers & Mayford, 2009). Most importantly, c-Fos and Arc promoters are substrate to label engrams (Gallo et al., 2018; Gobbo & Cattaneo, 2020; Q. He et al., 2019; Kawashima et al., 2014; W. Wang et al., 2019). Nevertheless, like all methods to image the neuronal activity, IEGs hold their share of limitations. For starters, IEGs are not only expressed in neurons, but can be expressed in many different cell-types. Furthermore, expression of IEGs can be triggered by various stimuli, and not only depolarisation (Nambu, Lin, Reuschenbach, & Tanaka, 2022; Okuno, 2011; Yap & Greenberg, 2018). Especially relevant nowadays, when sensors like genetically encoded voltage indicators enable a very high temporal resolution, IEGs are used as an indirect measure of neuronal activity with a very poor temporal resolution (Gallo et al., 2018; L. Reijmers & Mayford, 2009; Terstege & Epp, 2022; W. Wang et al., 2019). Additionally, expression of IEGs is heterogeneous in the brain. Some brain regions have very high basal level of IEGs, and other are simply not expressing some IEGs when activated (Q. He et al., 2019; Hudson, 2018; Kleim, Lussnig, Schwarz, Comery, & Greenough, 1996; Kovács, 2008; Q. Zhang, He, Wang, Fu, & Hu, 2018). Moreover, discrete activities may not be captured by c-Fos promoter tools, because the latter needs a certain threshold to be activated (Q. He et al., 2019; Hudson, 2018). Finally, the causal relationship between c-Fos expression and functional relevance in neurons is still unknown (Gallo et al., 2018; Leslie & Nedivi, 2011; Minatohara et al., 2016; Yap & Greenberg, 2018). To be mentioned, classically

c-Fos is not imaged in vivo. However, due to the new state of the art of neuronal activity recording, enabling to track the same cells chronically in awake animals, some groups attempted to used c-Fos-based tools as in vivo tracers of IEGs expression (Ivashkina, Gruzdeva, Roshchina, Toropova, & Anokhin, 2021; Mahringer et al., 2019; Mahringer, Zmarz, Okuno, Bito, & Keller, 2022; Meenakshi, Kumar, & Balaji, 2021).

Because of all the drawbacks mentioned for c-Fos-based tools, we wanted to test how far such a reporter allow a direct correlation of c-Fos expression with neuronal activity. Therefore, we used a TetTag system (L. G. Reijmers et al., 2007) in parallel to the calcium indicator mentioned above, GCaMP6m. TetTag is composed of two parts. The first one uses c-Fos promoter to drive the expression of a transactivator protein (c-Fos-tTA), controlled by tetracycline. In our case, a tet-off configuration was used. In absence of tetracycline, tTA binds to the second part of the system, a tetracycline-responsive element put upstream of a blue fluorescent protein (TRE-BFP), and activate the expression of the fluorophore. Thus, cells expressing c-Fos are tagged with the blue fluorescent protein.

1.5 Tools to deliver genes: adeno-associated viruses (AAVs)

There is to date two main methods to deliver genes, used in both research and gene therapy: non-viral and viral vector gene delivery systems. Non-viral vectors can be further separated into two groups, the physical methods to create pores in cellular membranes (needle injection, electroporation, sonoporation, photoporation, etc…), and the chemical methods taking advantage of endocytosis (liposomes, polymers, nanoparticles, etc…). Viral vectors can either be delivered in germline or somatic cells. The most popular viruses used to deliver genes include retrovirus, adenovirus, adeno-associated virus and herpes simplex virus (Sung & Kim, 2019). Classically, to deliver viruses in the brain of rodents, three routes exist: intracranial, intra-cerebrospinal fluid, or intravenous (Bedbrook, Deverman, & Gradinaru, 2018; Haery et al., 2019; Nectow & Nestler, 2020; Zhou, Han, Wang, Zhang, & Zhu, 2022). To achieve cell-type specificity, regulatory elements like promoters and enhancers are added to the transgene (Bedbrook et al., 2018; Haery et al., 2019). In this section, I will write about viral vectors, with a focus on adeno-associated viruses, delivered by stereotactic injection, as this is the method I used for this project.

The history of gene delivery begins in 1944, when Oswald Avery and colleagues discovered that deoxyribonucleic acid (DNA) is the agent transforming pneumococcus

types. They reasoned from the experiment that DNA is the agent able to transmit hereditary characters (Avery, MacLeod, & McCarty, 1944). Thanks to the development of mammalian cell lines, Ellen Borenfreund and Aaron Bendich could transform mammalian cells with human and bacterial derived DNA (Borenfreund & Bendich, 1961). On account of studies on transformation of cells from the normal to the neoplastic phenotype with the viruses, researchers soon realised that viral DNA can stably and heritably integrate the target genome (Friedmann, 1992; Hill & Hillova, 1972; Sambrook, Westphal, Srinivasan, & Dulbecco, 1968). This marks the beginning of the use of viral vectors as an efficient way to deliver DNA.

Adeno-associated viruses (AAVs) were discovered in 1965, in rhesus-monkey-kidney-cell culture infected with the simian adenovirus type 15 (SV15), by Robert Atchison and colleagues (Atchison, Casto, & McD. Hammon, 1965). Using electron microscopy, they noticed inside SV15 multiple virus-like particles. After 15-20 years of intensive characterisation of the Dependoparvovirus family, unravelling AAVs genome composition (rep genes encoding for replication proteins, and cap genes encoding for proteins to form the viral capsid), as well as replication, transcription and infection mechanisms (D. Wang, Tai, & Gao, 2019), Richard Samulski and colleagues successfully cloned AAV2 into bacterial plasmids (Samulski, Berns, Tan, & Muzyczka, 1982). This achievement allowed two groups to use the virus or the cloned AAV2 sequence as a vector to deliver genes from viral, bacterial and mouse origin into human and mouse cell lines (Hermonat & Muzyczka, 1984; Tratschin, West, Sandbank, & Carter, 1984). Inspired by these methods, about ten years later, the first in vivo delivery of recombinant AAVs (rAAV) was applied in rabbit lung (T. R. Flotte et al., 1993). Soon after, the technique was exploited to deliver genes in the brain of rats (Kaplitt et al., 1994). The latest was already using a rAAV sequence as classically used nowadays, cutting out the viral genes and keeping only the inverted terminal repeats to flank the transgene (Kantor, Bailey, Wimberly, Kalburgi, & Gray, 2014). Without a helper virus, AAVs cannot replicate their genome in the host cells, and the recombinant AAVs genome is episomal, meaning they do not integrate the host DNA. Those are the main reason why those viruses are barely activating the immune systems when injected into animals (Aschauer, Kreuz, & Rumpel, 2013; Bedbrook et al., 2018; Haery et al., 2019; Kantor et al., 2014; D. Wang et al., 2019). Therefore, they are widely used for gene therapy in humans, as well as gene delivery for research purposes. After the first application of the virus for human patient for the treatment of cystic fibrosis (T. Flotte

et al., 1996), AAVs became more and more popular and scientists optimised further the technique, finding new capsids to target different organs and cell-types, and combining capsids and genome from different serotypes to increase gene delivery efficiency. This is how AAV8 capsid packaging AAV2 genome was discovered (Carter, 2004; Gao et al., 2002). It is a common practice to package AAV2-based genomes in the different capsids for an optimal and specialised application (Gao et al., 2002; L. He, Binari, Huang, Falo-Sanjuan, & Perrimon, 2019; Lisowski, Tay, & Alexander, 2015; Mietzsch et al., 2021; Nectow & Nestler, 2020; Watakabe et al., 2015). In the central nervous system, the main capsids used are AAV1, AAV2, AAV5, AAV8 and AAV9 (Haery et al., 2019; Kantor et al., 2014; Nectow & Nestler, 2020). AAV8 can transduce neurons, but also at a lower rate astrocytes and oligodendrocytes (Aschauer et al., 2013; Haery et al., 2019; T. He et al., 2019; Kantor et al., 2014). The transduction level and the spread from the injection site of the capsid was repeatedly reported to be higher compared to AAV2, but lower compared to other serotypes like AAV5 and AAV9 (Gao et al., 2002; Haery et al., 2019; T. He et al., 2019; Kantor et al., 2014). AAV8 is transported in an anterograde and a retrograde manner, and its expression is stable for months (Haery et al., 2019; Reimsnider, Manfredsson, Muzyczka, & Mandel, 2007).

Advantages of AAVs, as mentioned above, include low pathogenicity, efficient in vivo infection, and long-term expression. Limitations are genome packaging size (4.7Kb max), episomal genome, meaning potentially different expression compared to chromosomal genes (F. Inoue et al., 2017), and potential dose dependent toxicity (Bedbrook et al., 2018; Bijlani, Pang, Sivanandam, Singh, & Chatterjee, 2022; Kantor et al., 2014; Nectow & Nestler, 2020).

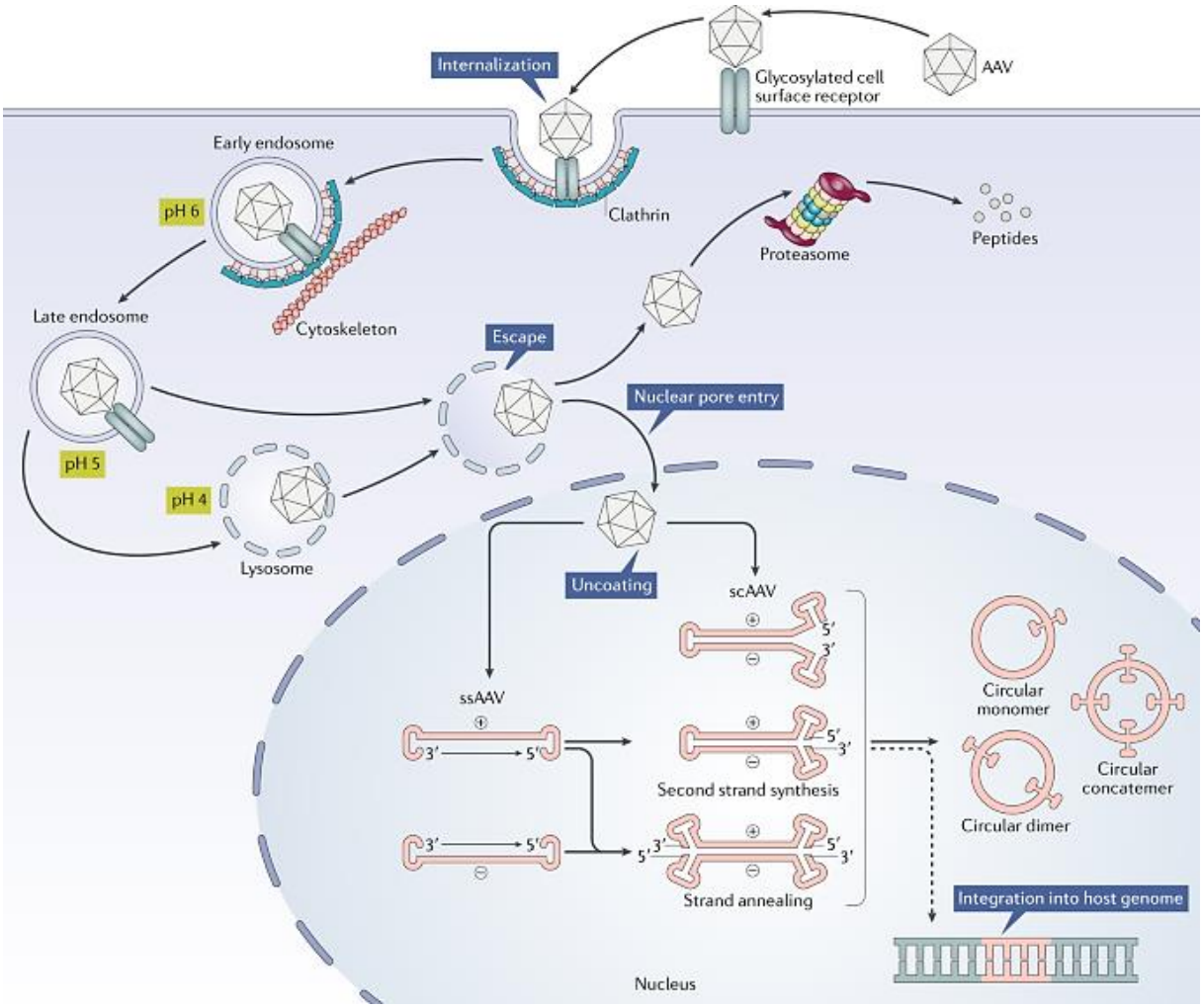

Figure 4. rAAV transduction pathway.

(D. Wang et al., 2019)

AAV capsid is binding to a glycosylated cell surface receptor, triggering clathrin-mediated endocytosis. The vesicle is transported by the cytoskeletal network, and either fuses with a lysosome to break the vesicle or escape it. The capsid moves then to the nucleus, where it dissociates in order to release the DNA. If the DNA is single stranded, it is converted to double-strand first and then circularised. If the DNA is self-complementary, it can directly form the episomal circularised genome and be transcribed. Occasionally, the linear double-stranded DNA can integrate the host genome.

Advantages of stereotactic injection (Sir Horsley & Clarke, 1908) in adult mice comprise, lower volumes of virus load and higher expression level compared to systemic and intra-CSF (cerebrospinal fluid) delivery. In addition, the transgene can be expressed in very specific brain regions and only when the animal has a mature and developed brain, limiting side effects of inducing the expression of an artificial

protein in neurons. Limitation of the delivery method are the need of an invasive surgery (craniotomy) as well as surgical expertise to deliver the virus, compared to systemic and intra-CSF injections (Haery et al., 2019; Nectow & Nestler, 2020).

For this project, we used the recombinant AAV2/8 to package four transgenes: the calcium indicator GCaMP6m and the TetTag system described above, as well as a nuclear marker (fusion protein H2B-mCherry) to track the same cells chronically. The calcium indicator and the nuclear marker were expressed under the human synapsin I promoter, allowing neuronal-specific expression (Kügler, Kilic, & Bähr, 2003). We delivered the viral particles by stereotactic injection in the auditory cortex of adult mice.

1.6 Chronical calcium imaging in vivo: two-photon microscopy

Longitudinal calcium imaging involves different topics of research: calcium indicators, gene delivery methods, fluorescence microscopy and optical access to the brain.

I covered the two first topics under sections 1.4.2 and 1.5, respectively.
As mentioned above, development of fluorescence microscopes began about 50 years before the discovery of fluorescent proteins (Heimstädt, 1911; Shimomura et al., 1962), and was used to observe autofluorescent specimens, like plants and stones. Since then, the field evolved and several fluorescence microscopes were developed, becoming more and more optimal and suited for in vivo imaging. Widefield or epifluorescence microscopy, exploits the principle discovered by Sir George Stokes, using filters in order to illuminate the fluorescent sample with a specific wavelength, to excite the fluorophore and observe the emitted light of longer wavelength through an objective (Grienberger & Konnerth, 2012). The confocal microscope improves the image quality, introducing laser scanning for point illumination and a pinhole, in order to reduce the area of the sample exposed to the light and emission of out-of-focus photons, respectively (Minsky, 1988). Finally, two-photon microscopy increases the range of application possible (Denk, Strickler, & Webb, 1990). Indeed, this method has several benefits over single photon techniques like epifluorescence and confocal microscopy, as mentioned in Figure 5: deeper penetration of the sample, less out-of-focus absorption and emission, increased signal intensity and reduced photodamage (Svoboda & Yasuda, 2006). For all those reasons, two-photon microscopy is the method of choice for in vivo imaging. The principle of two-photon microscopy is

described in Figure 5. State-of-the-art method for imaging calcium in awake mice with a two-photon microscope is with head-fixed animals (Dombeck, Khabbaz, Collman, Adelman, & Tank, 2007). Nonetheless, the recent development of miniaturised microscopes, epifluorescence and two-photon miniscopes, also allows imaging in freely moving animals, preventing the stress from head fixation, and enabling neuronal activity measure during natural behaviour (Flusberg et al., 2008; Helmchen, Fee, Tank, & Denk, 2001; Sabharwal, Rouse, Donaldson, Hopkins, & Gmitro, 1999). The high success of the miniscopes pushes scientists to optimise the method, which will hopefully and in a near future reach the imaging quality obtained with head-fixed animals. Additionally, three-photon microscopy improves further deep imaging, and is becoming a new cutting age for in vivo imaging, especially for subcortical regions like hippocampus (Xiao, Deng, Zhao, Yang, & Li, 2023). Also, multiphoton microscopy is beginning to be used for label-free preparations, in order to image endogenous sources of autofluorescence (metabolic substrates, structural proteins, lipofuscins and melatonin) and second- and third harmonics of the molecules (Borile, Sandrin, Filippi, Anderson, & Romanato, 2021). Maybe this method could be refined further in order to image other natural changes in cells and therefore circumvolve the disadvantage of introducing artificial dyes or fluorescent proteins, hence imaging more physiological events.

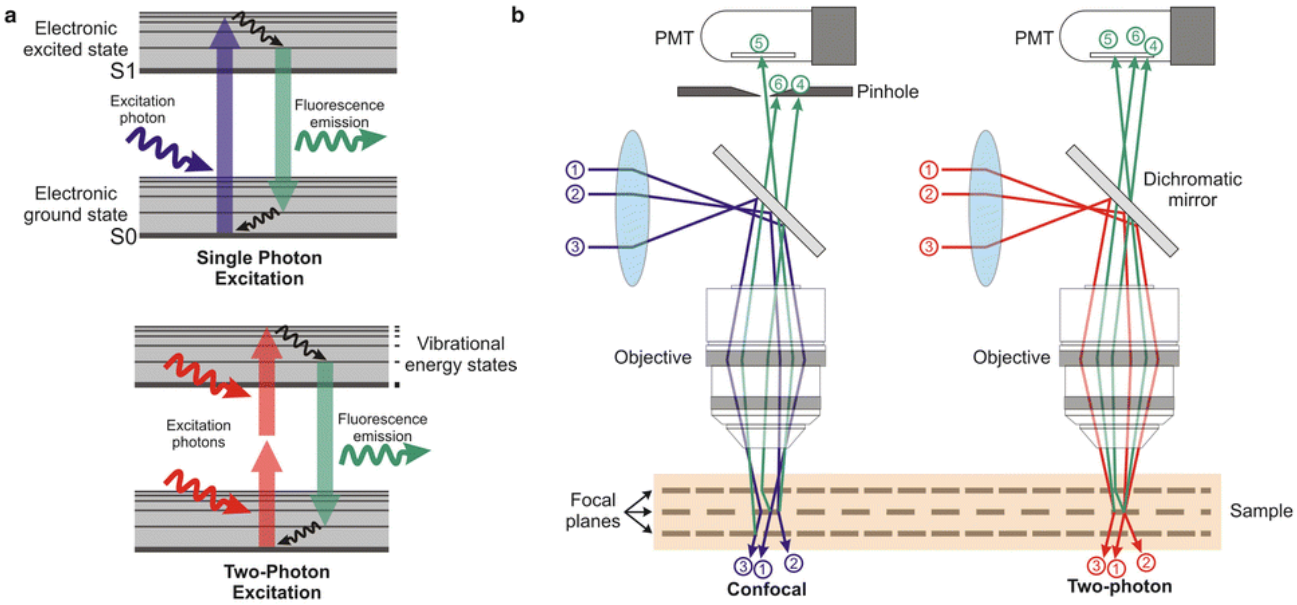

Figure 5. Comparison of confocal and two-photon microscopy.

(Mostany, Miquelajauregui, Shtrahman, & Portera-Cailliau, 2015)

a. Jablonski energy diagram: Excitation process for single- and two-photon technologies. Top: A single photon of high energy is needed to excite a fluorophore. Bottom: Two quasi-simultaneous photons of low energy (near infrared) have to be absorbed by the fluorophore to transform the state of the protein. Near-infrared light penetrates tissues better, allowing deeper imaging. **b**. Left: In a confocal microscope, the out-of-focus emitted photons are blocked by the pinhole. Right: For the two-photon microscope, emission is only coming from the focal plane. Therefore, out-of-focus excitation and bleaching are significantly reduced, and emitted light intensity is higher because there is no need of a pinhole to block photons. For the two-photon to simultaneously hit the focal point, light source needs to be powerful, thus only pulsed lasers (short pulses of ~100 femtoseconds duration) makes two-photon microscopy possible (Grienberger & Konnerth, 2012; Svoboda & Yasuda, 2006).

In order to do calcium imaging at a high resolution, one have to create optical access to the brain. To date, there are three main methods to allow calcium imaging through the skull: implantation of a cranial window, thinning the skull, using skull optical clearing agents to make it transparent (Cramer et al., 2021). Window implantation is a very old method, already used in 1928 by Henry Forbes on monkeys, to observe the cerebral blood vessels (Forbes, 1928), described in details about thirty years later, with a protocol applied on rabbits (Levasseur, Wei, Raper, Kontos, & Patterson, 1975), and further refined at the end of the 20th century for intrinsic imaging in monkeys (Grinvald, Frostig, Siegel, & Bartfeld, 1991). Thinning of the skull was only developed later, to perform imaging of amyloid plaques in a label-free mouse model for Alzheimer's disease, using a two-photon microscope (Christie et al., 2001). As for the clearing agent for skull, it was developed only very recently, alongside with other tissues clearing agents in Dan Zhu's laboratory (Qi et al., 2019). The latest is not yet used for in vivo imaging.

The very first longitudinal imaging was performed by the group mentioned above, for inventing the thinning skull method (Christie et al., 2001). A year later, two groups performed chronical imaging also with a two-photon microscope, to assess the dynamics of spines in transgenic mice, expressing fluorescent protein in pyramidal cells. The first group imaged spines in the barrel cortex through a cranial window (Trachtenberg et al., 2002), and the other in the visual cortex through a thinned skull (Grutzendler, Kasthuri, & Gan, 2002). The first longitudinal calcium imaging was reported in 2008, testing a newly optimised troponin C-based calcium indicator TN-

XXL, created by the group, in flies and visual cortex of mice (Mank et al., 2008). To track the same cells over weeks, they took advantage of the vessel patterns observed through a cranial window, at the surface of the brain, and the coordinates of the cells. This experiment, and the following few with other GECIs were proof-of-principle experiments (Andermann, Kerlin, & Reid, 2010; Crowe & Ellis-Davies, 2014; Tian et al., 2009), but soon after those studies, groups using the established chronic in vivo optical imaging, discovered unknown biological mechanisms, such as representational drift (C. R. Lee et al., 2020). To track the cells in a reliable manner, some groups have added a structural marker expressed in nuclei of cells, in parallel to the calcium indicator, developed by Tobias Rose and colleagues in 2016 (Rose, Jaepel, Hübener, & Bonhoeffer, 2016).

Advantages of two-photon microscopy were discussed above. Limitations of the method were in part mentioned previously as well, when compared to three-photon microscopy enabling deeper imaging (Xiao et al., 2023). In addition, despite improvement of photodamage over confocal and epifluorescence microscopes, repeated light applied on the same cortical regions can lead to bleaching and phototoxicity (Ricard et al., 2018). In case of head fixation, animals are exposed to stress, but the quality of miniscopes allowing freely-moving animals, is not yet comparable to head-fixed two-photon microscopy (K. Chen, Tian, & Kong, 2022). And miniscopes are not allowing simultaneous measurement of millions of cells, which is reachable with head-fixed mice (Urai, Doiron, Leifer, & Churchland, 2022). Finally, there is room for improvement of the image quality, as it is not comparable to confocal microscopes yet (Borile et al., 2021; Grienberger & Konnerth, 2012).

Regarding advantages and limitations of cranial window implantation: compared to thinning of the skull, cranial window allows bigger area to be imaged (Cramer et al., 2021; Drew et al., 2010). Moreover, if performed carefully, the surgery do not need to be repeated, unlike skull thinning. Thanks to the “crystal skull” method (T. H. Kim et al., 2016), cranial window can reach very big size, similar to that reached with the skull clearing agent (Guo et al., 2014; Qi et al., 2019). Limitations of cranial windows comprise the need of technical skills to perform the surgery, hence reducing the success rate for a chronical window (Cramer et al., 2021). Furthermore, it has been reported several times that the surgery induces inflammation, preventing observation of the brain activity in physiological conditions (Cramer et al., 2021; Drew et al., 2010).

Furthermore, scars can grow underneath the window, covering the brain surface and preventing optical access to the brain.

Here, we used a two-photon microscope to chronically image the calcium indicator GCaMP6m and the molecular neuronal activity marker c-Fos (TetTag system), in head-fixed and awake mice. Aforementioned, we included a nuclear marker (H2B-mCherry) to track the same cells over weeks, at various intervals, a method developed previously in our lab (Aschauer et al., 2022). This structural marker provides an improvement over usual classical longitudinal studies using calcium imaging. Instead of relying on the variable calcium transients in neurons, we identify the same neurons with a stable marker. Therefore, the tracking is more reliable.

1.7 Scientific question of the project

As explained above (see 1.4.3), the immediate early gene c-Fos is a neuronal activity marker widely used ever since the discovery of its induction from depolarised neurons (Morgan et al., 1987), and as a marker of engrams since the discovery of its role in fear memory (X. Liu et al., 2012). Nonetheless, the causal link of this IEG to the function of neurons remains unclear (Gallo et al., 2018; Leslie & Nedivi, 2011; Minatohara et al., 2016; Yap & Greenberg, 2018). Moreover, it is known from the eighties that c-Fos expression is triggered by various molecules, not only by depolarisation (Okuno, 2011; Yap & Greenberg, 2018).

Taking advantage of the representational drift in the auditory cortex (Chambers et al., 2022), and hypothesizing that neuronal function is controlled by gene expression (Crick F. H., 1958), we wanted to compare two neuronal activity markers. The first one reporting activity at the gene expression level, c-Fos. For this, we used a TetTag system, like experiments revealing the existence of engrams (Garner et al., 2012; X. Liu et al., 2012). The second one able to capture the subtle dynamics of representational drift, hence reporting functional level of neurons, by measuring changes in calcium levels in the neurons, GCaMP6m (T. W. Chen et al., 2013). We did a longitudinal monitoring of the two neuronal activity markers in basal conditions and during learning in order to answer the following central question for this project:

How tight is the correlation of c-Fos levels and neuronal activity?

Chapter 2. Model for chronical in vivo imaging of two neuronal activity markers in parallel

2.1 Nuclear marker, calcium indicator and c-Fos reporter system

To answer the main question, we developed a model of adult C57BL/6J mice, expressing a calcium indicator (GcAMP6m) and a c-Fos reporter (TetTag system) in the auditory cortex (Figure 6). To reliably track the same cells for weeks, neurons were also tagged with a nuclear marker (H2B-mCherry), a method previously developed by colleagues in our lab (Aschauer et al., 2022).

Transduction efficiency and specificity depends mainly on AAV serotypes, but also on viral titer, route of delivery and promoters (Aschauer et al., 2013; Bedbrook et al., 2018; Haery et al., 2019; S. S. Issa, Shaimardanova, Solovyeva, & Rizvanov, 2023; Kantor et al., 2014; D. Wang et al., 2019). To ensure a homogenous distribution in the neurons, we packaged the four DNA constructs in the same viral particles (AAV2/8). We injected the particles simultaneously, at a similar titer (~10^12 VG/ml, see 2.1.1). Additionally, a colleague performed a control to ensure equal distribution of different transgenes, expressed under the same promoter, packaged in the same AAV capsids and injected with a comparable titer. The results are part of an unpublished manuscript “An unbiased AAV-STARR-seq screen revealing the enhancer activity map of genomic regions in the mouse brain in vivo” (Figure S1).

2.1.1 General material and methods for in vivo experiments

The sections 2.1.1.2-2.1.1.4 (plasmids, cloning and virus production) were done by Eike Kienle[1] and described as in the unpublished manuscript “An unbiased AAV-STARR-seq screen revealing the enhancer activity map of genomic regions in the mouse brain in vivo.” by Eike Kienle[1], Ya-Chien Chan[1] and Martin Otis. The DNA constructs hSyn-GCaMP6m and hSyn-H2B-mCherry (see 2.1.1.3) were produced by Dominik Aschauer[1] (Aschauer et al., 2022).

I[1] did perform the stereotactic injections (section 2.1.1.5) as previously in our lab (Aschauer et al., 2022).

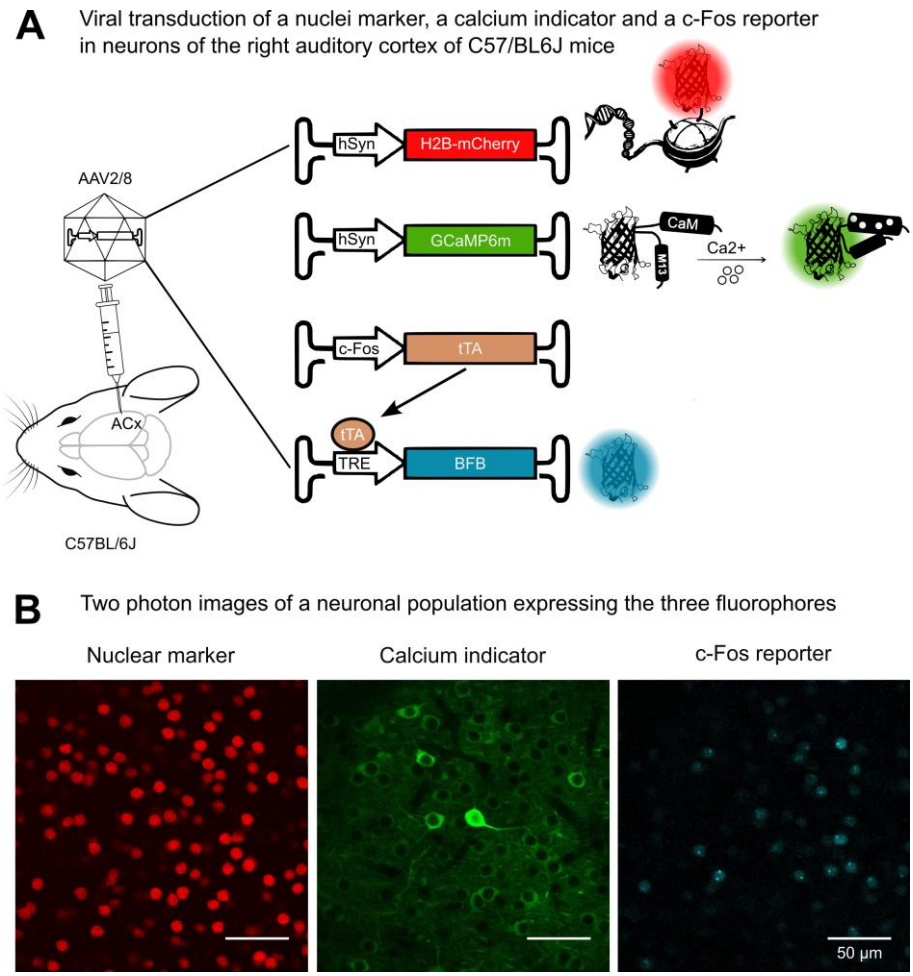

Figure 6. Animal model.

(**A**) Stereotactic injection of adult wild type black six mice (C57BL/6J) in the auditory cortex (ACx), with recombinant adeno-associated virus of serotype eight (AAV2/8), packaging four different DNA constructs: 1. A neuronal nuclear marker: under human synapsin promoter (hSyn (Kügler et al., 2003)), a red fluorescent protein (mCherry (Shaner et al., 2004)) fused to a histone (H2B). 2. A neuronal activity reporter: under hSyn promoter, a green calcium indicator (GCaMP6m (T. W. Chen et al., 2013)). 3. First part of a c-Fos reporter: under c-Fos promoter, a tetracycline-controlled transactivator (tTA) (Z. Zhang et al., 2015). 4. Second part of a c-Fos reporter: under tetracycline-responsive element (TRE (W. Wang et al., 2017)), a blue fluorescent protein (BFP (Subach et al., 2008)). The two later constructs form a Tet-Off system (L. G. Reijmers et al., 2007). (**B**) Two-photon images of a population of neurons virally transduced with the four DNA constructs, excited with different wavelengths. Left: red channel to image the nuclear marker (810 nm or 920 nm). Middle: green channel to image the calcium indicator (920 nm). Right: blue channel to image the c-Fos reporter (810 nm). Dichroic mirrors were used to separate red and green (570 nm) or red and blue (505 nm) signals, imaged in parallel.

2.1.1.1 Mice

Experimental subjects were male C57BL/6JRj (Janvier laboratory) between five and sixteen weeks of age from Janvier laboratories. Before surgical procedures, mice were kept in groups of five, and housed in 530 cm^2 cages on a 12 h light/dark cycle, with unlimited access to dry food and water. Experiments were carried out during the light period. All animal experiments conducted in this study were in accordance with national and European laws for the use of animals in research (2010/63/EU) and were approved by the local ethical committee (Landesuntersuchungsamt Rheinland-Pfalz, 23 177-07/G 17-1-051).

2.1.1.2 Cell culture

HEK293 (human embryonic kidney) cells (ATCC; cat. no. CRL-1573) were cultured in Dulbecco's Modified Eagle Medium (DMEM from Gibco; cat. no. 52100-047), supplemented with 10% heat-inactivated FBS (Sigma; cat. no. F7524), 2 mM L-glutamine (Sigma; cat. no. G7513) and 1% Penicillin-Streptomycin (Sigma-Aldrich cat. no. P0781-100ML). They were kept in a carbon dioxide incubator (37°C temperature, 95% relative humidity and 5% CO_2) and plated at 80% confluence by removing the medium, washing with 1x PBS (phosphate buffered saline), treating with 0.25% Trypsin-EDTA (Gibco; cat. no. 25200-056) until dispersion of the cell layer and resuspension in complete medium.

2.1.1.3 Plasmids and molecular cloning

The plasmid coding for the tetracycline-controlled transactivator (tTA) under the c-Fos promoter was purchased from Addgene (Plasmid #66794).

To elaborate the plasmid containing the blue fluorescent protein (BFP) preceded with three nuclear localisation signals (3xNLS) and the tetracycline-inducible expression sequence/tet-responsive element (TRE), the commercially available plasmid #92202 from Addgene was modified as follows: The plasmid was cut open with restriction enzymes EcoRI (NEB) and BamHI (NEB) and purified after gel electrophoresis. The sequence for 3xNLS was ordered from Sigma as single stranded oligos (3xNLS_oligo_forw: AATTCGCCACCATGGACCCAAAAAAGAAGCGGAAGGTCCCAAAAAAGAAGCGGAAGGTCCCAAAAAAGAAGCGGAAGGTCG. 3xNLS_oligo_rev: GATCCGACCTTCCGCTTCTTTTTTGGGACCTTCCGCTTCTTTTTTGGGACCTTCCGCTTCTTTTTTGGGTCCATGGTGGCG). Oligos were annealed, creating EcoRI and BamHI matching overhangs and subsequently ligated into the cut plasmid #92202.

The resulting plasmid #92202-3NLS was again digested with BamHI (NEB) and SpeI (NEB) to remove the mCherry sequence. A mTagBFP sequence (Subach et al., 2008) was PCR amplified from plasmid pAAVCamKIItagBFP (#104, internal numbering), which was available in our lab, with primers introducing overhangs with BamHI (5'; underlined, italic) and SpeI (3'; underlined, bold)) recognition sites (BFP_BamHI_forw: 5'-CGC*GGATCC*ATGAGCGAGCTGATTAAGGA-3'; BFP_SpeI_rev: 5'- GG**ACTAGT-**TTAATTAAGCTTGTGCCCCA -3'). The resulting PCR product was digested with the respective enzymes, purified and ligated into the cut and also purified plasmid #92202-3NLS. Integrity of the final plasmid #92202-3NLS-BFP was confirmed by Sanger sequencing.

For the recombinant AAV (rAAV) genome encoding for GCaMP6m under the human Synapsin I promoter (hSyn), and the rAAV encoding for H2B-mCherry, two plasmids were generated like described before (Aschauer et al., 2022).

Briefly, the gene coding for GCaMP6m (Addgene plasmid #40754) was amplified with PCR and inserted in a plasmid (Addgene plasmid #26973) containing AAV inverted terminal repeats (ITRs), hSyn, Woodchuck Hepatitis Posttranscriptional Regulatory Element (WPRE), and a human Growth Hormone polyadenylation site (hGH-pA). The digestion of the second plasmid was done with BamHI and AccIII. After insertion of GCaMP6m, the removal of the original transgene was done using AccIII and HindIII. Additionally, 3' overhangs were remove, and 5' overhangs of Klenow fragment were added.

For the elaboration of H2B-mCherry plasmid, a gene coding for mCherry was amplified with PCR and inserted in a plasmid containing H2B directly after its coding sequence, using *ClaI* and *SpeI*. The fusion protein was then inserted in a recombinant AAV genome containing ITRs, hSyn, WPRE and hGH-pA using KpnI and HindIII. The WPRE section was then excised by HindIII and XhoI. Similar to the GcaMP6m plasmid, 3'overhangs were blunted and 5' overhangs were filled in using Klenow fragment.

2.1.1.4 Viruses

All plasmids described above were packaged in serotype AAV2/8 viral particles as follows: $3x10^7$ HEK293 cells were plated in a 16-layer Celldisc (Greiner; Cat. no. 678916) with 1L complete DMEM growth media (described above) and cultured for 48 h in a CO_2 incubator (described above). Cells were then chemically transfected with

calcium phosphate as described below, mixing in an equimolar ratio the helper plasmid pADDeltaF6 (Addgene plasmid #112867), the packaging plasmid pAAV2/8 (Addgene plasmid #112864) and the plasmid to be packaged in the viral capsid. 69 ml of 300 mM CaCl2 was added to the plasmid DNA. The mixture was slowly added to 69ml 2xHBS solution (Aesar; Cat. no. J62623), and after 5 minutes of incubation, added to 500ml DMEM supplemented with 5% fetal calf serum (FCS), without addition of antibiotics. After a careful decantation, the culture media was replaced in the Celldisc with the transfection media. The cells were incubated 6 h, and the media was decanted and replaced with 1L of fresh full growth media, before incubation for additional 72h.

To harvest the cells, growth media was carefully decanted and collected. 500ml of kept growth media was supplemented with 7ml 0.5M EDTA (Invitrogen; Cat. No. 15575-020). 400ml of the latest was added to the Celldisc, and after 5 minutes incubation at room temperature (RT), cells detached from the disc. The cell suspension was transferred to a 500ml centrifugation flask (Corning; Cat. no. 431123). The remaining 100ml was used to wash the Celldisc and added to the centrifugation flask. After centrifugation at 800xg at 4°C for 15min, supernatant was carefully removed. Cell pellet was resuspended in 2x10ml PBS and transferred to a 50ml conical tube and centrifuged again at 800xg at 4°C for 15min. PBS was carefully removed and the cell pellet was resuspended in lysis buffer. Subsequently AAV purification was done by ultracentrifugation over a iodixanol gradient, as described previously (Zolotukhin et al., 1999).

2.1.1.5 Unilateral stereotactic injection (right hemisphere)

The surgical tools were sterilized with 70% ethanol before use. Mice were first anesthetised for 20 minutes in an induction box with 1.5-2% isoflurane (Isofluran-Piramal, Piramal Critical Care, Germany), and intraperitoneally injected with dexamethasone (4mg/ml ~100x diluted in PBS, Bela-pharm, Germany) diluted in Dulbecco's phosphate-buffered saline PBS (Sigma (Merk), Cat. no. D8537) to prevent inflammation after the surgery. Mice were then fixed with metal earplugs to the stereotactic instrument (Kopf Instruments, Tujunga, CA, USA; Stereotactic System Kopf, 1900), beforehand calibrated to a zero position. During the rest of the surgery, anesthesia was maintained by a continuous delivery to the snout (flow rate ~200 mL/min) of 1.2-1.5% of isoflurane mixed with air (UNO, Netherland, univentor 400 or 410 anesthesia unit). Mice body temperature was maintained with a heating pad (32-

37°C). Their eyes were covered with Vaseline and a piece of aluminium foil, in order to protect them from dehydration and light. After sterilisation of the surgical area (above the skull) with ethanol, a local anesthetic containing lidocaine and adrenaline (Xylonest 1% mit Adrenalin, Aspen, Cat. no. PZN-03079396) was subcutaneously injected. A sagittal cut of the skin allowed to expose the skull. The stereotactic coordinates for the auditory cortex were based on a mouse brain atlas (Paxinos & Franklin, 2001), and found as follows: a scope was used to localise by eye bregma. The position of the mouse head was adjusted until the skull surface aligned to the horizontal plane. An injector (World Precision Instruments, Sarasota, FL, USA; Nanoliter, 2000 Injector) mounted with a pooled glass capillary (tip ⌀ 20-40 mm, Sutter instrument, Novato, CA, USA) and a surgical pen were used to find and mark the coordinates on the skull. Finally, a craniotomy above the auditory cortex was performed with a motorized drill (Pana Max, NSK dental, Germany), leaving the dura mater intact. A mixture of four different rAAV viruses in PBS (1. rAAV2/8 ITR-pAAV-hSyn-GCaMP6m-pA; titer: 2.96x10^11 viral genomes (VG)/ml; 2. rAAV2/8 ITR-pAAV-hSyn-H2BmCherry-pA; titer: 8.85x10^12 VG/ml, 3. rAAV2/8 ITR-pAAV-c-Fos-tTA-pA; titer: 1.02x10^13 VG/ml, and 4. rAAV2/8 ITR-pAAV-3xNLS-TRE_BFP-pA; titer: 3.53x10^12 VG/ml) was loaded in the glass pipette. 150 mL were injected at a flow rate of 20 mL/min in six locations along the anterior-posterior axis, from bregma: x/lateral = 4,3-4,6 mm; y/ant-post = -3,6/-3,3/-3/-2,7/-2,4/-2,1 mm; z = -2,5 mm (caudal, lateral and ventral to bregma), resulting in a total injection volume of 800nL. After each injection, the pipette was left for 3 minutes before being slowly withdrawn and moved to the next coordinate.

After the injections, the skull surface and skin were cleaned and hydrated with PBS, and the skin was sealed using a tissue adhesive (3M Animal Care Products, St. Paul, MN, USA; 3M Vetbond Tissue Adhesive). Finally, a painkiller (50mg/ml carpofen ~100x diluted in PBS, Rimadyl Injektionslösung für Hunde und Katzen, Zoetis, NJ, USA) was injected intraperitoneally, the Vaseline and aluminium foil were remove with a cotton stick and the mice were put back in a pre-warmed cage. After surgery, the mouse stayed overnight isolated, before being put back in the home cage together with the previous cage mates.

2.2 Chronical imaging in the auditory cortex

To chronically measure both activity markers (Figure 7), GCaMP6m and c-Fos, we waited about three weeks for the transduction of the viruses. In the meantime, we created a cranial window above the site of injection. We confirmed the location of the window above the auditory cortex using a tonotopic map, acquired with an optical imaging of intrinsic signals during pure tones presentation. A week of recovery after the surgery allowed the window to stabilise. Mice were then habituated for about a week to head fixation in a two-photon microscope. To track the same cells over several sessions of recording, we used the vessel patterns, the coordinates, and the nuclear marker to compare the population to a reference picture acquired the first session. Both neuronal activity markers were imaged in parallel to the nuclear marker, thanks to dichroic mirrors to separate the emitted wavelengths of the different fluorophores (described in Figure 6).

Due to differences in temporal dynamics of calcium transients and c-Fos expression, we recorded both signals with a different time resolution. Calcium transients change at a time scale of milliseconds, whereas c-Fos protein is expressed upon minutes and the cellular concentration of the protein returns to baseline levels after a few hours (Day-Cooney et al., 2022; L. Reijmers & Mayford, 2009; W. Wang et al., 2019). Therefore, image acquisition for calcium indicator fluorescence was perform as video (*t-serie)* at five images per second (5 Hz), for each session (Figure 11). For c-Fos reporter fluorescence, we only took one image per population and per time point (interval of one hour, one day or 2 days). c-Fos was imaged in the same population of neurons as the calcium indicator, as *single scans*. Additionally, c-Fos signal was acquired as series of scans along z-axis, *z-stacks*, to increase the sample size (Figure 8).

2.2.1 General material and methods for in vivo experiments

I[1] did the cranial window implantations, the intrinsic imaging sessions, the habituation sessions and the two-photon imaging sessions, as previously in our lab. The description is inspired by Dominik Aschauer[1] and Anna Chambers paper (Aschauer et al., 2022; Chambers et al., 2022). In order to image BFP for the first time in our lab with the two-photon microscope, I developed the protocol described in section 2.2.1.4, § 2.

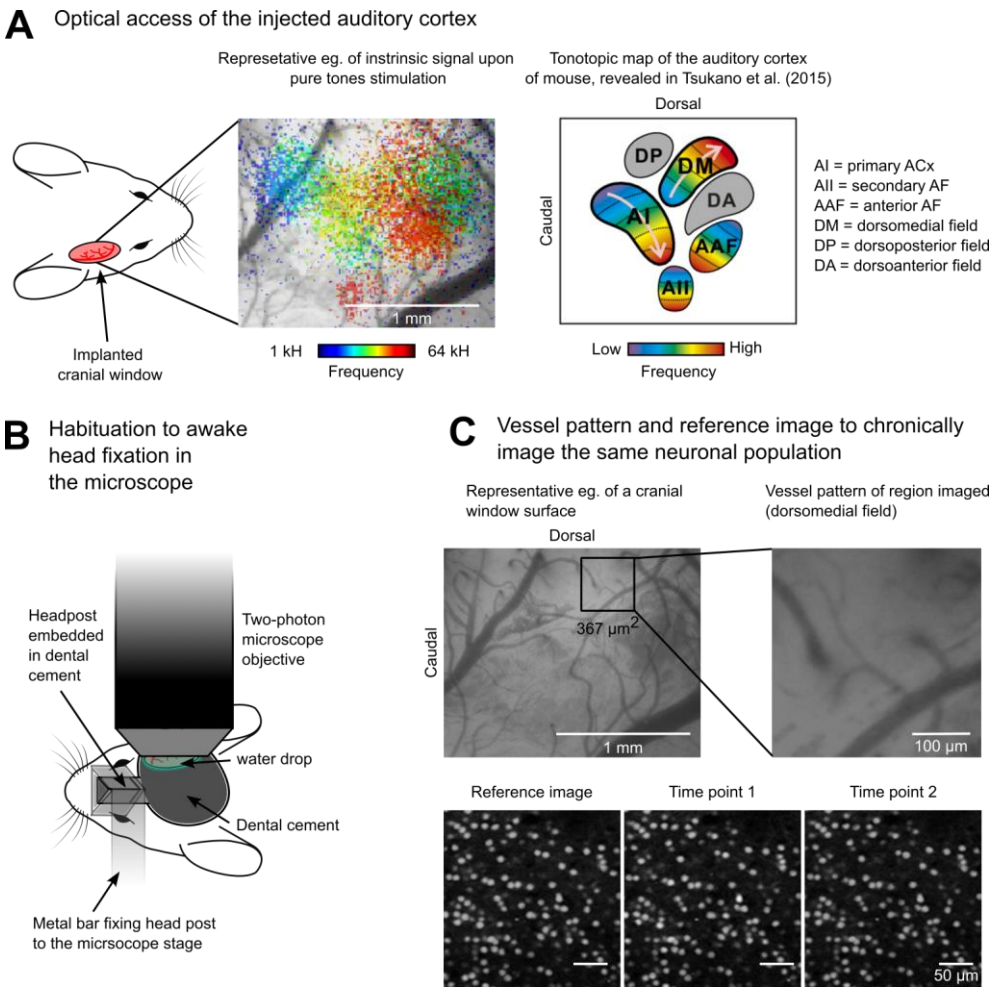

Figure 7. Chronical neuronal population imaging strategy.

(**A**) Left: Cranial window implantation for visual access to the virally transduced cells in the ACx. Middle: Intrinsic signals imaged through the cranial window, to confirm window position above the ACx. Right: Tonotopic map from the literature as a reference to localise imaging area in the ACx (J. B. Issa et al., 2014; Tsukano et al., 2015). (**B**) Two-photon microscope setup to image neuronal populations in an awake head-fixed mouse. (**C**) Top left: CCD camera picture of a window surface. Top right: Zoom in the area imaged (~360 µm^2). The blood vessels are the gross reference to localise the area imaged from one time point to the next. Fine localisation of the population was achieved with the nuclear marker signal from the first time point of recording. Bottom: Exemplary neuronal population (nuclear marker) imaged at three different time points with the two-photon microscope.

2.2.1.1 Unilateral cranial implantation (right hemisphere)

2-3 weeks after the stereotactic injection (see 2.1.1.5), a cranial window was implanted above the area injected (auditory cortex), as follows:

The surgical tools were sterilised. Mice were anesthetised and intraperitoneally injected with an anti-inflammatory drug, as described in section 2.1.1.5. For fixation, on the right side of the skull, instead of a metal earplug, a custom-made v-shape tool was used to allow access to the skull above the auditory cortex. Isoflurane anesthesia and body temperature were maintained all along the surgery, as described in section 2.1.1.5. Mice eyes were covered with Vaseline and aluminium foil, the surgical area (above the skull) was sterilized and a local anesthetic was delivered subcutaneously, as described in chapter 2.1.1.5. The adrenaline allowed limiting the bleeding due to its vasoconstrictive property. A piece of skin covering the temporal and parietal area, as well as part of the occipital bone, was removed with a scissor. The local anesthetic was applied in the musculus temporalis, and the part of the muscle covering the skull above the right temporal bone was detached and cut. To clean the surface of the skull, sponges immersed in PBS (Spongostam Standard, Ethicon, NJ, USA) and cotton stick to dry the liquid were used. The motorized drill was then employed to smoothen and flatten the entire skull surrounding the temporal bone, including part of the zygomatic process. A thin layer of instant glue (Best-CA 221, Best Klebstoffe, Germany) was applied on the skull, sparing the temporal bone (⌀ ~6 mm^2), and once dried, a layer of black dental cement (Steady-resin polymer powder and liquid, Cat. Num. 8130.1 and 8141.1, Scheu dental, Germany) was added on top of the glue. An oval shape groove was then carefully drilled into the skull, above the auditory cortex (~4 by ~5 mm), and the bone was carefully lifted while applying some PBS between the skull and the dura matter to separate both, without disrupting the later. The exposed brain area was directly covered with PBS and kept moist, and carefully cleaned with sponges and cotton sticks. The craniotomy was covered with a 5 mm diameter glass coverslip (Electron Microscopy Sciences, PA, USA; cat. no. 72195-05), and sealed using the 3M vetbond tissue adhesive described in 2.1.1.5. Around the window, a small pool was formed with the dental cement to allow the water to stay under the water-immersed objective when imaging with the two-photon microscope. Lastly, a custom-made titanium headpost was embedded in dental cement on the top of the skull, between the eyes, to allow fixation of the mice in the microscope. To ensure the window to be

perpendicular to the microscope objective, the headpost was fixed in a specific position, determined by a custom-made tool with a laser reflected on the window. In order to let the dental cement dry, the mouse was kept under anesthesia 15 more minutes, and afterwards put back in a pre-warmed cage. After surgery, the mouse stayed overnight isolated, before being put back in the home cage together with the previous cage mates.

2.2.1.2 Optical imaging of intrinsic signals

In order to verify the position of the window above the auditory cortex, intrinsic imaging technique was used as follows:

2-5 days after the cranial implantation, the recording of intrinsic activity was done in a soundproofed box, during the presentation of pure tones: 1, 2, 4, 8, 16, 32, and 64 kHz (2 seconds long: 20 pips of 80 ms, with 20 ms gaps), each presented 30 times in randomized trials. To measure the activity, a CCD camera (model IEEE-1394, Vosskuehler, Germany; 25 Hz frame rate) attached to a microscope, consisting of 2 objectives placed face to face (Nikon 135 and 50 mm) and 2 LEDs (470 and 780 nm) was used. Mice were lightly anesthetized with 0.8-1.2% isoflurane, like described above. They were then placed on a heating pad, under the CCD camera, using the custom-made headpost so that the window was perpendicular to the camera. The blue LED and white light were used to acquire images of the brain surface and hence the blood vessel pattern. The focal plane was moved to 400 µm under the surface. The infrared LED (20-60 mW) was then used to measure a baseline and response image for each sound (2 s before and 2 s after stimulus onset, respectively). The intrinsic activity was calculated as the change in light reflectance, comparing the pre- and post-stimulus image (averaged for all trials of the respective stimulus).

2.2.1.3 Habituation to fixation in two-photon microscope

3-6 days after the cranial implantation, mice were daily brought to the two-photon microscope setup. For 5-10 days during progressively 5 min - 1 hour, they were put in an acrylic glass tube and the headpost was fixed such that the cranial window (and therefore the brain surface) was perpendicular to the objective. Mice were habituated to the microscope sounds for acquisition of the images (shutters), as well as to the darkness and silence of the soundproofed box.

2.2.1.4 Two-photon microscopy

The two-photon microscope (Ultima IV, Prairie technologies (Bruker), WI, USA) consists of a 20x objective (Olympus, Tokyo, Japan; XLUMPlan FI, NA= 0.95) and a pulsed laser (Coherent, CA, USA; Chameleon Ultra). The objective and the stage to carry the mice were surrounded by a soundproofed box (~40 dB noise reduction).

To image BFP (c-Fos reporter) and H2B-mCherry (nuclear marker) in parallel, the fluorophores were co-excited at a wavelength of 810nm, and the emission wavelength was separated with a dichroic mirror (filter 1: BP 460–490nm; filter 2: LP 515nm; dichromatic mirror: DM 505nm; Olympus, Tokyo, Japan; U-MWIB 3). Imaging of reference single scans and z-stacks was done using a field of view (FOV) of 367 μm^2 (1024x1024 px). The stacks of the z-stacks were separated with 1 µm of depth (sampling period: 3.19s), and imaged in layer 2/3 of the auditory cortex (50-300 µm under the brain surface). Imaging of the following z-stacks was done with the same FOV size, but a lower resolution (256x256 px), and each stack was separated with 2 µm (sampling period: 393.72 ms). For further analyses, the reference single scans and stacks were downsized to 256x256 px.

To image GCaMP6m (calcium indicator) and H2B-mCherry in parallel, the fluorophores were co-excited at a wavelength of 920nm, and emission wavelength was separated with a dichroic mirror (filter 1: BP 480–550 nm; filter 2: LP 590 nm; dichromatic mirror: DM 570nm; Olympus, Tokyo, Japan; U-MSWG2). To image the t-series, the size of the FOV was 367 μm^2 as well, but the resolution was lower compared to the z-stacks (256x128 px). The acquisition was done with a 5 Hz frame rate (sampling period: 196.86 ms). For further analysis, the lines in the y dimension of each frame was doubled to obtain a quadratic FOV (256x256 px).

For chronical acquisition of the same cells over time, the vessel pattern was used for gross localisation of the region imaged. To target the auditory cortex, the tonotopic map acquired with the intrinsic imaging setup was overlapped with the vessel pattern. For fine localisation of the neuronal population, a reference image from the H2B-mCherry channel was acquired in layer 1 of the cortex, and on the neuronal population imaged in layer 2/3 with the two neuronal activity markers. The three images for gross and fine localisation were used all along the experiment to acquire aligned z-stacks, single-scans or t-series, imaging the same cells every time point.

Chapter 3. Imaging analysis strategy

3.1 c-Fos analysis

Taking advantage of the nuclear marker, we could track the cells chronically (Figure 8). Z-stacks and single scans analysis pipelines are described in material and methods (see 3.1.1.1). Briefly, from one time point to the other, neuronal populations were aligned in order for the automatic pipeline to track the cells and extract information of nuclear marker (from nucleus), and c-Fos reporter (from nucleus) fluorescence intensities for the same cells over time. To keep only reliable signal from the recordings, quality criteria based on the nuclear marker were established for z-stacks and single scans (Figure 9). The criteria are described in material and methods (see 3.1.1.2). Finally, to binarize cells expressing c-Fos as c-Fos positive and c-Fos negative cells, criteria were established based on c-Fos signal (Figure 10). Criteria to define a c-Fos positive cell are describe in material and methods (3.1.1.3).

3.1.1 General material and methods

David Lüdke[3] and I collaborated to develop the pre-processing pipeline (Python scripts) to extract 2D populations from z-stack, match populations with z-stack from the next time point, detect the nuclei and align the populations xy-wise (section 3.1.1.1, steps 1-4).

Bastian Eppler[3] and Dominik Aschauer[1] collaborated to develop the processing pipeline (MATLAB scripts) to track the cells, exclude cells with a poor signal quality and extract the fluorescence signal (3.1.1.1 - z-stacks, steps 5-7). This was originally used for the analysis of calcium t-series, and I adapted the pipeline to analyse the c-Fos data from the z-stacks and the single scans. The pipeline is described in Dominik Aschauer[1] and Bastian Eppler[3] paper (Aschauer et al., 2022).

Johannes Seiler[1], Simon Rumpel[1] and I[1] teamed up to define inclusion criteria for the nuclei (3.1.1.2) and a fixed threshold to classify the cells as c-Fos positive and c-Fos negative (3.1.1.3) in the experiments described in chapters 4.2, 5, 6 and 7.1 (c-Fos data).

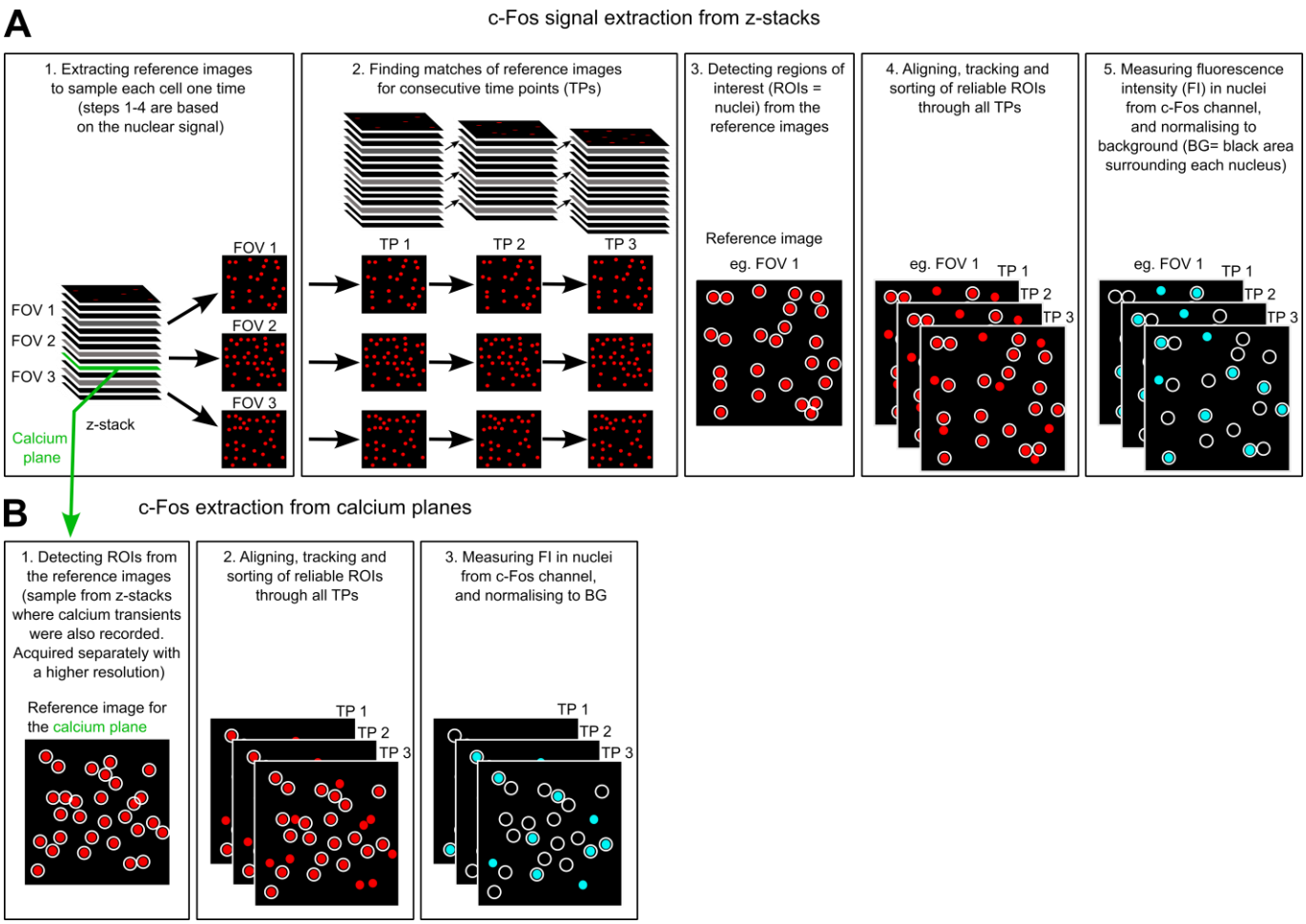

Figure 8. Chronical in vivo image analysis pipeline for c-Fos expression.

(**A**) c-Fos analysis pipeline for z-stacks (367 µm^2, 256x256 px), in five steps: 1. Image selection every 20 µm, to image every cell only once (nuclei size ~9 µm). 2. Finding same populations in following time points. Calculating key points on the images using SIFT algorithm (Scale-invariant feature transform) and crosschecking the key points with a brute force matching strategy (euclidean distance based match-validation). 3. Detecting regions of interest (ROIs=nuclei=cells). Equalize image (Gaussian blur), binarize image (otsu threshold) and use a blob detection (laplacian of Gaussian). 4. Align images (XY translation) and track ROIs with a local affine transformation for each new frame, and solve the six-dimensional optimization problem (rotation angle, scale in x, scale in y, off diagonal of scaling matrix, shift in x, shift in y) with the Nelder-Mead-Simplex algorithm. Exclude ROIs closer than 3 px, and with a poor signal-to-noise ratio. 5. Measure of mean grey value (MGV) in 2 px diameter around the ROIs (nuclei) and normalise to the mode of MGV in 10 px diameter (background), both in the blue channel for the c-Fos signal. (**B**) c-Fos analysis pipeline for calcium planes (367 µm^2, 1024x1024 px), sampled from the cortical region where the z-stacks were acquired. The calcium planes were imaged in the cell populations where calcium transients were also recorded. The three steps to extract c-Fos signals are the same described in (A), as steps 3-5.

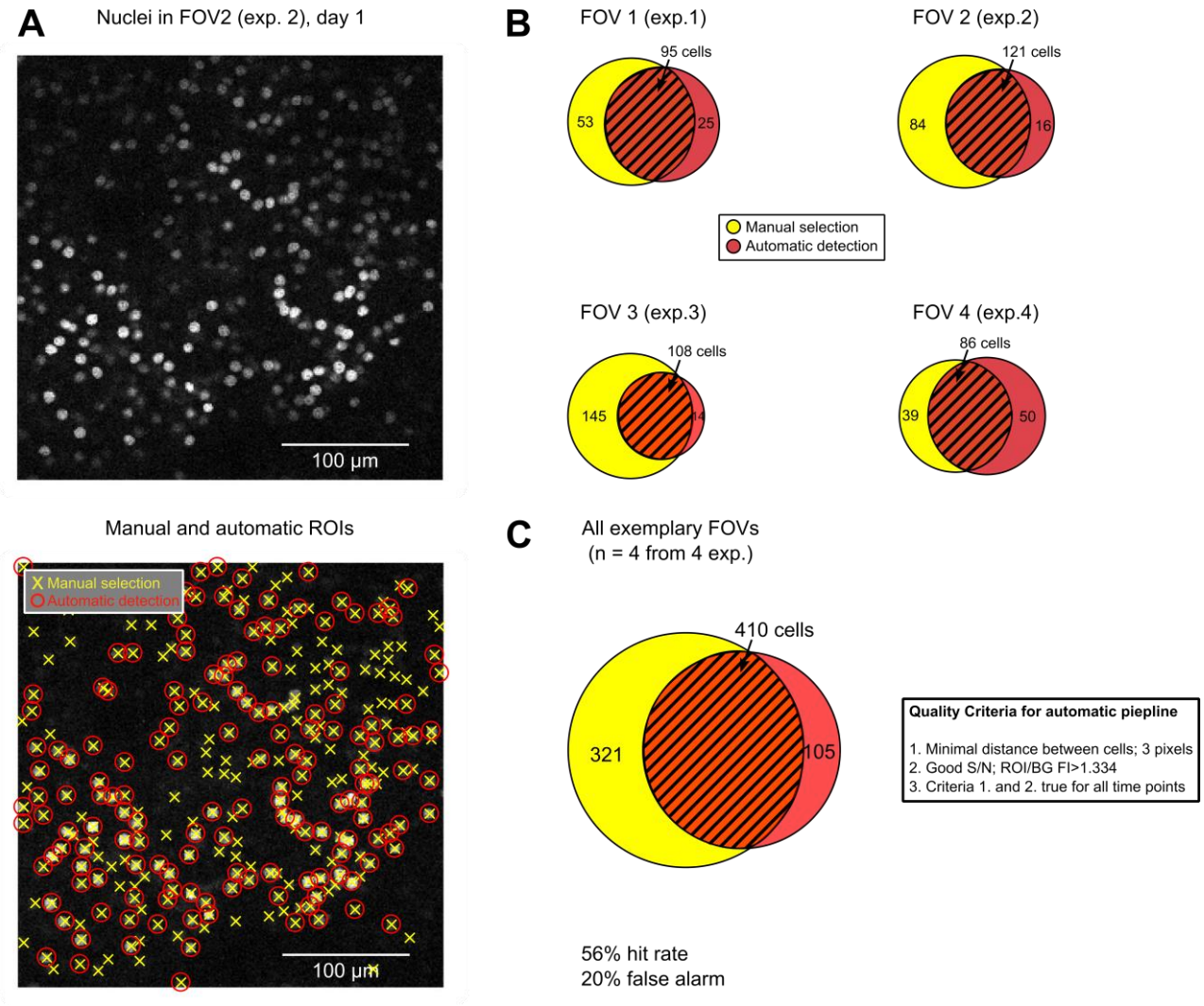

Figure 9. Quality criteria for ROIs inclusion; comparison of a manual selection and the automated detection of nuclei.

(**A**) Top: Two-photon image of an exemplary field of view (FOV), imaged in the nuclear marker channel. Bottom: FOV overlaid with ROIs manually selected (yellow crosses) and automatically detected (red circles). (**B**) Venn diagrams showing the overlap between the manual selection and the automatic detection for four individual examples, selected across the in vivo experiments performed during the project (experiment 1 in section 5.1.1.1, exp.2 in section 5.1.1.2, exp. 3 in Chapter 6 and exp. 4 in section 7.1). (**C**) Left: Venn diagram for the four FOVs pooled together. Right: Two thresholds were used to optimise the percentage of hit rate (56%) and false alarm (20%): a minimal distance (3 px) to avoid ROIs overlap, and a high signal-to-noise ratio (>1.344) to insure the quality of the signal detected (presence of a nucleus, and not noise). Both criteria had to be met throughout the imaging sessions (time points) in order for a ROI to be kept for further analyses.

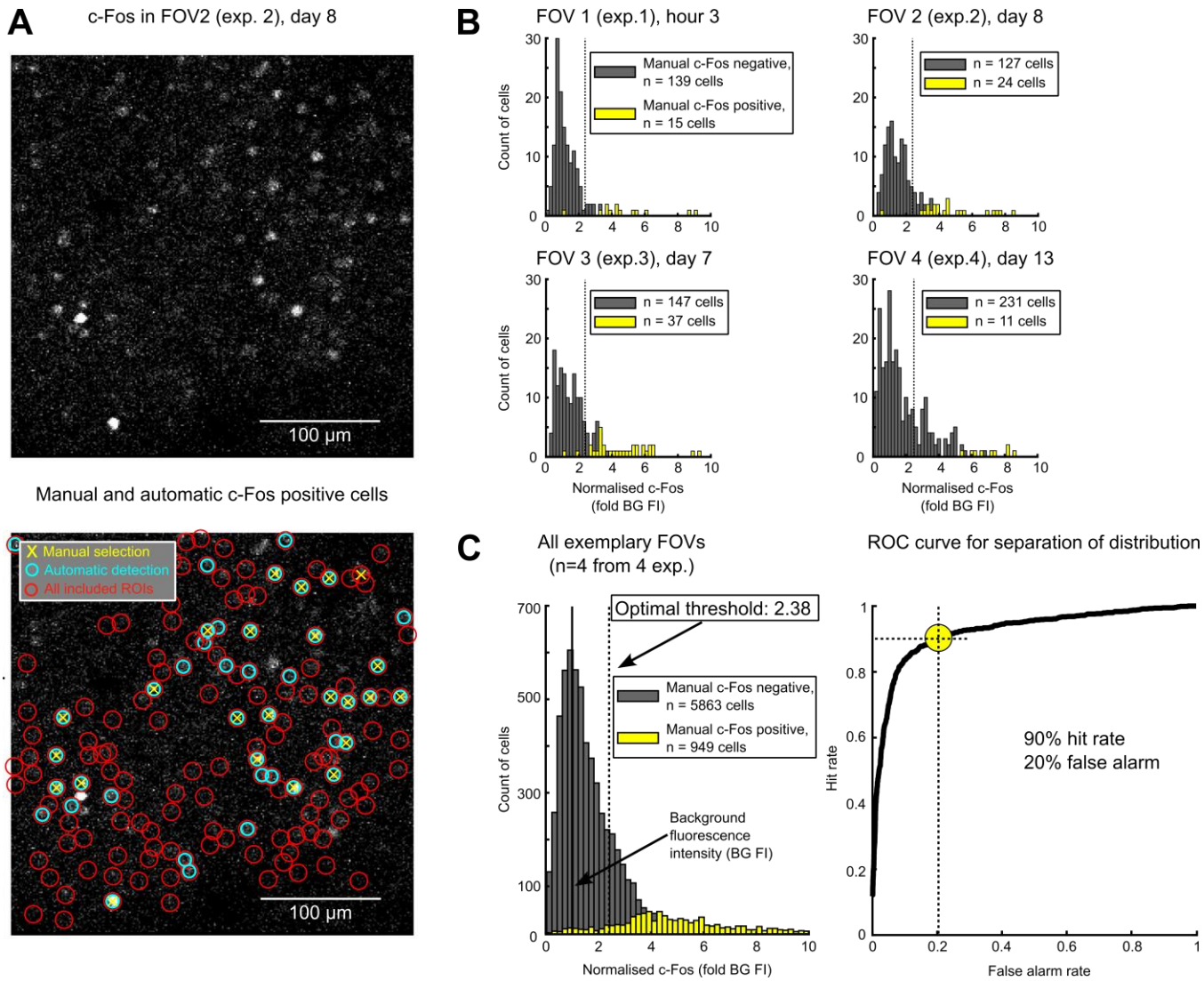

Figure 10. Threshold to binarize c-Fos signal: comparison of a manual selection and the automated detection of c-Fos.

(**A**) Top: Two-photon image of the exemplary FOV in Fig.9, imaged in the c-Fos reporter channel. Bottom: FOV overlaid with included ROIs (red circles), a manual selection of c-Fos positive cells (yellow crosses) and the automatic detection of c-Fos positive cells, applying the threshold (blue circles). (**B**) Histograms showing the distribution of the c-Fos signal values for cells manually selected as c-Fos negative or c-Fos positive among the ROIs, for the four individual examples FOVs shown in Fig.9. (**C**) Left: Histogram for the 4 FOVs pooled together. Right: Receiver operating characteristic curve (ROC) used to find the threshold, in order to reach a high hit rate (90%) and a low false alarm percentage (20%).

3.1.1.1 Chronical in vivo two-photon images processing

Z-stacks

A first imaging session with a high quality acquisition was performed in anesthetised mice (0.8-1.5% isoflurane). The following time points, z-stacks were imaged on awake mice with lower resolution in order to decrease acquisition time and limit motion artifacts in the images.

In order to track the cells over time, several processing steps were applied on the z-stacks (256x256 px), based on the H2B-mCherry signal (nuclei):

1. Extract 2D populations: from the reference z-stack (from first time point under anesthesia) acquired in layer 2/3 of the auditory cortex (50-300 µm of depth), a single stack every 20 µm was extracted. This distance allowed to image every cell only once (diameter of a nucleus ~9 µm).
2. Match populations across z-stacks/time points: to find the reference populations in the z-stacks from the following time points, a matching algorithm working as follows was used: calculation of key points on images using a SIFT (scale-invariant feature transform) algorithm and crosschecking the key points with brute force matching strategy (Euclidean distance based match-validation). The matching IDs in the z-stacks were used for both H2B-mCherry and BFP (c-Fos) channels.
3. Detect ROIs: to detect the cells nuclei from the reference populations, images were equalised (Gaussian blur), binarized (Otsu threshold) and a blob detection was used (laplacian of Gaussian).
4. Align same populations across time: the different time points for each population were aligned xy-wise as follows: equalisation of images (Gaussian blur with high- low-pass filter) and implementation of cross-correlation (fast Fourier transformation) to calculate similarity index and xy translation. The alignment was applied on both H2B-mCherry and BFP (c-Fos) channels.
5. Track the cells in the aligned images: to track the cells from the reference to the last time point, the set of ROIs was transformed for each frame by a two-dimensional affine transformation. Then, a Nelder-Mead-Simplex algorithm was used to solve the six dimensional problem (rotation angle, scale in x, scale in y, off diagonal of scaling matrix, shift in x, shift in y), with three iterations. First for the entire frame, then for four equally sized horizontal segments to correct for

full frame movements during the two-photon microscope scanning. In a third iteration, individual ROIs were moved to the maximum in a 2 px (2.87 µm) surrounding of a low-pass filtered image to allow for slight local distortions. The new ROIs generated for each time point were used for both channels.

6. Exclude cells if not detected across all time points (see inclusion criteria).
7. Extract signal: 2 px radius (2.87 µm) around each ROI was used to measure the mean grey value (MGV) in the nuclei. The background was measure as the mode of a 10 px radius (14.34 µm) around the ROI. Both measures were applied on the H2B-mCherry and BFP channel.
8. Normalise signal: the extracted signal from nuclei was normalised with the background signal, in order to compensate for variation in different part of the images, as well as in different time points due to changes of microscope settings and quality of the cranial window.

Single scans on calcium planes

c-Fos signal in the populations, where calcium was recorded as well, was imaged separately in higher resolution images (1024x1024 px).

All the steps described above to analyse the z-stacks were replicated in the single scans, except for the two first. The matching was done by eye, when acquiring the images, comparing the population to the reference image acquired on the first day under anesthesia.

3.1.1.2 ROIs inclusion criteria

In order to insure the quality of the cells tracked over time, two inclusion criteria were applied:

1. Nearest neighbour distance (NND): minimal distance between ROIs of 3 px (4.3 µm), to avoid cell overlap and decrease the risk to wrongly label individual cells.
2. Good signal-to-noise ratio. The threshold is based on manual selection of nuclei in four exemplary FOVs across the different experiments. The threshold for automatic pipeline was defined such that the hit rate (56%) and false alarm (20%) could be optimised to the manual selection of nuclei (Figure 9).

The two criteria had to be fulfil for every time point in order for a cell to be kept in the analysis.

3.1.1.3 c-Fos positive cells

To automatically binarize the c-Fos signal as positive and negative, a threshold was defined with a manual selection (Figure 10). The threshold was extracted from the distribution of c-Fos values selected as positive and c-Fos values selected as negative. From a receiver operating characteristic curve, the threshold was optimised such that the hit rate was high (90%) and the false alarm low (20%).

3.2 Calcium signal analysis

Similar to c-Fos signal, the nuclear marker was used as a reference to track the same cells. But the tracking was done in the same session, for each t-serie recording (Figure 11). The analysis pipeline is described in material and methods (3.2.1.1, 3.2.1.2). The t-series were aligned xy-wise from one session to the other, to facilitate the tracking of the same cells. The ROIs from the reference single scans from c-Fos recording were used on the same populations, in order to compare the signals from the calcium transients and c-Fos expression in the same cells. Calcium transients were extracted from the soma, and activity was calculated as ΔF/F0 (3.2.1.3).

3.2.1 General material and methods

The pipelines for image processing of t-series, ROIs inclusion criteria and ΔF/F0 calculation (all sections under 3.2.1) were developed by Bastian Eppler[3] and Dominik Aschauer[1], as mentioned before. My colleague Johannes Seiler[1] and I[1] used and adapted the MATLAB scripts available in the lab to analyse the calcium data I acquired in 4.2, Chapter 5, Chapter 6 and 7.1. Description of the pipeline was previously published (Aschauer et al., 2022).

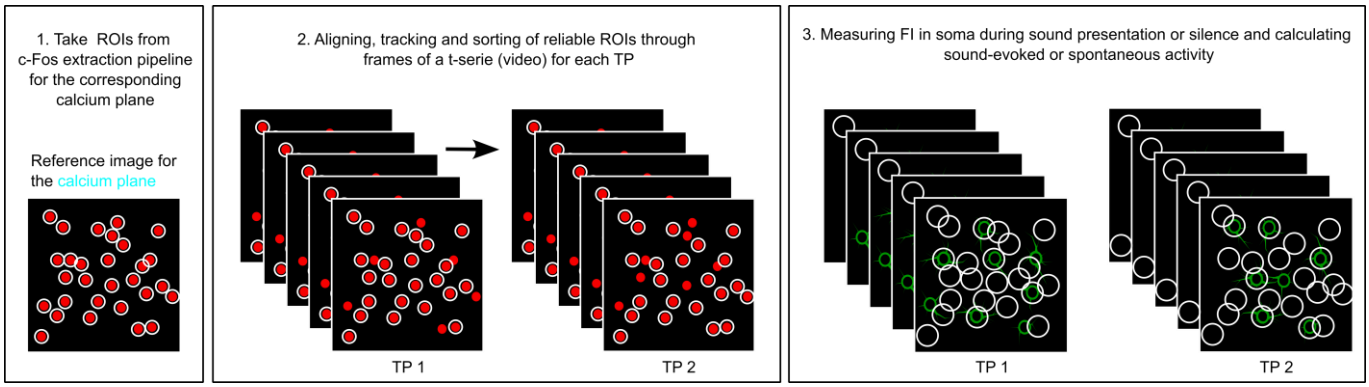

Figure 11. Chronical in vivo image analysis pipeline for calcium transients.

Calcium analysis pipeline of the t-series (367 μm^2, 256x128 px, 5 Hz) in the calcium planes, in three steps: 1. Detecting ROIs, as described in Fig.8A3. 2. Align t-serie to reference image (XY translation) and track ROIs as described in Fig.8A4, but in a single time point, across frames of the t-serie. Exclude ROIs closer than 3 px, ROIs with a poor signal-to-noise ratio, and additionally those with a poor normalised soma signal intensity. Exclude as well poor quality frames due to motion artifacts. 3. Measure the signal as the difference between the mean of 4 px and the mean of 2 px around the ROI (in the soma). F0 is the 30^{th} percentile of surrounding frames. $\Delta F/F0$ is deconvolved using the algorithm by Vogelstein et al. (Vogelstein et al., 2010).

3.2.1.1 Chronical in vivo two-photon images processing

As mentioned above, since the dynamics of calcium transients are faster (scale: milliseconds) compared to c-Fos expression (scale: minutes to hours), imaged were acquired as t-series (frame rate: 5 Hz). Each individual t-serie was analysed in a very similar way as described for c-Fos signal across time points, from step 3:

1. Detect ROIs: the ROIs were previously detected in the single scans acquired from the calcium plane. The same ROIs were therefore used to measure c-Fos and calcium signals in the same cells.
2. Align same populations across time: the t-series from different time points were aligned as follows: using MATLAB (R2016b), mean projection of the t-series were aligned with the reference image, xy-wise, by selecting by eyes the same point (a recognisable cell) on every projection and changing the coordinates accordingly on every frame of the t-series.
3. Track the cells in a t-serie: method described for c-Fos signal (3.1.1.1 - step 5).
4. Exclude cells if not detected across all time points (see 3.2.1.2).
5. Extract signal: In order to measure the MGV in the soma, MGV of 2 px radius (2.87 µm) were subtracted from MGV of 4 px radius (5.74 µm) around each ROI. The background was measured as the mode of a 10 px radius (14.34 µm) around the ROI. The three measures were done in each frame using the corresponding new ROIs.
6. Calculate activity (see 3.2.1.3)

3.2.1.2 ROIs inclusion criteria

In order to insure the quality of the cells tracked over frames, three inclusion criteria were applied on the cells and one on the entire frames:

1. Nearest neighbour distance (NND): minimal distance between ROIs of 3 px.
2. Normalised soma signal intensity (NSSI): for each cell in each frame, the 95 percentile of the difference between BG mode and nuclei MGV was computed. Cells with an intensity close to the background, an NSSI below the value of 0.2, were excluded. This measure was to assess the quality of the nuclear marker signal across the t-serie.
3. Soma Signal-to-Noise ratio (SSN): the difference of the mean intensity of the nucleus and the BG mode was defined as the reference signal for the nuclei. The standard deviation of a jittered version of the signal (same radii, but pseudo-

random location of the nucleus in the 10 px radius) was defined as noise. SSN of a cell had to be more than one to fulfil this quality criteria. This measure was to assess the quality of nuclear marker signal in a single frame.

4. Objective function value (OFV): The objective function value describes the pixel-wise overlap of the frame and the template (reference), based on the ROIs set. In order to eliminate motion artifacts, individual frames in which OFV was less than 3 standard deviations below the mode of the OFV for a given FOV were discarded.

All quality criteria were tested and cells were excluded on each individual frame. Excluded values were treated as missing entries in the data. Cells that were not reliably detected on at least 50% of the trials on a given day were completely excluded from the analysis.

3.2.1.3 Calculation of ΔF/F0 and deconvolution

The baseline F0 to calculate ΔF/F0 was defined as a moving rank order filter, the 30th percentile of the 200 surrounding frames (100 before and 100 after). This ΔF/F0 was then deconvolved using the algorithm published by Vogelstein and colleagues (Vogelstein et al., 2010).

Chapter 4. c-Fos reporter kinetics

4.1 Synthesis time (in vitro)

The blue fluorescent protein is not reporting directly c-Fos expression, but rather how the tetracycline-controlled transactivator (tTA) is expressed under c-Fos promoter and binds to the tetracycline-responsive element (TRE). To understand the delay caused by the indirect expression of BFP, we decided to use an in vitro approach, allowing to depolarise the neurons in a time constricted manner (Figure 12).

4.1.1 Results

As described in Figure 12, we first transduced primary cortical cells from black six new-born mice with the c-Fos reporter system (Figure 6), and acutely (15min) activated the cultures with a mixture of neurotransmitters, a GABA (gamma-aminobutyric acid) antagonist and a cholinergic agonist. The sodium channel blocker, tetradotoxin, was used to block spontaneous activity in mature cell cultures before the treatment, and after the treatment, to stop the depolarisation due to the mixture. Finally, the cultures were fixed with PFA at different time points (0-72h), and stained with c-Fos antibody in order to compare the reporter and the endogenous c-Fos expressions (Fig.12A). After pre-processing of the epifluorescence images from 2-3 replicats, c-Fos reporter and c-Fos antibody signals could be extracted from ~800-1800 (8-12 FOVs) cells for each time point (Fig.12B).
The results (Fig.12C and D) indicate a delay of several hours for the reporter to express BFP at a significantly higher level (Wilcoxon rank sum tests comparing 0h-12h: p=1.0744e-16) than before treatment, compared to c-Fos endogenous expression (Wilcoxon rank sum tests comparing 0h-2h, p=5.0784e-178).

The cell culture may not reflect the timing of the system in vivo, as previous groups using TetTag mice and comparing control and fear-conditioned mice did observe a significantly higher overlap of the reporter and the antibody 1.5 h after fear conditioning (Garner et al., 2012; X. Liu et al., 2012; Ramirez et al., 2013). The activity cocktail used to depolarise the cells is an artificial way to mimic activity in vivo, maybe not involving the same molecules. Also, the amount and timing of c-Fos expression can vary depending on the brain regions (Cowansage et al., 2014; Ramirez et al., 2013; D. S. Roy et al., 2022; Q. Zhang et al., 2018), which is not captured in the cell culture.

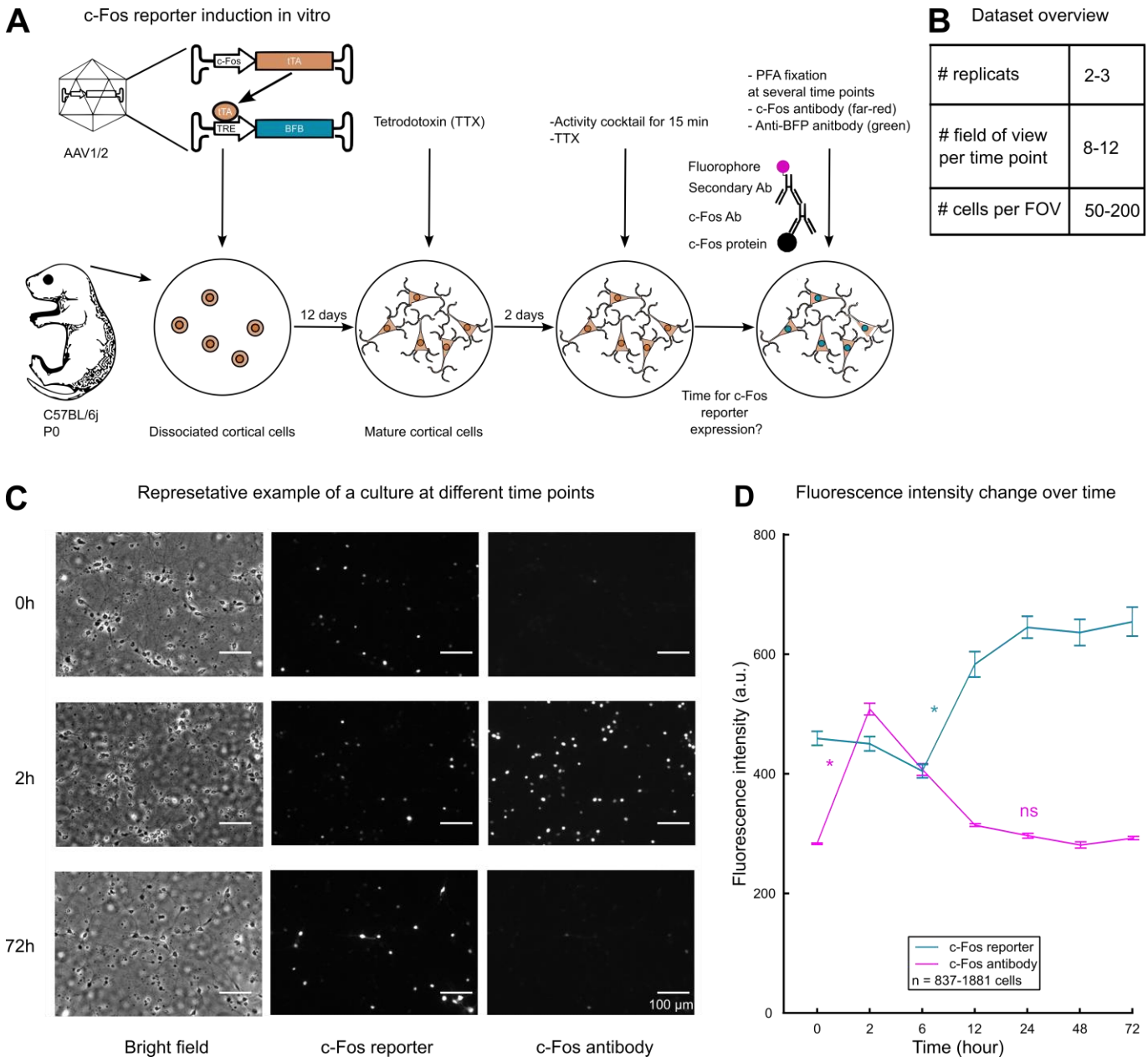

Figure 12. c-Fos reporter synthesis time in vitro: several hours delayed compared to the endogenous c-Fos expression.

(**A**) Experimental design to estimate c-Fos reporter expression time. Primary cortical neurons culture were obtained from new-born mice (C57BL/6J), and transduced with the c-Fos reporter system described in Fig.6A (3 and 4). Spontaneous activity is blocked in mature cells with tetradotoxin (TTX) for two days. Cells are then activated with an activity cocktail (bicuculline, noradrenaline, carbachol, dopamine and serotonin) for 15 minutes, and activity is immediately blocked again with TTX. Finally, cultures are fixed with PFA and stained with c-Fos antibody (Cell signalling Technology, Cat. No. 2250), to report c-Fos endogenous expression, at seven different time points. (**B**) The dataset consists in 3 replicats (mixture of primary cortical cells from several pups), each imaged in 8-12 FOVs, containing 50-200 cells. (**C**) 3 examples of cultures fixed at 0, 2 and 72 h, respectively. Images of each culture were obtained from the bright field, the far-red (c-Fos antibody) and the green (c-Fos reporter) channels of an epifluorescence microscope. (**D**) Graph showing the fluorescence intensity for the c-Fos reporter and the c-Fos antibody in cultures fixed at different time points. Wilcoxon rank sum tests showing beginning and end of significant difference with the first time point. * p=1.0744e-16 (c-Fos reporter), * p=5.0784e-178, ns p=0.0376 (c-Fos antibody).

4.1.2 Material and methods

Jonas Schroer[2], Anne Sinning[2], Simon Rumpel[1] and I[1] collaborated to design the experiment with the primary cortical neurons. Jonas[2] did the experiments and Anne[2] helped for the analysis and the correction of the material and method section.

4.1.2.1 Cell culture

Primary cortical neurons were dissociated from new-born mice (C57BL6J) cortices at postnatal day 0, as described previously (Manuel Peter et al., 2021). Briefly, immediately after brain extraction and dissection, cortical tissue was immerged in ice-cold Ca^{2+}-and Mg^{2+}-free HBSS (Gibco, Invitrogen, Carlsbad, CA, USA) supplemented with penicillin and streptomycin (50 units/ml), sodium pyruvate (11 mg/ml), glucose (0.1%), and HEPES (10 mM). After 20 minutes of trypsin and DNAse digestion at RT, and consecutive washing steps to block the trypsin (HBSS, Minimal Essential Medium (MEM, Gibco), supplemented with 10% horse serum and 0.6% glucose), cortical cells were mechanically dissociated with fire-polished glass pipettes of decreasing diameter. To plate ~1000 cells per mm^2 on coverslips, cells were counted via a trypan blue staining. To enhance the cell adhesion, a poly-ornithine treatment was applied before the platting of cells. After 45 minutes, the medium was replaced by a Neurobasal medium (Gibco) supplemented with 2% B27 (Gibco) and 1 mM L-glutamine. Neurons were kept in an incubator (37°C, 95% air and 5% CO_2) for 12 days. At day in vitro (DIV) 2, 5 µM of AraC was added to the medium to inhibit glial cell proliferation. At DIV 7, half of the medium was replaced with BrainPhys™ Neuronal Medium (supplemented with SM1 supplement; Stem cell technologies, Vancouver, Canada).

4.1.2.2 Viral transduction in cell culture

Cortical neurons were transduced at DIV 1 with two recombinant adeno-associated viruses (rAAV1/2, ~1–4 × 10^4 viral genomes per cell). The first one carrying the c-Fos-tTA plasmid, the second TRE-BFP plasmid, both described above. Viral production was done as described in a previous publication (Warm, Bassetti, Schroer, Luhmann, & Sinning, 2022). In brief, HEK293 cells were transfected with a helper plasmid, a plasmid carrying the rep and capsid sequences, and one of the plasmid mentioned above. After 48 h of incubation, rAAV was harvested, extracted and purified via Heparin columns (HiTrap®Heparin columns, Sigma-Aldrich). The virus titer was determined with a quantitative real time PCR.

4.1.2.3 Pharmacological treatment in cell culture

To inhibit spontaneous spiking activity, Tetrodotoxin (TTX, 1 µM) was added to the primary cortical neurons culture medium (see above) at DIV 12. 2 days after, medium was replaced by medium with a cocktail containing 50 µM of (-)-Bicuculline methiodide, 100 µM of DL-Norepinephrin hydrochloride, 50 µM of Carbamoylcholine chloride, 100 µM of Dopamine hydrochloride, 40 µM of Ascorbic Acid and 100 µM of Serotonin hydrochloride (all from Sigma-Aldrich, MO, USA) to increase neuronal activity (Manuel Peter et al., 2021). After 15 minutes of incubation, TTX was added to the medium in order to block the activation until the end of the experiment.

4.1.2.4 Immunocytochemistry

At six different time points (2, 6, 12, 24, 48 and 72 h) after the addition of the activity cocktail to the primary cortical neurons culture medium (see above), neurons were fixed in 2% paraformaldehyde (PFA) in phosphate-buffered saline (PBS) for 5 minutes. An additional 15 minutes of incubation in 4% PFA was carried out before washing with PBS. To block unspecific bindings of the antibodies, the cultures were treated with 7% normal donkey serum and 0.3% Triton diluted in PBS for 2 hours at RT. The primary rabbit monoclonal c-Fos antibody (Cell signalling Technology, Cat. no. 2250) was diluted 1:800 in PBS with 2% bovine serum albumin, 0.05% azide and 0.1% Triton, and the staining was applied on the cells overnight. After three washing steps with PBS, the secondary goat anti-rabbit Alexa Fluor647 IgG antibody (1:500, Invitrogen Cat. no. A32733) diluted in PBS with 2% bovine serum and 0.05% azide, was applied for 2 hours at RT.

In parallel to the secondary antibody staining, BFP signal was stained with the anti-TagFP-At488 (1:1000, N0501 Synaptic systems) diluted in 2% bovine serum albumin (001-000-161, Jackson ImmunoResearch)/0.05% sodium azide (S002, Sigma-Aldrich)/0.1% triton in PBS (2 h, RT). Finally, a last washing step was performed with PBS before mounting the coverslips with Fluoromount for imaging.

Images were acquired on an Olympus IX81 epifluorescence microscope (Olympus Life Sciences, Germany), and the subsequent analyses were performed with ImageJ, Microsoft Excel and MATLAB (statistics). In brief, regions of interest (neuronal somas) were manually selected based on bright field images, and mean grey values were subsequently measured based on the correspondent images with green and far-red fluorescent proteins (i.e. overexpressed BFP and intrinsic c-Fos signal).

4.1.2.5 Statistics

Figure 12D:

To compare each time point with the first one, for both c-Fos signals, a Wilcoxon rank sum test was applied. Each time point came from a different population, therefore independent groups.

4.2 Decaying time (in vivo)

mTagBFP is a very stable protein, with a half-life in PBS of 54±4 h (Subach, Cranfill, Davidson, & Verkhusha, 2011). In comparison, c-Fos protein is degrading after 6 h only (Barros et al., 2015; Bisler et al., 2002). To evaluate the decaying time for BFP in vivo, we used the mouse model, chronical imaging strategy and analysis pipeline described in Chapter 2 and 3.1 (Figure 6, Figure 7, Figure 8). We took advantage of the TetTag system to block the expression of BFP with doxycycline (of tetracycline class), and observed the decaying time for the remaining fluorescent protein in the neurons (Figure 13).

4.2.1 Results

After stereotactic injection of the four constructs in the ACx of C57BL/6J mice, cranial window implantation, intrinsic imaging and habituation of mice for head fixation in the two-photon setup, we began the imaging sessions. We tracked the same neuronal populations for up to ten days, before and after blocking the expression of the c-Fos reporter system with doxycycline (food supplemented with 46mg/Kg of doxycycline) (Fig.13A).

After two-photon image pre-processing, c-Fos reporter signal was extracted from ~2000 cells, distributed in 23 FOVs (50-150 cells per FOV) and 4 mice (Fig.13B and C).

The results (Fig.13D and E top) indicate a significant decrease up to 10 days after blocking the expression of BFP (Wilcoxon signed-rank test comparing d7-d10: $p=0.0285$). Levels of fluorescence comparable to the background were observed after 10 days on doxycycline-supplemented food. Surprisingly, the fluorescence in the nuclei, expected to be stable over time, was decreasing significantly between the first and second time point. This indicates a reduction of signal-to-noise ratio, which could be due to the declining quality of the window over time, or photobleaching attributed to repeated exposure of the fluorophore to the two-photon microscope laser. The stability of the nuclear signal for the following time point (Wilcoxon signed-rank test comparing time points d4-d7: $p=0.4470$) suggests that the decrease observed for c-Fos is probably due to the protein degradation rather than an artifact of the window quality, or photobleaching. Similar results were observed when binarizing c-Fos signal (Fig.13E, bottom).

To recapitulate in a concise manner, mTagBFP is very stable in vivo and is degrading completely only after 10 days once expressed in neurons. The delay for the reporter to be expressed and the very long half-life of the protein should be taken into account for the interpretation of the following results, keeping in mind that this c-Fos reporter has a low temporal resolution, poorly reflecting the dynamic of c-Fos endogenous expression.

4.2.2 Material and methods

4.2.2.1 Mice

For this experiment and the analyses, I[1] did the following steps described in sections 2.1.1, 2.2.1 and 3.1, using the viruses produced by Eike Kienle[1] and described in section 2.1.1:

- Injection in auditory cortex of C57BL/6J mice, of AAV2/8 packaging c-Fos-tTA, TRE-BFP, hSyn-H2B-mCherry and hSyn-GCaMP6m plasmids
- Cranial implantation
- Intrinsic imaging
- Habituation for fixation in two-photon microscope
- Two-photon microscopy sessions (described below)
- Image processing of chronical in vivo two-photon z-stacks
- Analyses using rois inclusion criteria and the c-Fos threshold (3.1.1)

Mice for this experiment were previously used for the chronical fear conditioning experiment (see 7.1).

4.2.2.2 Doxycycline supplemented food

Mice received pellets supplemented with 46mg/Kg of doxycycline (Ssniff, Germany) for 10 days.

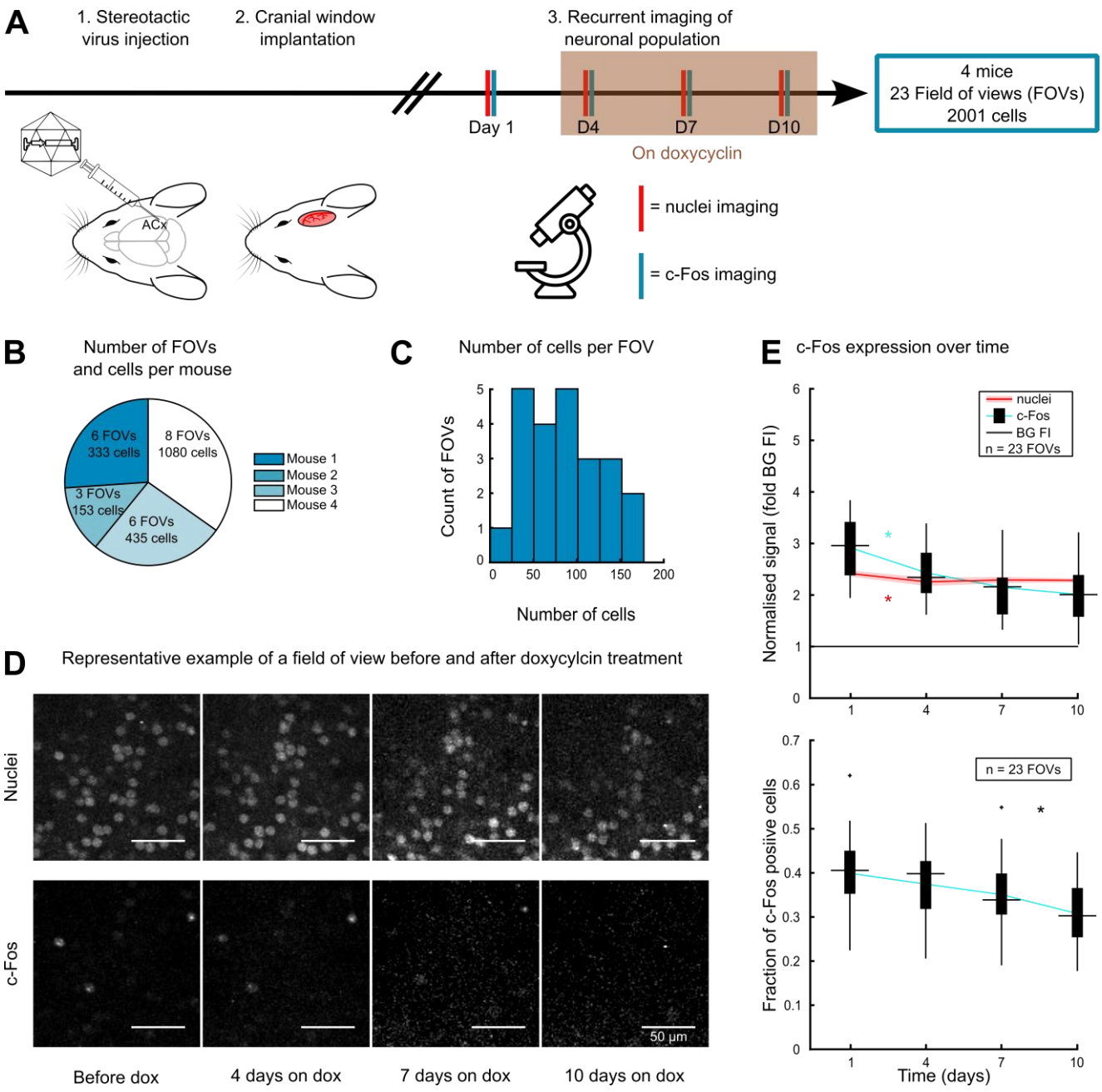

Figure 13. c-Fos reporter decaying time in vivo: several days of delay compared to c-Fos protein half-life.

(**A**) Experimental design to measure the c-Fos reporter decaying time. About four weeks after stereotaxic viral injection, cranial window implantation, and habituation, two-photon imaging sessions were performed every three days for ten days (four time points). After image processing, data from 4 mice, 23 FOVs and 2001 cells could be kept for further analyses. (**B**) Pie chart showing the distribution of the FOVs and cells in the 4 mice. (**C**) Histogram showing the number of cells per FOV (0-175). (**D**) Two-photon images of the same neuronal population at four time points (before treatment with doxycycline, and 4, 7, and 10 days on doxycycline). First row: H2B-mCherry signal, in nuclei. Second row: BFP signal, indirectly expressed under c-Fos promoter. Data were acquired as described in Fig.14D. (**E**) Top: Boxplots (black) and mean ± SEM of normalised c-Fos (blue line), and mean ± SEM of normalised nuclear (red line) signals per FOV of the entire dataset. Bottom: Boxplots (black) and mean ±SEM (blue line) of fraction of c-Fos positive cells per FOV of the entire dataset. Friedman tests from top to bottom: * p=6.7652e-09, * p=0.0210, * p=3.9442e-05.

4.2.2.3 Imaging sessions

After habituation, one session was conducted in order to localise regions to be imaged based on the intrinsic maps and the quality of the window. Mice were anesthetised with 1.2-1.5% isoflurane (see description above) to allow the acquisition of good quality reference images. All the following sessions were performed in an awake state.

To estimate the decaying time of the BFP using doxycycline, z-stacks were acquired every 3 days, one session before mice received the doxycycline supplemented food and three after. Mice did not receive any stimuli during the imaging session.

4.2.2.4 Statistics

Figure 13E:

To estimate if the changes were significantly different over time for the normalised c-Fos and the fraction of c-Fos positive cells, Friedman tests were applied. This test was selected because normalised c-Fos values are not normally distributed and the measures were repeated. The normalised nuclear signal (structural marker, assumed to be stably expressed in the cells) was also measured, to understand if the differences observed for c-Fos were due to changes in expression or to the variations of the cranial window quality, or of the imaging sessions.

Chapter 5. Basal c-Fos dynamics

As mentioned in the introduction, c-Fos expression is not specific to neurons, and can be triggered by many molecules, including growth factors, hormones, cytokines and neurotransmitters (Okuno, 2011; Yap & Greenberg, 2018). Therefore, in the transgenic mouse model FosGFP developed by Barth and colleagues in 2004 (Barth et al., 2004), it is difficult to disentangle the background c-Fos and the signal coming from c-Fos expression triggered by depolarisation. Reijmers and colleagues developed another transgenic mouse (TetTag mouse) in 2007 (L. G. Reijmers et al., 2007), allowing to control c-Fos reporter expression in time, preventing untargeted c-Fos expression before or after a specific event. Despite this additional control, c-Fos expression during this event cannot be attributed solely to neuronal activity. The c-Fos reporter system we choose for our experiment originates from the TetTag mouse. In order to better understand the dynamic of "background" c-Fos expression under basal condition, we designed the experiment described in Figure 14 and Figure 16, comparing two time scales.

For both experiment, we used the mouse model, the chronical imaging strategy and the image analysis pipelines described in chapters 2 and 3.1.

5.1.1 Results

5.1.1.1 Hour time scale

We acquired z-stacks under basal condition, every hour. We could follow more than 13000 cells for up to 6 hours, from 3 mice (Fig.14A and B). In the field of views (367 μm^2), 50-200 cells out of approximately 300 passed the quality criteria based on the nuclear marker (Figure 9) to track the cell from the first to the last time point (Fig.14C). We imaged the dataset mainly in the primary auditory field (A1), the anterior auditory field (AAF) and the dorsomedial field (DM) (Figure S2), in layers 2/3 (z-stacks from 50-300 µm) (Fig.14D).

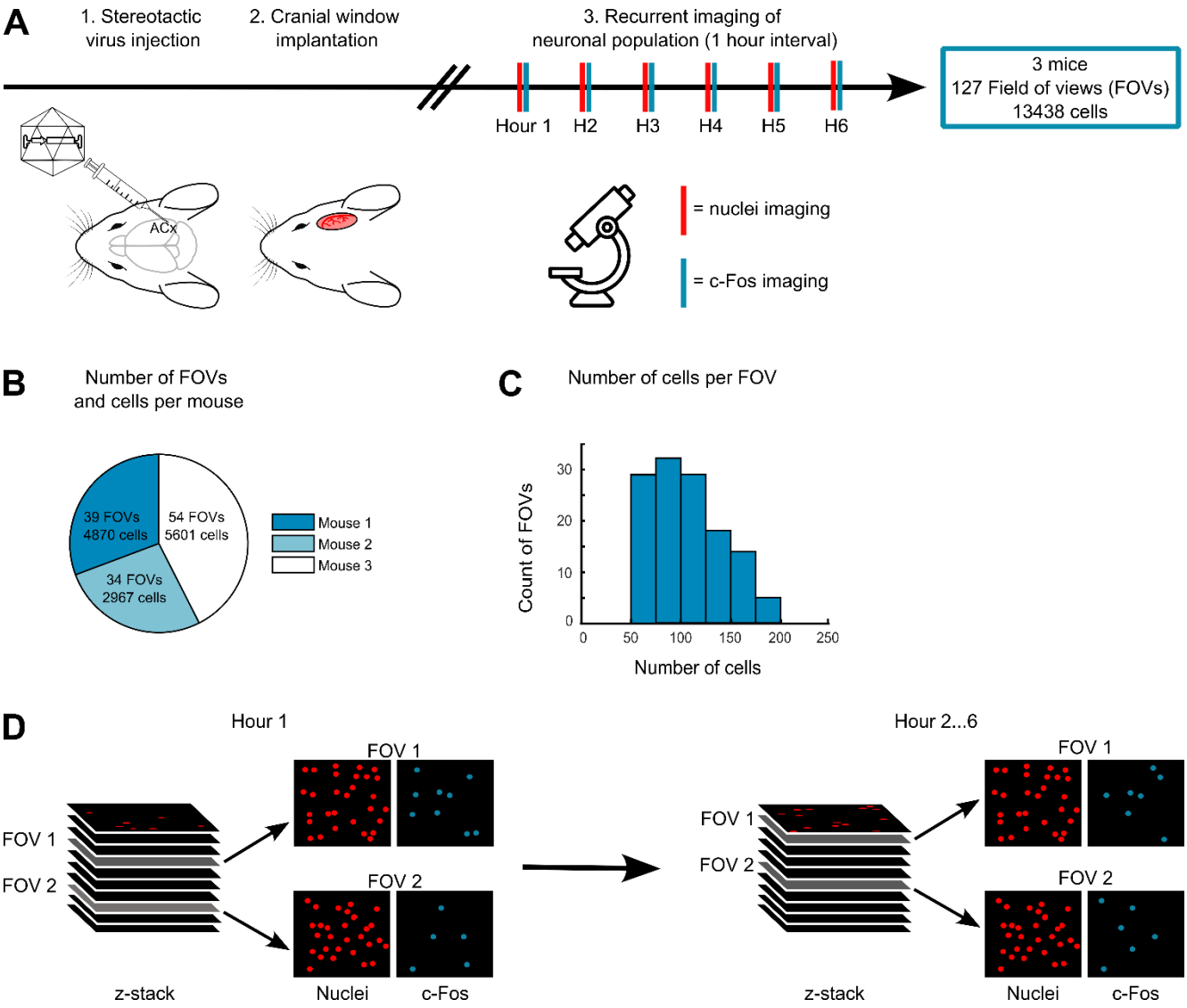

Figure 14. c-Fos basal dynamics, hour scale: experimental design and dataset overview.

(**A**) Experimental design to evaluate c-Fos basal dynamic in an hour scale. About four weeks after stereotactic viral injection, cranial window implantation, and habituation, two-photon imaging sessions were performed every hour for six hours. After image processing, data from 3 mice, 127 field of views and 13438 cells could be kept for further analyses. (**B**) Distribution of acquired data across mice. (**C**) Histogram showing the number of cells per FOV (50-200). FOVs with less than 50 cells were discarded. (**D**) Scheme showing how the data were acquired during the imaging sessions. H2B-mCherry nuclear marker and BFP c-Fos reporter were imaged in parallel (excitation wavelength: 810 nm), using a dichroic mirror (505 nm) to separate both signals in the two-photon microscope. Stacks (367 µm^2, 256x256 px) from 50-300 µm under the brain surface (target: layer 2/3 of the auditory cortex) were acquired every 2 µm. From one session to the other, the vessel pattern on the brain surface served as gross localisation of the cell populations. For fine xy and z alignment of the z-stacks, a neuronal population (nuclear marker) in layer 1 was used as reference.

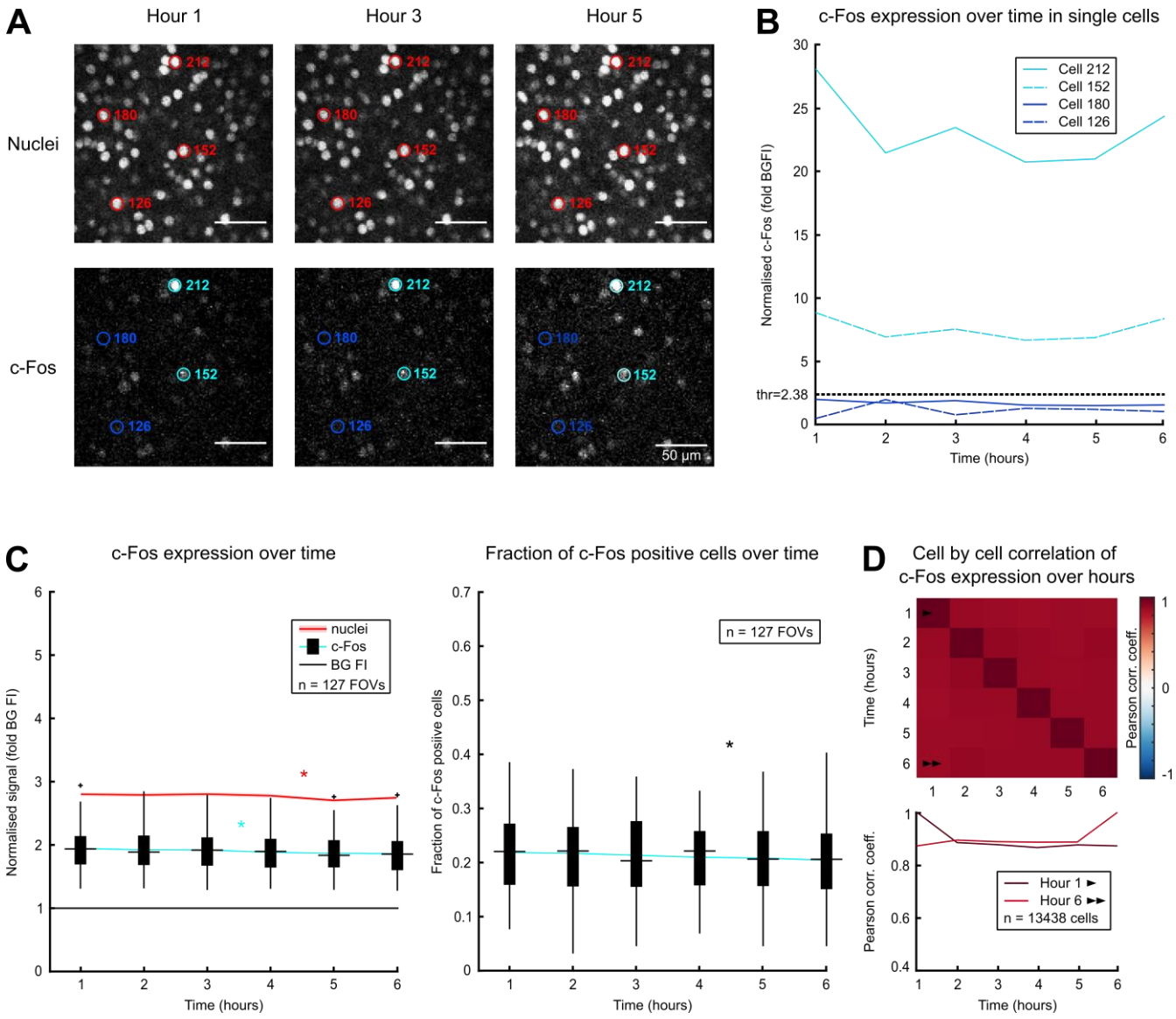

Figure 15. c-Fos basal dynamics, hour scale: stable c-Fos reporter expression.

(**A**) Images of the same neuronal population at three time points (hour 1, hour 3 and hour 5). First row: The nuclear marker is overlaid with four ROIs (red circles). Second row: The c-Fos reporter is overlaid with the same ROIs, showing two cells detected as c-Fos positive (light blue circles) and two cells as c-Fos negative (dark blue circles). (**B**) Normalised c-Fos signal for the individual ROIs showed in (A). (**C**) Left: Boxplots (black) and mean ± SEM of normalised c-Fos (blue line), and mean ± SEM of normalised nuclei (red line) signals per FOV of the entire dataset. Right: Boxplots (black) and mean ± SEM (blue line) of fraction of c-Fos positive cells per FOV of the entire dataset. Friedman tests from left to right: * p=5.9865e-14, * p=1.2427e-8, * p=1.2109e-5. (**D**) Top: Self-correlation matrix of c-Fos expression over time for every cell of the dataset. Bottom: Pearson correlation values for the first and last line of the self-correlation matrix.

The results show that for single cell examples, c-Fos signal is stable from the first to the last time point (Fig.15A and B), for cells above or under the threshold to classify them as c-Fos positive or c-Fos negative cells. The mean fluorescence intensity (Fig.15C) decreases significantly for c-Fos signal as well as for the nuclear marker (Friedman test to evaluate the overall change over time: p=5.9865e-14 for c-Fos, p=1.2427e-8 for nuclei), suggesting a reduction of signal-to-noise ratio. The parallel change of the nuclear marker and c-Fos reporter indicate a stable expression of the IEG. We obtained very similar results when measuring c-Fos as a binary signal (Friedman test: p=1.2109e-5). As mentioned above (4.2.1), the decline of signal quality could be due to photobleaching of the fluorophore after the repetitive imaging sessions of the same cells on the same day. Comparing the signal in individual cells in a correlation matrix, we observed very high Pearson correlation values, suggesting further a stable signal over time for the c-Fos reporter (Fig.15D).

5.1.1.2 Day time scale

We acquired z-stacks under basal condition, every day. We could follow more than 13000 cells for up to 10 days, from 5 mice (Fig.16A and B). Alike the Hour experiment, in the field of views (367 μm^2), 50-200 cells out of approximately 300 passed the quality criteria based on the nuclear marker to track the cell from the first to the last time point (Fig.16C). Here also, we imaged the dataset mainly in A1, AAF and DM (Figure S2), in layers 2/3 (z-stacks from 50-300 µm) (Fig.16D).

The results show that for single cell examples, c-Fos signal can decrease, increase or be stable (Fig.17A and B). Comparable to the Hour experiment though, the mean fluorescence intensity (Fig.17C) decreases significantly for c-Fos signal as well as for the nuclear marker (Friedman test to evaluate the overall change over time: p= 7.3754e-105 for c-Fos, p=1.8228e-112 for nuclei), indicating a parallel change and therefore a stable signal from the reporter, and a reduction of signal-to-noise ratio. The fraction of c-Fos positive cells decreases significantly as well (Friedman test: p=5.1828e-99). Here also, the decline of signal quality could be due to photobleaching of the fluorophores, and additionally to the quality of the window.

Indeed, the window is exposed to pressures due to the movements of the mouse being awake during the imaging sessions, leading to increasing distance and formation of scars between the window and the brain surface, worsening the optical access.

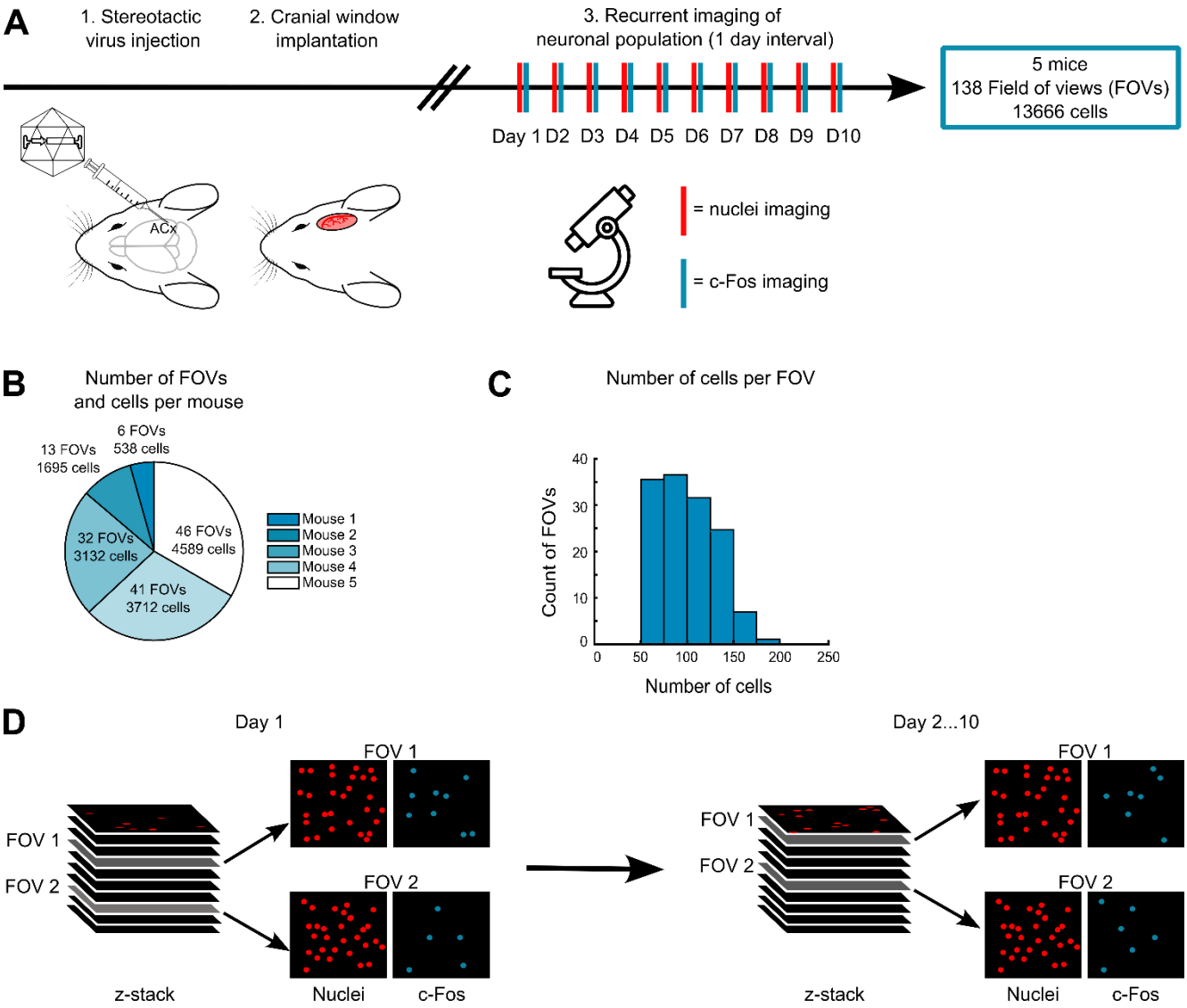

Figure 16. c-Fos basal dynamics, day scale: experimental design and dataset overview.

(**A**) Experimental design to evaluate c-Fos basal dynamic in a day scale. About four weeks after stereotactic viral injection, cranial window implantation, and habituation, two-photon imaging sessions were performed every day for ten days. After image processing, data from 5 mice, 138 FOVs and 13666 cells could be kept for further analyses. (**B**) Distribution of acquired data across mice. (**C**) Histogram showing the number of cells per FOV (50-200). FOVs with less than 50 cells were discarded. (**D**) Scheme showing how the data were acquired during the imaging sessions, as described in Fig.14D.

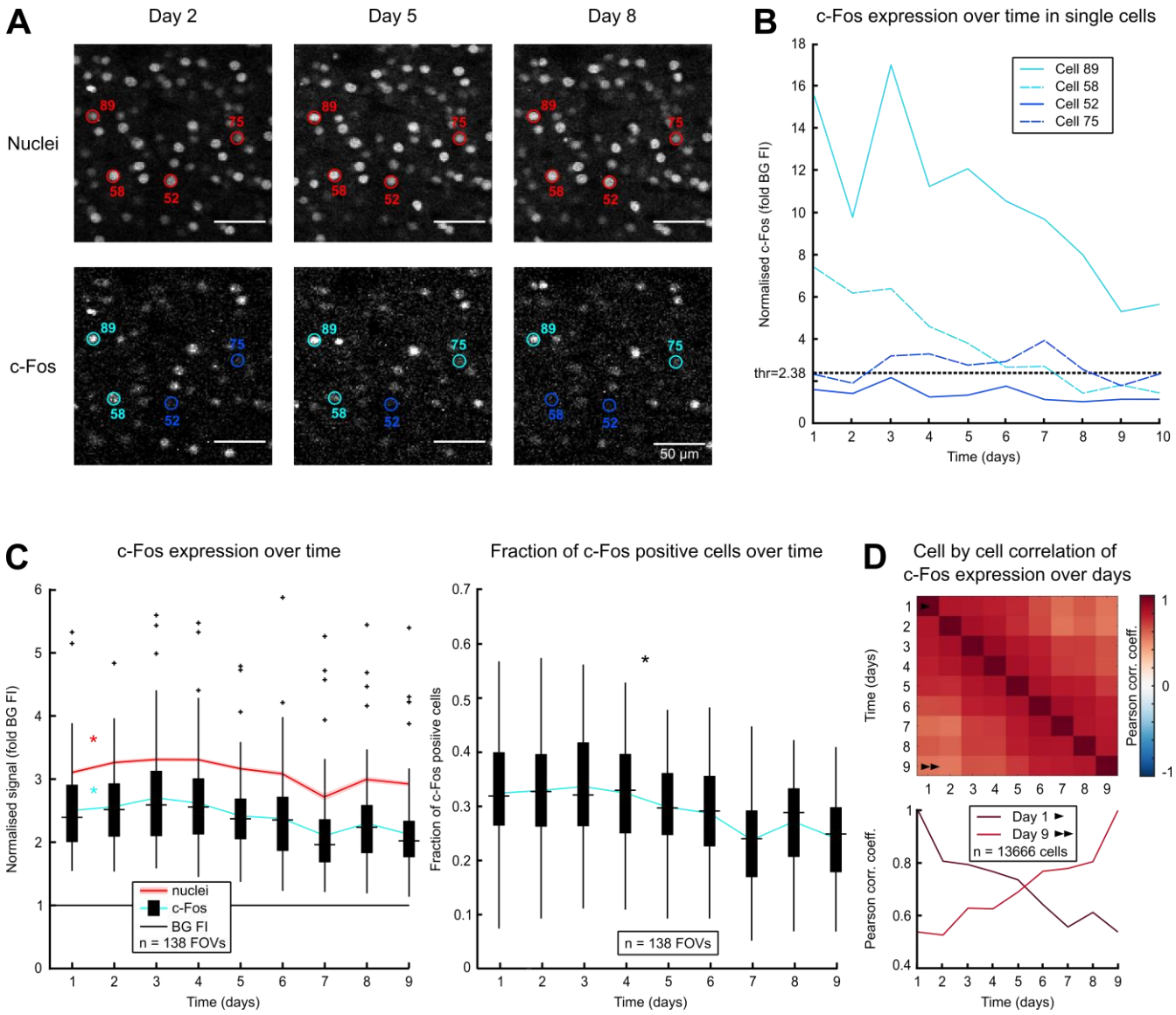

Figure 17. c-Fos basal dynamics, day scale: stable c-Fos reporter expression.

(**A**) Two-photon images of the same neuronal population at three time points (day 2, day 5 and day 8). The nuclear marker (first row) is overlaid with four ROIs (red circles). The c-Fos reporter (second row) is overlaid with the same ROIs, showing examples of cells with a constant signal (positive: 89 and negative: 52) or a signal changing over time (58 and 75), according to the fixed threshold from Figure 10. (**B**) Normalised c-Fos signal for the individual ROIs showed in (A). (**C**) Left: Boxplots (black) and mean ± SEM of normalised c-Fos (blue line), and mean ± SEM of normalised nuclei (red line) signals per FOV of the entire dataset. Right: Boxplots (black) and mean ±SEM (blue line) of fraction of c-Fos positive cells per FOV of the entire dataset. Friedman tests from left to right: * p= 7.3754e-105, * p=1.8228e-112, * p=5.1828e-99 (**D**) Top: Self-correlation matrix of c-Fos expression over time for every cell of the dataset. Bottom: Pearson correlation values for the first and last line of the self-correlation matrix.

Comparing the signal in individual cells in a correlation matrix, we observed lower Pearson correlation values compared to the hour experiment (Fig.17D). This observation suggests a higher variation of signal over time in comparison with changes over hours. However, similar changes were also observed for the nuclear marker signal, which means the variation is probably only due to the variations of the window quality, and not the signal per se (Figure S4).

To conclude, c-Fos reporter signal was very stable under basal conditions, in an every hour as well as in an every day interval time scale. The decrease observed in the signal-to-noise ratio for the c-Fos reporter and the nulcei marker can be signs of photobleaching, and decline in window quality on a longer time scale.

5.1.2 Material and methods

5.1.2.1 Mice

For the hour and day time scale experiments and the analyses, I[1] did the following steps described in sections 2.1.1, 2.2.1 and 3.1, using the viruses produced by Eike Kienle[1] and described in section 2.1.1:

- Injection in auditory cortex of C57BL/6J mice, of AAV2/8 packaging c-Fos-tTA, TRE-BFP, hSyn-H2B-mCherry and hSyn-GCaMP6m plasmids
- Cranial implantation
- Intrinsic imaging
- Habituation for fixation in two-photon microscope
- Two-photon microscopy sessions (described below)
- Image processing of chronical in vivo two-photon z-stacks
- Analyses using rois inclusion criteria and the c-Fos threshold (3.1.1)

The mice in the hour interval experiment were previously used for the day interval experiment.

5.1.2.2 Imaging sessions

As described in chapter 4.2.2., mice were anesthetised for the first session, and awake for all the following time points

5.1.2.3 Hour time scale

To measure the basal dynamic of c-Fos, z-stacks were acquired every hour. Mice did not receive any stimuli during the imaging sessions.

5.1.2.4 Day time scale

To measure the basal dynamic of c-Fos, z-stacks were acquired every day. Mice did not receive any stimuli during the imaging sessions.

5.1.2.5 Cell-by-cell correlation matrix

To display the changes of normalised c-Fos expression over time for individual cells, Pearson's linear correlation coefficients were measured pairwise to compare time points for each cell. The correlation coefficients were then displayed as an image with scaled custom colours.

The correlation coefficients for the first and last line were also plotted under the matrix.

5.1.2.6 Statistics

Fig.15C and 17C

Friedman tests (see 4.2.2.3).

Chapter 6. c-Fos dynamics and calcium transients in the auditory cortex, under sound stimulation

As mentioned in the introduction, despite the wide use of the neuroscientific community of c-Fos as a neuronal activity marker from the moment the gene was linked to depolarisation (Morgan et al., 1987), the function of the genes targeted by the transcription factor formed by c-Fos and c-Jun (AP-1) in the context of depolarisation remains unclear (Gallo et al., 2018; Leslie & Nedivi, 2011; Minatohara et al., 2016; Yap & Greenberg, 2018). In order to investigate more precisely the correlation of c-Fos with neuronal activity, we took advantage of the complex activity patterns observed during representational drift, measured in several brain area (see 1.3), and recently witnessed also in the auditory cortex in our group (Chambers et al., 2022). We used the mouse model, the chronical imaging strategy and the image analysis pipelines described in Chapter 2 and Chapter 3 (Figure 6, Figure 7, Figure 8, and Figure 11). We measured c-Fos reporter expression and the calcium indicator changes of fluorescence in the auditory cortex of mice, under basal condition and during stimulation with pure tones and complex sounds (Figure 18).

6.1.1 Results

The three first time points were imaging sessions under basal condition, without presenting any sound, and the following five time points we presented a set of 34 stimuli (see 6.1.2.1) of mixed pure tones and complex sounds (Fig.18A). We could follow thousands of cells passing the quality criteria (c-Fos: 3.1.1.2, calcium: 3.2.1.2) for all the time points (c-Fos from z-stacks: ~7700; c-Fos from calcium planes: ~1000; spontaneous activity from t-series in calcium planes: ~1000; sound-evoked activity from t-series in calcium planes: ~2600) for up to 15 days, from 4 mice (Fig.18A and B). From those cells, only a subset (561 cells, Fig.18A) was of good quality during the 15 days and for all three signals in the calcium planes (c-Fos, spontaneous and sound-evoked activity). We selected these cells in order to compare the signals in further analyses (Figure 21). In the FOVs (367 μm^2), on average 1/3 of the cells (~100 out of ~300) passed the quality criteria (Fig.18C). Here we imaged the datasets mainly in A1, AAF, DM and also in the secondary auditory field (A2) (Figure S2), in layers 2/3 (z-stacks from 50-300 µm, and calcium planes in ~120 µm depth under the brain surface) (Fig.18D).

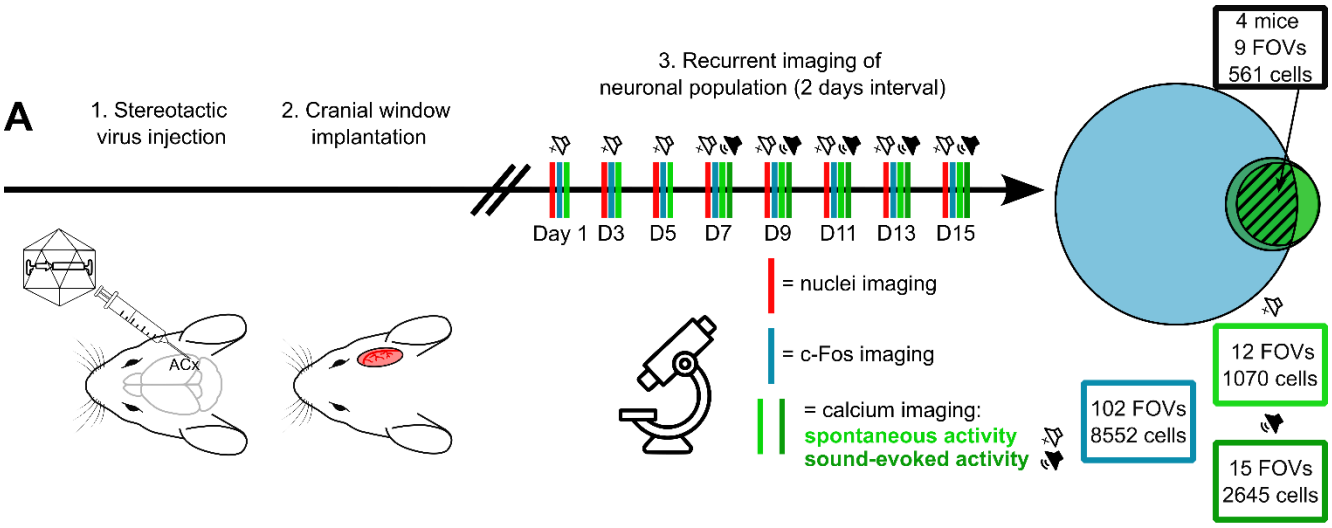
A
1. Stereotactic virus injection
2. Cranial window implantation
3. Recurrent imaging of neuronal population (2 days interval)
Day 1 D3 D5 D7 D9 D11 D13 D15
ACx
= nuclei imaging
= c-Fos imaging
= calcium imaging:
spontaneous activity
sound-evoked activity
4 mice
9 FOVs
561 cells
12 FOVs
1070 cells
15 FOVs
2645 cells
102 FOVs
8552 cells

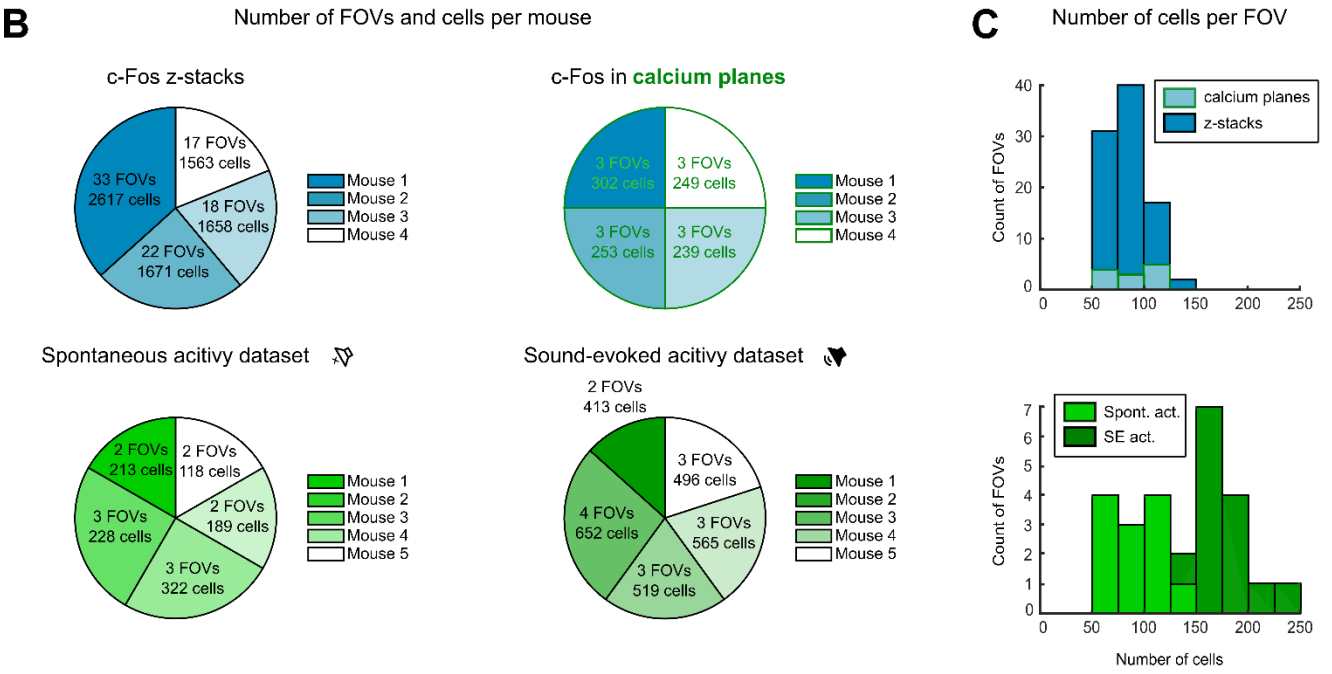
B
Number of FOVs and cells per mouse
c-Fos z-stacks
33 FOVs
2617 cells
17 FOVs
1563 cells
18 FOVs
1658 cells
22 FOVs
1671 cells
Mouse 1
Mouse 2
Mouse 3
Mouse 4
c-Fos in calcium planes
3 FOVs
302 cells
3 FOVs
249 cells
3 FOVs
253 cells
3 FOVs
239 cells
Mouse 1
Mouse 2
Mouse 3
Mouse 4
Spontaneous acitivy dataset
2 FOVs
213 cells
2 FOVs
118 cells
3 FOVs
228 cells
2 FOVs
189 cells
3 FOVs
322 cells
Mouse 1
Mouse 2
Mouse 3
Mouse 4
Mouse 5
Sound-evoked acitivy dataset
2 FOVs
413 cells
3 FOVs
496 cells
4 FOVs
652 cells
3 FOVs
565 cells
3 FOVs
519 cells
Mouse 1
Mouse 2
Mouse 3
Mouse 4
Mouse 5
C
Number of cells per FOV
calcium planes
z-stacks
Count of FOVs
Spont. act.
SE act.
Count of FOVs
Number of cells

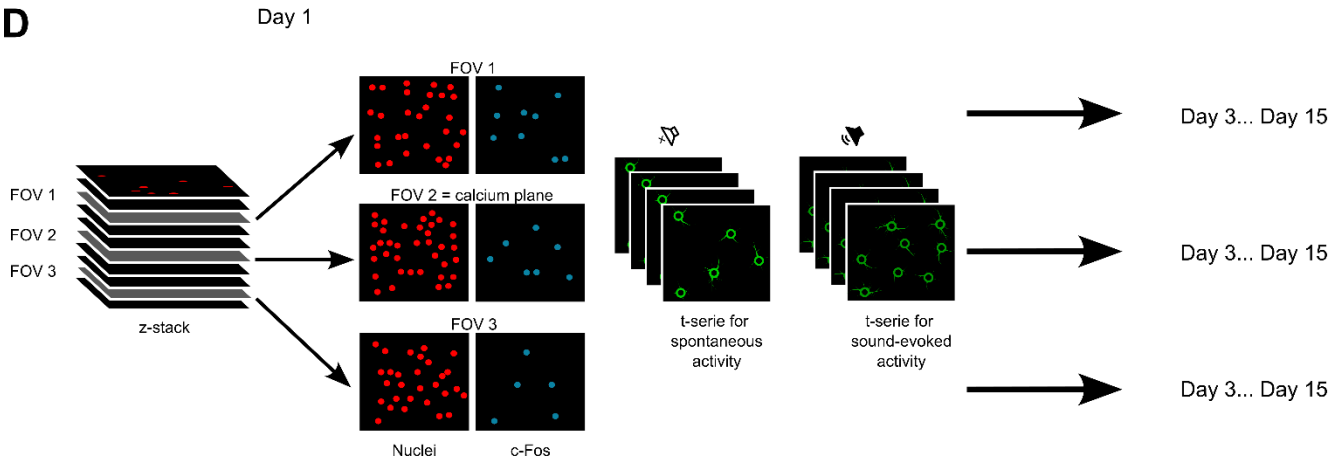
D
Day 1
FOV 1
FOV 2
FOV 3
z-stack
FOV 1
FOV 2 = calcium plane
FOV 3
Nuclei
c-Fos
t-serie for spontaneous activity
t-serie for sound-evoked activity
Day 3... Day 15
Day 3... Day 15
Day 3... Day 15

Figure 18. c-Fos and calcium dynamics throughout sound stimulation: experimental design and dataset overview.

(**A**) Experimental design to observe c-Fos and calcium dynamics throughout time. About four weeks after stereotactic viral injection, cranial window implantation, and habituation, two-photon imaging sessions were performed every other day for fifteen days (eight time points). Three time points were imaged prior to sound presentation, and five time points while presenting a set of 34 simuli (19 pure tones, 50 ms; 2-45 kHz, and 15 complex sounds, 70 ms; four folds speed of animal calls, and pieces of music). After image processing, 4 mice, 9 FOVs and 561 cells could be used to compare c-Fos signal, spontaneous and sound-evoked activity in the same cells (more FOVs and cells for the individual signals). (**B**) Distribution of acquired data across mice. Top: for c-Fos signal. Top left: From z-stacks. Top right: From calcium planes. Bottom: for calcium signal. Bottom left: From t-series recorded without sound presentation (spontaneous activity). Bottom right: From t-series recorded during sound presentation (sound-evoked activity). (**C**) Top: Histogram showing the number of cells per FOV for c-Fos signal, in both the z-stacks and calcium planes datasets. Bottom: Histogram for the calcium signal, in both the spontaneous and sound-evoked datasets. (**D**) Scheme showing how the data were acquired during the imaging sessions. For c-Fos z-stacks, acquisition was done as described in Fig.14D. For the calcium planes, extra high quality images were acquired for c-Fos (367 μm^2, 1024x1024 px). On the same planes, calcium transient was recorded as t-series (367 μm^2, 256x128 px, 5 Hz), during silence (spontaneous recording) and sound presentation (sound-evoked recording). H2B-mCherry and GCaMP6 calcium indicator were also imaged in parallel (excitation wavelength: 920 nm), with another dichroic mirror (570 nm).

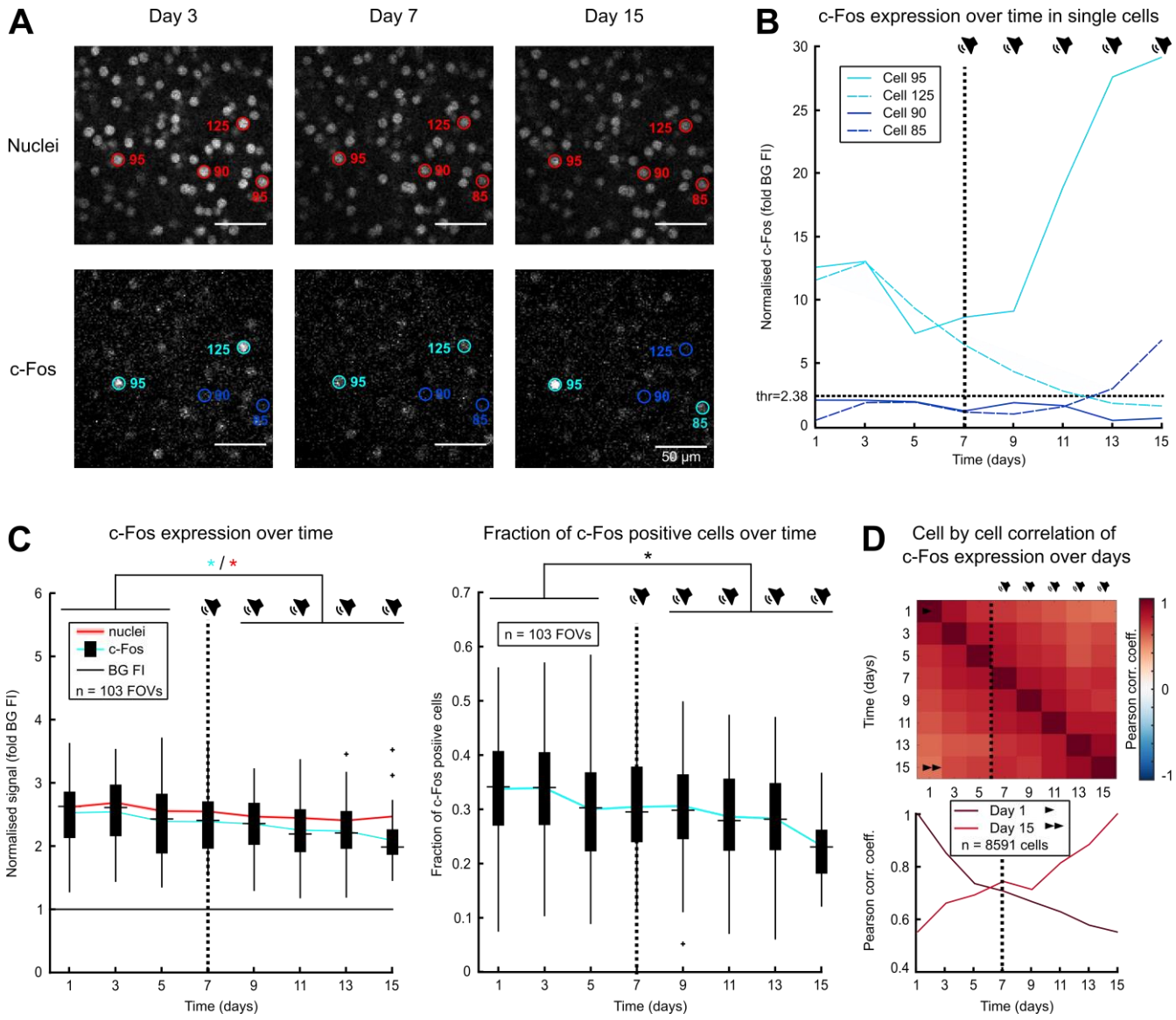

Figure 19. c-Fos dynamics throughout sound stimulation: slight decrease of c-Fos reporter signal over time.

(**A**) Two-photon images of the same neuronal population at three time points (day 3, day 7 and day 15). The nuclear marker (first row) is overlaid with four ROIs (red circles). The c-Fos reporter (second row) is overlaid with the same ROIs, showing examples of cells with a constant signal (positive: 95 and negative: 90) or a signal changing over time (125 and 85), according to the fixed threshold from Figure 10. (**B**) Normalised c-Fos signal for the individual ROIs showed in (A). (**C**) Left: Boxplots (black) and mean ± SEM of normalised c-Fos (blue line), and mean ± SEM of normalised nuclear (red line) signal per FOV of the entire dataset. Right: Boxplots (black) and mean ±SEM (blue line) of fraction of c-Fos positive cells per FOV of the entire dataset. Wilcoxon signed rank tests to compare the 3 baseline time points with the 5 time points when sound was presented; from left to right: * p=1.6922e-14 * p=3.4897e-13 * p=1.7995e-11 (**D**) Top: Self-correlation matrix of c-Fos expression over time for every cell of the dataset. Bottom: Pearson correlation values for the first and last line of the self-correlation matrix.

Measuring c-Fos reporter expression over time, the results show that for single cell examples, c-Fos signal can decrease, increase or be stable (Fig.19A and B). Surprisingly, the mean fluorescence intensity (Fig.19C, left) decreases significantly for c-Fos signal as well as for the nuclear marker (Wilcoxon rank sum test to compare the signals before and after sound presentation: p=1.6922e-14 for c-Fos, p=3.4897e-13 for nuclei). The fraction of c-Fos (Fig.19C, right) positive cells drops significantly as well (Wilcoxon rank sum test: p=1.7995e-11). The decrease in nuclear signal is again suggesting a decline of signal quality due to either photobleaching of the fluorophores, or of the quality of the window. Importantly, the reduction of nuclear marker fluorescence intensity is less abrupt compared to the c-Fos signal, implying either a real effect on c-Fos expression or a difference in photobleaching sensitivity for BFP and mCherry. Given that mTagBFP is known to have a lower photostability compared to mCherry (Shaner et al., 2004; Subach et al., 2011), and that recording was performed on a longer time scale and repeated more time than in the Day experiment, it is reasonable to attribute the drop of c-Fos signal to photobleaching. Besides, comparing the signal in individual cells over time in a correlation matrix, we observed similar Pearson correlation coefficients (1-0.5) compared to the Day experiment (Fig.19D). This observation also suggests no systematic change of c-Fos reporter expression in the auditory cortex of mice under sound exposure, in comparison to variations under basal conditions.

This is in contradiction with a recent publication, finding that c-Fos expression was higher in the auditory cortex of mice learning a sound discrimination task (Hoz et al., 2018). When blocking the protein, the performance of the mice decreased, suggesting a role of c-Fos in sound processing. Unlike this paper, mice in our experiments only listened to sounds passively, and this may not be enough to trigger c-Fos expression in the auditory cortex.

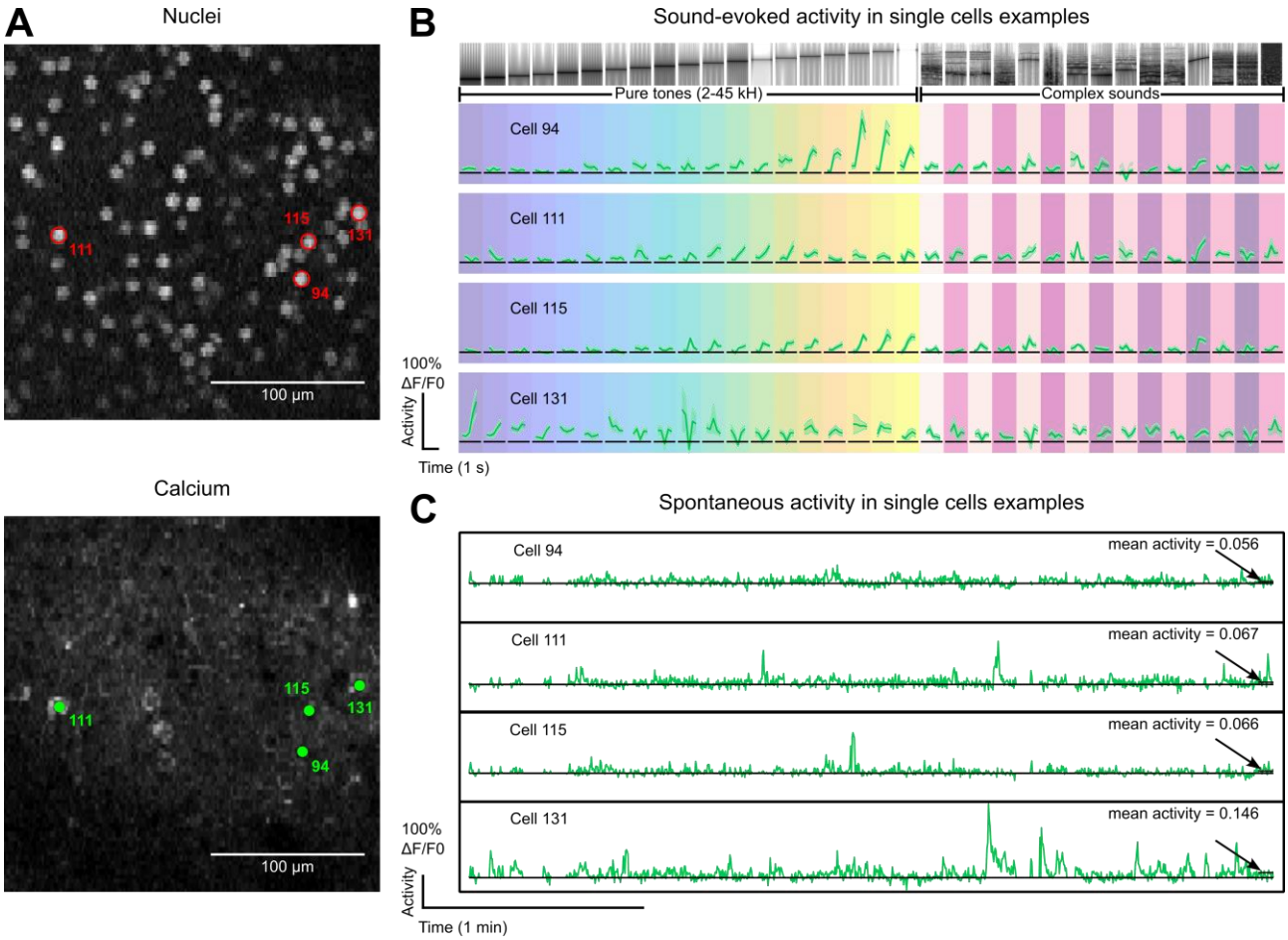
A
Nuclei
111
115
131
94
100 µm
Calcium
111
115
131
94
100 µm
B
Sound-evoked activity in single cells examples
Pure tones (2-45 kH)
Complex sounds
Cell 94
Cell 111
Cell 115
Cell 131
100%
ΔF/F0
Activity
Time (1 s)
C
Spontaneous activity in single cells examples
Cell 94
mean activity = 0.056
Cell 111
mean activity = 0.067
Cell 115
mean activity = 0.066
Cell 131
mean activity = 0.146
100%
ΔF/F0
Activity
Time (1 min)
D
Sound responsiveness over time
n = 15 FOVs
*
Fraction of sound repsonsive cells
Time (days)
E
Spontaneous activity over time
n = 15 FOVs
ns
Mean spontaneous activity (ΔF/F0)
Time (days)
F
Tuning curves for pure tone and complex sounds at day 7
n = 178 cells
Best response (norm. ΔF/F0)
Frequency shift (octaves)
n = 149 cells
Complex sounds (sorted by day 7 resp.)
Best response amplitude of all stimuli over days
ns
n = 14 FOVs
Mean best response (ΔF/F0)
Time (days)

Figure 20. Calcium dynamics throughout sound stimulation: decrease of sound responsiveness, but stable best response amplitude and stable spontaneous activity over time.

(**A**) Two-photon images of the same neuronal population. Top: nuclear signal with four exemplary ROIs (red circles). Bottom: calcium signal in one frame, with the same four exemplary cells (green dots). (**B**) Sound-evoked activity for the exemplary ROIs shown in (A), during presentation of each of the 34 stimuli (pure tones and complex sounds). Activity is shown as mean ΔF/F0 ± SEM over 20 trials. (**C**) Spontaneous activity for the exemplary ROIs shown in (A). Activity is shown for the last time point (day 15), as ΔF/F0. The black arrow and line indicate the mean spontaneous activity of the cell at day 15. (**D**) Mean ± SEM fraction of sound-responsive cells per FOV, for the five time points when sounds were played. Kruskal-Wallis test: ***** p=0.0380. A sound-responsive cell was defined as follows: p value<0.5 for at least one sound, after a rank-sum test comparing sound-evoked activity (20 trials of 400 ms of ΔF/F0 after the sound presentation) with spontaneous activity (20 times of random 400 ms of ΔF/F0 during silence), and after a Benjamini-Hochberg correction for multiple comparison (number of cells in a FOV). (**E**) Mean ± SEM spontaneous activity per FOV (all cells pooled, each with one value as mean activity described in (C)), for the eight time points. Friedman test: **ns** p=0.1763 (**F**) Left and middle: Tuning curves of sound-responsive cells (left: pure tones, middle: complex sounds) measured as mean ± SEM activity maximum-normalized to the best response amplitude on the given day (day 7 = first day of sound presentation). Right: Best response amplitude measured in each cell as higher mean ± SEM activity of the 20 trials, comparing the 34 sounds. Shown is the mean per FOV (all cells pooled). Kruskal-Wallis test: **ns** p= 0.2551.

Measuring GCaMP6m fluorescence intensity and calculating activity in individual cells (Fig.20A), we observed unique calcium transients during sound-evoked (Fig.20B) and spontaneous (Fig.20C) recordings for each cell. Some cells are very active during a specific sound presentation, others are activated by a broader set of sounds, and other cells are not responsive to any stimulation at a given time point. Similarly, some cells are spontaneously very active and others are less active. In the whole dataset, only a fraction of cells were sound-responsive in the auditory cortex (Fig.20D), with a significant portion of cells not responding to any sound stimulation at a given time point, as previously observed (Chambers et al., 2022). The mean fraction of sound-responsive cells in field of views significantly decreased over time (Kruskal-Wallis test to compare multiple groups of independent cells, sound-responsive on a specific day: $p=0.0380$), which was consistent with a previous report in our lab (Chambers et al., 2022), and can be attributed to habituation (Thompson, 2009). On the other hand, the mean best response amplitude (Fig.20F, right) was stable over time (Kruskal-Wallis-test: $p= 0.2551$), indicating a stable coding performance for the sound-responsive cells.

Likewise, mean spontaneous activity in FOVs (Fig.20E) did not change significantly over time (Friedman test: $p=0.1763$), although the trend to increase after sound presentation is to be highlighted. Finally, the tuning curves of sound-responsive cells during the first day of sound presentation resembled what was previously observed in our lab for the same set of 34 stimuli with pure tones and complex sounds (Fig. 20F, left and middle) (Chambers et al., 2022, supplementary data).

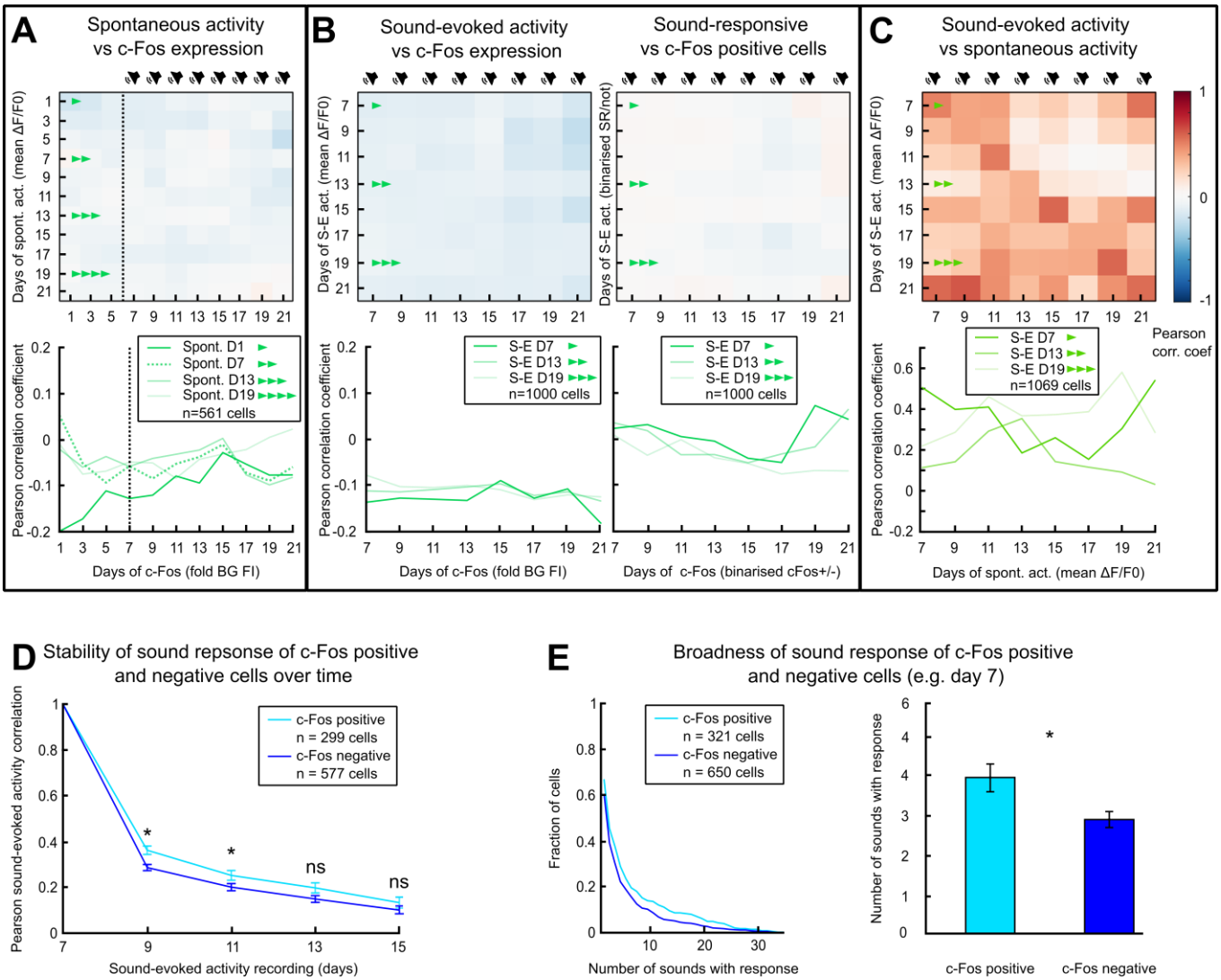

Figure 21. c-Fos reporter and calcium indicator signal correlation throughout sound stimulation: poor correlation, and broader/less-specific responsiveness to sounds for c-Fos positive cells.

(**A**) Top: cell-by-cell correlation matrix (n=561 cells) of spontaneous activity (mean ΔF/F0, as described in Fig.20C, as one value per cell for every time point (TP)) and c-Fos expression (fold background fluorescence intensity, as described in Fig.8A5, as one value per cell for every time point). Bottom: Pearson correlation values from the cell-by-cell correlation matrix, for one TP before, the first TP of sound presentation, and two TPs after. (**B**) Top left: cell-by-cell correlation matrix (n=1000 cells) of sound-evoked activity (mean ΔF/F0 during sounds presentation, as one value per cell for every time point) and c-Fos expression. Bottom left: Pearson correlation values from the cell-by-cell correlation matrix, for the first TP of sound presentation, and two TPs after. Top right: cell-by-cell correlation matrix (n=1000cells) of binarized sound-evoked (sound-responsive cell described in Fig.20) activity and binarized c-Fos expression (c-Fos positive cell described in Figure 10). Bottom right: as bottom left, but for the top right matrix. (**C**) Top: cell-by-cell correlation matrix (n=1069 cells) of sound-evoked activity and spontaneous activity described in (A) and (B). Bottom: as bottom left in (B), for matrix in (C). (**D**) Mean ± SEM of Pearson signal correlation of sound responses to the initial day of sound presentation (day-to-day correlation of response vectors over sound stimuli per cell). Cells were grouped according to their c-Fos expression into c-Fos positive and c-Fos negative cells. Wilcoxon rank sum to compare groups for each time point, from left to right: ***** p= 5.7772e-04, ***** p = 0.0443, **ns** p= 0.0847, **ns** p= 0.3115 (**E**) Left: Fraction of sound-responsive cells on the first day of sound presentation, for an increasing number of sounds. The dataset was also grouped for c-Fos positive and negative cells. Right: Quantitative comparison of the average number of sound responses for the c-Fos positive group vs. c-Fos negative group of cells. Wilcoxon rank sum test: ***** p= 0.0127.

After observing the trends of c-Fos reporter expression and the calcium indicator signal individually, we next wanted to compare the signals for both neuronal activity markers in the same cells. We first set side by side the spontaneous activity with the c-Fos reporter expression in a correlation matrix (Fig.21A). Considering that c-Fos reporter signal dropped, regardless of the cause, and spontaneous activity had a tendency to increase after sound presentation, it is with no wonder that the correlation between the signals is low or even negative (Pearson correlation coefficients: -0.2 to 0.05). When comparing sound-evoked activity and c-Fos signal (Fig.21B), taking into account the drop of c-Fos reporter signal and the decrease of fraction of sound-responsive cells, we could expect a higher correlation of the signals. However, the drop of sound-evoked activity is linked to habituation to sound presentation, while c-Fos reporter signal is probably declining because of photobleaching, irrespective of external stimuli. This could partially explain the very low correlation (Pearson corr. coeff.: -0.2 to -0.1) between the two signals in the left part of Fig.21B. Furthermore, sound-evoked activity here is the activity of all cells during sound presentation. As mentioned above, most of the cells are not sound-responsive at a given time point, therefore the measure is dominated by cells not activated by sounds.

To understand if the correlation is higher between cells active during sound presentation (sound-responsive cells) and cells with a high c-Fos reporter expression level (c-Fos positive cells), we binarized both signal and ran the same analysis (Fig.21B, right). Despite the slightly higher Pearson correlation coefficients (-0.05 to 0.1), the values in the correlation matrix were still low, suggesting a decrease in both signals from different cell populations. This results are in line with very recent measures in the mouse visual cortex, failing to observe comparable changes of c-Fos expression level in cells when activated by visual stimuli (Mahringer et al., 2022). To further investigate the unexpected finding that c-Fos is expressed upon depolarisation, but does not seem to be directly linked to stimuli-driven activity, we compared neuronal activity in c-Fos positive and negative cells (Fig.21D and E). Not only c-Fos positive cells have a more stable sound-evoked activity over time (Fig.21D), but very interestingly, they seem to have a less specific response to sounds compared to c-Fos negative cells (Fig.21E).

In our experiments, what we call spontaneous activity is the activity in awake mice not occurring during the response time window after a sound stimulation. This activity could be triggered by offset responses, multisensory processes, motor activity, complex

behaviour and replay events of previous sensory-evoked activity (Bizley & Dai, 2020; Caras et al., 2022; Farley & Noreña, 2013; Filipchuk et al., 2022; Kuchibhotla & Bathellier, 2018; Luczak et al., 2009; Sakata & Harris, 2009). As mentioned above, the idea to utilize c-Fos as a neuronal activity marker derives essentially from an experiment based on seizure (Morgan et al., 1987). Neuronal activity during seizure is different from stimuli-driven activity and from spontaneous activity as well. Therefore, we decided not only to compare c-Fos to sound-evoked activity, but also to spontaneous activity. To characterise how comparable are the two activities, we correlated both in the same cells (Fig.21C). The Pearson correlation coefficients are about six times higher (0.1 to 0.6), compared to those of both signals correlated to c-Fos reporter signal.

To summarise the findings for this experiment, we could not observe any change in c-Fos reporter expression in the auditory cortex of mice after sound presentation. As previously reported (Chambers et al., 2022), sound-response activity decreased over time as a sign of habituation to the stimuli, while spontaneous slightly increased. The direct correlation between c-Fos and spontaneous or sound-evoked activity in the same cells was very low, as recently observed in the visual cortex of mice as well (Mahringer et al., 2022). Appealingly, c-Fos positive cells seem to have a more stable sound-evoked activity, and a broader response to sounds, compared to c-Fos negative cells.

6.1.2 Material and methods

For this experiment and the analyses, I[1] did the following steps described in Chapter 2, Chapter 3 and section 5.1.2, using the viruses produced by Eike Kienle[1] and described in section 2.1.1:

- Injection in auditory cortex of C57BL/6J mice, of AAV2/8 packaging c-Fos-tTA, TRE-BFP, hSyn-H2B-mCherry and hSyn-GCaMP6m plasmids
- Cranial implantation
- Intrinsic imaging
- Habituation for fixation in two-photon microscope
- Two-photon microscopy sessions (described below)
- Image processing of chronical in vivo two-photon z-stacks
- Image processing of chronical in vivo two-photon single scans
- Image processing of chronical in vivo two-photon t-series
- Analyses using rois inclusion criteria and the c-Fos threshold (3.1)
- Analyses using rois inclusion criteria and ΔF/F0 calculation (3.2)

- Cell-by-cell correlation matrix (5.1.2.5)

6.1.2.1 Sound presentation

The custom-made system to deliver sound, and the 34 stimuli set were previously described (Chambers et al., 2022).

In a soundproofed box, together with the two-photon microscope objective and the mouse stage, a ribbon loudspeaker (AudioComm, Austria) was placed ~25 cm from the mice's head. The linear amplifier delivered the sound with a sampling rate of 192 kHz, through a transfer function measured using a probe microphone (Brüel & Kjær, Bremen, Germany; 4939- L-002). A compensation was numerically done by filtering the sound files with the inverse transfer function, in order to obtain a flat frequency response at the mouse ear (between 0.5 and 64 kHz ±4 dB). Control and equalization of sound was performed with a standard computer equipped with Lynx 22 sound card (Lynx Studio Technology, CA, USA), from a custom MATLAB program.

The stimulus set for the experiment described in Figure 18 is composed by 34 sound stimuli:
- 19 pure tone pips, lasting each 50 ms: 2-45 kHz every quarter octave
- 15 complex sounds, lasting each 70 ms: characterised by broad frequency content and temporal modulation, generated from arbitrary samples of music pieces or animal calls, at 4 folds speed.

All stimuli were played at 70 dB sound pressure level, and their on- and offsets were smoothened with a 10 ms long half-period cosine function.

6.1.2.2 Imaging sessions

To measure the dynamic of c-Fos and change of activity during sound presentation (Fig.12), z-stacks, single scans and t-series were acquired every 2nd day. A baseline without any stimuli presentation was recorded for three time points. During those sessions, z-stacks and single scans were acquired to measure c-Fos level and t-series to measure the spontaneous activity. The next sessions, the following sequence of acquisition was performed for every FOV to be imaged in a mouse: 1. z-stack to image c-Fos in layer 2/3 of the auditory cortex, 2. Single scan on the calcium planes (selected depths of the z-stack at ~120 µm from the brain surface) 3. t-serie to record the spontaneous activity in the calcium planes 4. t-series to record the sound-evoked activity in the calcium planes. 34 stimuli of mixed pure tones and complex sounds

(described above) were each presented 20 times, in a pseudo-randomized order. A gap of 1 second was left between each sound presentation.

6.1.2.3 Sound-evoked responsiveness

To classify single cells as sound-responsive or not, all trials from a given stimulus were compared in a rank-sum test against twenty randomly picked patterns of spontaneous activity (from periods without sound presentation). A cell was classified as significantly responsive, if the p value was below 0.05 after a Benjamini-Hochberg correction for multiple comparisons against number of cells for at least one stimulus (Benjamini & Hochberg, 1995).

6.1.2.4 Best response

For a sound-responsive cell, the best response was the highest mean ΔF/F0 for the 20 repetitions of a sound. This value was also used to normalise the response of the 34 sounds (maximum-normalization).

6.1.2.5 Correlation matrices to compare c-Fos and calcium signals

Pearson's linear correlation coefficients were measured pairwise to compare c-Fos and calcium signals in the same cell, over time. The correlation coefficients were then displayed as an image with scaled custom colours.

Normalised c-Fos expression was measured as described in section 3.1.1.1, steps 7-8, resulting in one value per time point per cell.

Spontaneous activity was measured as mean ΔF/F0 over the whole spontaneous activity recording, to obtain one value per time point per cell.

Sound-evoked activity was extracted from the parts of the sound-evoked recording where sounds were presented, and also calculated as mean ΔF/F0 to get one value per time point per cell.

6.1.2.6 Statistics

Figure 19C:

To compare group of dependent measurements before sound presentation with the time points after sound presentation, a Wilcoxon signed rank test was used.

Figure 20E:

For repeated measures in the same cells of the spontaneous activity, a Friedman test was applied to estimate the significance of changes over time.

Figure 20D and F:

For independent multiple measures, a Kruskal-Wallis test was used to estimate change of fraction of sound-responsive cells between time points, and change of best response amplitude between time points.

Figure 21D and E:

Finally, to compare the sound-evoked activity in independent c-Fos positive and negative cells, a Wilcoxon rank sum test was applied.

Chapter 7. c-Fos dynamics and calcium transients in the auditory cortex, under fear conditioning

7.1 Chronic

As already stated in the introduction, genetic tools using c-Fos promoter became very popular after the experiment showing that reactivation of cells highly expressing c-Fos during fear conditioning in the hippocampus, can trigger fear memory through freezing behaviour (X. Liu et al., 2012). Here, we used the mouse model, chronical imaging strategy and the analyses pipelines described in Chapter 2 and Chapter 3. A group of mice was auditory cued fear conditioned, to measure changes of both c-Fos expression and calcium transients chronically before and after conditioning and a memory test session (Figure 22). To control for c-Fos expression due to everything else but fear memory, we did the experiment with another group of mice, without associating sound with fear (Figure 23).

7.1.1 Results

For the fear-conditioned group (Figure 22), we imaged c-Fos reporter signal and calcium transients every other day, as described in section 6.1.1 for Figure 18 (c-Fos: z-stacks and calcium planes; calcium: t-series for spontaneous and sound-evoked activity). The three first time points were imaging sessions under basal condition. On the day of fear conditioning, mice were first exposed to paired shock-sound stimuli (see 7.1.2.1, 7.1.2.2). After three hours, we imaged c-Fos reporter expression, and calcium transients during silence or presentation of the conditioning sound (CS) and the non-conditioning sound (nonCS). For the following two time points, we imaged c-Fos reporter and calcium transients under basal conditions again. Finally, on the day of memory test, we put the mice in behavioural boxes and played CS to record fear memory as freezing behaviour. Three hours later, we repeated an imaging session as described after the fear conditioning. We could follow thousands of cells passing the quality criteria (c-Fos: 3.1.1.2, calcium: 3.2.1.2) for all the time points (c-Fos from z-stacks: ~2500; c-Fos from calcium planes: ~1100; spontaneous activity from t-series in calcium planes: ~3300; sound-evoked activity from t-series in calcium planes: ~4500) for up to 13 days, from 4 mice (Fig.22 A and B).

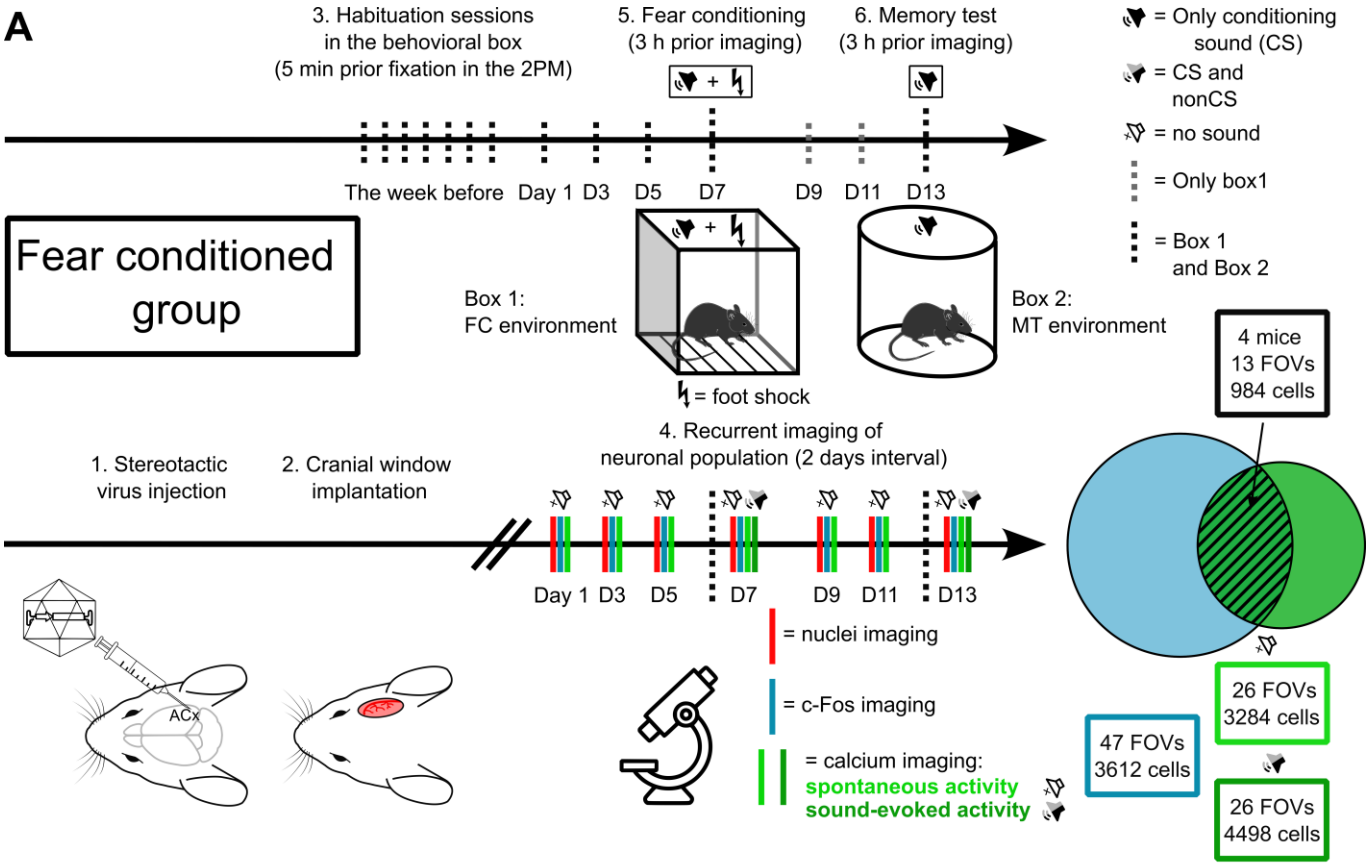
A
3. Habituation sessions in the behovioral box (5 min prior fixation in the 2PM)
5. Fear conditioning (3 h prior imaging)
6. Memory test (3 h prior imaging)
= Only conditioning sound (CS)
= CS and nonCS
= no sound
= Only box1
= Box 1 and Box 2
The week before Day 1 D3 D5 D7 D9 D11 D13
Fear conditioned group
Box 1: FC environment
Box 2: MT environment
= foot shock
1. Stereotactic virus injection
2. Cranial window implantation
4. Recurrent imaging of neuronal population (2 days interval)
Day 1 D3 D5 D7 D9 D11 D13
= nuclei imaging
= c-Fos imaging
= calcium imaging:
spontaneous activity
sound-evoked activity
ACx
4 mice
13 FOVs
984 cells
47 FOVs
3612 cells
26 FOVs
3284 cells
26 FOVs
4498 cells

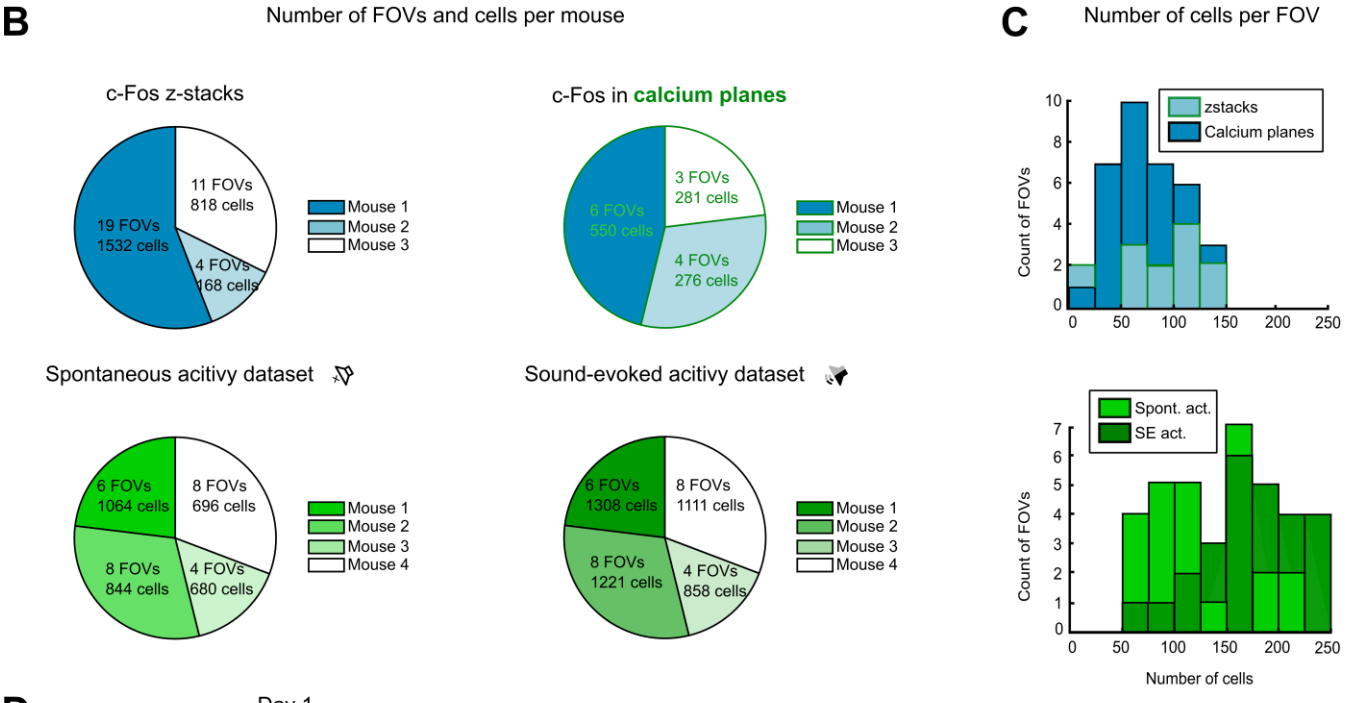
B
Number of FOVs and cells per mouse
c-Fos z-stacks
11 FOVs
818 cells
19 FOVs
1532 cells
4 FOVs
168 cells
Mouse 1
Mouse 2
Mouse 3
c-Fos in calcium planes
3 FOVs
281 cells
6 FOVs
550 cells
4 FOVs
276 cells
Mouse 1
Mouse 2
Mouse 3
Spontaneous acitivy dataset
6 FOVs
1064 cells
8 FOVs
696 cells
8 FOVs
844 cells
4 FOVs
680 cells
Mouse 1
Mouse 2
Mouse 3
Mouse 4
Sound-evoked acitivy dataset
6 FOVs
1308 cells
8 FOVs
1111 cells
8 FOVs
1221 cells
4 FOVs
858 cells
Mouse 1
Mouse 2
Mouse 3
Mouse 4
C
Number of cells per FOV
zstacks
Calcium planes
Count of FOVs
Spont. act.
SE act.
Count of FOVs
Number of cells

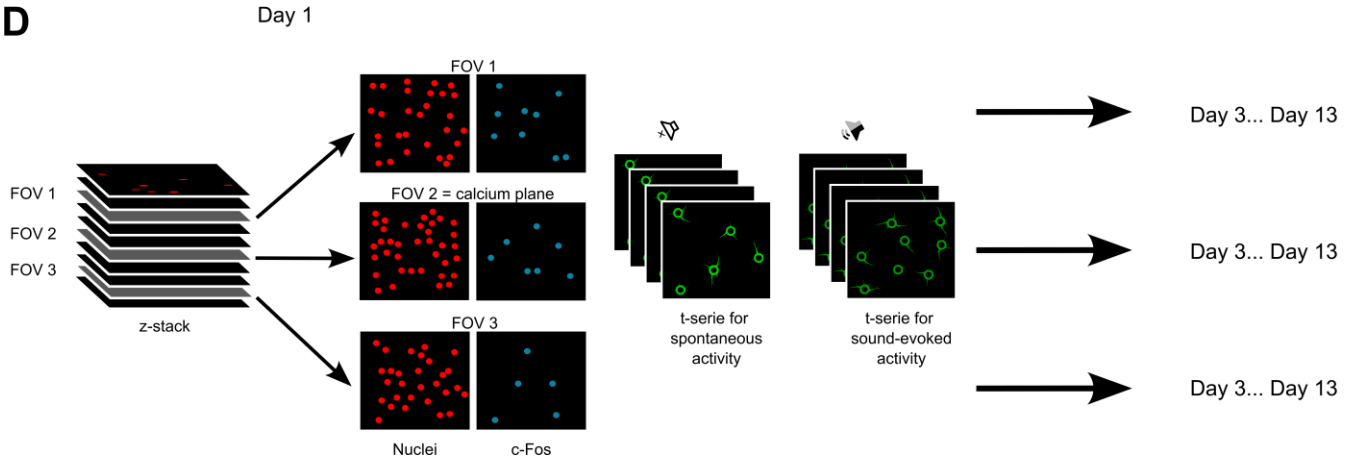
D
Day 1
FOV 1
FOV 2
FOV 3
z-stack
FOV 1
FOV 2 = calcium plane
FOV 3
Nuclei
c-Fos
t-serie for spontaneous activity
t-serie for sound-evoked activity
Day 3... Day 13
Day 3... Day 13
Day 3... Day 13

Figure 22. c-Fos reporter and calcium indicator dynamics throughout fear conditioning: experimental design and dataset overview for the fear-conditioned group.

(**A**) Experimental design to observe c-Fos and calcium dynamics before and after fear conditioning and memory test. About four weeks after stereotactic viral injection, cranial window implantation, and habituation, two-photon imaging sessions were performed every other day for thirteen days (seven time points). Three TPs were imaged prior to fear conditioning, and four TPs after, including the last TP after memory test. After image processing, 4 mice, 13 FOVs and 984 cells could be used to compare c-Fos signal, spontaneous and sound-evoked activity in the same cells (more FOVs and cells for the individual signals). Fear conditioning session: 5 repetitions of paired conditioning sound (CS)-shock. Memory test session: 2 repetitions of 5 consecutive CS presentation. During the imaging session following both the fear conditioning and memory test (3 h interval), we presented CS and nonCS, in order to add a control for sound-evoked activity during another sound, not associated with fear. CS is derived from Beethoven 9^{th} symphonie, mvt 2 (8s). This complex sound was clipped for frequencies (0-4 kHz) and played fourfold faster than the original piece (2 s). The nonCS sound was derived from a birdcall (marbled wood-quail), not clipped for frequencies (0-40 kHz), also played fourfold faster than the original call (2s). (**B**) (**C**) (**D**) See description in Fig.18B-D.

From those cells, only a subset (984 cells, Fig.22A) was of good quality during the 13 days and for all three signals in the calcium planes (c-Fos, spontaneous and sound-evoked activity). We selected these cells in order to compare the signals in further analyses (Fig.26). In the FOVs (367 μm^2), on average 1/3 of the cells (~100 out of ~300) passed the quality criteria (Fig.22C). Here we imaged the datasets mainly in A1, AAF, and DM (Figure S2), in layers 2/3 (z-stacks from 50-300 µm, and calcium planes in ~120 µm depth under the brain surface) (Fig. 22D).

For the control group (Figure 23), we had the same experimental design as for the fear-conditioned group, except for the fear conditioning session. During the behavioural protocol, we put the mice in the box for the same time as the fear-conditioned group, but we did not present any stimulation; no shock nor sound. We could follow thousands of cells passing the quality criteria (c-Fos: 3.1.1.2, calcium: 3.2.1.2) for all the time points (c-Fos from z-stacks: ~1100; c-Fos from calcium planes: ~1000; spontaneous activity from t-series in calcium planes: ~2600; sound-evoked activity from t-series in calcium planes: ~3800) for up to 13 days, from 4 mice (Fig.23A and B). From those cells, only a subset (811 cells, Fig.23A) was of good quality during the 13 days and for all three signals in the calcium planes (c-Fos, spontaneous and sound-evoked activity). We selected these cells in order to compare the signals in further analyses (Fig.26).

In the FOVs (367 μm^2), on average 1/3 of the cells (~100 out of ~300) passed the quality criteria (Fig.23C). Here we imaged the datasets mainly in A1, AAF, DM and A2 (Figure S2), in layers 2/3 (z-stacks from 50-300 µm, and calcium planes in ~120 µm depth under the brain surface) (Fig.23D).

The results show that the fear conditioning protocol did elicit freezing in conditioned mice, and the session for the control did not induce fear memory (Fig.24D). Indeed, during the memory test, movements during baseline and CS presentation were significantly decreased for the fear-conditioned group and not for the control group (Paired t-test: FC gr.: $p=0.0241$, ctl gr.: $p=0.4638$).

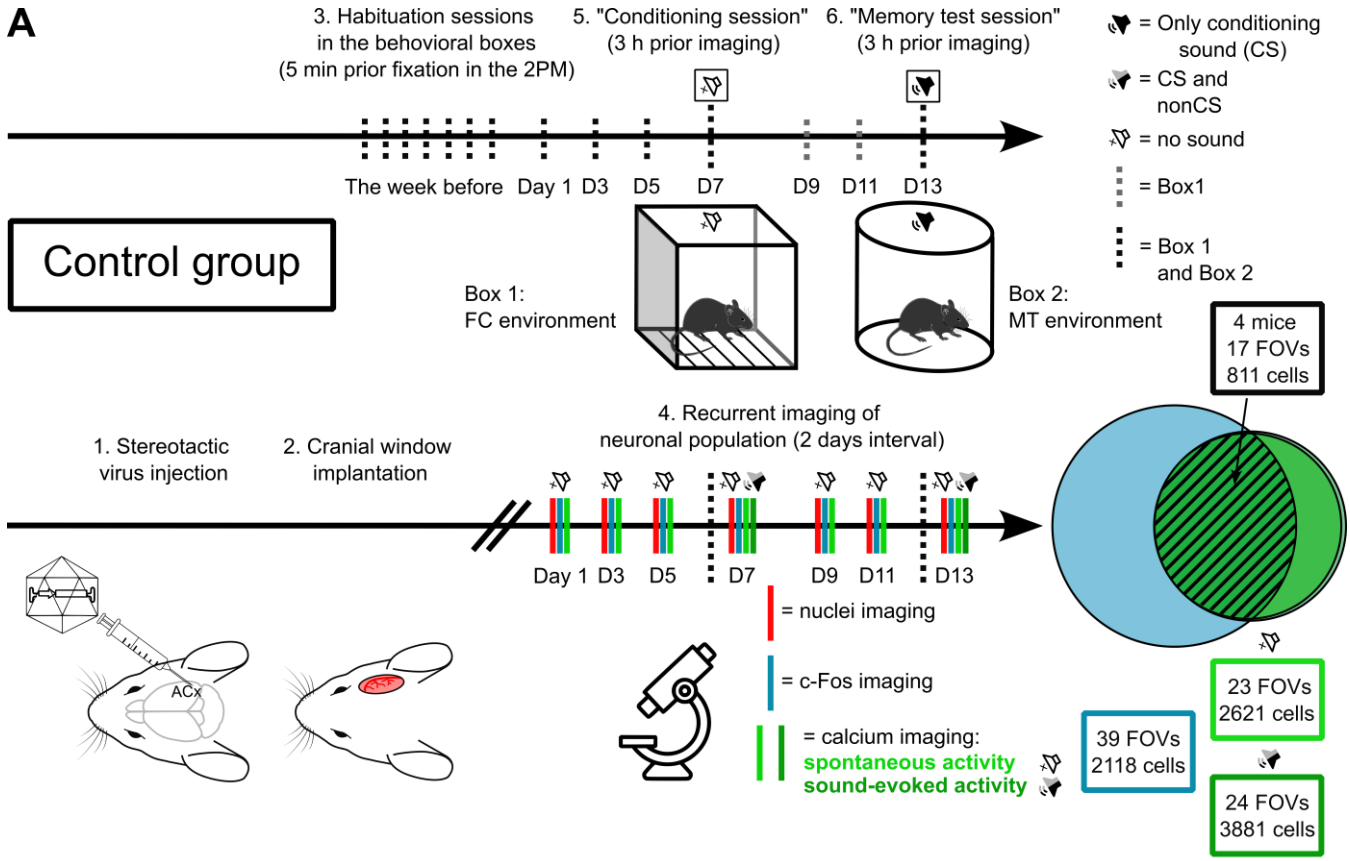
A
3. Habituation sessions in the behovioral boxes (5 min prior fixation in the 2PM)
5. "Conditioning session" (3 h prior imaging)
6. "Memory test session" (3 h prior imaging)
= Only conditioning sound (CS)
= CS and nonCS
= no sound
= Box1
= Box 1 and Box 2
The week before
Day 1
D3
D5
D7
D9
D11
D13
Control group
Box 1: FC environment
Box 2: MT environment
1. Stereotactic virus injection
2. Cranial window implantation
4. Recurrent imaging of neuronal population (2 days interval)
ACx
= nuclei imaging
= c-Fos imaging
= calcium imaging:
spontaneous activity
sound-evoked activity
4 mice
17 FOVs
811 cells
39 FOVs
2118 cells
23 FOVs
2621 cells
24 FOVs
3881 cells

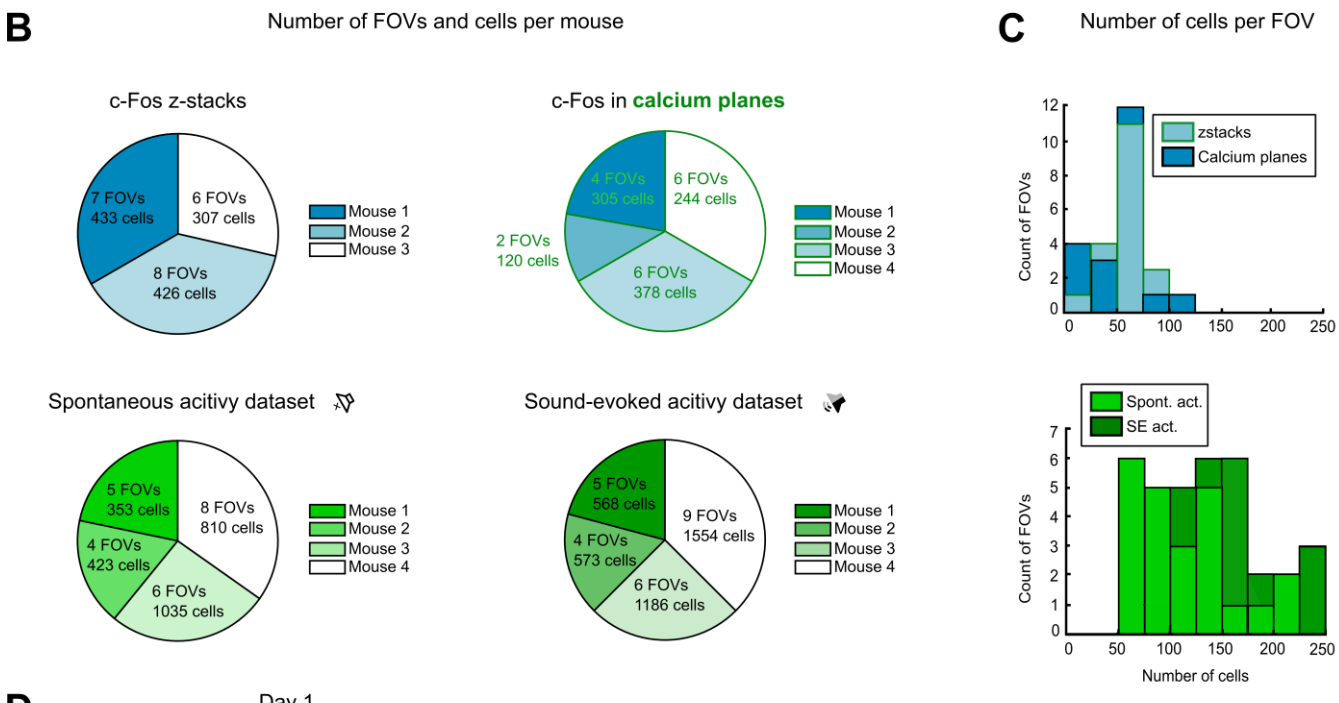
B
Number of FOVs and cells per mouse
c-Fos z-stacks
7 FOVs
433 cells
6 FOVs
307 cells
8 FOVs
426 cells
Mouse 1
Mouse 2
Mouse 3
c-Fos in calcium planes
4 FOVs
305 cells
6 FOVs
244 cells
2 FOVs
120 cells
6 FOVs
378 cells
Mouse 1
Mouse 2
Mouse 3
Mouse 4
Spontaneous acitivy dataset
5 FOVs
353 cells
8 FOVs
810 cells
4 FOVs
423 cells
6 FOVs
1035 cells
Mouse 1
Mouse 2
Mouse 3
Mouse 4
Sound-evoked acitivy dataset
5 FOVs
568 cells
9 FOVs
1554 cells
4 FOVs
573 cells
6 FOVs
1186 cells
Mouse 1
Mouse 2
Mouse 3
Mouse 4
C
Number of cells per FOV
zstacks
Calcium planes
Count of FOVs
Spont. act.
SE act.
Count of FOVs
Number of cells

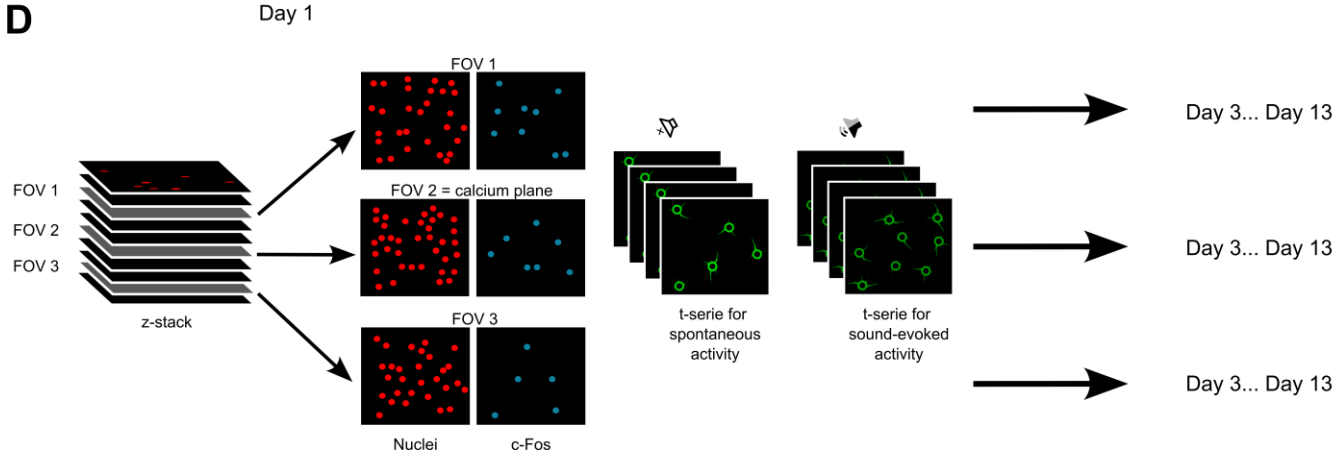
D
Day 1
FOV 1
FOV 2
FOV 3
z-stack
FOV 1
FOV 2 = calcium plane
FOV 3
Nuclei
c-Fos
t-serie for spontaneous activity
t-serie for sound-evoked activity
Day 3... Day 13
Day 3... Day 13
Day 3... Day 13

Figure 23. c-Fos and calcium dynamics throughout fear conditioning: experimental design and dataset overview for the control group.

(**A**) Experimental design to observe c-Fos and calcium dynamics before and after “conditioning session” and “memory test session”. About four weeks after stereotactic viral injection, cranial window implantation, and habituation, two-photon imaging sessions were performed every other day for thirteen days (seven time points). Three TPs were imaged prior to the conditioning session, and four TPs after, including the last TP after memory test. After image processing, 4 mice, 17 FOVs and 811 cells could be used to compare c-Fos signal, spontaneous and sound-evoked activity in the same cells (more FOVs and cells for the individual signals). Conditioning session: no CS and no shock, but mice were put in the behavioural box for the same duration as the fear-conditioned group. Memory test session: 2 repetitions of 5 consecutive CS presentation. Same sounds and imaging sessions after the conditioning and memory test sessions as for the fear-conditioned group (Fig.22A). (**B**) (**C**) (**D**) See description in Fig.18B-D.

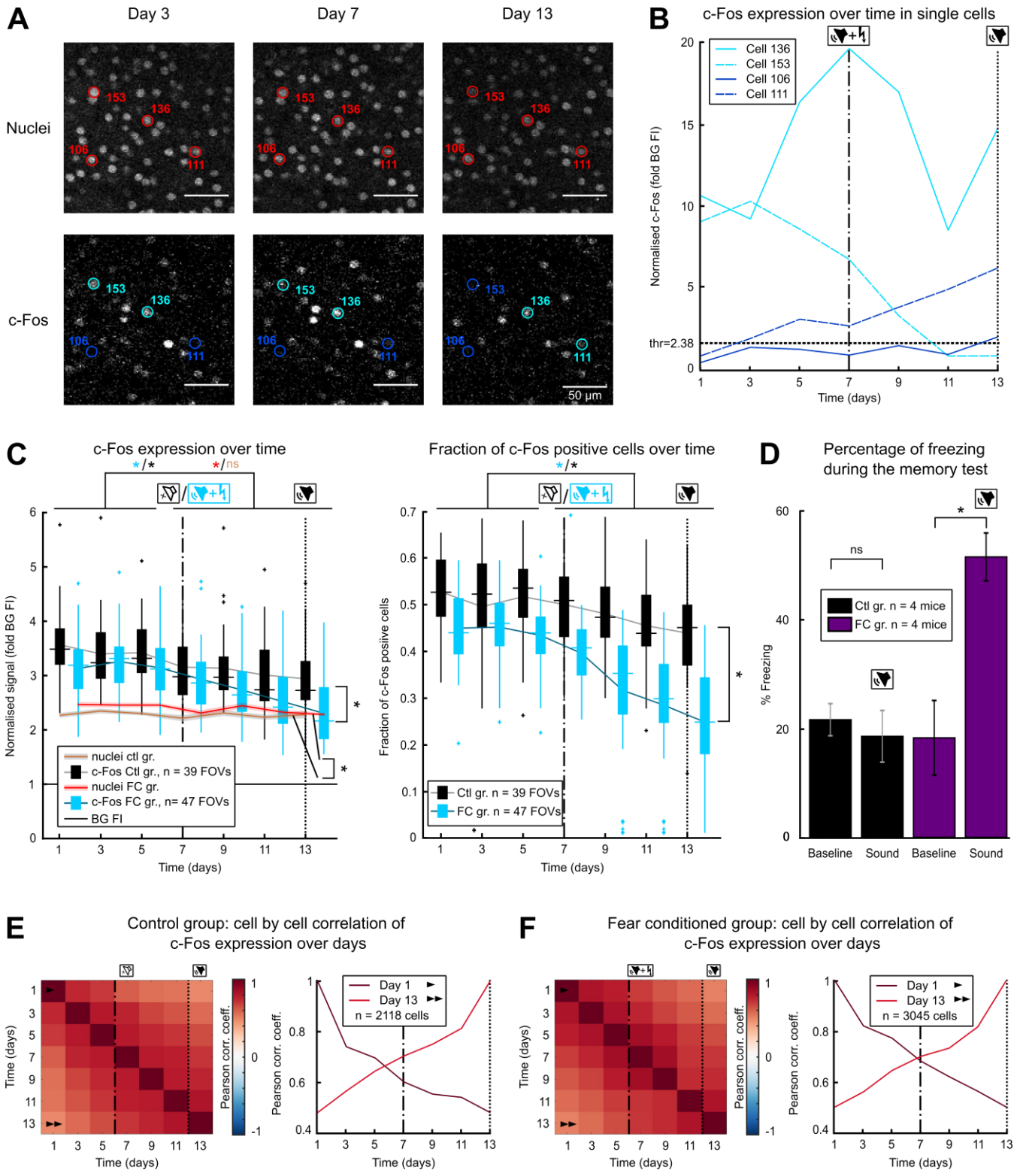
A
Day 3
Day 7
Day 13
Nuclei
c-Fos
153
136
106
111
50 µm
B
c-Fos expression over time in single cells
Cell 136
Cell 153
Cell 106
Cell 111
Normalised c-Fos (fold BG FI)
thr=2.38
Time (days)
C
c-Fos expression over time
Normalised signal (fold BG FI)
nuclei ctl gr.
c-Fos Ctl gr., n = 39 FOVs
nuclei FC gr.
c-Fos FC gr., n= 47 FOVs
BG FI
Time (days)
Fraction of c-Fos positive cells over time
Fraction of c-Fos posiive cells
Ctl gr. n = 39 FOVs
FC gr. n = 47 FOVs
Time (days)
D
Percentage of freezing during the memory test
% Freezing
ns
Ctl gr. n = 4 mice
FC gr. n = 4 mice
Baseline
Sound
Baseline
Sound
E
Control group: cell by cell correlation of c-Fos expression over days
Time (days)
Pearson corr. coeff.
Day 1
Day 13
n = 2118 cells
F
Fear conditioned group: cell by cell correlation of c-Fos expression over days
n = 3045 cells

Figure 24. c-Fos dynamics throughout fear conditioning: higher basal c-Fos reporter signal and decrease over time for the control and fear-conditioned group.

(**A**) Two-photon images of the same neuronal population at three time points (day 3, day 7 = fear conditioning session and day 13 = memory test session). First row: the nuclear marker is overlaid with four ROIs (red circles). Second row: the c-Fos reporter is overlaid with the same ROIs, showing examples of cells with a constant signal (positive: 136 and negative: 106) or a signal changing over time (153 and 111), according to the fixed threshold from Fig.10. (**B**) Normalised c-Fos signal for the individual ROIs showed in (A). (**C**) Left: Boxplots (FC gr.: blue, ctl gr.: black) and mean ± SEM of normalised c-Fos (FC gr.: blue line, ctl gr.: grey line), and mean ± SEM of normalised nuclear (FC gr.: red line, ctl gr.: brown line) signals per FOV of the entire dataset, for conditioned and control group of mice. Right: Boxplots (FC gr.: blue, ctl gr.: black) and mean ±SEM (FC gr.: blue line, ctl gr.: grey line) of fraction of c-Fos positive cells per FOV of the entire dataset. Wilcoxon signed rank tests to compared the 3 baseline time points with the 4 time points after the conditioning session; from left to right: * p=1.5009e-08 (c-Fos, FC gr.), ***** p=2.0888e-07 (c-Fos, ctl gr.), ***** p=4.1597e-06 (nuclei, FC gr.), ns p=0.2301 (nuclei, ctl gr.), * p=6.6702e-09 (c-Fos fraction, FC gr.), ***** p=1.4719e-04 (c-Fos fraction, ctl gr.). Wilcoxon rank sum test to compare the ctl and FC groups: from left to right: ***** p=5.2347e-09 (c-Fos), ***** p=4.3512e-09 (nuclei), ***** p=8.8420e-24 (fraction of c-Fos positive cells). (**D**) Freezing analysis during memory test session, for the control and the fear-conditioned group during CS presentation, compared to mouse movement during silence. Paired t-test: ctl gr.: **ns** p=0.4638, ***** FC gr.: p=0.0241 (**E**) Left: Self-correlation matrix of c-Fos expression over time for every cell of the control group dataset. Right: Pearson correlation values for the first and last line of the self-correlation matrix. (**F**) Same as (E), but for the fear-conditioned group.

Measuring c-Fos reporter expression over time, the results show that for single cell examples, c-Fos signal can decrease, increase or be stable (Fig.24A and B). Here again, the mean fluorescence intensity (Fig.24C, left) decreases significantly for c-Fos signal in both group of mice, and in a lesser extend for nuclear marker (Wilcoxon rank sum test to compare the signals before and after sound presentation: c-Fos; FC gr.: p=1.5009e-08, ctl gr.: p=2.0888e-07, and nuclei; FC gr.: p=4.1597e-06, ctl gr.: p=0.2301). The fraction of c-Fos (Fig.24C, right) positive cells drops significantly as well (Wilcoxon rank sum test: FC gr.: p=6.6702e-09, ctl gr.: p=1.4719e-04). The decrease in nuclear signal is once more suggesting for this dataset a diminution of signal quality, due to photobleaching and decline of window quality. The steeper slope for c-Fos reporter signal could be due to the higher sensitivity of the mTagBFP to photobleaching compared to mCherry. Nonetheless, when comparing c-Fos reporter signal for the control and the fear-conditioned group, we see a significant difference describing the more abrupt drop of the signal for the fear-conditioned group, both for the continuous and binarized data (Wilcoxon rank sum test: p=5.2347e-09 and p=8.8420e-24, respectively). Notably, the difference between the groups for the nuclear signal is also statistically significant (Wilcoxon rank sum test: p=4.3512e-09), but the trend is flat in both group. Another surprising finding is the very high level of c-Fos reporter expression for this specific experiment, compared to the experiments described in chapters 5 and 6. Indeed, in those experiments, nuclear marker fluorescence intensity was higher compared to c-Fos reporter. Given that c-Fos expression in the auditory cortex was shown to be triggered by exposure to new environment (Cho, Rendall, & Gray, 2017), the higher c-Fos level could be due to additional handling of mice in behavioural boxes, during habituation sessions. If this is the case, the decrease of c-Fos reporter expression to basal levels could be an effect of habituation. The explanation for the fear-conditioned group reaching the basal level faster compared to the control group is difficult to provide.

When comparing c-Fos reporter signal in individual cells over time in a correlation matrix, we observed similar Pearson correlation coefficients (1-0.5) compared to the Day experiment. For the control group (Fig.24E), the decrease in correlation appears more gradual in comparison with the fear-conditioned group (Fig.24F), which seem to create clusters. Plotting the Pearson correlation coefficients of the first and last lines of the matrices, the FC group seem to have a more stable c-Fos reporter expression before and after fear conditioning, whereas the correlation between time points in the

control group is dropping abruptly. However, here also the tendencies observed for c-Fos signal are comparable to those observed for the nuclear marker signal, which means the variation could be only due to the variations of the window quality, and not the signal per se (Figure S4).

These results are in contradiction with the literature, reporting an increase in c-Fos expression after fear conditioning, also in the auditory cortex (Cho et al., 2017; Gallo et al., 2018; Garner et al., 2012; Hoz et al., 2018; Josselyn & Tonegawa, 2020; X. Liu et al., 2012; L. G. Reijmers et al., 2007; D. S. Roy et al., 2022), suggesting that the c-Fos reporter signal measured may not reflect endogenous c-Fos expression, and the system may not be suited for chronical in vivo imaging. It could also suggest unspecific triggering of c-Fos expression, not related to neuronal activity.

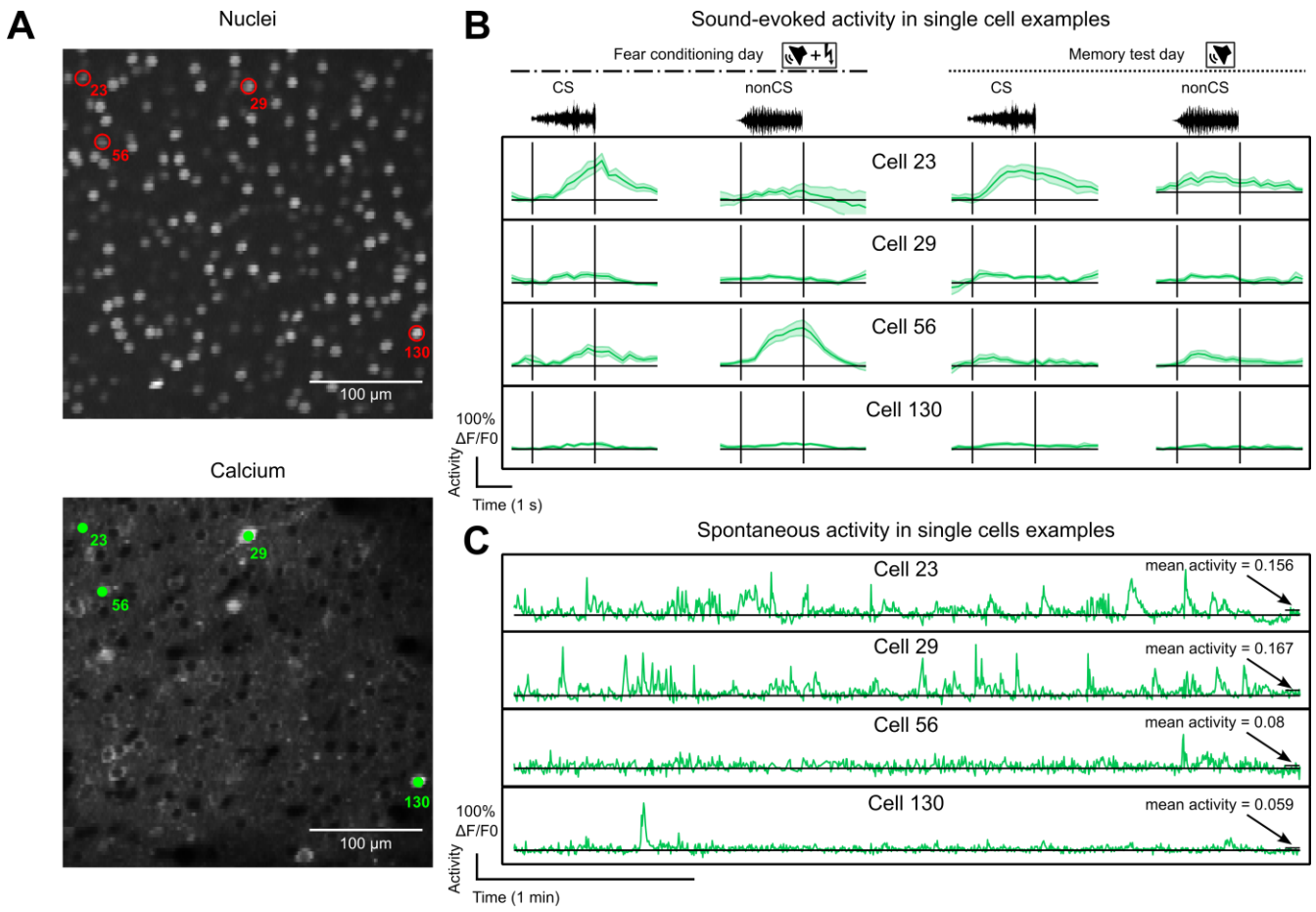
A
Nuclei
23
29
56
130
100 µm
Calcium
23
29
56
130
100 µm
B
Sound-evoked activity in single cell examples
Fear conditioning day
Memory test day
CS
nonCS
CS
nonCS
Cell 23
Cell 29
Cell 56
Cell 130
100%
ΔF/F0
Activity
Time (1 s)
C
Spontaneous activity in single cells examples
Cell 23
mean activity = 0.156
Cell 29
mean activity = 0.167
Cell 56
mean activity = 0.08
Cell 130
mean activity = 0.059
100%
ΔF/F0
Activity
Time (1 min)

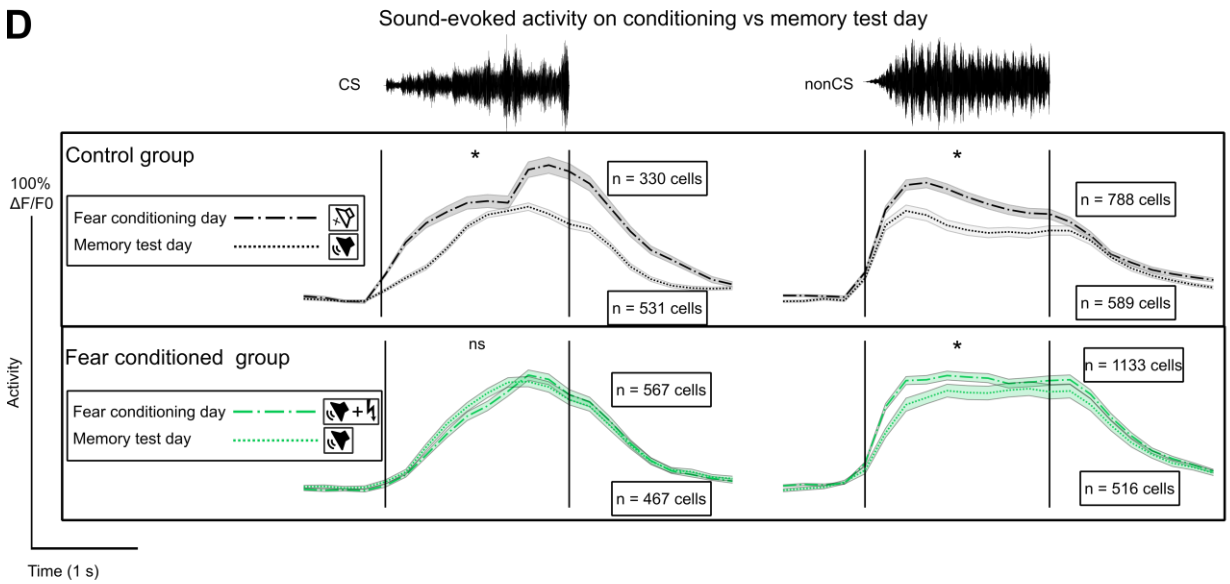
D
Sound-evoked activity on conditioning vs memory test day
CS
nonCS
Control group
Fear conditioning day
Memory test day
n = 330 cells
n = 531 cells
n = 788 cells
n = 589 cells
Fear conditioned group
Fear conditioning day
Memory test day
ns
n = 567 cells
n = 467 cells
n = 1133 cells
n = 516 cells
100%
ΔF/F0
Activity
Time (1 s)

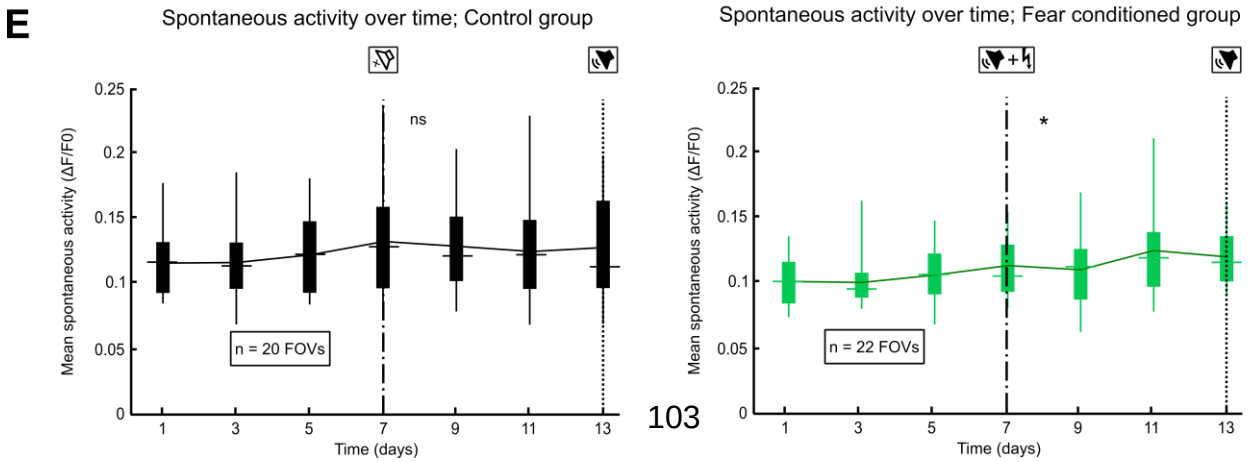
E
Spontaneous activity over time; Control group
Spontaneous activity over time; Fear conditioned group
Mean spontaneous activity (ΔF/F0)
ns
n = 20 FOVs
n = 22 FOVs
Time (days)
Time (days)

Figure 25. Calcium dynamics throughout fear conditioning: stable responsiveness to conditioning sound, decrease to non-conditioning sound and increase of spontaneous activity over time.

(**A**) See description in Fig.20A. (**B**) Sound-evoked activity for the individual ROIs shown in (A), throughout conditioning and non-conditioning sound presentation, during conditioning and memory test sessions. Activity is shown as mean ΔF/F0 ± SEM of 10 trials. (**C**) Spontaneous activity for the individual ROIs shown in (A). Activity is shown for the last time point (day 13), as ΔF/F0. The black arrow and line indicate the mean spontaneous activity of the cell at day 13. (**D**) Mean sound-evoked activity for all sound-responsive cells, during CS and nonCS presentation in conditioning and memory test sessions, for control and fear-conditioned group of mice. Wilcoxon rank sum tests to compare sound-evoked activity during fear conditioning and memory test sessions: From upper left to bottom right; ***** p= 2.1145e-22 (ctl gr. CS), ***** p=3.4258e-09 (ctl gr. nonCS), **ns** p=0.23718 (FC gr. CS), and ***** p=8.5336e-10 (FC gr. nonCS). Here, a sound-responsive cell was defined as follows: p value<0.5 for CS or nonCS, after a rank-sum test comparing sound-evoked activity (10 trials of 2s of ΔF/F0 after the sound presentation) with spontaneous activity (10 times of random 2s of ΔF/F0 during silence), and after a Bonferoni correction for multiple comparison (number of cells in a FOV). (**E**) Left: control group. Right: fear-conditioned group. Mean ± SEM spontaneous activity per FOV (all cells pooled, each with one value as mean activity described in (C)), for the seven time points. Friedman tests, from left to right: **ns** p=0.7478, ***** p=2.5205e-05.

Recording calcium transients and calculating activity in individual cells (Fig.25A) for every time point during silence, or during the fear conditioning and the memory test day, in response to either CS or nonCS, we observed unique calcium transients. Similarly to what we observed for the experiment in Chapter 6, some cells are very active during a specific sound presentation, others are activated during both CS and nonCS presentation, and other cells are not responsive to any stimulation at a given time point (Fig.25B). As for the spontaneous activity, some cells are very active, but others are quite silent (Fig.25C). In the entire dataset for the control group, comparing the sound-evoked activity during the fear conditioning and the memory test days (Fig.25D, upper), we detected a significant decrease of activity in response to both CS and nonCS during the memory test day (Wilcoxon rank sum: p= 2.1145e-22 for CS and p=3.4258e-09 for nonCS). On the contrary, in the FC group (Fig.25D, bottom), we observed this decrease for nonCS but not for CS (Wilcoxon rank sum: p=0.23718 for CS, and p=8.5336e-10 for nonCS), suggesting a slower habituation effect to CS. The mean spontaneous activity in FOVs (Fig.25E) did not change significantly over time for the control group (Friedman tests: p=0.7478), but increased for the FC group (Friedman tests: p=2.5205e-05). The observations for the control group are consistent with spontaneous and sound-evoked activity in Fig.20D-E, from Chapter 6.

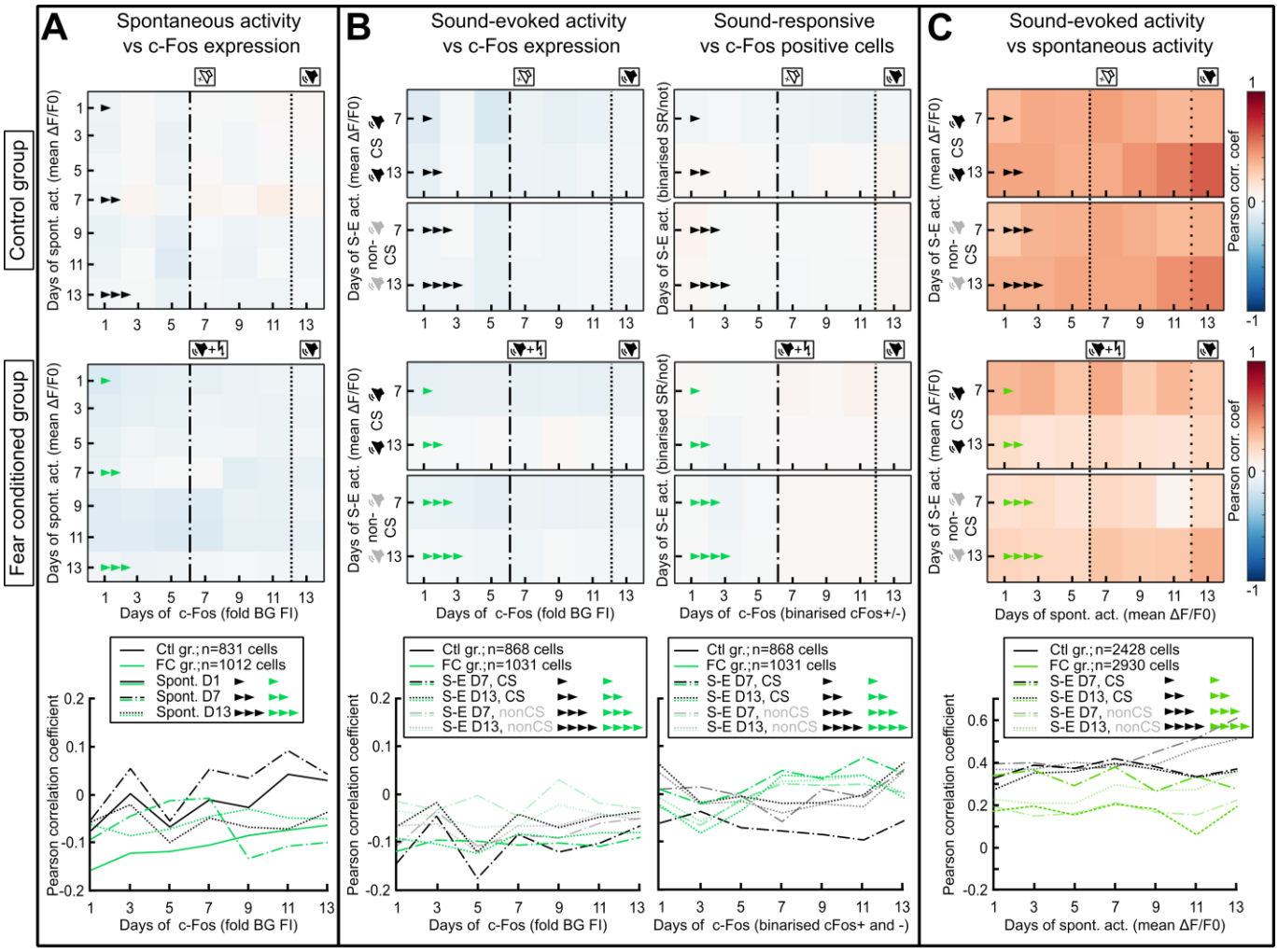
A
Spontaneous activity
vs c-Fos expression
B
Sound-evoked activity
vs c-Fos expression
Sound-responsive
vs c-Fos positive cells
C
Sound-evoked activity
vs spontaneous activity
Control group
Fear conditioned group
Days of spont. act. (mean ΔF/F0)
Days of S-E act. (mean ΔF/F0)
Days of S-E act. (binarised SR/not)
CS
non-CS
Pearson corr. coef
Days of c-Fos (fold BG FI)
Days of c-Fos (binarised cFos+/-)
Days of spont. act. (mean ΔF/F0)
Pearson correlation coefficient
Ctl gr.; n=831 cells
FC gr.; n=1012 cells
Spont. D1
Spont. D7
Spont. D13
Ctl gr.; n=868 cells
FC gr.; n=1031 cells
S-E D7, CS
S-E D13, CS
S-E D7, nonCS
S-E D13, nonCS
Ctl gr.; n=2428 cells
FC gr.; n=2930 cells
Days of c-Fos (fold BG FI)
Days of c-Fos (binarised cFos+ and -)
Days of spont. act. (mean ΔF/F0)

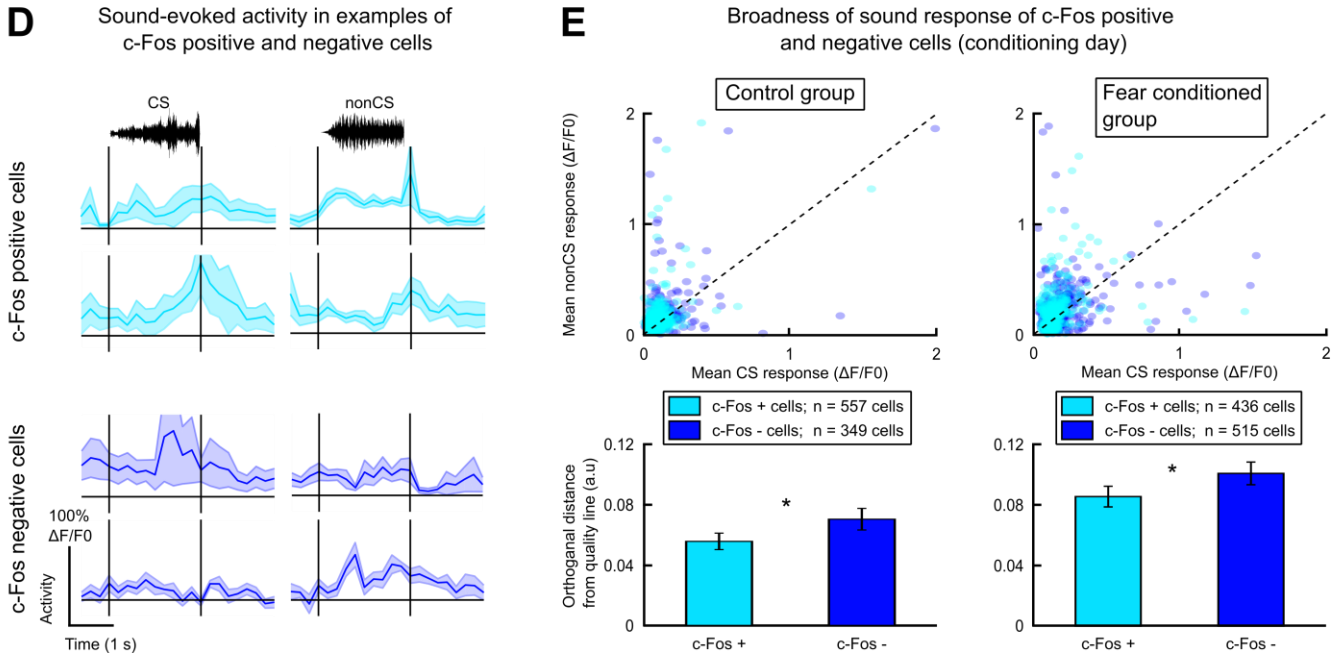
D
Sound-evoked activity in examples of
c-Fos positive and negative cells
CS
nonCS
c-Fos positive cells
c-Fos negative cells
100%
ΔF/F0
Activity
Time (1 s)
E
Broadness of sound response of c-Fos positive
and negative cells (conditioning day)
Control group
Fear conditioned
group
Mean nonCS response (ΔF/F0)
Mean CS response (ΔF/F0)
c-Fos + cells; n = 557 cells
c-Fos - cells; n = 349 cells
c-Fos + cells; n = 436 cells
c-Fos - cells; n = 515 cells
Orthoganal distance
from quality line (a.u)
c-Fos +
c-Fos -

Figure 26. c-Fos and calcium correlation throughout fear conditioning: poor correlation, and broader/less-specific responsiveness to sounds for c-Fos positive cells.

(**A**) Top and middle: cell-by-cell correlation matrices (ctl gr.: n=831 cells, FC gr.: n=1012 cells) of spontaneous activity and c-Fos expression. Bottom: Pearson correlation values from the cell-by-cell correlation matrices (black for ctl gr. and green for the FC gr.), for one TP before conditioning, the fear conditioning session and the memory test session. (**B**) Top and middle left: cell-by-cell correlation matrices (ctl gr.: n=868 cells, FC gr.: n=1031 cells) of sound-evoked activity (mean ΔF/F0 during CS or nonCS presentations) and c-Fos expression. Bottom left: Pearson correlation values from the cell-by-cell correlation matrices (black for ctl gr. and green for the FC gr.), for the fear conditioning session and the memory test session. Top and middle right: same as Top and middle left, with binarized data (sound-responsive vs c-Fos positive cells) (see description in Fig. 21B). Bottom right: same description as Bottom left. (**C**) Top: cell-by-cell correlation matrices (ctl gr.: n=2428 cells, FC gr.: n=2939 cells) of sound-evoked activity and spontaneous activity. Bottom: same description as (B) Bottom left. (**D**) Sound-evoked activity in two c-Fos positive and two c-Fos negative exemplary cells, during CS or nonCS presentation. Sound-evoked activity is presented as mean ΔF/F0 ± SEM over 10 repetitions. (**E**) In order to test if c-Fos positive and c-Fos negative cells differ in the selectivity of their response, the mean response to both stimuli, CS and nonCS, were compared in a scatter plot. Top: Scatter plots (left: ctl gr., right: FC gr.) of the mean sound-evoked activity in all sound-responsive cells (grouped as c-Fos positive and negative cells) during the conditioning session, for CS (x axis) compared to nonCS (y axis) sounds. Bottom: Bar graphs quantifying the difference in mean response to CS and nonCS, for c-Fos positive and negative cells. The difference is measured as the orthogonal distance between the points and the diagonal line that reflects equality in responses. Wilcoxon rank sum tests, from left to right: ***** p= 0.0415, ***** p=0.0492.

To compare c-Fos reporter expression with calcium transients during silence or relevant sound presentation, we used the strategy described in Chapter 6, Figure 21. Here again, we observed a decrease of c-Fos reporter signal for both groups, whereas spontaneous activity stayed relatively stable for the control group, and even increased for the FC group. It is with no surprise then that we see a low correlation of the signals for both group, and slightly lower for the FC group (Pearson correlation coefficients: -0.15 to 0.1). Intriguingly, for the FC group, the spontaneous activity during fear conditioning day is more correlated to c-Fos reporter expression before the conditioning compared to after. To be noticed as well is the higher and increasing correlation for the control group compared to the FC group. Alike the observation in Fig.21, about the decline of both c-Fos reporter signal and sound-evoked activity for the control group and in response to nonCS for FC group, in Fig.26B we would expect higher correlation values compared to the matrices in Fig.26A. But, if c-Fos is initially higher due to expression unrelated to sound stimulation and decreases due to habituation to handling, and on the other hand the sound-evoked activity is decreasing due to habituation to sound presentation, the low correlation in the left part of Fig.26B can be expected (Pearson correlation coefficients: -0.15 to 0). Considering sound-evoked activity was extracted from the activity of all cells, during either CS or nonCS presentations, it may be that the activity is more representative for not sound-responsive cells. In order to specifically target cells responsive for the sounds and cells expressing highly c-Fos, we repeated the correlation with binarized data (sound-responsive cells and c-Fos positive cells). In this matrices for the control and the FC group (Fig.26B, right) the correlation values were low as well, although slightly higher (-0.1 to 0.1). Noticeably, the correlation values increase after fear conditioning for the FC group in all conditions, meaning c-Fos expression in the cells reflects the sound-responsiveness of cells during both sessions and in response to both sounds. We next wanted to compare the sound-evoked activity in c-Fos positive and c-Fos negative cells (single cell example: Fig.26D and whole population: Fig.26E). Alike what we observed in Fig.21E, c-Fos positive cells appear to be responsive to both CS and nonCS, whereas c-Fos negative cells are more specifically activated by either nonCS or CS.

For the reasons mentioned in Chapter 6, for the Fig.21C, we also compared sound-evoked and spontaneous activity (Fig.26C). The correlation values were comparable to what observed for Fig.21C (0.1 to 0.6), indicating a high correlation for spontaneous

and sound-evoked activity. This result goes in line with papers linking spontaneous activity to evoked activity, observing replays of the latest in awake animals when the brain region is not stimulated (Luczak et al., 2009; Pfeiffer, 2020; Sakata & Harris, 2009), supposedly participating to memory consolidation. In our dataset we did similar observations (Figure S3) and c-Fos positive cells from the fear-conditioned group appear to have a higher number of replay events, in comparison to c-Fos negative cells.

To recapitulate briefly the findings for this experiment, c-Fos reporter expression was higher to begin with, compared to previous similar experiments in Chapter 5 and Chapter 6. The signal decreased to reach a level observed under basal conditions, faster for the FC group compared to the control. Regarding calcium transients, spontaneous activity was stable in the control group, but increased in the FC group. Sound-evoked activity decreased from the conditioning day to the memory test day, in response to both CS and nonCS in the control group. Surprisingly, the same decline was also observed in the FC group for nonCS, but not for CS, suggesting less adaptation for the conditioning sound. This result is in line with what was previously reported in our group (Aschauer et al., 2022). When comparing c-Fos reporter expression with spontaneous activity, correlation values were very low, but higher for the control group compared to the FC group. On the contrary, c-Fos positive cells correlated better with sound-responsive cells in FC group, even though the values were also low. In line with recent observation on the spontaneous activity, the latter was highly correlated to evoked activity. Interestingly, similar to what we observed in Chapter 6, c-Fos positive cells had a broader sound-responsiveness compared to c-Fos negative cells. Finally, c-Fos positive cells have a higher number of replay events in the spontaneous activity, when compared to sound-evoked activity.

7.1.2 Material and methods

For this experiment and the analyses, I[1] did the following steps described in in Chapter 2, Chapter 3 and section 5.1.2, using the viruses produced by Eike Kienle[1] and described in section 2.1.1:

- Injection in auditory cortex of C57BL/6J mice, of AAV2/8 packaging c-Fos-tTA, TRE-BFP, hSyn-H2B-mCherry and hSyn-GCaMP6m plasmids
- Cranial implantation
- Intrinsic imaging

- Habituation for fixation in two-photon microscope and to behavioural boxes
- Two-photon microscopy sessions (described below)
- Image processing of chronical in vivo two-photon z-stacks
- Image processing of chronical in vivo two-photon single scans
- Image processing of chronical in vivo two-photon t-series
- Analyses using rois inclusion criteria and the c-Fos threshold (3.1)
- Analyses using rois inclusion criteria and ΔF/F0 calculation (3.2)
- Cell-by-cell correlation matrix (5.1.2.5)
- Correlation matrices to compare c-Fos and calcium signals (6.1.2.5)

7.1.2.1 Sound presentation

The conditioning and non-conditioning stimuli in the experiment described in Fig.22 and 23 were complex sounds derived from the stimulus set described above, both lasting 2 seconds:

- The conditioning sound (CS) was obtained from a short sequence (8s) of Beethoven's 9th symphony, 2nd mvt. Frequencies were clipped (0-4 kHz) and the recording was played fourfold faster than the original piece.

- The non-conditioning sound (nonCS) was a birdcall (marbled wood-quail), also played fourfold faster but not clipped for frequencies (0-40 kHz).

Both stimuli were played at 70 dB sound pressure level. Only the conditioning sound was played during the conditioning and memory test sessions in the behavioural box. The non-conditioning sound was played in the two-photon microscope, together with the conditioning sound, 3 hours after both behavioural sessions.

7.1.2.2 Auditory cued fear conditioning

The auditory cued fear conditioning was performed similarly as described previously (Aschauer et al., 2022).

Behavioural setup

The behavioural boxes for conditioning and memory test sessions (H10-24, Coulbourn Instruments, Whitehall, PA, USA) contained white LEDs as house light, a microphone and a CCDKB-R3138 camera with infrared LEDs (LG Electronics Austria, Vienna, Austria) which was connected to a Cronos frame grabber (Matrox, Dorval, QC, Canada). The setup was soundproofed and controlled by a computer with WINDOWS 10, Version 2021, (Microsoft, Redmond, WA, USA) operating system running custom MATLAB R2016b software (MathWorks, Natick, MA, USA). An external shocker (Precision Animal shocker, Coulbourn Instruments) allowed to deliver foot shock.

Sounds were played from a gaming soundcard with a maximal sampling frequency of 192 kHz (Xonar AE, PCIe 7.1, ASUS, Taiwan) and delivered via an amplifier (Model SLA-1, Applied Research and Technology, TEAC Europe GmbH, TASCAM Division, Wiesbaden, Germany), a modified equalizer (Model #351, Applied Research and Technology, TEAC Europe GmbH, TASCAM Division, Wiesbaden, Germany) and a custom-made speaker for free field delivery of sounds.

Fear conditioning and memory test sessions

To create different environmental contexts for the conditioning and memory test sessions, floor, smell, walls, and lights were changed. Mice were habituated to both context on an everyday basis (5 minutes per day) for about a week prior to the conditioning session.
The environment during the conditioning session contained:
- A stainless-steel shock grid for the floor
- Ethanol on the shock grid
- A custom-made round-shaped wall
- Infrared LED (invisible for the mouse, but allowing the CCD camera to record the mouse behaviour in the closed soundroofed box)

The environment during the memory test session included:
- A container covered with a fine metal grid, for the floor
- Cage bedding in the container (home cage smell)
- A square-shape wall
- White LED, allowing the CCD camera to record the mouse freezing behaviour

For the fear-conditioned group of mice, the conditioning session was as follows: after 90 s of baseline, 5x paired conditioning sound (2 s) - foot shock (0.75 mA, 1 s) were delivered (inter-trial-interval (ITI): randomly 50-75 s). The memory test consisted in 90 s of baseline, and 2 blocks of 5x conditioning sounds (2 s, ITI: 2 s), separated with randomly 20-35 s.

For the control group of mice, the conditioning session was as long as for the fear-conditioned group (~7 minutes), but no sound nor shock were delivered. The memory test session was the same as for the fear-conditioned group.

For both sessions, the conditioning sound was played at 70 dB.

7.1.2.3 Analysis of freezing

The freezing analysis was performed similarly to a previous paper (Aschauer et al., 2022).

During the memory test session, movies were recorded (one frame every 2.8 seconds = ~0.36 frames per second). The number of "significant motion pixels" (SMP), i.e. pixels varying from a fixed threshold of gray values, was calculated for all pairs of consecutive frames, using a custom MATLAB R2016b script (MathWorks). The size of the mouse was estimated by the median SMP value of the 25% highest SMPs calculated from pairs of frames at least 2 minutes apart, in order to capture the mouse at different positions in the behavioural box. The threshold for freezing was defined as less SMP compared to the 0.3% of the mouse size, separating SMP values during freezing and movement periods. Baseline freezing was assessed during the 90 s baseline period.

7.1.2.4 Imaging sessions

To measure the dynamic of c-Fos and change of activity before and after fear conditioning and memory test sessions (Fig.22 and 23), z-stacks, single scans and t-series were acquired every 2nd day. A baseline without any stimuli presented was recorder for three time points prior to the fear conditioning session, as well as for two time points between the fear conditioning session and the memory test session. z-stacks and single scans were acquired to assess c-Fos expression level, and t-series were recorded to measure the spontaneous activity. 3 h after the fear conditioning and memory test sessions, in addition to the z-stacks, single scans and spontaneous recordings, t-series for sound-evoked activity were recorded in the same sequence as described in 6.1.2.2, but the c-Fos and spontaneous activity were recorded in every FOV prior to any sound presentation. The conditioning and the non-conditioning sounds (described above) were presented 10 times, in a randomized order. A gap of 3-7 seconds was left between each sound presentation.

7.1.2.5 Sound-evoked responsiveness

To classify single cells as sound-responsive or not, all trials from a given stimulus (10 repetitions) were compared in a rank-sum test against spontaneous activity (randomly drawn frames from the stimulus-free intervals). A cell was classified as significantly responsive, if the p value was below 0.05 after a Bonferroni correction for

multiple comparisons against number of days, number of stimuli, and number of cells for CS and nonCS.

7.1.2.6 Orthogonal distance

Modification of Pythagoras law to measure the distance of each point to the diagonal (orthogonal linear regression). Custom MATLAB function from a file exchange (https://de.mathworks.com/matlabcentral/fileexchange/64396-point-to-line-distance)

7.1.2.7 Statistics

Figure 24C:

To compare time points before and after the conditioning session (dependent measurements), a Wilcoxon signed rank test was used for both groups of mice.

To evaluate the difference between control and fear-conditioned group of mice (independent measurements), of normalised nuclear marker and c-Fos expression, a Wilcoxon rank sum test was applied.

Figure 24D:

For the freezing data, the significant change of a specific mouse movements during silence and presentation of the conditioning sound was estimated with a paired t-test.

Figure 25D

To compare sound-evoked activity in independent sound-responsive cells, during conditioning and memory test session, a Wilcoxon rank sum test was used.

Figure 25E:

For repeated measures in the same cells (spontaneous activity), a Friedman test was applied to estimate the significance of changes over time, for both group of mice.

Figure 26E:

Finally, to compare the orthogonal distance of sound-evoked activity to CS and nonCS in independent c-Fos positive and negative cells, a Wilcoxon rank sum test was applied.

7.2 Acute

Aforementioned, before the development of genetic tools to report c-Fos expression, c-Fos was detected either as protein, by immunostaining, or as mRNA, by in situ hybridisation. Those methods are still widely applied on brain slices or in cell cultures to mark activated neurons, and to control for overlap with the c-Fos promoter-based genetic tools (Clayton, 2000; Kawashima et al., 2014; Terstege & Epp, 2022; Yap & Greenberg, 2018). Here we repeated the fear conditioning protocol described in 7.1, and instead of chronic imaging, we sacrificed the mice 3 h after the conditioning session and stained endogenous c-Fos with an antibody, to measure the overlap with c-Fos reporter. Mice were separated in three groups: fear-conditioned group, control group and another control group treated with doxycycline from the day of injection (Figure 27).

7.2.1 Results

After confocal imaging (Fig.27D) and image processing, we kept data from 3 mice, 15 FOVs and about 6000 cells per group (Fig.27B). About 400 cells per FOV were detected (Fig.27C).

The results indicate a higher fluorescence intensity for both c-Fos endogenous, stained with the antibody, and c-Fos reporter in the FC group compared to the control group (Fig.27E and F). The difference is not significant when binarizing the data and comparing the reporter expression between the control and the fear-conditioned group. Surprisingly, the nuclear signal is significantly higher in the FC and on-doxycycline group compared to the control group, suggesting a heterogeneous fluorescence signal between the groups. Hence, increase of c-Fos signal in the FC group compared to the control group for the reporter is to be interpreted cautiously. Furthermore, the increase of c-Fos reporter observed in the fear-conditioned group compare to the controls is quite mild. That being said, this outcome is consistent with the literature, demonstrating an increase of c-Fos expression after fear conditioning in the hippocampus, and the auditory cortex (Cho et al., 2017; Gallo et al., 2018; Garner et al., 2012; Hoz et al., 2018; Josselyn & Tonegawa, 2020; X. Liu et al., 2012; L. G. Reijmers et al., 2007; D. S. Roy et al., 2022). To be noted, increase of c-Fos expression has also been shown to occur in mice only due to electrical shock, not due to conditioning (M. Peter et al., 2012).

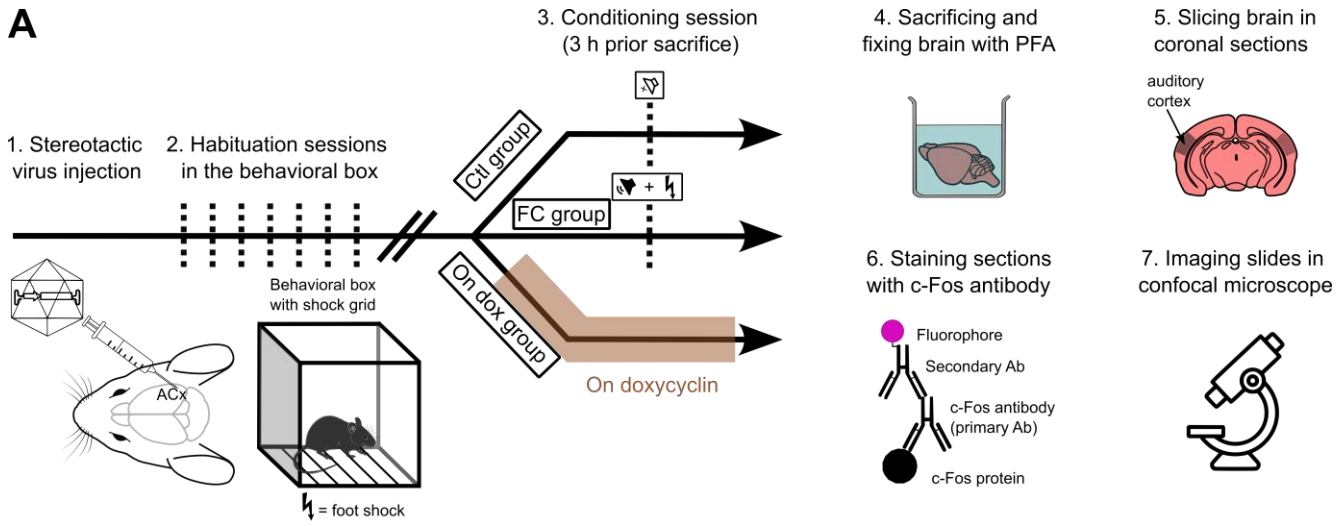
A
1. Stereotactic virus injection
2. Habituation sessions in the behavioral box
3. Conditioning session (3 h prior sacrifice)
4. Sacrificing and fixing brain with PFA
5. Slicing brain in coronal sections
auditory cortex
Ctl group
FC group
On dox group
On doxycyclin
ACx
Behavioral box with shock grid
= foot shock
6. Staining sections with c-Fos antibody
Fluorophore
Secondary Ab
c-Fos antibody (primary Ab)
c-Fos protein
7. Imaging slides in confocal microscope

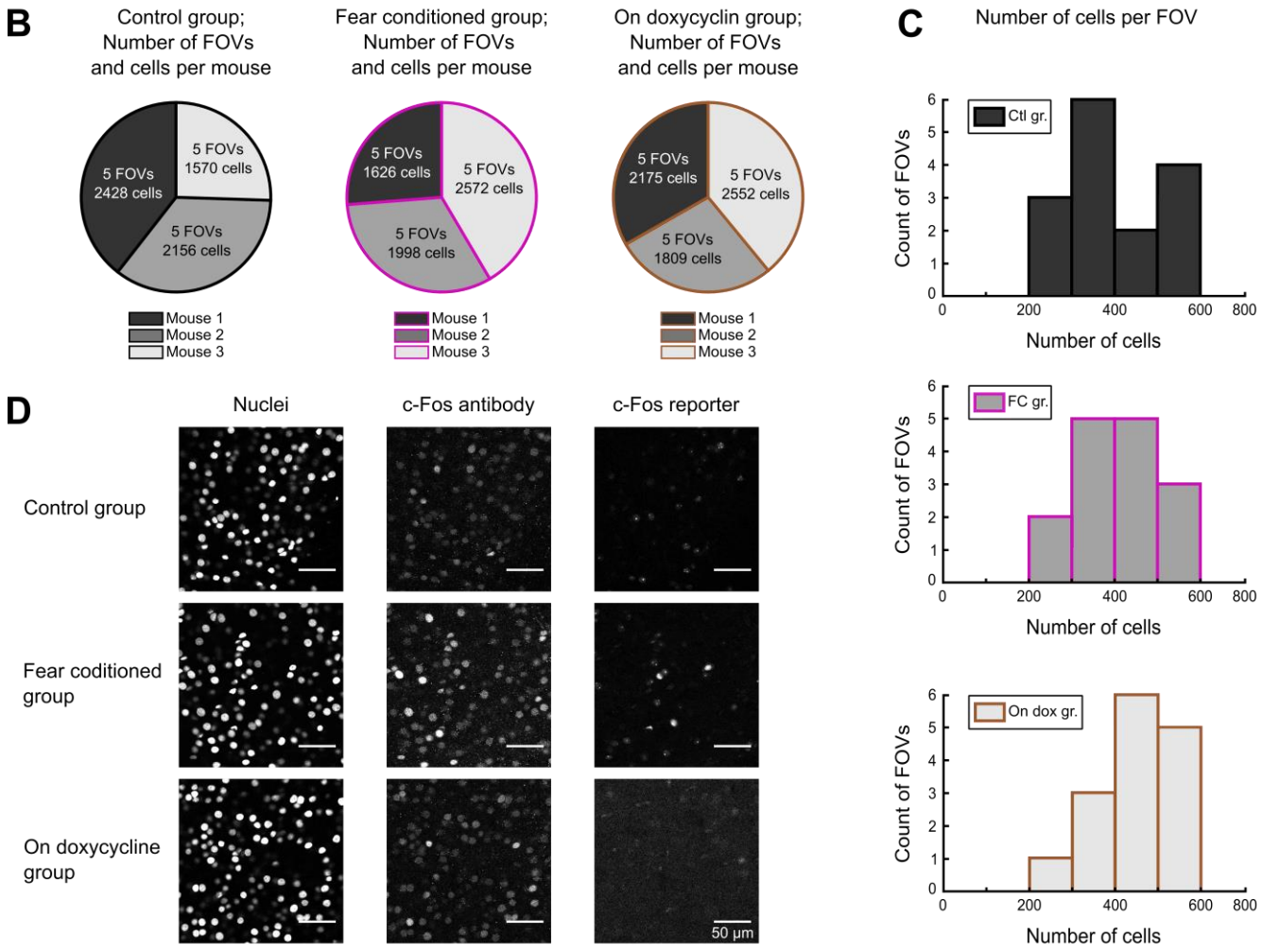
B
Control group; Number of FOVs and cells per mouse
Fear conditioned group; Number of FOVs and cells per mouse
On doxycyclin group; Number of FOVs and cells per mouse
5 FOVs 2428 cells
5 FOVs 1570 cells
5 FOVs 2156 cells
5 FOVs 1626 cells
5 FOVs 2572 cells
5 FOVs 1998 cells
5 FOVs 2175 cells
5 FOVs 2552 cells
5 FOVs 1809 cells
Mouse 1
Mouse 2
Mouse 3
C
Number of cells per FOV
Ctl gr.
FC gr.
On dox gr.
Count of FOVs
Number of cells
D
Nuclei
c-Fos antibody
c-Fos reporter
Control group
Fear coditioned group
On doxycycline group
50 µm

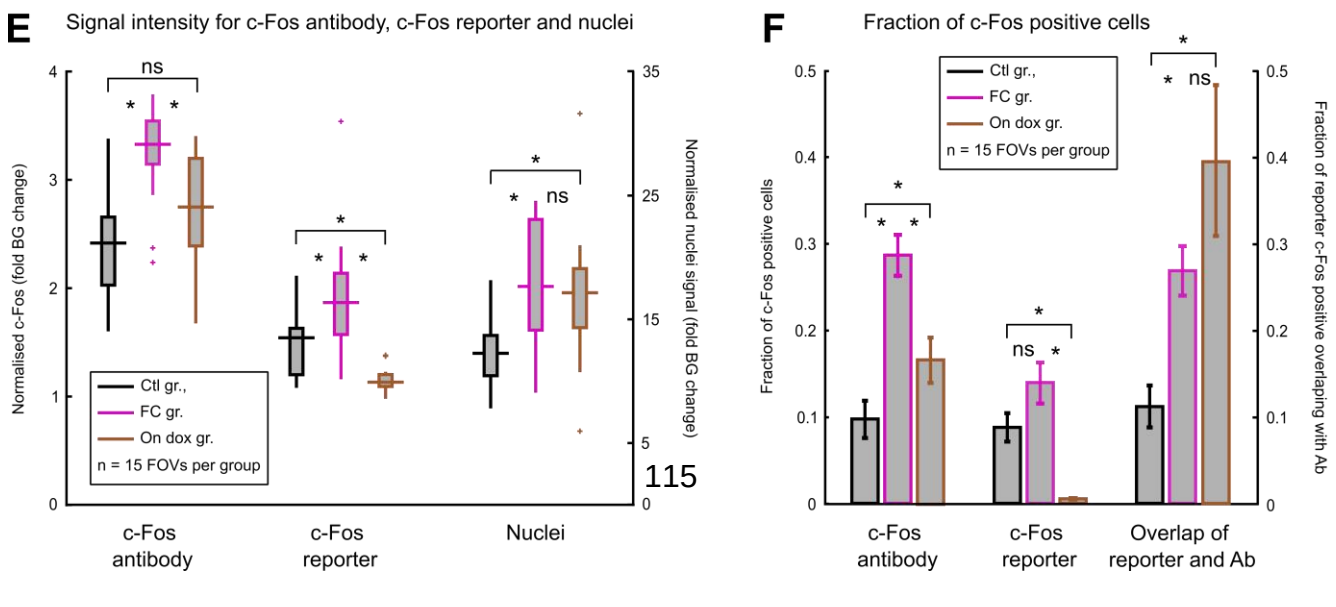
E
Signal intensity for c-Fos antibody, c-Fos reporter and nuclei
Normalised c-Fos (fold BG change)
Normalised nuclei signal (fold BG change)
Ctl gr.,
FC gr.
On dox gr.
n = 15 FOVs per group
ns
c-Fos antibody
c-Fos reporter
Nuclei
115
F
Fraction of c-Fos positive cells
Fraction of c-Fos positive cells
Fraction of reporter c-Fos positive overlaping with Ab
Overlap of reporter and Ab

Figure 27. c-Fos reporter compared to endogenous c-Fos expression after fear conditioning: increase of both c-Fos expression 3 hours after fear conditioning.

(**A**) Experimental design to compare c-Fos reporter and c-Fos endogenous expression, in a control (ctl gr.) and a fear-conditioned group (FC gr.) of mice. An additional group of mice received doxycycline (on-dox gr.) supplemented food (~40 mg/Kg) from the day of injection of the 4 constructs in the auditory cortex (Fig.6), to test for reporter leakiness. About 3 weeks after injection, mice were habituated for a week to the conditioning environment. After habituation, one group of 3 mice was fear-conditioned (as described in Fig.22A for the fear conditioning session), another 6 mice (3 on and 3 off doxycycline) served as control (see description in Fig. 23A, the conditioning session). 3 h after the conditioning session, mice were sacrificed, their brain was extracted and directly immerged in PFA for tissue fixation. The brains were then sliced with a vibratome (70 µm) and stained with c-Fos antibody (Cell signalling Technology, Cat. No. 2250). Lastly, slices were mounted on slides and imaged with a confocal microscope for the three fluorophores (nuclear marker H2B-mCherry, c-Fos reporter BFP and c-Fos secondary antibody alexa fluor 647). (**B**) Pie charts showing the distribution of the signals in the 3 mice, for each group. (**C**) Histogram showing the number of cells per FOV (200-600), for the three groups. (**D**) Confocal images of three neuronal populations in the three groups, and imaged for the three fluorophores. (**E**) Boxplots showing the mean of normalised c-Fos signals in the FOVs for the reporter and the antibody, as well as for the nuclear signal in the three groups. Wilcoxon rank sum tests, from left to right: * p=2.6217e-04, **ns** p=0.0745, * p=0.0079 (c-Fos antibody), * p=0.0161, * p=0.0021, * p=1.9352e-05 (c-Fos reporter:), * p=0.0101, * p=0.0070, **ns** p=0.7400 (nuclear signal). (**F**) Bar plots showing the fraction and overlap of c-Fos positive cells in FOVs for each group of mice. Wilcoxon rank sum tests, from left to right: * p= 1.6033e-04, * p=0.0421, * p=0.0048 (c-Fos antibody). **ns** p=0.1057, * p= 5.0040e-06, * p=3.3580e-06 (c-Fos reporter). * p=4.4947e-04, * p=0.0129, ns p=0.2039 (overlap).

Additionally, the overlap of c-Fos antibody and c-Fos reporter (Fig.27F) is relatively low (>30%), when compared to previous reports after conditioning, observing an overlap of 80-90% (Garner et al., 2012; Khalaf et al., 2018; X. Liu et al., 2012). This dissimilarity may be due to the different antibody used (polyclonal in the literature and monoclonal in this experiment), brain region stained (hippocampus in the literature and auditory cortex in this experiment), or incubation time after the experiment (1.5-2 h in the literature and 3 h in this experiment).

The discrepancy between the two experiments for fear conditioning, chronic and acute, is probably derived from the differences in the design. In the chronic experiment, mice were handled extensively to be habituated to both setups, the two-photon microscope, and the behavioural boxes. In the acute experiment, mice were only being habituated to the behavioural boxes, and to the conditioning environment and not the memory test environment. Exploratory behaviour can trigger c-Fos expression in the auditory cortex (Cho et al., 2017). Moreover, in the chronical experiment, awake mice were head-fixed to the two-photon microscope, which is a source of stress, also a factor inducing c-Fos expression (De Medeiros, Reis, & Mello, 2005; Matsuda et al., 1996; Senba, Matsunaga, Tohyama, & Noguchi, 1993). Furthermore, mice for chronical imaging sessions were implanted with a window, which is known to induce inflammation (Cramer et al., 2021; Drew et al., 2010). The latter is also increasing c-Fos expression (Mckay, Bromhaar, Jongste, & Hoogsteden, 2001; Noguchi, Dubner, & Ruda, 1992). Finally, chronic imaging sessions did probably induce photobleaching, when mice from this experiment had intact fluorescence when sacrificed. Altogether, the induction of c-Fos expression, unspecific to neuronal activity in both groups, and the photobleaching, could hide the subtle increase observed in the acute experiment.

7.2.2 Material and methods

For this experiment, I did the following steps described in sections 2.1.1 and 7.1.2, using the viruses produced by Eike Kienle[1] and described in section 2.1.1:

- Injection in auditory cortex of C57BL/6J mice, of AAV2/8 packaging c-Fos-tTA, TRE-BFP, hSyn-H2B-mCherry and hSyn-GCaMP6m plasmids
- Habituation to behavioural boxes
- Conditioning session: Auditory cued fear conditioning for the “fear-conditioned” group, no conditioning for the “control” and “on-doxycycline” groups.
- Sacrifice 3 h after conditioning

7.2.2.1 Doxycycline supplemented food

The “on-doxycycline” group of mice received pellets supplemented with 46mg/Kg of doxycycline (Ssniff, Germany), from the day of viral injection and until they have been sacrificed.

7.2.2.2 Brain fixation and slicing

Mice were sacrificed by dislocation 3 hours after the conditioning session, and their brain were extracted and immerged in 4% PFA solution (Electron Microscopy Sciences, Cat. Num. 15710), and kept overnight at 4°C. The day after, PFA was replaced with PBS. 70 µm-thick coronal slices of the brain were cut with a vibratome (Leica Biosystems, Germany; VT 1000 S), and kept in 24-wells plates (greiner bio-one, Cellstar, Cat. no. 662 160) filled with PBS.

7.2.2.3 Immunostaining

The PFA-fixed 70 µm-thick brain coronal slices were treated with a blocking solution (10% normal goat serum (NGS) and 1% Triton X-100 in PBS) at RT for 2 hours. After three washing steps, slices were incubated overnight at 4°C in the primary antibody solution (1% NGS, 0.1% Triton X-100 and 1:500 of the rabbit monoclonal c-Fos antibody in PBS (Cell signalling Technology, Cat. no. 2250)). The 24-wells plate was put on a plate shaker to insure homogeneous staining of the slices. The day after, the slices were left for 2 hours at RT, and washed three times. Then, the secondary antibody solution (1% NGS, 0.1% Triton X-100 and 1:500 of the Alexa Fluor 647 conjugated secondary antibody in PBS (goat anti-rabbit IgG, Invitrogen, Cat. no. A21244)) was applied on the slice at RT for 2 more hours. Finally, after three washings, the slices were mounted on microscope slides (mounting medium Fluoromount-G from Invitrogen).

7.2.2.4 Confocal and image analyses

Confocal images were acquired on a TCS SP5 microscope (Leica, Germany), using a 20x/0.7 dry objective.

Images processing was executed on FIJI as follows: 1. Nuclei and background (4 regions ~24x bigger than nuclei) detection based on H2B-mCherry channel (5% threshold to binarize, median filter, analyse particles tool) 2. Measure of the mean grey values from the ROIs in the 4 channels.

Analyses were carried out using MATLAB (R2016b). c-Fos antibody and c-Fos reporter signals were normalised to their respective background signal. c-Fos positive cells for antibody and reporter signals were selected with a threshold based on the distribution of the values in the control group. A cell with a value higher than the 90% of the distribution was considered positive for the signal. This thresholds for the antibody and the reporter were then applied on the “fear conditioning” and “on-doxycycline” groups.

7.2.2.5 Statistics

Figure 27E:

To compare the three independent groups for the reporter and the antibody expression, a Wilcoxon rank sum tests was applied.

Figure 27F:

Same tests as for Figure 26E: Wilcoxon rank sum tests.

Chapter 8. Discussion

8.1 Summary of background and Main Question

c-Fos is the first immediate early gene that was shown to be expressed upon neuronal depolarisation, demonstrated by drug-induced seizure and high c-Fos in hippocampus and piriform cortex (Morgan et al., 1987; Saffen et al., 1988). Because reactivation of cells expressing c-Fos in the hippocampus during fear memory formation can create freezing, they are thought to be engrams, the substrate for memory (Garner et al., 2012; X. Liu et al., 2012). Therefore, c-Fos is a tool widely used to tag and manipulate active neurons and engrams. c-Fos is coding for a protein fusing with c-Jun and binding to other molecules to create the transcription factor AP-1 (Okuno, 2011; Sheng & Greenberg, 1990). The transcription factor has been shown to trigger the expression of many late-response genes, but the function of those genes, linking c-Fos expression to neuronal activity or memory, remains unclear (Gallo et al., 2018; Leslie & Nedivi, 2011; Minatohara et al., 2016; Yap & Greenberg, 2018). Moreover, c-Fos expression is not specific to neurons, and not neither to neuronal activity (Okuno, 2011; Yap & Greenberg, 2018). Therefore, the question we tried to answer with this PhD project is: How tight is the correlation of c-Fos levels and neuronal activity?

8.2 Summary of model and analysis strategy

To answer the question, we employed state-of-the-art methods to chronically image in parallel a c-Fos reporter and the very popular neuronal activity marker, a calcium indicator, GCaMP6 (T. W. Chen et al., 2013). The c-Fos reporter was based on the TetTag transgenic mouse developed in 2007 (L. G. Reijmers et al., 2007), and later used to tag engrams (Garner et al., 2012; X. Liu et al., 2012) . We packaged DNA coding for the two neuronal activity markers, and additionally a nuclear marker, in AAV2/8 (Carter, 2004; Gao et al., 2002). The viral particles were injected in the auditory cortex of adult black 6 mice. Then, we implanted a cranial window and habituated mice to be head-fixed to a two-photon microscope, in order to chronically image the three signals in the auditory cortex under basal conditions, during sound presentation and during fear conditioning (Chapter 2).

In order to analyse the acquired data, we developed pipelines, based on the nuclear signal, to follow the same cells over weeks and extract signals from the nuclear marker,

c-Fos reporter and calcium indicator (Chapter 3). We successfully apply the pipelines to follow thousands of cells for up to three weeks.

8.3 Summary and interpretation of the results

8.3.1 c-Fos reporter kinetic

To assess the kinetic of c-Fos reporter, we performed one experiment to evaluate the synthesis time and another to measure the decaying time.

8.3.1.1 Synthesis time

For the first experiment (4.1), we transduced cortical neurons with the c-Fos reporter. Then, we acutely depolarise the cultures with a mixture of neurotransmitters, GABA antagonist and cholinergic agonist. We fixed different cultures at different time points after the depolarisation and stained them with c-Fos antibody. When comparing c-Fos antibody and c-Fos reporter, we measured a delay of several hours (more than 6 h) for the reporter, compared to endogenous c-Fos expression (c-Fos antibody staining).

8.3.1.2 Decaying time

For the second experiment (4.2), we used the mouse model we developed, and blocked c-Fos reporter system with doxycycline. Subsequently, we repeatedly measured the fluorescence intensity in the same cells for up to 10 days. The results show that mTagBFP, as reported before, is a very stable protein, also in vivo, and cells need up to 10 days to degrade the fluorescent protein and reach the background fluorescence levels.

In conclusion, the time resolution of the model is very poor to report endogenous c-Fos expression.

8.3.2 Basal c-Fos dynamics

Both model for transgenic mice reporting c-Fos expression (Barth et al., 2004; L. G. Reijmers et al., 2007) shows very high “background” expression of c-Fos, an expression that cannot be related to experimental manipulations. In order to evaluate how this expression can alone vary over time, and the amount of c-Fos expressed during basal conditions, we measured c-Fos reporter chronically in the mouse model we developed, in habituated animals. We compared two time scales: hours (5.1.1.1) and days (5.1.1.2) intervals. In both experiments, the signal was very stable, and the

small variations observed were parallel to the nuclear signal, supposed to be stable, suggesting that the changes are due to the degrading quality of the implanted window, photobleaching and variations of two-photon microscope settings.

8.3.3 c-Fos dynamics and calcium transients in the auditory cortex, under sound stimulation

When chronically recording neuronal activity in the auditory cortex of mice, presenting every day the same set of sounds, our lab recently noticed that the neuronal population active for a specific sound is changing over time (Chambers et al., 2022). This phenomenon is called representational drift, and was already observed in several other brain regions, like the motor cortex, the hippocampus and other sensory cortices (Clopath et al., 2017; Driscoll et al., 2022; Masset et al., 2022; Rule et al., 2019). We took advantage of the complexity of this neuronal activity patterns, and hypothesised that these changes observed at a functional level could originate from changes at the gene expression level, based on the central dogma of molecular biology (DNA makes RNA, and RNA makes protein, (Crick F. H., 1958)). To test the hypothesis, we used the mouse model we developed and chronically recorded neuronal activity and c-Fos expression during sound presentation (Chapter 6).

Similar to the results for the baseline conditions, c-Fos expression did decrease over time, slightly more than the nuclear marker, probably due to photobleaching of the mTagBFP, more sensitive compared to mCherry.

Spontaneous activity was stable over time, with a tendency to increase.

However, as reported in our lab previously (Chambers et al., 2022), the amount of sound-responsive cells dropped, what could be attributed to a habituation effect (Thompson, 2009). The coding performance of sound-responsive cells was nevertheless stable, demonstrated by the unchanged best response amplitude.

When correlating c-Fos expression and the activity from the calcium indicator, in the same cells over time, the correlation was very poor for both spontaneous and sound-evoked activity. Noticeably, when comparing the binarized version of both signals, classifying cells as c-Fos positive and negative, and sound-responsive or not sound-responsive, the correlation was slightly higher.

Finally, when observing the activity in c-Fos positive and c-Fos negative cells, we measured a systematic difference across days, in the two classes of cells: c-Fos positive cells appear to be responsive to a broader range of sounds compared to c-Fos negative cells.

8.3.4 c-Fos dynamics and calcium transients in the auditory cortex, under fear conditioning

8.3.4.1 Chronic

To reproduce an experiment classically performed on the transgenic TetTag mice, to manipulate cells tagged during memory formation (Garner et al., 2012; X. Liu et al., 2012; L. G. Reijmers et al., 2007), we measured c-Fos chronically before and after fear conditioning and memory test (7.1). We used the mouse model we developed, and separated mice in two groups: control and fear-conditioned. During the behavioural protocols for the conditioning session, the control group did not receive any shock, nor sound. The fear-conditioned group was exposed to a set of paired shock-sound stimuli. During the behavioural protocol for the memory test, both group were exposed to the conditioning sound. During the imaging sessions following both the conditioning and the memory test sessions, we presented the conditioning sound and another complex sound, the non-conditioning sound.

Comparing both group for c-Fos expression, the fear-conditioned group had a more dramatic drop of signal, but this change was similarly observed for the nuclear signal (Figure S4), supposed to be stable, indicating that the results may reflect the decreasing quality of the window rather than the real signal for c-Fos.

Spontaneous activity was stable in the control group, with a tendency to increase, alike the group of mice exposed to sound only in Chapter 6. In the fear-conditioned group, the spontaneous activity increased significantly over time.

Interestingly, the sound-evoked activity during the presentation of the CS and nonCS decreased over time in the control group, similar to what observed in Chapter 6. However, in the conditioned group, the activity decreased significantly for nonCS, but was stable over time for CS, suggesting a slower adaptation for the conditioning sound. This is in line with what our group already observed previously (Aschauer et al., 2022).

Similarly to what we observed in Chapter 6, the correlation of c-Fos expression to either spontaneous or sound-evoked activity was poor, for the control and the fear-conditioned group. Additionally, when binarizing the signals, the correlation increased slightly.

Spontaneous and sound-evoked activity are very highly correlated in both Chapter 6 and 7.1. We investigated this further, inspired by the knowledge of replay events occurring in the spontaneous activity, believed to represent memory during sleep and awake states (Hoffman et al., 2007; Ji & Wilson, 2007; Luczak et al., 2009; Pfeiffer, 2020; Sakata & Harris, 2009). A fascinating result followed when comparing spontaneous activity in cells expressing highly c-Fos and cells expressing low levels of c-Fos; c-Fos positive cells from the fear-conditioned group seem to have a higher rate of replay events, compared to c-Fos negative cells, again suggesting a role of neurons expressing c-Fos in memory formation (Figure S3). This results support the engram theory (Josselyn & Tonegawa, 2020), and extend it to a sensory cortex.

The last result, not less interesting and consistent with Chapter 6, shows that c-Fos positive cells appear to encode a broader range of sounds (CS and nonCS) compared to c-Fos negative cells (specific for either CS or nonCS). This result was observable for both the control and the fear-conditioned group.

8.3.4.2 Acute

In order to see the overlap between c-Fos reporter and c-Fos endogenous, we applied a similar protocol to the fear conditioning for chronical imaging (7.2). We used the mouse model we developed and separated the mice in three groups: control, fear-conditioned, and on-doxycycline. The on-doxycycline group received the antibiotic from the injection day and was treated as the control group for the behavioural session. For this experiment, we only injected the mice, and habituated them to the behavioural setup, but we did not implant a window and therefore also not image activity under the two-photon microscope. The three groups of mice were sacrificed after the conditioning session, and the brains were stained for c-Fos endogenous protein, with an antibody.

Comparing the three groups of mice, c-Fos antibody was significantly higher in the fear-conditioned group than in the two other groups of mice. c-Fos reporter was as well higher in the fear-conditioned group, but surprisingly the difference was also significant for the control group compared to the group on doxycycline. Unexpectedly, the level of

nuclear signal, which is a structural marker, expected to be stable and comparable in the three groups, is also significantly higher in the fear-conditioned and on-doxycycline groups when compared to the control group. In addition, the overlap of c-Fos antibody and c-Fos reporter is relatively low compared to previous reports (Garner et al., 2012; Khalaf et al., 2018; X. Liu et al., 2012). Put together, the significance of the difference in the fluorescence intensity for those results should be interpreted with caution.

Although the difference in fluorescence in the nuclear signal and the low overlap between the two markers of c-Fos are troubling, the increase in c-Fos expression upon fear conditioning is what is expected, based on the literature (Cho et al., 2017; Gallo et al., 2018; Garner et al., 2012; Hoz et al., 2018; Josselyn & Tonegawa, 2020; X. Liu et al., 2012; L. G. Reijmers et al., 2007; D. S. Roy et al., 2022). Inconsistency between the results found in the chronic and acute experiment can be explained as follows: mice from the chronic experiments are stressed and over-stimulated compared to mice in the acute experiment, because of the additional habituation sessions to the behavioural and two-photon setup, and the awake head-fixed imaging sessions. In addition, mice from the chronic experiment were implanted with cranial window, shown to induce inflammation. Exploration, stress and inflammation are triggering c-Fos expression (Cho et al., 2017; De Medeiros et al., 2005; Matsuda et al., 1996; Mckay et al., 2001; Noguchi et al., 1992; Senba et al., 1993). The very high basal level of c-Fos observed in the chronic fear conditioning experiment in comparison to the experiments in Chapter 5 and Chapter 6 supports the claim. This unusual high level of c-Fos, combined with the photobleaching, degradation of cranial window quality, the parallel change of nuclear signal and the very poor temporal resolution of c-Fos reporter could hide c-Fos dynamics. All those clues point towards the fact that this model is not suitable for chronic imaging and probably not capturing the subtle dynamics of c-Fos triggered by neuronal activity, maybe not inducing c-Fos as strongly as exploration, stress and inflammation.

8.4 Implications of the results

The results of the experiments reporting the expression of c-Fos in the mouse model we developed cannot be used to answer the main question, because the model does probably not capture c-Fos dynamics (Figure 15, Figure 17, Figure 19 and Figure 24). The results exploitable to interpret the physiological relevance of c-Fos in the auditory cortex are those using the reporter to classify cells as c-Fos positive and c-Fos

negative, and comparing the neuronal activity in the two groups (Figure 21D-E, Figure 26D-E, and Figure S3). The latter are systematic and consistent across experiments and group of mice, and less sensitive to time and levels of c-Fos expression. As the TetTag system was originally developed for long tagging of cells expressing highly c-Fos, in a restricted time window, the analysis of c-Fos positive and negative groups is probably better suited for this tool, compared to chronic in vivo imaging of c-Fos dynamics.

The fact that c-Fos positive cells are activated by a broader set of sounds (Figure 21D-E, and Figure 26D-E), and have a higher replay events rate in conditioned mice (Figure S3), implies a role of the IEG in stimuli generalisation and further suggests a role in memory formation. The stable coding of c-Fos positive cells for all sounds across days resembles a recent report in the hippocampus (Pettit, Yap, Greenberg, & Harvey, 2022). The group found that c-Fos expressing cells form an ensemble of cells stably tuned to place fields. Hence, the role of the IEG is probably not directly correlated to neuronal activity, but rather to population coding and memory formation, and the precise mechanisms involving the protein in these processes should be further investigated. Therefore, and because of the very low correlation of c-Fos expression and neuronal activity reported by the calcium indicator at any time point compared, using the IEG as a neuronal activity marker is likely not reasonable.

The results from chapter 7.2, in line with the literature, suggest that the mouse model without the cranial window, without the habituation sessions, and awake head fixation in the two-photon microscope, can report c-Fos expression level comparable to the endogenous protein. Nevertheless, because of the low overlap of c-Fos reporter and c-Fos antibody shown in Figure 27, compared to previous reports with overlaps of 80-90% (Garner et al., 2012; Khalaf et al., 2018; X. Liu et al., 2012) and the variations in the nuclear marker signal between groups, the results do not seem to be very robust.

The stress due to head fixation and inflammation due to window implantation also imply that chronic calcium imaging with head-fixed mice is not reporting activity under physiological conditions.

8.5 Limitations of the model and experimental design, solutions and future perspectives

8.5.1 c-Fos expression in many different cell-types and triggered by various pathways

As previously mentioned, c-Fos expression is unspecific to neurons and can be triggered by various molecules (Nambu et al., 2022; Okuno, 2011; Yap & Greenberg, 2018). To achieve cell-type specificity here, we co-labelled cells with c-Fos and a nuclear marker expressed under the promoter human synapsin 1. The promoter is active specifically in neurons (Kügler et al., 2003), and c-Fos signal was only measured in cells also labelled with the nuclear marker.

It is also possible to minimise external factors activating expression of c-Fos in order to measure c-Fos expression essentially triggered by neuronal activity. Indeed, to reduce the stress induced to the mice during the experiments, one could take advantage of the miniscopes and measure neuronal activity in freely moving animals (Stamatakis et al., 2021). The popularity of this tool allows rapid development and improvements, and the method will hopefully soon match the quality obtained with head-fixed measurement in two-photon microscopes. Moreover, the recent discovery of agents to make tissues transparent is promising to eventually circumvolve inflammation due to surgeries, like window implantation, and allow recording through an intact skull (Cramer et al., 2021; Drew et al., 2010). Additionally, c-Fos expression can be triggered by exposure to novel environments, also in the auditory cortex, and in mice habituated to the environment (Cho et al., 2017). Hence, to minimise c-Fos expression due to exploratory behaviour, c-Fos should be measured in the home cage. Lastly, shock only can induce c-Fos expression in the auditory cortex (Cho et al., 2017; M. Peter et al., 2012), meaning fear conditioning paradigms with another aversive stimulus, like air puff for instance, could be used instead. To find the appropriate aversive stimulus, not triggering c-Fos expression in the auditory cortex, one should first test the protocol and measure c-Fos by immunostaining.

To measure c-Fos in the home cage, and expression due to sound stimulation or sound-cued fear conditioning, one could imagine an experiment with a miniscope and a cage equipped with a speaker, an air tube and a camera, like the recently developed IntelliCages (Iman et al., 2021).

8.5.2 Heterogeneous expression of c-Fos in the brain

Another limitation of c-Fos-based tools is the disparity of expression in the different brain regions (Q. He et al., 2019; Hudson, 2018; Kleim et al., 1996; Kovács, 2008; Q. Zhang et al., 2018). As TetTag systems have essentially been utilized to tag engrams in the brain regions involved in fear-memory, like hippocampus, amygdala and prefrontal cortex (Josselyn & Tonegawa, 2020; H. Lee & Kaang, 2023), it is difficult to rely on the literature to back up our findings in the auditory cortex. Therefore, to compare our data, we relied also on papers measuring c-Fos expression in the auditory cortex, with other markers of c-Fos (Cho et al., 2017; Hoz et al., 2018; M. Peter et al., 2012; D. S. Roy et al., 2022).However, the different tools to measure c-Fos may report different results.

8.5.3 mRNA vs protein expression; c-Fos reporter vs c-Fos antibody

The c-Fos reporter in our experiment is supposedly active when the c-Fos endogeneous promoter is active, meaning what is reported is c-Fos transcription and not c-Fos translation. However, c-Fos transcription and translation rates are not necessarily proportional (Takeuchi et al., 2001). And c-Fos mRNA is subject to alternative splicing, and in the brain about 5% of c-Fos mRNA is transcribed into a truncated version of the protein (Jurado, Fuentes-Almagro, Prieto-Álamo, & Pueyo, 2007), which is not captured by our c-Fos reporter. The difference in c-Fos mRNA and c-Fos protein levels is one possible explanation for the low overlap of the reporter and c-Fos antibody staining. Nevertheless, previous groups could measure very high overlap between c-Fos antibody and c-Fos expression reported by TetTag systems (Garner et al., 2012; Khalaf et al., 2018; X. Liu et al., 2012).

To measure a higher overlap of c-Fos reporter and antibody in our last experiment (7.2), we could decrease the time interval between conditioning and sacrifice to match the successful 1.5-2 h reported previously. To optimise further the measure of c-Fos protein, an ideal method would be tagging the endogenous c-Fos protein in vivo, without changing its physiological properties in cells.

8.5.4 Poor temporal resolution of c-Fos as a neuronal activity marker

A further concerned of c-Fos-based tools as a marker for active neurons is the poor temporal resolution. In the experiments using the TetTag system, expression of c-Fos is usually blocked to allow tagging of active cells only in a restricted time window. Expression of c-Fos reporter is unblocked (doxycycline given in tet-on system, or retrieved in tet-off system) 1-2 days before the experiment, and blocked on the day of experiment, 1.5-2 h after the conditioning or artificial (optogenetic, chemogenetic) activation of cells (Garner et al., 2012; X. Liu et al., 2012; Poll et al., 2020; Z. Zhang et al., 2015). Here, we wanted to investigate the function of c-Fos expressed at any time, to understand the role of this “unspecific” expression. The disadvantage of this system when comparing c-Fos to neuronal activity is the delay of synthesis caused by the two layers tool (c-Fos-tTA and TRE-BFP), as demonstrated by the experiments in cell cultures (4.1). Recently, similar groups investigated chronically c-Fos expression in parallel to neuronal activity, but instead of the TetTag systems, they recorded the IEG in the transgenic mouse expressing a fusion protein of c-Fos and GFP (Ivashkina et al., 2021; Mahringer et al., 2019, 2022; Meenakshi et al., 2021). In these cases, the delay of c-Fos expression is about 30-60 minutes (Lamothe-Molina et al., 2020; Meenakshi et al., 2021), compared to over 6 h in pyramidal cells acutely depolarised. Of note, the cell culture does probably not reflect the dynamic of TetTag system in vivo, as previous groups reported a higher overlap of the reporter and the antibody 1.5 h after the activated cells or conditioning mice, in comparison to unstimulated mice or cells (Garner et al., 2012; X. Liu et al., 2012; Ramirez et al., 2013).

On top of the delayed synthesis time, the c-Fos reporter has also a delayed decaying time, as demonstrated in 4.2. c-Fos protein returns to basal levels about 6 h after activity-induced expression in neurons (Barros et al., 2015; Bisler et al., 2002). The blue fluorescent protein has a long half-life of ~54 h and need up to 10 days to be degraded in vivo. To study gene expression, unstable fluorescent proteins have been developed to degrade very rapidly (Andersen et al., 1998; L. He et al., 2019).

Hence to improve the temporal resolution of our model, we could use a short half-life fluorescent protein, expressed directly under the c-Fos promoter.

8.5.5 No causal relation between c-Fos and neuronal activity or memory

The initial question is still open, as late genes targeted by the transcription factor formed by c-Fos are involved in various cellular processes, but none of those could so far be causally linked to neuronal activity or memory (Gallo et al., 2018; Leslie & Nedivi, 2011; Minatohara et al., 2016; Yap & Greenberg, 2018). Since c-Fos is widely used as a tool to mark and manipulate active neurons and engrams in all brain regions, since the eighties, it is essential to investigate the precise mechanism of the gene and the protein in neurons, to justify applications with c-Fos-based tools.

8.5.6 Artificial gene expression: episomal vs chromosomal context, missing regulatory elements, strain specific c-Fos promoter

The safety of adeno-associated viruses relies on the fact that most of the DNA delivered to cells is not integrating into the genome. However, this advantage could as well be a limitation. Indeed, expression of genes depends on the chromatin state (Huisinga, Brower-toland, & Elgin, 2006) and on regulatory elements that could be far away from the gene, like enhancers (Shlyueva, Stampfel, & Stark, 2014). Consequently, the introduced episomal c-Fos promoter may not be active and controlled in a similar way as the endogenous c-Fos promoter. In addition, c-Fos promoter used in all the modern tools derives from a sequence isolated from BALB/c mice (Curran et al., 1983). The homologous sequence of c-Fos promoter may be different in the black six strain.

Transgenic mice have the transgene integrated into the genome, and according to the recent studies using FosGFP mice, the fusion protein mimics quite reliably the expression of the endogenous c-Fos protein (Lamothe-Molina et al., 2020; Meenakshi et al., 2021).

8.5.7 Impaired habituation due to anesthesia-induced loss of memory?

In the experiments described in Chapter 5, Chapter 6 and section 7.1, mice were anesthetised with isoflurane for the injection, about two weeks later for the cranial

implantation, a few days later for the intrinsic imaging session, and after the week of habituation to the awake head fixation in the two-photon microscope, for the first recording session. Each anesthesia lasted 1-3 h. It has previously been shown that memory formation can be impaired after long and repetitive exposure to isoflurane (P. Liu et al., 2021; Saab et al., 2010). Even though the topic is controversial (Wu, Zhao, Weng, & Ma, 2019), the repetitive and long exposure to isoflurane may had an effect on the cognitive function of mice, preventing them to habituate and reduce the stress of imaging sessions.

To limit exposure to anesthesia, one may imagine an experiment using tail injection to deliver the transgenes (FosBFP and GCaMP6m for instance), packaged in AAV capsids able to cross the blood brain barrier, like AAV9 (Stoica, S.Ahmed, Gao, & Sena-Esteves, 2013; Zhou et al., 2022). This would allow to prevent anesthesia during injection. The mice could be implanted with a two-photon miniscope, so that they could undergo only one surgery, and the fixed position of the image could avoid motions artifacts and therefore the necessity of a recording session under anesthesia.

8.5.8 Just a thought: RNA, DNA and protein are indeed universal

The mouse model developed here was created on systems deriving from twelve different living organisms (considering viruses as part of the tree of life):

- C57BL/6J mouse (Jackson laboratory developed the strain in 1948)
- c-Fos promoter from BALB/c mouse (Curran et al., 1983)
- tTA protein from herpes simplex virus (Gossen et al., 1995)
- TRE sequence from Escherichia Coli bacteria (Gossen et al., 1995)
- BFP protein from Entacmaea quadricolor anemone (Subach et al., 2008)
- hSyn promoter from human (Kügler et al., 2003)
- GCamP6m indicator is a fusion protein with three components (T. W. Chen et al., 2013; Nakai et al., 2001), GFP deriving from Aequorea victoria jellyfish (Shimomura et al., 1962), Calmodulin derived from rat (Mori et al., 2000) and myosin light chain derived from chicken (Romoser et al., 1997)
- mCherry protein was originally found in Discosoma anemone (Shaner et al., 2004)
- Viral capsid from adeno-associated virus, serotype 8 (AAV8) (Gao et al., 2002)
- Viral genome from adeno-associated virus, serotype 2 (AAV2) (Samulski et al., 1982)

Chapter 9. References

Adesnik, H., & Naka, A. (2018). Cracking the Function of Layers in the Sensory Cortex. *Neuron*, *100*(5), 1028–1043. https://doi.org/10.1016/j.neuron.2018.10.032

Afrashteh, N., Inayat, S., Bermudez-Contreras, E., Luczak, A., McNaughton, B. L., & Mohajerani, M. H. (2021). Spatiotemporal structure of sensory-evoked and spontaneous activity revealed by mesoscale imaging in anesthetized and awake mice. *Cell Reports*, *37*(10), 1–15. https://doi.org/10.1016/j.celrep.2021.110081

Allen, W. E., Chen, M. Z., Pichamoorthy, N., Tien, R. H., Pachitariu, M., Luo, L., & Deisseroth, K. (2019). Thirst regulates motivated behavior through modulation of brainwide neural population dynamics. *Science*, *364*(6437), 1–25. https://doi.org/10.1126/science.aav3932

Almendral, J. M., Sommer, D., Macdonald-bravo, H., Burckhardt, J., Perera, J., & Bravo, R. (1988). Complexity of the Early Genetic Response to growth factors in mouse fibroblasts. *Molecular and Cellular Biology*, *8*(5), 2140–2148. https://doi.org/10.1128/mcb.8.5.2140-2148.1988

Andermann, M. L., Kerlin, A. M., & Reid, R. C. (2010). Chronic cellular imaging of mouse visual cortex during operant behavior and passive viewing. *Frontiers in Cellular Neuroscience*, *4*(3), 1–16. https://doi.org/10.3389/fncel.2010.00003

Andersen, J. B. O., Sternberg, C., Poulsen, L. K., Bjørn, S. P., Givskov, M., & Molin, S. (1998). New Unstable Variants of Green Fluorescent Protein for Studies of Transient Gene Expression in Bacteria New Unstable Variants of Green Fluorescent Protein for Studies of Transient Gene Expression in Bacteria. *Applied and Environmental Microbiology*, *64*(6), 2240–2246. https://doi.org/10.1128/AEM.64.6.2240-2246.1998

Aravanis, A. M., Wang, L. P., Zhang, F., Meltzer, L. A., Mogri, M. Z., Schneider, M. B., & Deisseroth, K. (2007). An optical neural interface: in vivo control of rodent motor cortex with integrated fiberoptic and optogenetic technology. *Journal of Neural Engineering*, *4*(3), 143–156. https://doi.org/10.1088/1741-2560/4/3/S02

Arieli, A., Sterkin, A., Grinvald, A., & Aertsen, A. (1996). Dynamics of Ongoing Activity : Explanation of the Large Variability in Evoked Cortical Responses. *Science*, *273*(5283), 1868–1871. https://doi.org/10.1126/science.273.5283.1868

Aschauer, D. F., Eppler, J. B., Ewig, L., Chambers, A. R., Pokorny, C., Kaschube, M., & Rumpel, S. (2022). Learning-induced biases in the ongoing dynamics of sensory representations predict stimulus generalization. *Cell Reports*, *38*(6), 1–8. https://doi.org/10.1016/j.celrep.2022.110340

Aschauer, D. F., Kreuz, S., & Rumpel, S. (2013). Analysis of Transduction Efficiency, Tropism and Axonal Transport of AAV Serotypes 1, 2, 5, 6, 8 and 9 in the Mouse Brain. *PLOS ONE*, *8*(9), 1–16. https://doi.org/10.1371/journal.pone.0076310

Atchison, R. W., Casto, B. C., & McD. Hammon, W. (1965). Adenovirus-Associated Defective Virus Particles. *Science*, *149*(3685), 754–756. https://doi.org/10.1126/science.149.3685.754

Avery, O. T., MacLeod, C. M., & McCarty, M. (1944). Studies on the chemical nature of the substance inducing transformation of pneumococcal types. *Journal of Experimental Medicine*, *79*(2), 137–158. https://doi.org/10.1084/jem.79.2.137

Baird, G. S., Zacharias, D. A., & Tsien, R. Y. (1999). Circular permutation and receptor insertion within green fluorescent proteins. *Proceedings of the National Academy of Sciences (PNAS)*, *96*(20), 11241–11246. https://doi.org/10.1073/pnas.96.20.11241

Bandyopadhyay, S., Shamma, S. A., & Kanold, P. O. (2010). Dichotomy of functional organization in the mouse auditory cortex. *Nature Neuroscience*, *13*(3), 361–368. https://doi.org/10.1038/nn.2490.

Barbarosa, F. F., & Silva, R. H. (2018). Chapter 18 - Immediate-Early Gene Expression in Neural Circuits Related to Object Recognition Memory. In *Handbook of Behavioral Neuroscience* (Vol. 27, pp. 261–271). https://doi.org/10.1016/b978-0-12-812012-5.21001-x

Barkat, T. R., Polley, D. B., & Hensch, T. K. (2011). A critical period for auditory thalamocortical connectivity. *Nature Neuroscience*, *14*(9), 1189–1996. https://doi.org/10.1038/nn.2882

Barros, V. N., Mundim, M., Galindo, L. T., Bittencourt, S., Porcionatto, M., & Mello, L. E. (2015). The pattern of c-Fos expression and its refractory period in the brain of rats and monkeys. *Frontiers in Cellular Neuroscience*, *9*(72), 1–8. https://doi.org/10.3389/fncel.2015.00072

Barth, A. L., Gerkin, R. C., & Dean, K. L. (2004). Alteration of neuronal firing properties after in vivo experience in a FosGFP transgenic mouse. *The Journal of Neuroscience*, *24*(29), 6466–6475. https://doi.org/10.1523/JNEUROSCI.4737-03.2004

Bathellier, B., Ushakova, L., & Rumpel, S. (2012). Discrete Neocortical Dynamics Predict Behavioral Categorization of Sounds. *Neuron*, *76*(2), 435–449. https://doi.org/10.1016/j.neuron.2012.07.008

Bedbrook, C. N., Deverman, B. E., & Gradinaru, V. (2018). Viral strategies for targeting the central and peripheral nervous systems. *Annual Review of Neuroscience*, *41*, 323–348. https://doi.org/10.1146/annurev-neuro-080317-062048

Benito, E., & Barco, A. (2015). The Neuronal Activity-Driven Transcriptome. *Molecular Neurobiology*, *51*, 1071–1088. https://doi.org/10.1007/s12035-014-8772-z

Benjamini, Y., & Hochberg, Y. (1995). Controlling the false discovery rate: A practical and powerful approach to multiple testing. *Journal of the Royal Statistical Society: Series B*, *57*(1), 289–300.

Berger, H. (1929). Über das Elektrenkephalogramm des Menschen - Dritte Mitteilung. *Archiv Für Psychiatrie Und Nervenkrankheiten*, *87*(1), 527–570. https://doi.org/10.1007/BF01835097

Berti, V., Mosconi, L., & Pupi, A. (2014). Brain: Normal Variations and Benign Findings in FDG PET/CT imaging. *PET Clinics*, *9*(2), 129–140. https://doi.org/10.1016/j.cpet.2013.10.006

Bijlani, S., Pang, K. M., Sivanandam, V., Singh, A., & Chatterjee, S. (2022). The Role of Recombinant AAV in Precise Genome Editing. *Frontiers in Genome Editing*, *3*(799722), 1–16. https://doi.org/10.3389/fgeed.2021.799722

Bisler, S., Schleicher, A., Gass, P., Stehle, J. H., Zilles, K., & Staiger, J. F. (2002). Expression of c-Fos , ICER , Krox-24 and JunB in the whisker-to-barrel pathway of rats : time course of induction upon whisker stimulation by tactile exploration of an enriched environment. *Journal of Chemical Neuroanatomy*, *23*(3), 187–198. https://doi.org/10.1016/s0891-0618(01)00155-7

Bizley, J. K., & Dai, Y. (2020). Non-auditory processing in the central auditory pathway. *Current Opinion in Physiology*, *18*, 100–105.

https://doi.org/10.1016/j.cophys.2020.09.003

Blinks, J. R. (1990). Use of photoproteins as intracellular calcium indicators. *Environmental Health Perspectives*, *84*, 75–81. https://doi.org/10.1289/ehp.908475

Borenfreund, E., & Bendich, A. (1961). A study of the penetration of mammalian cells by deoxyribonucleic acids. *The Journal of Biophysical and Biochemical Cytology*, *9*(1), 81–91. https://doi.org/10.1083/jcb.9.1.81

Borile, G., Sandrin, D., Filippi, A., Anderson, K. I., & Romanato, F. (2021). Label-free multiphoton microscopy: Much more than fancy images. *International Journal of Molecular Sciences*, *22*(5), 1–20. https://doi.org/10.3390/ijms22052657

Bowen, Z., Winkowski, D. E., & Kanold, P. O. (2020). Functional organization of mouse primary auditory cortex in adult C57BL/6 and F1 (CBAxC57) mice. *Scientific Reports*, *10*(10905), 1–14. https://doi.org/10.1038/s41598-020-67819-4

Bowl, M. R., & Dawson, S. J. (2014). The mouse as a model for age-related hearing loss - A mini-review. *Gerontology*, *61*(2), 149–157. https://doi.org/10.1159/000368399

Bozon, B., Davis, S., & Laroche, S. (2003). A requirement for the immediate early gene zif268 in reconsolidation of recognition memory after retrieval. *Neuron*, *40*(4), 695–701. https://doi.org/10.1016/S0896-6273(03)00674-3

Brazier, M. A. B. (1984). Pioneers in the discovery of evoked potentials. *Electroencephalography and Clinical Neurophysiology/ Evoked Potentials*, *59*(1), 2–8. https://doi.org/10.1016/0168-5597(84)90015-7

Broussard, G. J., Liang, R., & Tian, L. (2014). Monitoring activity in neural circuits with genetically encoded indicators. *Frontiers in Molecular Neuroscience*, *7*(97), 1–17. https://doi.org/10.3389/fnmol.2014.00097

Campi, K. L., Bales, K. L., Grunewald, R., & Krubitzer, L. (2010). Connections of auditory and visual cortex in the prairie vole (microtus ochrogaster): Evidence for multisensory processing in primary sensory areas. *Cerebral Cortex*, *20*(1), 89–108. https://doi.org/10.1093/cercor/bhp082

Caras, M. L., Happel, M. F. K., Chandrasekaran, B., Ripollés, P., Keesom, S. M.,

Hurley, L. M., … Wright, B. A. (2022). Non-sensory Influences on Auditory Learning and Plasticity. *Journal of the Association for Research in Otolaryngology*, *23*(2), 151–166. https://doi.org/10.1007/s10162-022-00837-3

Carter, B. J. (2004). Adeno-associated virus and the development of adeno-associated virus vectors: A historical perspective. *Molecular Therapy*, *10*(6), 981–989. https://doi.org/10.1016/j.ymthe.2004.09.011

Castro, A. C., & Monteiro, P. (2022). Auditory Dysfunction in Animal Models of Autism Spectrum Disorder. *Frontiers in Molecular Neuroscience*, *15*(845155), 1–11. https://doi.org/10.3389/fnmol.2022.845155

Chambers, A. R., Aschauer, D. F., Eppler, J.-B., Kaschube, M., & Rumpel, S. (2022). A stable sensory map emerges from a dynamic equilibrium of neurons with unstable tuning properties. *Cerebral Cortex*, *bhac445*, 1–16. https://doi.org/10.1093/cercor/bhac445

Chen, K., Tian, Z., & Kong, L. (2022). Advances of optical miniscopes for in vivo imaging of neural activity in freely moving animals. *Frontiers in Neuroscience*, *16*(994079), 1–9. https://doi.org/10.3389/fnins.2022.994079

Chen, T. W., Wardill, T. J., Sun, Y., Pulver, S. R., Renninger, S. L., Baohan, A., … Kim, D. S. (2013). Ultrasensitive fluorescent proteins for imaging neuronal activity. *Nature*, *499*(7458), 295–300. https://doi.org/10.1038/nature12354

Cho, J., Rendall, S. D., & Gray, J. M. (2017). Brain-wide maps of Fos expression during fear learning and recall. *Learning and Memory*, *24*(4), 169–181. https://doi.org/10.1101/lm.044446.116

Chowdhury, S., Shepherd, J. D., Okuno, H., Lyford, G., Petralia, R. S., Plath, N., … Worley, P. F. (2006). Arc/Arg3.1 Interacts with the Endocytic Machinery to Regulate AMPA Receptor Trafficking. *Neuron*, *52*(3), 445–459. https://doi.org/10.1016/j.neuron.2006.08.033

Christie, R. H., Bacskai, B. J., Zipfel, W. R., Williams, R. M., Kajdasz, S. T., Webb, W. W., & Hyman, B. T. (2001). Growth arrest of individual senile plaques in a model of Alzheimer's disease observed by in vivo multiphoton microscopy. *The Journal of Neuroscience*, *21*(3), 858–864. https://doi.org/10.1523/jneurosci.21-03-00858.2001

Clayton, D. F. (2000). The genomic action potential. *Neurobiology of Learning and Memory*, *74*(3), 185–216. https://doi.org/10.1006/nlme.2000.3967

Clopath, C., Bonhoeffer, T., Hübener, M., & Rose, T. (2017). Variance and invariance of neuronal long-term representations. *Philosophical Transactions of the Royal Society B: Biological Sciences*, *372*(1715), 1–10. https://doi.org/10.1098/rstb.2016.0161

Cowansage, K. K., Shuman, T., Dillingham, B. C., Chang, A., Golshani, P., & Mayford, M. (2014). Direct Reactivation of a Coherent Neocortical Memory of Context. *Neuron*, *84*(2), 432–441. https://doi.org/10.1016/j.neuron.2014.09.022

Cramer, S. W., Carter, R. E., Aronson, J. D., Kodandaramaiah, S. B., Ebner, T. J., & Chen, C. C. (2021). Through the looking glass: A review of cranial window technology for optical access to the brain. *Journal of Neuroscience Methods*, *354*(109100), 1–11. https://doi.org/10.1016/j.jneumeth.2021.109100

Crick F. H. (1958). On Protein Synthesis. *Symposia of the Society for Experimental Biology*, *12*, 138–163. Retrieved from https://pubmed.ncbi.nlm.nih.gov/13580867/

Crowe, S. E., & Ellis-Davies, G. C. R. (2014). Longitudinal in vivo two-photon fluorescence imaging. *The Journal of Comparative Neurology*, *522*(8), 1708–1727. https://doi.org/10.1002/cne.23502

Curran, T., MacConnell, W. P., van Straaten, F., & Verma, I. M. (1983). Structure of the FBJ murine osteosarcoma virus genome: molecular cloning of its associated helper virus and the cellular homolog of the v-fos gene from mouse and human cells. *Molecular and Cellular Biology*, *3*(5), 914–921. https://doi.org/10.1128/mcb.3.5.914-921.1983

Curran, T., & Teich, N. M. (1982). Candidate product of the FBJ murine osteosarcoma virus oncogene: characterization of a 55,000-dalton phosphoprotein. *Journal of Virology*, *42*(1), 114–122. https://doi.org/10.1128/JVI.42.1.114-122.1982

Dana, H., Sun, Y., Mohar, B., Hulse, B. K., Kerlin, A. M., Hasseman, J. P., … Kim, D. S. (2019). High-performance calcium sensors for imaging activity in neuronal populations and microcompartments. *Nature Methods*, *16*(7), 649–657. https://doi.org/10.1038/s41592-019-0435-6

Day-Cooney, J., Dalangin, R., Zhong, H., & Mao, T. (2022). Genetically encoded

fluorescent sensors for imaging neuronal dynamics in vivo. *Journal of Neurochemistry*, *164*(3), 284–308. https://doi.org/10.1111/jnc.15608

De Medeiros, M. A., Reis, L. C., & Mello, L. E. (2005). Stress-induced c-Fos expression is differentially modulated by dexamethasone, diazepam and imipramine. *Neuropsychopharmacology*, *30*(7), 1246–1256. https://doi.org/10.1038/sj.npp.1300694

Denk, W., Strickler, J. H., & Webb, W. W. (1990). Two-photon laser scanning fluorescence microscopy. *Science*, *248*(4951), 73–76. https://doi.org/10.1126/science.2321027.

Dolphin, A. C. (2018). Voltage-gated calcium channels: Their discovery, function and importance as drug targets. *Brain and Neuroscience Advances*, *2*, 1–8. https://doi.org/10.1177/2398212818794805

Dombeck, D. A., Khabbaz, A. N., Collman, F., Adelman, T. L., & Tank, D. W. (2007). Imaging Large-Scale Neural Activity with Cellular Resolution in Awake, Mobile Mice. *Neuron*, *56*(1), 43–57. https://doi.org/10.1016/j.neuron.2007.08.003

Dragunow, M., Yamada, N., Bilkey, D. K., & Lawlor, P. (1992). Induction of immediate-early gene proteins in dentate granule cells and somatostatin interneurons after hippocampal seizures. *Molecular Brain Research*, *13*(1–2), 119–126. https://doi.org/10.1016/0169-328X(92)90051-C

Drew, P. J., Shih, A. Y., Driscoll, J. D., Knutsen, P. M., Blinder, P., Davalos, D., … Kleinfeld, D. (2010). Chronic optical access through a polished and reinforced thinned skull. *Nature Methods*, *7*(12), 981–984. https://doi.org/10.1038/nmeth.1530

Driscoll, L. N., Duncker, L., & Harvey, C. D. (2022). Representational drift: Emerging theories for continual learning and experimental future directions. *Current Opinion in Neurobiology*, *76*(102609), 1–9. https://doi.org/10.1016/j.conb.2022.102609

Duclot, F., & Kabbaj, M. (2015). The estrous cycle surpasses sex differences in regulating the transcriptome in the rat medial prefrontal cortex and reveals an underlying role of early growth response 1. *Genome Biology*, *16*(256), 1–20. https://doi.org/10.1186/s13059-015-0815-x

Ericsson, A. C., Crim, M. J., & Franklin, C. L. (2013). A brief history of animal modeling.

Missouri Medicine, *110*(3), 201–205. Retrieved from https://www.ncbi.nlm.nih.gov/pmc/articles/PMC3979591/

Farley, B. J., & Noreña, A. J. (2013). Spatiotemporal coordination of slow-wave ongoing activity across auditory cortical areas. *The Journal of Neuroscience*, *33*(8), 3299–3310. https://doi.org/10.1523/JNEUROSCI.5079-12.2013

Fatt, P., & Ginsborg, B. L. (1958). The ionic requirements for the production of action potentials in crustacean muscle fibres. *The Journal of Physiology*, *142*(3), 516–543. https://doi.org/10.1113/jphysiol.1958.sp006034

Fatt, P., & Katz, B. (1953). The electrical properties of crustacean muscle fibres. *The Journal of Physiology*, *120*(1–2), 171–204. https://doi.org/10.1113/jphysiol.1953.sp004884

Fenwick, E. M., Marty, A., & Neher, E. (1982). Sodium and calcium channels in bovine chromaffin cells. *The Journal of Physiology*, *331*(1), 599–635. https://doi.org/10.1113/jphysiol.1982.sp014394

Filipchuk, A., Schwenkgrub, J., Destexhe, A., & Bathellier, B. (2022). Awake perception is associated with dedicated neuronal assemblies in the cerebral cortex. *Nature Neuroscience*, *25*(10), 1327–1338. https://doi.org/10.1038/s41593-022-01168-5

Flotte, T., Carter, B., Conrad, C., Guggino, W., Reynolds, T., Rosenstein, B., … Wetzel, R. (1996). A phase I study of an adeno-associated Virus-CFTR gene vector in adult CF patients with mild lung disease. *Human Gene Therapy*, *7*(9), 1145–1159. https://doi.org/10.1089/hum.1996.7.9-1145

Flotte, T. R., Afione, S. A., Conrad, C., McGrath, S. A., Solow, R., Oka, H., … Carter, B. J. (1993). Stable in vivo expression of the cystic fibrosis transmembrane conductance regulator with an adeno-associated virus vector. *Proceedings of the National Academy of Sciences (PNAS)*, *90*(22), 10613–10617. https://doi.org/10.1073/pnas.90.22.10613

Flusberg, B. A., Nimmerjahn, A., Cocker, E. D., Mukamel, E. A., Barretto, R. P. J., Ko, T. H., … Schnitzer, M. J. (2008). High-speed, miniaturized fluorescence microscopy in freely moving mice. *Nature Methods*, *5*(11), 935–938. https://doi.org/10.1038/nmeth.1256

Forbes, H. S. (1928). Cerebral circulation. I. Observation and measure- ment of pial

vessels. *Archives of Neurology & Psychiatry*, *19*(5), 751–761. https://doi.org/10.1001/archneurpsyc.1928.02210110003001

Fox, B. Y. A. P., Nowyckyt, M. C., & Tsient, R. W. (1987). Single-channel recording of three types of calcium channels in chick sensory neurones. *The Journal of Physiology*, *394*(1), 173–200. https://doi.org/10.1113/jphysiol.1987.sp016865

Friedmann, T. (1992). A Brief History of Gene Editing. *Nature Genetics*, *2*(2), 93–98. Retrieved from https://doi.org/10.1038/ng1092-93

Fritsch, G., & Hitzig, E. (1870). Ueber die elektrische Erregbarkeit des Grosshirns. *Epilepsy & Behavior*, *15*(2), 131–132. https://doi.org/10.1016/j.yebeh.2009.03.002

Frostig, R. D., Lieke, E. E., Ts'o, D. Y., & Grinvald, A. (1990). Cortical functional architecture and local coupling between neuronal activity and the microcirculation revealed by in vivo high-resolution optical imaging of intrinsic signals. *Proceedings of the National Academy of Sciences (PNAS)*, *87*(16), 6082–6086. https://doi.org/10.1073/pnas.87.16.6082

Gallo, F. T., Katche, C., Morici, J. F., Medina, J. H., & Weisstaub, N. V. (2018). Immediate early genes, memory and psychiatric disorders: Focus on c-Fos, Egr1 and Arc. *Frontiers in Behavioral Neuroscience*, *12*(79), 1–16. https://doi.org/10.3389/fnbeh.2018.00079

Gao, G.-P., Alvira, M. R., Wang, L., Calcedo, R., Johnston, J., & Wilson, J. M. (2002). Novel adeno-associated viruses from rhesus monkeys. *Proceedings of the National Academy of Sciences (PNAS)*, *99*(18), 11854–11859. Retrieved from https://doi.org/10.1073/pnas.182412299

Garner, A. R., Rowland, D. C., Hwang, S. Y., Baumgaertel, K., Roth, B. L., Kentros, C., & Mayford, M. (2012). Generation of a synthetic memory trace. *Science*, *335*(6075), 1513–1516. https://doi.org/10.1126/science.1214985

Gobbo, F., & Cattaneo, A. (2020). Neuronal Activity at Synapse Resolution: Reporters and Effectors for Synaptic Neuroscience. *Frontiers in Molecular Neuroscience*, *13*(572312), 1–22. https://doi.org/10.3389/fnmol.2020.572312

Gordon, J. W., Scangos, G. A., Plotkin, D. J., Barbosa, J. A., & Ruddle, F. H. (1980). Genetic transformation of mouse embryos by microinjection of purified DNA. *Proceedings of the National Academy of Sciences (PNAS)*, *77*(12), 7380–7384.

https://doi.org/10.1073/pnas.77.12.7380

Gossen, M., Freundlieb, S., Bender, G., Müller, G., Hillen, W., & Bujard, H. (1995). Transcriptional activation by tetracyclines in mammalian cells. *Science*, *268*(5218), 1766–1769. https://doi.org/10.1126/science.7792603

Granado, N., Ortiz, O., Suárez, L. M., Martín, E. D., Ceña, V., Solís, J. M., & Moratalla, R. (2008). D1 but not D5 dopamine receptors are critical for LTP, spatial learning, and LTP-induced arc and zif268 expression in the hippocampus. *Cerebral Cortex*, *18*(1), 1–12. https://doi.org/10.1093/cercor/bhm026

Greenberg, M. E., & Ziff, E. B. (1984). Stimulation of 3T3 cells induces transcription of the c-fos proto-oncogeneo. *Nature*, *311*(5985), 433–438. Retrieved from https://doi.org/10.1038/311433a0

Grienberger, C., & Konnerth, A. (2012). Imaging Calcium in Neurons. *Neuron*, *73*(5), 862–885. https://doi.org/10.1016/j.neuron.2012.02.011

Grinvald, A., Frostig, R. D., Siegel, R. M., & Bartfeld, E. (1991). High-resolution optical imaging of functional brain architecture in the awake monkey. *Proceedings of the National Academy of Sciences (PNAS)*, *88*(24), 11559–11563. https://doi.org/10.1073/pnas.88.24.11559

Grinvald, A., Lieke, E., Frostig, R. D., Gilbert, C. D., & Wiesel, T. N. (1986). Functional architecture of cortex revealed by optical imaging of intrinsic signals. *Nature*, *324*(6095), 361–364. Retrieved from https://doi.org/10.1038/324361a0

Gründemann, J., Bitterman, Y., Lu, T., Krabbe, S., Grewe, B. F., Schnitzer, M. J., & Lüthi, A. (2019). Amygdala ensembles encode behavioral states. *Science*, *364*(6437), 1–9. https://doi.org/10.1126/science.aav8736

Grutzendler, J., Kasthuri, N., & Gan, W.-B. (2002). Long-term dendritic spine stability in the adult cortex. *Nature*, *420*(6917), 812–816. https://doi.org/10.1038/nature01276

Guo, Z. V., Li, N., Huber, D., Ophir, E., Gutnisky, D., Ting, J. T., … Svoboda, K. (2014). Flow of cortical activity underlying a tactile decision in mice. *Neuron*, *81*(1), 179–194. https://doi.org/10.1016/j.neuron.2013.10.020

Guzowski, J. F., McNaughton, B. L., Barnes, C. A., & Worley, P. F. (1999).

Environment-specific expression of the immediate-early gene Arc in hippocampal neuronal ensembles. *Nature Neuroscience*, *2*(12), 1120–1124. Retrieved from https://doi.org/10.1038/16046

Hackett, T. A., Barkat, T. R., O'Brien, B. M. J., Hensch, T. K., & Polley, D. B. (2011). Linking topography to tonotopy in the mouse auditory thalamocortical circuit. *The Journal of Neuroscience*, *31*(8), 2983–2995. https://doi.org/10.1523/JNEUROSCI.5333-10.2011

Haery, L., Deverman, B. E., Matho, K. S., Cetin, A., Woodard, K., Cepko, C., … Fan, M. (2019). Adeno-Associated Virus Technologies and Methods for Targeted Neuronal Manipulation. *Frontiers in Neuroanatomy*, *13*(93), 1–16. https://doi.org/10.3389/fnana.2019.00093

Hagiwara, S., & Takahashi, K. (1967). Surface density of calcium ions and calcium spikes in the barnacle muscle fiber membrane. *The Journal of General Physiology*, *50*(3), 583–601. https://doi.org/10.1085/jgp.50.3.583

He, L., Binari, R., Huang, J., Falo-Sanjuan, J., & Perrimon, N. (2019). In vivo study of gene expression with an enhanced dual-color fluorescent transcriptional timer. *ELife*, *8*(e46181), 1–20. https://doi.org/10.7554/eLife.46181

He, Q., Wang, J., & Hu, H. (2019). Illuminating the Activated Brain: Emerging Activity-Dependent Tools to Capture and Control Functional Neural Circuits. *Neuroscience Bulletin*, *35*(3), 369–377. https://doi.org/10.1007/s12264-018-0291-x

He, T., Itano, M. S., Earley, L. F., Hall, N. E., Riddick, N., Samulski, R. J., & Li, C. (2019). The Influence of Murine Genetic Background in Adeno-Associated Virus Transduction of the Mouse Brain. *Human Gene Therapy Clinical Development*, *30*(4), 169–181. https://doi.org/10.1089/humc.2019.030

Heffner, H. E. (1987). Ferrier and the Study of Auditory Cortex. *Archives of Neurology*, *44*(2), 218–221. https://doi.org/10.1001/archneur.1987.00520140078021

Heim, R., & Tsien, R. Y. (1996). Engineering green fluorescent protein for improved brightness, longer wavelengths and fluorescence resonance energy transfer. *Current Biology*, *6*(2), 178–182. https://doi.org/10.1016/S0960-9822(02)00450-5

Heimstädt, O. (1911). Das Fluoreszenzmikroskop. In *Mikroskopie* (pp. 330–320). Retrieved from

https://www.biodiversitylibrary.org/item/25024#page/380/mode/1up

Heintzman, N. D., Hon, G. C., Hawkins, R. D., Kheradpour, P., Stark, A., Harp, L. F., … Ren, B. (2009). Histone modifications at human enhancers reflect global cell-type-specific gene expression. *Nature*, *459*(7243), 108–112. https://doi.org/10.1038/nature07829

Heinz, S., Romanoski, C. E., Benner, C., Allison, K. A., Kaikkonen, M. U., Orozco, L. D., & Glass, C. K. (2013). Effect of natural genetic variation on enhancer selection and function. *Nature*, *503*(7477), 487–492. https://doi.org/10.1038/nature12615

Helmchen, F., Fee, M. S., Tank, D. W., & Denk, W. (2001). A miniature head-mounted two-photon microscope: High-resolution brain imaging in freely moving animals. *Neuron*, *31*(6), 903–912. https://doi.org/10.1016/S0896-6273(01)00421-4

Henry, K. R., & Chloe, R. A. (1980). Genotypic differences in behavioral, physiological and anatomical expressions of age-related hearing loss in the laboratory mouse: Original papers travaux originaux. *International Journal of Audiology*, *19*(5), 369–383. https://doi.org/10.3109/00206098009070071

Herdegen, T., Leah, J. D., Manisali, A., Bravo, R., & Zimmermann, M. (1991). c-JUN-like immunoreactivity in the CNS of the adult rat: Basal and transynaptically induced expression of an immediate-early gene. *Neuroscience*, *41*(2–3), 643–654. https://doi.org/10.1016/0306-4522(91)90356-S

Hermonat, P. L., & Muzyczka, N. (1984). Use of adeno-associated virus as a mammalian DNA cloning vector: Transduction of neomycin resistance into mammalian tissue culture cells. *Proceedings of the National Academy of Sciences (PNAS)*, *81*(20), 6466–6470. https://doi.org/10.1073/pnas.81.20.6466

Hill, M., & Hillova, J. (1972). Virus recovery in chicken cells tested with rous sarcoma cell DNA. *Nature*, *237*(71), 35–39. https://doi.org/10.1038/239137a0

Hillman, E. M. C. (2007). Optical brain imaging in vivo: techniques and applications from animal to man. *Journal of Biomedical Optics*, *12*(5), 1–49. https://doi.org/10.1117/1.2789693

Hodgkin, A. L., & Huxley, A. F. (1952). A quantitative description of membrane current and its application to conduction and excitation in nerve. *The Journal of Physiology*, *117*(4), 500–544. https://doi.org/10.1113/jphysiol.1952.sp004764

Hoffman, K. L., Battaglia, F. P., Harris, K., Maclean, J. N., Marshall, L., & Mehta, M. R. (2007). The Upshot of Up States in the Neocortex : From Slow Oscillations to Memory Formation. *The Journal of Neuroscience*, *27*(44), 11838–11841. https://doi.org/10.1523/JNEUROSCI.3501-07.2007

Hofstetter, K. M., & Ehret, G. (1992). The auditory cortex of the mouse: Connections of the ultrasonic field. *Journal of Comparative Neurology*, *323*(3), 370–386. https://doi.org/10.1002/cne.903230306

Honma, Y., Tsukano, H., Horie, M., Ohshima, S., Tohmi, M., Kubota, Y., … Shibuki, K. (2013). Auditory Cortical Areas Activated by Slow Frequency-Modulated Sounds in Mice. *PLOS ONE*, *8*(7), 1–12. https://doi.org/10.1371/journal.pone.0068113

Hoz, L. De, Gierej, D., Lioudyno, V., Jaworski, J., Blazejczyk, M., Cruces-solís, H., … Kaczmarek, L. (2018). Blocking c-Fos Expression Reveals the Role of Auditory Cortex Plasticity in Sound Frequency Discrimination Learning. *Cerebral Cortex*, *28*(5), 1645–1655. https://doi.org/10.1093/cercor/bhx060

Hrvatin, S., Hochbaum, D. R., Nagy, M. A., Cicconet, M., Robertson, K., Cheadle, L., … Greenberg, M. E. (2018). Single-cell analysis of experience-dependent transcriptomic states in the mouse visual cortex. *Nature Neuroscience*, *21*(1), 120–129. Retrieved from https://doi.org/10.1038/s41593-017-0029-5

Hu, P., Fabyanic, E., Kwon, D. Y., Tang, S., Zhou, Z., & Wu, H. (2017). Dissecting Cell-Type Composition and Activity-Dependent Transcriptional State in Mammalian Brains by Massively Parallel Single-Nucleus RNA-Seq. *Molecular Cell*, *68*(5), 1006–1015. https://doi.org/10.1016/j.molcel.2017.11.017

Huang, L., Ledochowitsch, P., Knoblich, U., Lecoq, J., Murphy, G. J., Reid, R. C., … Li, L. (2021). Relationship between simultaneously recorded spiking activity and fluorescence signal in gcamp6 transgenic mice. *ELife*, *10*(e51675), 1–19. https://doi.org/10.7554/eLife.51675

Hudson, A. E. (2018). Chapter 12 - Genetic Reporters of Neuronal Activity: c-Fos and G-CaMP6. In *Methods in Enzymology* (Vol. 603, pp. 197–220). https://doi.org/10.1016/bs.mie.2018.01.023

Huisinga, K. L., Brower-toland, B., & Elgin, S. C. R. (2006). The contradictory definitions of heterochromatin : transcription and silencing. *Chromosoma*, *115*(2),

110–122. https://doi.org/10.1007/s00412-006-0052-x

Iman, I. N., Yusof, N. A. M., Talib, U. N., Ahmad, N. A. Z., Norazit, A., Kumar, J., … Muzaimi, M. (2021). The IntelliCage System : A Review of Its Utility as a Novel Behavioral Platform for a Rodent Model of Substance Use Disorder. *Frontiers in Behavioral Neuroscience*, *15*(683780), 1–13. https://doi.org/10.3389/fnbeh.2021.683780

Inoue, F., Kircher, M., Martin, B., Cooper, G. M., Witten, D. M., McManus, M. T., … Shendure, J. (2017). A systematic comparison reveals substantial differences in chromosomal versus episomal encoding of enhancer activity. *Genome Research*, *27*(1), 38–52. https://doi.org/10.1101/gr.212092.116

Inoue, M. (2021). Genetically encoded calcium indicators to probe complex brain circuit dynamics in vivo. *Neuroscience Research*, *169*, 2–8. https://doi.org/10.1016/j.neures.2020.05.013

Issa, J. B., Haeffele, B. D., Agarwal, A., Bergles, D. E., Young, E. D., & Yue, D. T. (2014). Multiscale Optical Ca2+ Imaging of Tonal Organization in Mouse Auditory Cortex. *Neuron*, *83*(4), 944–959. https://doi.org/10.1016/j.neuron.2014.07.009

Issa, S. S., Shaimardanova, A. A., Solovyeva, V. V, & Rizvanov, A. A. (2023). Various AAV Serotypes and Their Applications in Gene Therapy: An Overview. *Cells*, *12*(5), 1–41. https://doi.org/10.3390/cells12050785

Ivashkina, O. I., Gruzdeva, A. M., Roshchina, M. A., Toropova, K. A., & Anokhin, K. V. (2021). Imaging of C-fos Activity in Neurons of the Mouse Parietal Association Cortex during Acquisition and Retrieval of Associative Fear Memory. *International Journal of Molecular Sciences*, *22*(15), 1–14. https://doi.org/10.3390/ijms22158244

Jaenisch, R. (1976). Germ line integration and Mendelian transmission of the exogenous Moloney leukemia virus. *Proceedings of the National Academy of Sciences (PNAS)*, *73*(4), 1260–1264. https://doi.org/10.1073/pnas.73.4.1260

Ji, D., & Wilson, M. A. (2007). Coordinated memory replay in the visual cortex and hippocampus during sleep. *Nature Neuroscience*, *10*(1), 100–107. https://doi.org/10.1038/nn1825

Johnson, K. R., Erway, L. C., Cook, S. A., Willott, J. F., & Zheng, Q. Y. (1997). A major

gene affecting age-related hearing loss in C57BL/6J mice. *Hearing Research*, *114*(1–2), 83–92. https://doi.org/10.1016/S0378-5955(97)00155-X

Jones, S. M., Jones, T. A., Johnson, K. R., Yu, H., Erway, L. C., & Zheng, Q. Y. (2006). A comparison of vestibular and auditory phenotypes in inbred mouse strains. *Brain Research*, *1091*(1), 40–46. https://doi.org/10.1016/j.brainres.2006.01.066

Josselyn, S. A., & Tonegawa, S. (2020). Memory engrams: Recalling the past and imagining the future. *Science*, *367*(6473), 1–14. https://doi.org/10.1126/science.aaw4325

Jurado, J., Fuentes-Almagro, C. A., Prieto-Álamo, M. J., & Pueyo, C. (2007). Alternative splicing of c-fos pre-mRNA: Contribution of the rates of synthesis and degradation to the copy number of each transcript isoform and detection of a truncated c-Fos immunoreactive species. *BMC Molecular Biology*, *8*(83), 1–14. https://doi.org/10.1186/1471-2199-8-83

Kanold, P. O., Nelken, I., & Polley, D. B. (2014). Local versus global scales of organization in auditory cortex. *Trends in Neurosciences*, *37*(9), 502–510. https://doi.org/10.1016/j.tins.2014.06.003

Kantor, B., Bailey, R. M., Wimberly, K., Kalburgi, S. N., & Gray, S. J. (2014). Chapter 3 - Methods for gene transfer to the central nervous system. In *Advances in Genetics* (Vol. 87, pp. 125–197). Elsevier. https://doi.org/10.1016/B978-0-12-800149-3.00003-2

Kaplitt, M. G., Leone, P., Samulski, R. J., Xiao, X., Pfaff, D. W., O'Malley, K. L., & During, M. J. (1994). Long-term gene expression and phenotypic correction using adeno-associated virus vectors in mammalian brain. *Nature Genetics*, *8*(2), 148–154. Retrieved from https://doi.org/10.1038/ng1094-148

Karabeg, M. M., Grauthoff, S., Kollert, S. Y., Weidner, M., Heiming, R. S., Jansen, F., … Lewejohann, L. (2013). 5-HTT Deficiency Affects Neuroplasticity and Increases Stress Sensitivity Resulting in Altered Spatial Learning Performance in the Morris Water Maze but Not in the Barnes Maze. *PLOS ONE*, *8*(10), 1–19. https://doi.org/10.1371/journal.pone.0078238

Katz, B., & Miledi, R. (1967). A study of synaptic transmission in the absence of nerve impulses. *The Journal of Physiology*, *192*(2), 407–436.

https://doi.org/10.1113/jphysiol.1967.sp008307

Kawashima, T., Okuno, H., & Bito, H. (2014). A new era for functional labeling of neurons: Activity-dependent promoters have come of age. *Frontiers in Neural Circuits*, *8*(37), 1–9. https://doi.org/10.3389/fncir.2014.00037

Keifer, J., & Summers, C. H. (2016). Putting the "biology" back into "neurobiology": The strength of diversity in animal model systems for neuroscience research. *Frontiers in Systems Neuroscience*, *10*(69), 1–9. https://doi.org/10.3389/fnsys.2016.00069

Kelly, K., Cochran, B. H., Stiles, C. D., & Leder, P. (1983). Cell-specific regulation of the c-myc gene by lymphocyte mitogens and platelet-derived growth factor. *Cell*, *35*(3), 603–610. https://doi.org/10.1016/0092-8674(83)90092-2

Kendall, A., & Schacht, J. (2014). Disparities in auditory physiology and pathology between C57BL/6J and C57BL/6N substrains. *Hearing Research*, *318*, 18–22. https://doi.org/10.1016/j.heares.2014.10.005

Khalaf, O., Resch, S., Dixsaut, L., Gorden, V., Glauser, L., & Gräff, J. (2018). Reactivation of recall-induced neurons contributes to remote fear memory attenuation. *Science*, *360*(6394), 1239–1242. https://doi.org/10.1126/science.aas9875

Kim, G. H., Kosterin, P., Obaid, A. L., & Salzberg, B. M. (2007). A mechanical spike accompanies the action potential in mammalian nerve terminals. *Biophysical Journal*, *92*(9), 3122–3129. https://doi.org/10.1529/biophysj.106.103754

Kim, T. H., Zhang, Y., Lecoq, J., Jung, J. C., Li, J., Zeng, H., … Schnitzer, M. J. (2016). Long-Term optical access to an estimated one million neurons in the live mouse cortex. *Cell Reports*, *17*(12), 3385–3394. https://doi.org/10.1016/j.celrep.2016.12.004

Kim, T. K., Hemberg, M., Gray, J. M., Costa, A. M., Bear, D. M., Wu, J., … Greenberg, M. E. (2010). Widespread transcription at neuronal activity-regulated enhancers. *Nature*, *465*(7295), 182–187. https://doi.org/10.1038/nature09033

Kleim, J. A., Lussnig, E., Schwarz, E. R., Comery, T. A., & Greenough, W. T. (1996). Synaptogenesis and FOS expression in the motor cortex of the adult rat after motor skill learning. *The Journal of Neuroscience*, *16*(14), 4529–4535. https://doi.org/10.1523/jneurosci.16-14-04529.1996

Koldamova, R., Schug, J., Lefterova, M., Cronican, A. A., Fitz, N. F., Davenport, F. A., … Lefterov, I. (2014). Genome-wide approaches reveal EGR1-controlled regulatory networks associated with neurodegeneration Radosveta. *Neurobiology of Disease*, *63*, 107–114. https://doi.org/10.1016/j.nbd.2013.11.005

Korb, E., & Finkbeiner, S. (2011). Arc in synaptic plasticity: From gene to behavior. *Trends in Neurosciences*, *34*(11), 591–598. https://doi.org/10.1016/j.tins.2011.08.007

Kovács, K. J. (2008). Measurement of immediate-early gene activation- c-fos and beyond. *Journal of Neuroendocrinology*, *20*(6), 665–672. https://doi.org/10.1111/j.1365-2826.2008.01734.x

Kruijer, W., Cooper, J. A., Hunter, T., & Verma, I. M. (1984). Platelet-derived growth factor induces rapid but transient expression of the c-fos gene and protein. *Nature*, *312*(5996), 711–716. https://doi.org/10.1038/312711a0

Kuchibhotla, K., & Bathellier, B. (2018). Neural encoding of sensory and behavioral complexity in the auditory cortex. *Current Opinion in Neurobiology*, *52*, 65–71. https://doi.org/10.1016/j.conb.2018.04.002

Kügler, S., Kilic, E., & Bähr, M. (2003). Human synapsin 1 gene promoter confers highly neuron-specific long-term transgene expression from an adenoviral vector in the adult rat brain depending on the transduced area. *Gene Therapy*, *10*(4), 337–347. https://doi.org/10.1038/sj.gt.3301905

Lacar, B., Linker, S. B., Jaeger, B. N., Krishnaswami, S., Barron, J., Kelder, M., … Gage, F. H. (2016). Nuclear RNA-seq of single neurons reveals molecular signatures of activation. *Nature Communications*, *7*(11022), 1–11. https://doi.org/10.1038/ncomms11022

Lamothe-Molina, P. J., Franzelin, A., Beck, L., Li, D., Auksutat, L., Fieblinger, T., … Oertner, T. G. (2020). cFos ensembles in the dentate gyrus rapidly segregate over time and do not form a stable map of space. *BioRxiv*. https://doi.org/10.1101/2020.08.29.273391

Lane, N. (2015). The unseen World: Reflections on Leeuwenhoek (1677) “Concerning little animals.” *Philosophical Transactions of the Royal Society B: Biological Sciences*, *370*(1666), 1–10. https://doi.org/10.1098/rstb.2014.0344

Lau, L. F., & Nathans, D. (1985). Identification of a set of genes expressed during the G0/G1 transition of cultured mouse cells. *The EMBO Journal*, *4*(12), 3145–3151. https://doi.org/10.1002/j.1460-2075.1985.tb04057.x

Leal, G., Comprido, D., & Duarte, C. B. (2014). BDNF-induced local protein synthesis and synaptic plasticity. *Neuropharmacology*, *76*(Part C), 639–656. https://doi.org/10.1016/j.neuropharm.2013.04.005

Lee, C. R., Najafizadeh, L., & Margolis, D. J. (2020). Investigating learning-related neural circuitry with chronic in vivo optical imaging. *Brain Structure and Function*, *225*(2), 467–480. https://doi.org/10.1007/s00429-019-02001-9

Lee, H., & Kaang, B.-K. (2023). How engram mediates learning, extinction, and relapse. *Current Opinion in Neurobiology*, *81*(102723), 1–7. https://doi.org/10.1016/j.conb.2023.102723

Lee, K. S., & Tsien, R. W. (1983). Mechanism of calcium channel blockade by verapamil, D600, diltiazem and nitrendipine in single dialysed heart cells. *Nature*, *302*(5911), 790–794. https://doi.org/10.1038/302790a0

Leslie, J. H., & Nedivi, E. (2011). Activity-regulated genes as mediators of neural circuit plasticity. *Progress in Neurobiology*, *94*(3), 223–237. https://doi.org/10.1016/j.pneurobio.2011.05.002

Levasseur, J. E., Wei, E. P., Raper, J. A., Kontos, H. A., & Patterson, J. L. (1975). Detailed description of a cranial window technique for acute and chronic experiments. *Stroke*, *6*(3), 308–317. https://doi.org/10.1161/01.STR.6.3.308

Lin, M. Z., & Schnitzer, M. J. (2016). Genetically encoded indicators of neuronal activity. *Nature Neuroscience*, *19*(9), 1142–1153. https://doi.org/10.1038/nn.4359

Lisowski, L., Tay, S. S., & Alexander, I. E. (2015). Adeno-associated virus serotypes for gene therapeutics. *Current Opinion in Pharmacology*, *24*, 59–67. https://doi.org/10.1016/j.coph.2015.07.006

Liu, P., Yuan, J., Feng, Y., Chen, X., Wang, G., & Zhao, L. (2021). Ferroptosis contributes to isoflurane-induced neurotoxicity and learning and memory impairment. *Cell Death Discovery*, *7*(1). https://doi.org/10.1038/s41420-021-00454-8

Liu, X., Ramirez, S., Pang, P. T., Puryear, C. B., Govindarajan, A., Deisseroth, K., & Tonegawa, S. (2012). Optogenetic stimulation of a hippocampal engram activates fear memory recall. *Nature*, *484*(7394), 381–385. https://doi.org/10.1038/nature11028

Loewi, von O. (1921). Ueber humorale Uebertragbarkeit der Herznervenwirkung. *Pflüger's Archiv Für Die Gesamte Physiologie Des Menschen Und Der Tiere*, *189*, 239–242. Retrieved from https://doi.org/10.1007/BF01722757

Long, H. K., Prescott, S. L., & Wysocka, J. (2016). Ever-Changing Landscapes: Transcriptional Enhancers in Development and Evolution. *Cell*, *167*(5), 1170–1187. https://doi.org/10.1016/j.cell.2016.09.018

Luczak, A., Barthó, P., & Harris, K. D. (2009). Spontaneous events outline the realm of possible sensory responses in neocortical populations. *Neuron*, *62*(3), 413–425. https://doi.org/10.1016/j.neuron.2009.03.014

Maddox, S. A., Monsey, M. S., & Schafe, G. E. (2011). Early growth response gene 1 (Egr-1) is required for new and reactivated fear memories in the lateral amygdala. *Learning and Memory*, *18*(1), 24–38. https://doi.org/10.1101/lm.1980211

Magrassi, L., Leto, K., & Rossi, F. (2013). Lifespan of neurons is uncoupled from organismal lifespan. *Proceedings of the National Academy of Sciences (PNAS)*, *110*(11), 4374–4379. https://doi.org/10.1073/pnas.1217505110

Mahringer, D., Petersen, A. V., Fiser, A., Okuno, H., Bito, H., Perrier, J. F., & Keller, G. B. (2019). Expression of c-Fos and Arc in hippocampal region CA1 marks neurons that exhibit learning-related activity changes. *BioRxiv*. Retrieved from https://doi.org/10.1101/644526

Mahringer, D., Zmarz, P., Okuno, H., Bito, H., & Keller, G. B. (2022). Functional correlates of immediate early gene expression in mouse visual cortex. *Peer Community Journal*, *2*(e45). Retrieved from https://doi.org/10.24072/pcjournal.156

Malik, A. N., Vierbuchen, T., Hemberg, M., Rubin, A. A., Ling, E., Couch, C. H., … Greenberg, M. E. (2014). Genome-wide identification and characterization of functional neuronal activity-dependent enhancers. *Nature Neuroscience*, *17*(10), 1330–1339. https://doi.org/10.1038/nn.3808

Managò, F., Mereu, M., Mastwal, S., Mastrogiacomo, R., Scheggia, D., Emanuele, M., … Papaleo, F. (2016). Genetic Disruption of Arc/Arg3.1 in Mice Causes Alterations in Dopamine and Neurobehavioral Phenotypes Related to Schizophrenia. *Cell Reports*, *16*(8), 2116–2128. https://doi.org/10.1016/j.celrep.2016.07.044

Mank, M., Santos, A. F., Direnberger, S., Mrsic-Flogel, T. D., Hofer, S. B., Stein, V., … Griesbeck, O. (2008). A genetically encoded calcium indicator for chronic in vivo two-photon imaging. *Nature Methods*, *5*(9), 805–811. https://doi.org/10.1038/nmeth.1243

Mansouri, C., & Kashou, N. H. (2012). Chapter 11 - New Window on Optical Brain Imaging; Medical Development, Simulations and Applications. In *Selected topics on optical fiber technology* (pp. 271–284). https://doi.org/10.5772/30609

Masset, P., Qin, S., & Zavatone-Veth, J. A. (2022). Drifting neuronal representations: Bug or feature? *Biological Cybernetics*, *116*(3), 253–266. https://doi.org/10.1007/s00422-021-00916-3

Mastwal, S., Cao, V., & Wang, K. H. (2016). Genetic feedback regulation of frontal cortical neuronal ensembles through activity-dependent arc expression and dopaminergic input. *Frontiers in Neural Circuits*, *10*(100), 1–10. https://doi.org/10.3389/fncir.2016.00100

Matsuda, S., Peng, H., Yoshimura, H., Wen, T. C., Fukuda, T., & Sakanaka, M. (1996). Persistent c-fos expression in the brains of mice with chronic social stress. *Neuroscience Research*, *26*(2), 157–170. https://doi.org/10.1016/S0168-0102(96)01088-7

Mckay, S., Bromhaar, M. M. G., Jongste, J. C. De, & Hoogsteden, H. C. (2001). Pro-inflammatory cytokines induce c-fos expression followed by IL-6 release in human airway smooth muscle cells. *Mediators of Inflammation*, *10*(3), 135–142. https://doi.org/10.1080/09629350120072707

Meenakshi, P., Kumar, S., & Balaji, J. (2021). In vivo imaging of immediate early gene expression dynamics segregates neuronal ensemble of memories of dual events. *Molecular Brain*, *14*(1), 1–19. https://doi.org/10.1186/s13041-021-00798-3

Mietzsch, M., Eddington, C., Jose, A., Hsi, J., Chipman, P., Henley, T., … Agbandje-

McKenna, M. (2021). Improved Genome Packaging Efficiency of Adeno-associated Virus Vectors Using Rep Hybrids. *Journal of Virology*, *95*(19), 1–19. https://doi.org/10.1128/jvi.00773-21

Minatohara, K., Akiyoshi, M., & Okuno, H. (2016). Role of immediate-early genes in synaptic plasticity and neuronal ensembles underlying the memory trace. *Frontiers in Molecular Neuroscience*, *8*(78), 1–11. https://doi.org/10.3389/fnmol.2015.00078

Minsky, M. (1988). Memoir on Inventing the Confocal Scanning Microscope. *Scanning*, *10*(4), 128–138.

Miyawaki, A., Llopis, J., Heim, R., Michael McCaffery, J., Adams, J. A., Ikura, M., & Tsien, R. Y. (1997). Fluorescent indicators for Ca2+ based on green fluorescent proteins and calmodulin. *Nature*, *388*(6645), 882–887. https://doi.org/10.1038/42264

Moisescu, D. G., Ashley, C. C., & Campbell, A. K. (1975). Comparative aspects of the calcium-sensitive photoproteins aequorin and obelin. *Biochimica e Biophysica Acta - Bioenergetics*, *396*(1), 133–140. https://doi.org/10.1016/0005-2728(75)90196-6

Morgan, J. I., Cohen, D. R., Hempstead, J. L., & Curran, T. (1987). Mapping patterns of c-fos expression in the central nervous system after seizure. *Science*, *237*(4811), 192–197. https://doi.org/10.1126/science.3037702

Mori, M., Konno, T., Ozawa, T., Murata, M., Imoto, K., & Nagayama, K. (2000). Novel interaction of the voltage-dependent sodium channel (VDSC) with calmodulin: Does VDSC acquire calmodulin-mediated Ca2+-sensitivity? *Biochemistry*, *39*(6), 1316–1323. https://doi.org/10.1021/bi9912600

Mostany, R., Miquelajauregui, A., Shtrahman, M., & Portera-Cailliau, C. (2015). Chapter 2 - Two-photon excitation micrsocopy and its applications in neuroscience. In *Advanced Fluorescence Microscopy* (Vol. 1251, pp. 25–42). https://doi.org/10.1007/978-1-4939-2080-8_7

Nakai, J., Ohkura, M., & Imoto, K. (2001). A high signal-to-noise Ca2+ probe composed of a single green fluorescent protein. *Nature Biotechnology*, *19*(2), 137–141. https://doi.org/10.1038/84397

Nambu, M. F., Lin, Y. J., Reuschenbach, J., & Tanaka, K. Z. (2022). What does engram encode?: Heterogeneous memory engrams for different aspects of experience. *Current Opinion in Neurobiology*, *75*(102568), 1–9. https://doi.org/10.1016/j.conb.2022.102568

Nectow, A. R., & Nestler, E. J. (2020). Viral tools for neuroscience. *Nature Reviews Neuroscience*, *21*(12), 669–681. https://doi.org/10.1038/s41583-020-00382-z

Nelken, I., Bizley, J. K., Nodal, F. R., Ahmed, B., Schnupp, J. W. H., & King, A. J. (2004). Large-scale organization of ferret auditory cortex revealed using continuous acquisition of intrinsic optical signals. *Journal of Neurophysiology*, *92*(4), 2574–2588. https://doi.org/10.1152/jn.00276.2004

Newton, I. (1704). *Opticks, Or, A treatise of the reflexions, refractions, inflexions and colours of light*. Retrieved from https://books.google.de/books?hl=de&lr=&id=bSiTKcLf07UC&oi=fnd&pg=PP1&dq=Opticks

Noguchi, K., Dubner, R., & Ruda, M. A. (1992). Preproenkephalin mRNA in spinal dorsal horn neurons is induced by peripheral inflammation and is co-locolized with Fos and Fos-related proteins. *Neuroscience*, *46*(3), 561–570. https://doi.org/10.1016/0306-4522(92)90144-q

Nowycky, M. C., Fox, A. P., & Tsien, R. W. (1985). Three types of neuronal calcium channel with different calcium agonist sensitivity. *Nature*, *316*(6027), 440–443. https://doi.org/10.1038/316440a0

Nsiangani, A., Del Rosario, J., Yeh, A. C., Shin, D., Wells, S., Lev-Ari, T., … Haider, B. (2022). Optimizing intact skull intrinsic signal imaging for subsequent targeted electrophysiology across mouse visual cortex. *Scientific Reports*, *12*(1), 1–15. https://doi.org/10.1038/s41598-022-05932-2

Ogawa, S., Lee, T. -M, Nayak, A. S., & Glynn, P. (1990). Oxygenation-sensitive contrast in magnetic resonance image of rodent brain at high magnetic fields. *Magnetic Resonance in Medicine*, *14*(1), 68–78. https://doi.org/10.1002/mrm.1910140108

Ohlemiller, K. K., Jones, S. M., & Johnson, K. R. (2016). Application of Mouse Models to Research in Hearing and Balance. *Journal of the Association for Research in*

Otolaryngology, *17*(6), 493–523. https://doi.org/10.1007/s10162-016-0589-1

Okuno, H. (2011). Regulation and function of immediate-early genes in the brain: Beyond neuronal activity markers. *Neuroscience Research*, *69*(3), 175–186. https://doi.org/10.1016/j.neures.2010.12.007

Omer, D. B., Fekete, T., Ulchin, Y., Hildesheim, R., & Grinvald, A. (2019). Dynamic patterns of spontaneous ongoing activity in the visual cortex of anesthetized and awake monkeys are different. *Cerebral Cortex*, *29*(3), 1291–1304. https://doi.org/10.1093/cercor/bhy099

Oviedo, H. V., Bureau, I., Svoboda, K., & Zador, A. M. (2010). The functional asymmetry of auditory cortex is reflected in the organization of local cortical circuits. *Nature Neuroscience*, *13*(11), 1413–1420. https://doi.org/10.1038/nn.2659

Panja, D., & Bramham, C. R. (2014). BDNF mechanisms in late LTP formation: A synthesis and breakdown. *Neuropharmacology*, *76*, 664–676. https://doi.org/10.1016/j.neuropharm.2013.06.024

Papaioannou, S., & Medini, P. (2022). Advantages, Pitfalls, and Developments of All Optical Interrogation Strategies of Microcircuits in vivo. *Frontiers in Neuroscience*, *16*(859803), 1–17. https://doi.org/10.3389/fnins.2022.859803

Pastuzyn, E. D., Day, C. E., Kearns, R. B., Kyrke-Smith, M., Taibi, A. V., McCormick, J., … Shepherd, J. D. (2018). The Neuronal Gene Arc Encodes a Repurposed Retrotransposon Gag Protein that Mediates Intercellular RNA Transfer. *Cell*, *172*(1–2), 275–288. https://doi.org/10.1016/j.cell.2017.12.024

Pauling, L., & Coryell, C. D. (1936). The Magnetic Properties and Structure of Hemoglobin, Oxyhemoglobin and Carbonmonoxyhemoglobin. *Proceedings of the National Academy of Sciences (PNAS)*, *22*(4), 210–216. https://doi.org/10.1073/pnas.22.4.210

Paxinos, G., & Franklin, K. B. J. (2001). *The Mouse Brain in Stereotaxic Coordinates (second edition)*. *Academic Press*. Retrieved from https://books.google.de/books/about/The_Mouse_Brain_in_Stereotaxic_Coordinat.html?id=tZdjQgAACAAJ&redir_esc=y

Pearce, J. M. S. (2009). Marie-Jean-Pierre Flourens (1794-1867) and cortical

localization. *European Neurology*, *61*(5), 311–314. https://doi.org/10.1159/000206858

Pereda, A. E. (2014). Electrical synapses and their functional interactions with chemical synapses. *Nature Reviews Neuroscience*, *15*(4), 250–263. https://doi.org/10.1038/nrn3708

Pérez Koldenkova, V., & Nagai, T. (2013). Genetically encoded Ca2+ indicators: Properties and evaluation. *Biochimica et Biophysica Acta - Molecular Cell Research*, *1833*(7), 1787–1797. https://doi.org/10.1016/j.bbamcr.2013.01.011

Peter, M., Scheuch, H., Burkard, T. R., Tinter, J., Wernle, T., & Rumpel, S. (2012). Induction of immediate early genes in the mouse auditory cortex after auditory cued fear conditioning to complex sounds. *Genes, Brain and Behavior*, *11*(3), 314–324. https://doi.org/10.1111/j.1601-183X.2011.00761.x

Peter, Manuel, Aschauer, D. F., Rose, R., Sinning, A., Grössl, F., Kargl, D., … Rumpel, S. (2021). Rapid nucleus-scale reorganization of chromatin in neurons enables transcriptional adaptation for memory consolidation. *PLOS ONE*, *16*(5), 1–35. https://doi.org/10.1371/JOURNAL.PONE.0244038

Pettit, N. L., Yap, E., Greenberg, M. E., & Harvey, C. D. (2022). Fos ensembles encode and shape stable spatial maps in the hippocampus. *Nature*, *609*(7926), 327–334. https://doi.org/10.1038/s41586-022-05113-1

Pfeiffer, B. E. (2020). The content of hippocampal " replay ." *Hippocampus*, *30*(1), 6–18. https://doi.org/10.1002/hipo.22824

Piccolino, M. (1997). Luigi Galvani and animal electricity: Two centuries after the foundation of electrophysiology. *Trends in Neurosciences*, *20*(10), 443–448. https://doi.org/10.1016/S0166-2236(97)01101-6

Poll, S., Mittag, M., Musacchio, F., Justus, L. C., Giovannetti, E. A., Steffen, J., … Fuhrmann, M. (2020). Memory trace interference impairs recall in a mouse model of Alzheimer's disease. *Nature Neuroscience*, *23*(8), 952–958. https://doi.org/10.1038/s41593-020-0652-4

Prakash, N., Uhlemann, F., Sheth, S. A., Bookheimer, S., Martin, N., & Toga, A. W. (2009). Current trends in intraoperative optical imaging for functional brain mapping and delineation of lesions of language cortex. *NeuroImage*,

47(Supplement 2), T116–T126. https://doi.org/10.1016/j.neuroimage.2008.07.066

Qi, Y., Yu, T., Xu, J., Wan, P., Ma, Y., Zhu, J., … Zhu, D. (2019). FDISCO: Advanced solvent-based clearing method for imaging whole organs. *Science Advances*, *5*(1), 1–13. https://doi.org/10.1126/sciadv.aau8355

Ramirez, S., Liu, X., Lin, P. A., Suh, J., Pignatelli, M., Redondo, R. L., … Tonegawa, S. (2013). Creating a false memory in the hippocampus. *Science*, *341*(6144), 387–391. https://doi.org/10.1126/science.1239073

Redolfi, N., García-Casas, P., Fornetto, C., Sonda, S., Pizzo, P., & Pendin, D. (2021). Lighting up ca2+ dynamics in animal models. *Cells*, *10*(8), 1–18. https://doi.org/10.3390/cells10082133

Reijmers, L. G., Perkins, B. L., Matsuo, N., & Mayford, M. (2007). Localization of a stable neural correlate of associative memory. *Science*, *317*(5842), 1230–1233. https://doi.org/10.1126/science.1143839

Reijmers, L., & Mayford, M. (2009). Genetic control of active neural circuits. *Frontiers in Molecular Neuroscience*, *2*(27), 1–8. https://doi.org/10.3389/neuro.02.027.2009

Reimsnider, S., Manfredsson, F. P., Muzyczka, N., & Mandel, R. J. (2007). Time course of transgene expression after intrastriatal pseudotyped rAAV2/1, rAAV2/2, rAAV2/5, and rAAV2/8 transduction in the rat. *Molecular Therapy*, *15*(8), 1504–1511. https://doi.org/10.1038/sj.mt.6300227

Reuter, H. (1967). The dependence of slow inward current in Purkinje fibres of the extracellular calcium-concentration. *The Journal of Physiology*, *192*(2), 479–492. https://doi.org/10.1113/jphysiol.1967.sp008310

Ricard, C., Arroyo, E. D., He, C. X., Portera-Cailliau, C., Lepousez, G., Canepari, M., & Fiole, D. (2018). Two-photon probes for in vivo multicolor microscopy of the structure and signals of brain cells. *Brain Structure and Function*, *223*(7), 3011–3043. https://doi.org/doi:10.1007/s00429-018-1678-1

Ringer, S. (1883). A further Contribution regarding the influence of the different Constituents of the Blood on the Contraction of the Heart. *The Journal of Physiology*, *4*(1), 29–42. https://doi.org/10.1113/jphysiol.1883.sp000120

Robbins, M., Christensen, C. N., Kaminski, C. F., & Zlatic, M. (2021). Calcium imaging analysis - how far have we come? *F1000Research*, *10*(258), 1–9. https://doi.org/10.12688/F1000RESEARCH.51755.1

Romoser, V. A., Hinkle, P. M., & Persechini, A. (1997). Detection in living cells of Ca2+-dependent changes in the fluorescence emission of an indicator composed of two green fluorescent protein variants linked by a calmodulin-binding sequence. *Journal of Biological Chemistry*, *272*(20), 13270–13274. https://doi.org/10.1074/jbc.272.20.13270

Rose, T., Jaepel, J., Hübener, M., & Bonhoeffer, T. (2016). Cell-specific restoration of stimulus preference after monocular deprivation in the visual cortex. *Science*, *352*(6291), 1319–1322. https://doi.org/10.1126/science.aad3358

Roth, R. H., & Ding, J. B. (2020). From Neurons to Cognition: Technologies for Precise Recording of Neural Activity Underlying Behavior. *BME Frontiers*, *2020*(7190517), 1–20. https://doi.org/10.34133/2020/7190517

Rothschild, G., Nelken, I., & Mizrahi, A. (2010). Functional organization and population dynamics in the mouse primary auditory cortex. *Nature Neuroscience*, *13*(3), 353–360. https://doi.org/10.1038/nn.2484

Rotschafer, S., & Razak, K. (2013). Altered auditory processing in a mouse model of fragile X syndrome. *Brain Research*, *1506*, 12–24. https://doi.org/10.1016/j.brainres.2013.02.038

Roy, C. S., & Sherrington, C. S. (1890). On the Regulation of the Blood-supply of the Brain. *The Journal of Physiology*, *11*(1–2), 85–158. https://doi.org/10.1113/jphysiol.1890.sp000321

Roy, D. S., Park, Y. G., Kim, M. E., Zhang, Y., Ogawa, S. K., DiNapoli, N., … Tonegawa, S. (2022). Brain-wide mapping reveals that engrams for a single memory are distributed across multiple brain regions. *Nature Communications*, *13*(1), 1–16. https://doi.org/10.1038/s41467-022-29384-4

Rule, M. E., O'Leary, T., & Harvey, C. D. (2019). Causes and consequences of representational drift. *Current Opinion in Neurobiology*, *58*, 141–147. https://doi.org/10.1016/j.conb.2019.08.005

Russell, J. T. (2010). Imaging calcium signals in vivo: a powerful tool in physiology and

pharmacology. *British Journal of Pharmacology*, *163*(8), 1605–1625. https://doi.org/10.1111/j.1476-5381.2010.00988.x

Saab, B. J., MacLean, A. J. B., Kanisek, M., Zurek, A. A., Martin, L. J., Roder, J. C., & Orser, B. A. (2010). Short-term memory impairment after isoflurane in mice is prevented by the α5 γ-aminobutyric acid type a receptor inverse agonist L-655,708. *Anesthesiology*, *113*(5), 1061–1071. https://doi.org/10.1097/ALN.0b013e3181f56228

Sabharwal, Y. S., Rouse, A. R., Donaldson, L., Hopkins, M. F., & Gmitro, A. F. (1999). Slit-scanning confocal microendoscope for high-resolution in vivo imaging. *Applied Optics*, *38*(34), 7133. https://doi.org/10.1364/ao.38.007133

Saffen, D. W., Cole, A. J., Worley, P. F., Christy, B. A., Ryder, K., & Baraban, J. M. (1988). Convulsant-induced increase in transcription factor messenger RNAs in rat brain. *Proceedings of the National Academy of Sciences (PNAS)*, *85*(20), 7795–7799. https://doi.org/10.1073/pnas.85.20.7795

Sakata, S., & Harris, K. D. (2009). Laminar Structure of Spontaneous and Sensory-Evoked Population Activity in Auditory Cortex. *Neuron*, *64*(3), 404–418. https://doi.org/10.1016/j.neuron.2009.09.020

Sakmann, B., & Neher, E. (1984). Patch clamp techniques for studying ionic channels in excitable membranes. *Annual Review of Physiology*, *46*, 455–472. https://doi.org/10.1146/annurev.ph.46.030184.002323

Salzberg, B. M., Obaid, A. L., & Gainer, H. (1985). Large and rapid changes in light scattering accompany secretion by nerve terminals in the mammalian neurohypophysis. *The Journal of General Physiology*, *86*(3), 395–411. https://doi.org/10.1085/jgp.86.3.395

Sambrook, J., Westphal, H., Srinivasan, P. R., & Dulbecco, R. (1968). The integrated state of viral DNA in SV40-transformed cells. *Proceedings of the National Academy of Sciences (PNAS)*, *60*(4), 1288–1295. https://doi.org/10.1073/pnas.60.4.1288

Samulski, R. J., Berns, K. I., Tan, M., & Muzyczka, N. (1982). Cloning of adeno-associated virus into pBR322: Rescue of intact virus from the recombinant plasmid in human cells. *Proceedings of the National Academy of Sciences (PNAS)*, *79*(6),

2077–2081. https://doi.org/10.1073/pnas.79.6.2077

Sato, K., Nariai, T., Momose-Sato, Y., & Kamino, K. (2016). Intraoperative intrinsic optical imaging of human somatosensory cortex during neurosurgical operations. *Neurophotonics*, *4*(3), 031205. https://doi.org/10.1117/1.nph.4.3.031205

Sawatari, H., Tanaka, Y., Takemoto, M., Nishimura, M., Hasegawa, K., Saitoh, K., & Song, W. J. (2011). Identification and characterization of an insular auditory field in mice. *European Journal of Neuroscience*, *34*(12), 1944–1952. https://doi.org/10.1111/j.1460-9568.2011.07926.x

Sellers, K. K., Bennett, D. V., Hutt, A., Williams, J. H., & Fröhlich, F. (2015). Awake vs. anesthetized: Layer-specific sensory processing in visual cortex and functional connectivity between cortical areas. *Journal of Neurophysiology*, *113*(10), 3798–3815. https://doi.org/10.1152/jn.00923.2014

Senba, E., Matsunaga, K., Tohyama, M., & Noguchi, K. (1993). Stress-induced c-fos expression in the rat brain: activation mechanism of sympathetic pathway. *Brain Research Bulletin*, *31*(3–4), 329–344. https://doi.org/10.1016/0361-9230(93)90225-Z

Sethi, A. K. (2016). Chapter 1 - Count Alessandro Giuseppe Antonio Anastasio Volta. In *The European Edisons* (pp. 1–35). Palgrave Macmillan, New York. https://doi.org/10.1057/978-1-137-49222-7_1

Shaner, N. C., Campbell, R. E., Steinbach, P. A., Giepmans, B. N. G., Palmer, A. E., & Tsien, R. Y. (2004). Improved monomeric red, orange and yellow fluorescent proteins derived from Discosoma sp. red fluorescent protein. *Nature Biotechnology*, *22*(12), 1567–1572. https://doi.org/10.1038/nbt1037

Sheng, M., & Greenberg, M. E. (1990). The regulation and function of c-fos and other immediate early genes in the nervous system. *Neuron*, *4*(4), 477–485. https://doi.org/10.1016/0896-6273(90)90106-P

Sherrington, C. S. (1906). *The integrative action of the nervous system*. *Yale University Press*. Retrieved from https://doi.org/10.1037/13798-000

Shimomura, O., Johnson, F. H., & Saiga, Y. (1962). Extraction, purification and properties of aequorin, a bioluminescent. *Journal of Cellular and Comparative Physiology*, *59*(3), 223–239. https://doi.org/10.1002/jcp.1030590302

Shlyueva, D., Stampfel, G., & Stark, A. (2014). Transcriptional enhancers : from properties to genome-wide predictions. *Nature Reviews Genetics*, *15*(4), 272–286. https://doi.org/10.1038/nrg3682

Siegel, M. S., & Isacoff, E. Y. (1997). A genetically encoded optical probe of membrane voltage. *Neuron*, *19*(4), 735–741. https://doi.org/10.1016/S0896-6273(00)80955-1

Singh, M., Lujan, B., & Renden, R. (2018). Presynaptic GCaMP expression decreases vesicle release probability at the calyx of Held. *Synapse*, *72*(12), 1–13. https://doi.org/10.1002/syn.22040

Sir Horsley, V., & Clarke, R. H. (1908). The structure and functions of the cerebellum examined by a new method. *Brain*, *31*(1), 45–124. Retrieved from https://doi.org/10.1093/brain/31.1.45

Smiley, john F., Hackett, T. A., Ulbert, I., Karmas, G., Lakatos, P., Javitt, D. C., & Schroeder, C. E. (2008). Multisensory Convergence in Auditory Cortex, I. Cortical Connections of the Caudal Superior Temporal Plane in Macaque Monkeys. *Journal of Comparative Neurology*, *502*(6), 894–923. https://doi.org/10.1002/cne.21325

Soloukey, S., Vincent, A. J. P. E., Smits, M., De Zeeuw, C. I., Koekkoek, S. K. E., Dirven, C. M. F., & Kruizinga, P. (2023). Functional imaging of the exposed brain. *Frontiers in Neuroscience*, *17*(1087912). https://doi.org/10.3389/fnins.2023.1087912

Sommerlandt, F. M. J., Brockmann, A., Rössler, W., & Spaethe, J. (2019). Immediate early genes in social insects: a tool to identify brain regions involved in complex behaviors and molecular processes underlying neuroplasticity. *Cellular and Molecular Life Sciences*, *76*(4), 637–651. https://doi.org/10.1007/s00018-018-2948-z

Sperry, R. W. (1961). Cerebral organization and behavior. *Science*, *133*(3466), 1749–1757. https://doi.org/10.1126/science.133.3466.1749

Spiegel, I., Mardinly, A. R., Gabel, H. W., Bazinet, J. E., Couch, C. H., Tzeng, C. P., … Greenberg, M. E. (2014). Npas4 regulates excitatory-inhibitory balance within neural circuits through cell-type-specific gene programs. *Cell*, *157*(5), 1216–1229.

https://doi.org/10.1016/j.cell.2014.03.058

Stamatakis, A. M., Resendez, S. L., Chen, K. S., Favero, M., Liang-Guallpa, J., Nassi, J. J., … Ghosh, K. K. (2021). Miniature microscopes for manipulating and recording in vivo brain activity. *Microscopy*, *70*(5), 399–414. https://doi.org/10.1093/jmicro/dfab028

Steinmetz, N. A., Buetfering, C., Lecoq, J., Lee, C. R., Peters, A. J., Jacobs, E. A. K., … Harris, K. D. (2017). Aberrant cortical activity in multiple GCaMP6-expressing transgenic mouse lines. *ENeuro*, *4*(5), 1–15. https://doi.org/10.1523/ENEURO.0207-17.2017

Stoica, L., S.Ahmed, S., Gao, G., & Sena-Esteves, M. (2013). Gene transfer to the CNS using recombinant adeno-associated virus. *Current Protocols in Microbiology*, (SUPPL.29). https://doi.org/10.1002/9780471729259.mc14d05s29

Stokes, G. G. (1852). Chapter 21 - On the change of refrangibility of light. In *Phylosophical Transactions of the Royal society of London for the Year MDCCCLII* (pp. 463–561). Retrieved from https://doi.org/10.1098/rstl.1852.0022

Stringer, C., Pachitariu, M., Steinmetz, N., Reddy, C. B., Carandini, M., & Harris, K. D. (2019). Spontaneous behaviors drive multidimensional, brainwide activity. *Science*, *364*(6437). https://doi.org/10.1126/science.aav7893

Strumwasser, F. (1958). Long-Term Recording from Single Neurons in Brain of Unrestrained Mammals. *Science*, *127*(3296), 469–470. https://doi.org/10.1126/science.127.3296.469

Subach, O. M., Cranfill, P. J., Davidson, M. W., & Verkhusha, V. V. (2011). An enhanced monomeric blue fluorescent protein with the high chemical stability of the chromophore. *PLOS ONE*, *6*(12). https://doi.org/10.1371/journal.pone.0028674

Subach, O. M., Gundorov, I. S., Yoshimura, M., Subach, F. V., Zhang, J., Grüenwald, D., … Verkhusha, V. V. (2008). Conversion of Red Fluorescent Protein into a Bright Blue Probe. *Chemistry and Biology*, *15*(10), 1116–1124. https://doi.org/10.1016/j.chembiol.2008.08.006

Sung, Y. K., & Kim, S. W. (2019). Recent advances in the development of gene delivery systems. *Biomaterials Research*, *23*(8). https://doi.org/10.1186/s40824-019-

0156-z

Svoboda, K., Denk, W., Kleinfeld, D., & Tank, D. W. (1997). In vivo dendritic calcium dynamics in neocortical pyramidal neurons. *Nature*, *385*(6612), 161–165. Retrieved from http://dx.doi.org/10.1038/385161a0

Svoboda, K., & Yasuda, R. (2006). Principles of Two-Photon Excitation Microscopy and Its Applications to Neuroscience. *Neuron*, *50*(6), 823–839. https://doi.org/10.1016/j.neuron.2006.05.019

Takahashi, K., Hishida, R., Kubota, Y., Kudoh, M., Takahashi, S., & Shibuki, K. (2006). Transcranial fluorescence imaging of auditory cortical plasticity regulated by acoustic environments in mice. *European Journal of Neuroscience*, *23*(5), 1365–1376. https://doi.org/10.1111/j.1460-9568.2006.04662.x

Takeuchi, K., Shibamoto, S., Nagamine, K., Shigemori, I., Omura, S., Kitamura, N., & Ito, F. (2001). Signaling Pathways Leading to Transcription and Translation Cooperatively Regulate the Transient Increase in Expression of c-Fos Protein. *Journal of Biological Chemistry*, *276*(28), 26077–26083. https://doi.org/10.1074/jbc.M102704200

Terstege, D. J., & Epp, J. R. (2022). Network Neuroscience Untethered: Brain-Wide Immediate Early Gene Expression for the Analysis of Functional Connectivity in Freely Behaving Animals. *Biology*, *12*(1). https://doi.org/10.3390/biology12010034

Thompson, R. F. (2009). Habituation: A History. *Neurobiology of Learning and Memory*, *92*(2), 127–134. https://doi.org/10.1016/j.nlm.2008.07.011

Tian, L., Hires, S. A., Mao, T., Huber, D., Chiappe, M. E., Chalasani, S. H., … Looger, L. L. (2009). Imaging neural activity in worms, flies and mice with improved GCaMP calcium indicators. *Nature Methods*, *6*(12), 875–881. https://doi.org/10.1038/nmeth.1398

Trachtenberg, J. T., Chen, B. E., Knott, G. W., Feng, G., Sanes, J. R., Welker, E., & Svoboda, K. (2002). Long-term in vivo imaging of experience-dependent synaptic plasticity in adult cortex. *Nature*, *420*(6917), 788–794. https://doi.org/10.1038/nature01273

Tratschin, J. D., West, M. H., Sandbank, T., & Carter, B. J. (1984). A human parvovirus,

adeno-associated virus, as a eucaryotic vector: transient expression and encapsidation of the procaryotic gene for chloramphenicol acetyltransferase. *Molecular and Cellular Biology*, *4*(10), 2072–2081. https://doi.org/10.1128/mcb.4.10.2072-2081.1984

Tsien, R. Y. (1980). New Calcium Indicators and Buffers with High Selectivity Against Magnesium and Protons: Design, Synthesis, and Properties of Prototype Structures. *Biochemistry*, *19*(11), 2396–2404. https://doi.org/10.1021/bi00552a018

Tsukano, H., Hishida, R., & Shibuki, K. (2011). Detection of virtual pitch up to 5kHz by mice. *Neuroscience Research*, *71*(2), 140–144. https://doi.org/10.1016/j.neures.2011.06.005

Tsukano, H., Horie, M., Bo, T., Uchimura, A., Hishida, R., Kudoh, M., … Shibuki, K. (2015). Delineation of a frequency-organized region isolated from the mouse primary auditory cortex. *Journal of Neurophysiology*, *113*(7), 2900–2920. https://doi.org/10.1152/jn.00932.2014

Urai, A. E., Doiron, B., Leifer, A. M., & Churchland, A. K. (2022). Large-scale neural recordings call for new insights to link brain and behavior. *Nature Neuroscience*, *25*(1), 11–19. https://doi.org/10.1038/s41593-021-00980-9

Valeur, B., & Berberan-Santos, M. N. (2011). Emergence of Quantum Theory. *Journal of Chemical Education*, *88*(6), 731–738. Retrieved from https://doi.org/10.1021/ed100182h

Vierbuchen, T., Ling, E., Cowley, C. J., Couch, C. H., Wang, X., Harmin, D. A., … Greenberg, M. E. (2017). AP-1 Transcription Factors and the BAF Complex Mediate Signal-Dependent Enhancer Selection. *Molecular Cell*, *68*(6), 1067–1082. https://doi.org/10.1016/j.molcel.2017.11.026

Vogelstein, J. T., Packer, A. M., Machado, T. A., Sippy, T., Babadi, B., Yuste, R., & Paninski, L. (2010). Fast nonnegative deconvolution for spike train inference from population calcium imaging. *Journal of Neurophysiology*, *104*(6), 3691–3704. https://doi.org/10.1152/JN.01073.2009

Wachowiak, M., & Cohen, L. B. (2001). Representation of odorants by receptor neuron input to the mouse olfactory bulb. *Neuron*, *32*(4), 723–735.

https://doi.org/10.1016/S0896-6273(01)00506-2

Waldeyer, W. (1891). *Ueber einige neuere Forschungen im Gebiete der Anatomie der Centralnervensystems*. (Dtsch Med Wochenschr, Ed.) (Vol. 17). https://doi.org/10.1055/s-0029-1206824

Wang, D., Tai, P. W. L., & Gao, G. (2019). Adeno-associated virus vector as a platform for gene therapy delivery. *Nature Reviews Drug Discovery*, *18*(5), 358–378. https://doi.org/10.1038/s41573-019-0012-9

Wang, H., Jing, M., & Li, Y. (2018). Lighting up the brain: genetically encoded fluorescent sensors for imaging neurotransmitters and neuromodulators. *Current Opinion in Neurobiology*, *50*, 171–178. https://doi.org/10.1016/j.conb.2018.03.010

Wang, L., Kempton, J. B., Jiang, H., Jodelka, F. M., Brigande, A. M., Dumont, R. A., … Brigande, J. V. (2020). Fetal antisense oligonucleotide therapy for congenital deafness and vestibular dysfunction. *Nucleic Acids Research*, *48*(9), 5065–5080. https://doi.org/10.1093/nar/gkaa194

Wang, W., Kim, C. K., & Ting, A. Y. (2019). Molecular tools for imaging and recording neuronal activity. *Nature Chemical Biology*, *15*(2), 101–110. https://doi.org/10.1038/s41589-018-0207-0

Wang, W., Wildes, C. P., Pattarabanjird, T., Sanchez, M. I., Glober, G. F., Matthews, G. A., … Ting, A. Y. (2017). A light- and calcium-gated transcription factor for imaging and manipulating activated neurons. *Nature Biotechnology*, *35*(9), 864–871. https://doi.org/10.1038/nbt.3909

Warm, D., Bassetti, D., Schroer, J., Luhmann, H. J., & Sinning, A. (2022). Spontaneous activity predicts survival of developing cortical neurons. *Frontiers in Cell and Developmental Biology*, *10*(937761). https://doi.org/10.3389/fcell.2022.937761

Watakabe, A., Ohtsuka, M., Kinoshita, M., Takaji, M., Isa, K., Mizukami, H., … Yamamori, T. (2015). Comparative analyses of adeno-associated viral vector serotypes 1, 2, 5, 8 and 9 in marmoset, mouse and macaque cerebral cortex. *Neuroscience Research*, *93*, 144–157. https://doi.org/10.1016/j.neures.2014.09.002

Watson, R. J., & Clements, J. B. (1980). A herpes simplex virus type 1 function continuously required for early and late virus RNA synthesis. *Nature*, *285*(5763),

329–330. https://doi.org/10.1038/285329a0

White, B. H. (2016). What genetic model organisms offer the study of behavior and neural circuits. *Journal of Neurogenetics*, *30*(2), 54–61. https://doi.org/10.1080/01677063.2016.1177049

Williams, J. M., Beckmann, A. M., Mason-Parker, S. E., Abraham, W. C., Wilce, P. A., & Tate, W. P. (2000). Sequential increase in Egr-1 and AP-1 DNA binding activity in the dentate gyrus following the induction of long-term potentiation. *Molecular Brain Research*, *77*(2), 258–266. https://doi.org/10.1016/S0169-328X(00)00061-9

Williams, M. E., Feldman, D. H., McCue, A. F., Brenner, R., Velicelebi, G., Ellis, S. B., & Harpold, M. M. (1992). Structure and functional expression of α1, α2, and β subunits of a novel human neuronal calcium channel subtype. *Neuron*, *8*(1), 71–84. https://doi.org/10.1016/0896-6273(92)90109-Q

Wise, K. D., Angell, J. B., & Starr, A. (1970). An Integrated-Circuit Approach to Extracellular Microelectrodes. *IEEE Transactions on Biomedical Engineering*, *17*(3), 238–247. https://doi.org/10.1109/TBME.1970.4502738

Worley, P. F., Christy, B. A., Nakabeppu, Y., Bhat, R. V., Cole, A. J., & Baraban, J. M. (1991). Constitutive expression of zif268 in neocortex is regulated by synaptic activity. *Proceedings of the National Academy of Sciences (PNAS)*, *88*(12), 5106–5110. https://doi.org/10.1073/pnas.88.12.5106

Wu, L., Zhao, H., Weng, H., & Ma, D. (2019). Lasting effects of general anesthetics on the brain in the young and elderly: “mixed picture” of neurotoxicity, neuroprotection and cognitive impairment. *Journal of Anesthesia*, *33*(2), 321–335. https://doi.org/10.1007/s00540-019-02623-7

Xiao, Y., Deng, P., Zhao, Y., Yang, S., & Li, B. (2023). Three-photon excited fluorescence imaging in neuroscience: From principles to applications. *Frontiers in Neuroscience*, *17*(1085682). https://doi.org/10.3389/fnins.2023.1085682

Xu, S., Jiang, W., Poo, M. M., & Dan, Y. (2012). Activity recall in a visual cortical ensemble. *Nature Neuroscience*, *15*(3), 449–455. https://doi.org/10.1038/nn.3036

Yap, E. L., & Greenberg, M. E. (2018). Activity-Regulated Transcription: Bridging the Gap between Neural Activity and Behavior. *Neuron*, *100*(2), 330–348.

https://doi.org/10.1016/j.neuron.2018.10.013

Yuste, R., & Denk, W. (1995). Dendritic spines as basic functional units of neuronal integration. *Nature*, *375*(6533), 682–684. Retrieved from https://doi.org/10.1038/375682a0

Zhang, Q., He, Q., Wang, J., Fu, C., & Hu, H. (2018). Use of TAI-FISH to visualize neural ensembles activated by multiple stimuli. *Nature Protocols*, *13*(1), 118–133. https://doi.org/10.1038/nprot.2017.134

Zhang, Y., Rózsa, M., Liang, Y., Bushey, D., Wei, Z., Zheng, J., … Looger, L. L. (2021). Fast and sensitive GCaMP calcium indicators for imaging neural populations. *BioRxiv*. Retrieved from https://doi.org/10.1101/2021.11.08.467793%0A

Zhang, Z., Ferretti, V., Güntan, I., Moro, A., Steinberg, E. A., Ye, Z., … Franks, N. P. (2015). Neuronal ensembles sufficient for recovery sleep and the sedative actions of α 2 adrenergic agonists. *Nature Neuroscience*, *18*(4), 553–561. https://doi.org/10.1038/nn.3957

Zhou, K., Han, J., Wang, Y., Zhang, Y., & Zhu, C. (2022). Routes of administration for adeno-associated viruses carrying gene therapies for brain diseases. *Frontiers in Molecular Neuroscience*, *15*(988914), 1–13. https://doi.org/10.3389/fnmol.2022.988914

Zolotukhin, S., Byrne, B. J., Mason, E., Zolotukhin, I., Potter, M., Chesnut, K., … Muzyczka, N. (1999). Recombinant adeno-associated virus purification using novel methods improves infectious titer and yield. *Gene Therapy*, *6*(6), 973–985. https://doi.org/10.1038/sj.gt.3300938

Chapter 10. Annexes

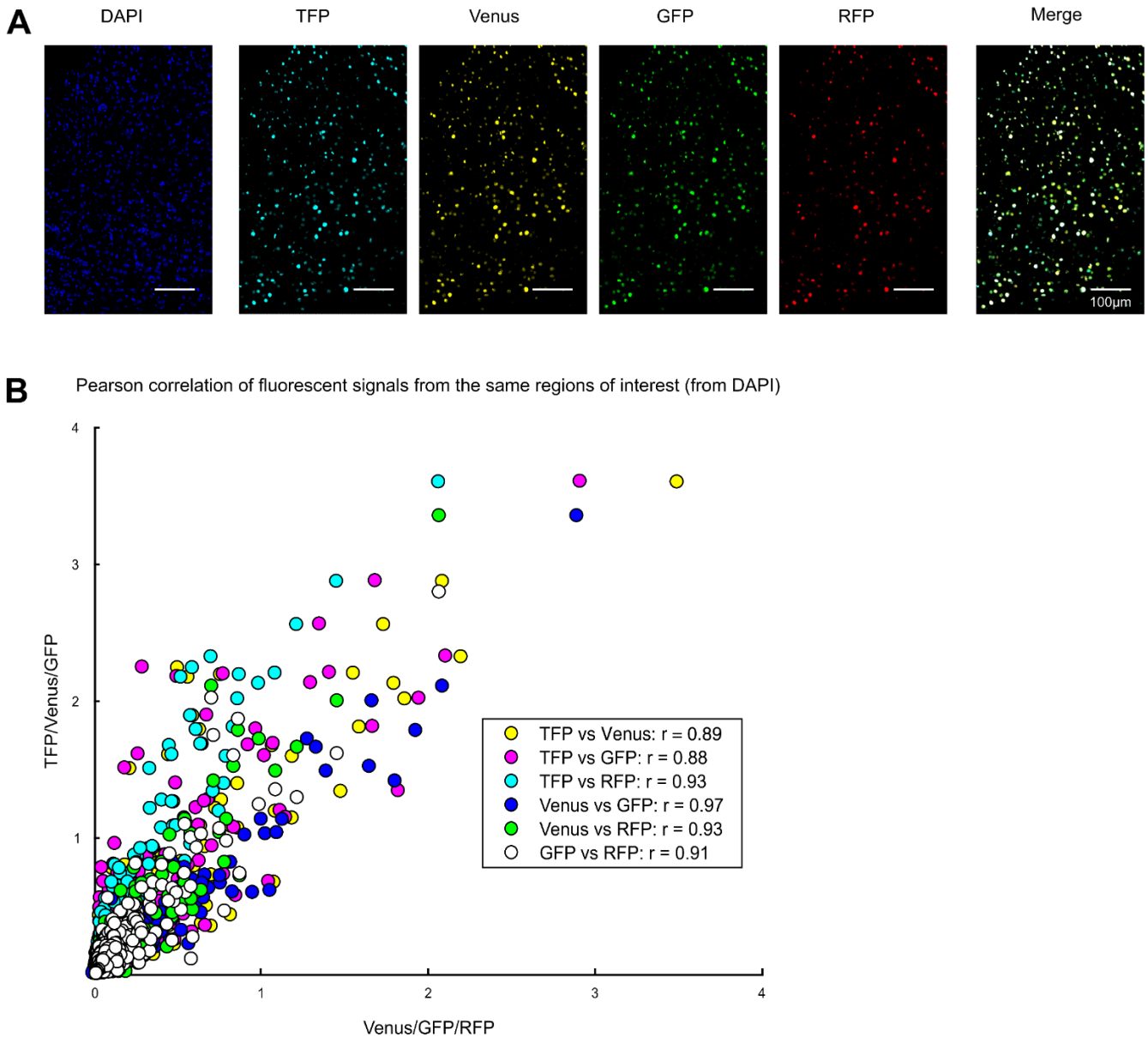

Figure S1. Co-transduction of four AAV2/8 viruses: high similarity of expression in the cells of mouse brain.

(**A**) Confocal images of a cell population from the cortex of a C57BL/6J mouse, imaged with five different wavelengths. The wild type adult mouse was injected with four AAV8 viruses at a comparable titer (see Method in chapter 2.1). The DNA constructs packaged by the viruses contained each a CMV promoter and a gene sequence coding for a fluorescent protein (TFP, Venus, GFP and RFP). About three weeks after the injection, the brain was extracted and fixed with PFA. Then, the brain was sliced, stained with DAPI and mounted on slides and finally imaged (see Method in chapter 7.2). (**B**) Quantification of the signal from the confocal images, based on the regions of interest derived from the DAPI signal (see Method in chapter 7.2). The mean grey values were scatter plotted and compared between the fluorophores with a Pearson correlation. TFP = teal fluorescent protein, GFP = green fluorescent protein, RFP = red fluorescent protein.

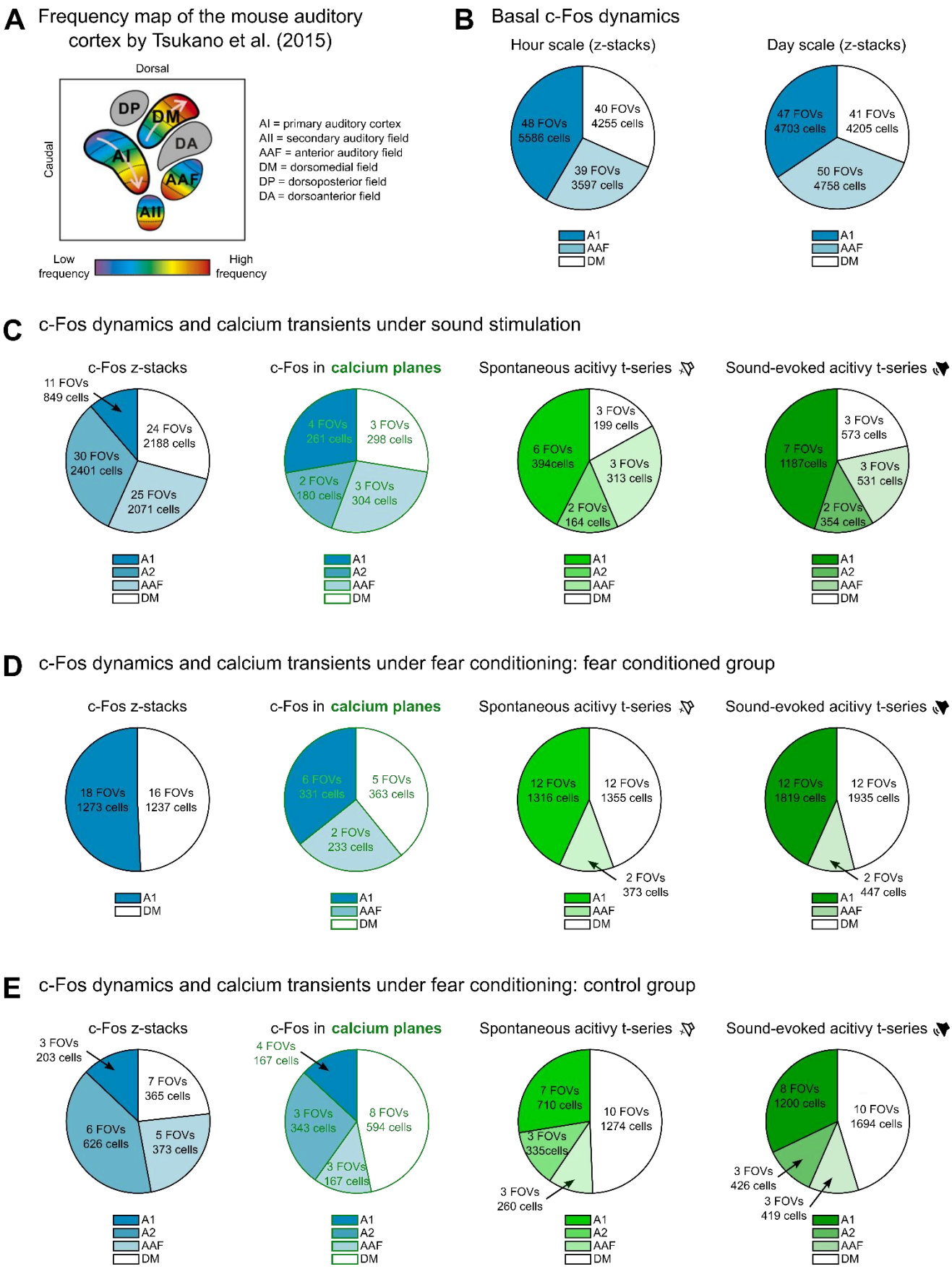

Figure S2. Distribution of cells and FOVs in the different regions of the auditory cortex, for all in vivo experiments.

(**A**) Scheme showing the mouse auditory cortex intrinsic signal during pure tones presentation, of different frequencies (Tsukano et al., 2015). The attribution of the regions from the auditory cortex is based on the intrinsic imaging signal for each mouse (see Method in chapter 2.2). (**B**) Distribution for the datasets from chapter 5. (**C**) Distribution for the datasets from chapter 6. (**D**) Distribution for the datasets from chapter 7.1, for the fear-conditioned group. (**E**) Distribution for the datasets from chapter 7.1, for the control group.

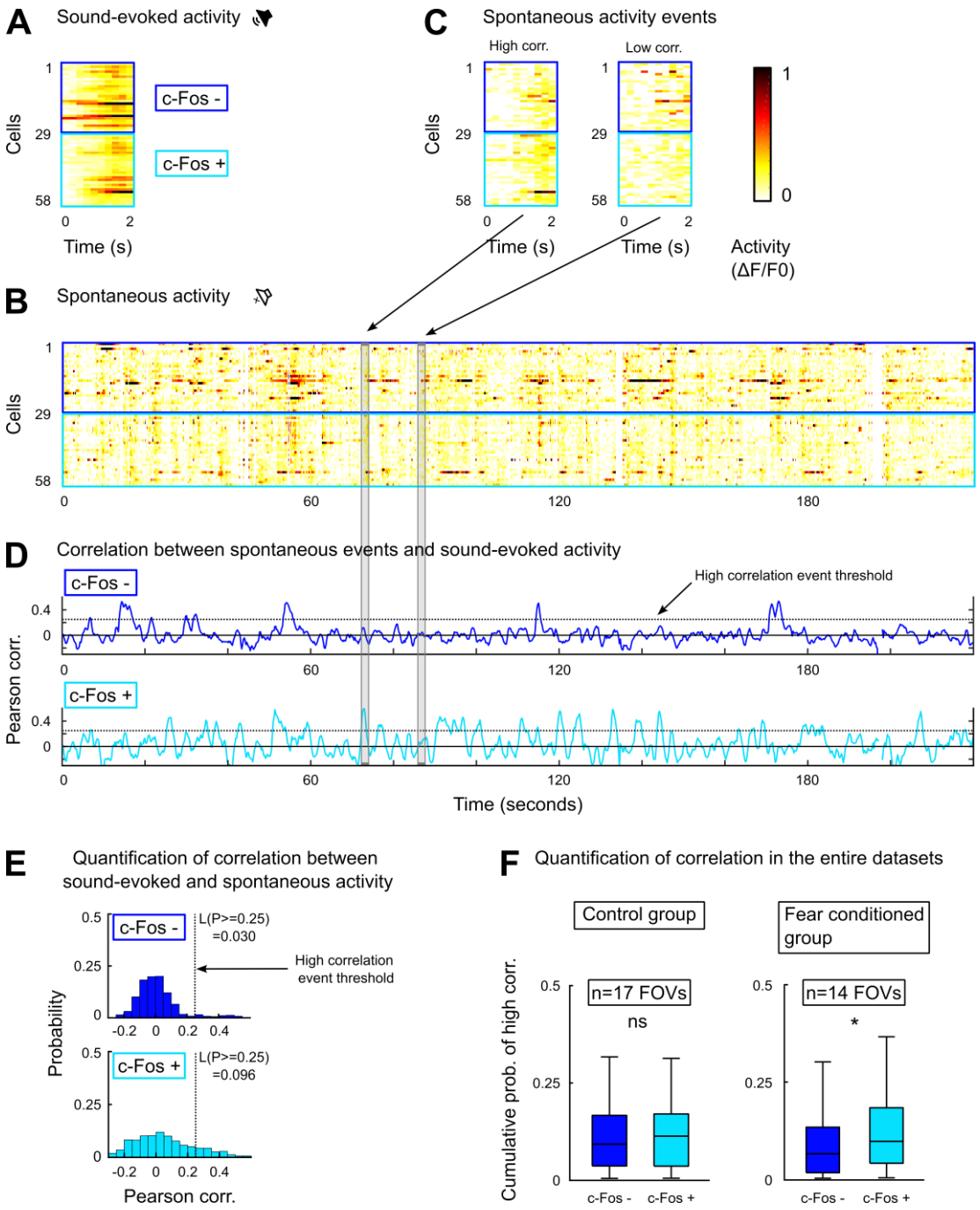

Figure S3. Sound-evoked and spontaneous activity patterns similarity in cells grouped by their c-Fos signal: increased replay events in c-Fos positive cells from fear-conditioned mice.

(**A**) Sound-evoked activity (ΔF/F0) in an exemplary FOV, at fear conditioning day. (**B**) Spontaneous activity (ΔF/F0) in the same exemplary FOV, at fear conditioning day. (**C**) Spontaneous events (part of the recording lasting 2s, like the sound-evoked activity) similar (left) and different (right) from the sound-evoked activity pattern. (**D**) Pearson correlations of the spontaneous and sound-evoked activity patterns along the entire spontaneous activity recording, for c-Fos negative and c-Fos positive cells. (**E**) Quantification of (D). Distribution of Pearson correlation values, and likelihood for these values to be higher than a threshold (0.25), for c-Fos negative and c-Fos positive cells. (**F**) Distribution of the Pearson correlation values in the entire dataset, grouped by c-Fos positive and c-Fos negative cells. Left: control group. Right: fear-conditioned group. Paired t-test: ^{ns} p=0.603, * p=0.007.

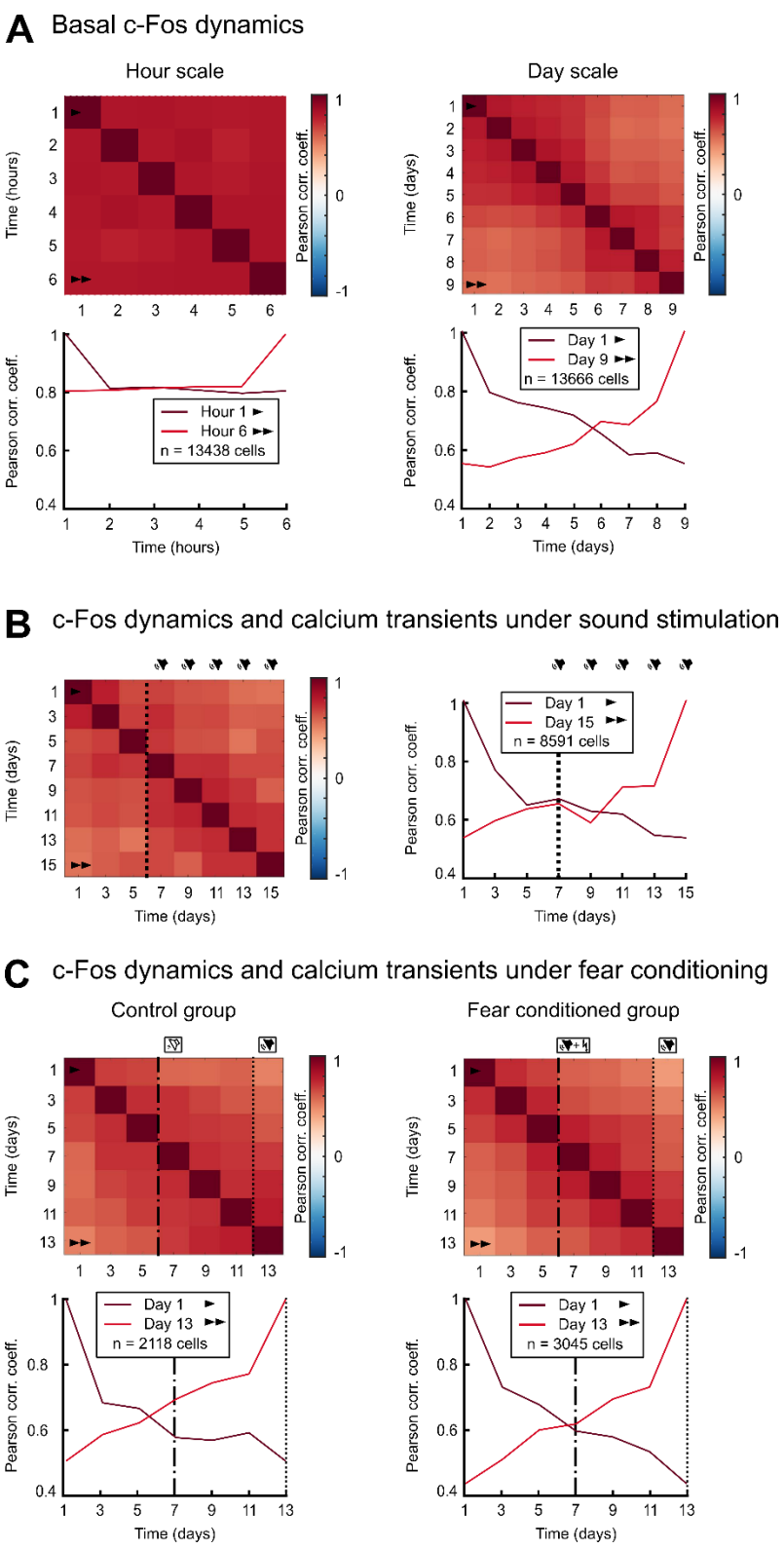

Figure S4. Cell by cell correlation of nuclear signal over time in all in vivo experiments.

(**A**) Correlation matrix and plot of Pearson correlation coefficients for the first and last line of the matrix, for the whole dataset used in the experiments described in chapter 5. (**B**) Same as (A) for the experiment described in chapter 6. (**C**) Same as (A) for the experiment described in chapter 7.1.